



XMM-Newton observations of Type-1
Active Galactic Nuclei

A thesis submitted for the degree of
Doctor of Philosophy
at the University of Leicester.

by

Kim Page

X-ray & Observational Astronomy Group
Department of Physics & Astronomy
University of Leicester

October 2003

© Kim Page 2003

This thesis is copyright material and no quotation from it may
be published without proper acknowledgement.

Declaration

I hereby declare that no part of this thesis has been previously submitted to this, or any other, University as part of the requirement for a higher degree. The work described herein was conducted by the undersigned, except for contributions from colleagues as acknowledged in the text.

Kim Page

October 2003

XMM-Newton observations of Type-1 Active Galactic Nuclei

Kim Page

Abstract

The X-ray spectra of active galaxies are, to a first approximation, power-law-like. Upon more detailed investigation, however, features become apparent: in particular, an emission line corresponding to iron, around 6.4 keV, and the so-called ‘soft-excess’ below ~ 2 keV, whereby an extrapolation of a power-law fit to the 2–10 keV energy band under-predicts the observed counts.

In this thesis, the soft X-ray excesses in samples of both low- and high-luminosity Active Galactic Nuclei (Seyfert galaxies and QSOs respectively) are analysed. This allows the parameters of the soft excess, such as strength and temperature, to be compared with X-ray luminosity. It is found, however, that there are very few differences between Seyfert galaxies and QSOs, leading to the idea that the soft excess is not strongly linked to the luminosity of the object.

Time variability of the soft excess is studied, by investigating three objects (3C 273, PKS 0558–504 and 1H 0419–577) which have each been observed a number of times in the X-ray band. The soft excess is found to vary in each, with the changes possibly due to the Compton cooling of the corona above the accretion disc, brought on by an increase in accretion rate.

Another sample, of high-redshift objects, is also discussed, finding that there is no evidence for spectral evolution or intrinsic absorption in these radio-quiet QSOs. When considering this sample as a whole, there is an indication of spectral flattening at higher energies, suggesting the presence of a Compton reflection hump.

Finally, the existence and strength of the neutral, narrow iron line is investigated, finding that, in the more luminous objects, the equivalent width is much lower; this is the X-ray equivalent of the Baldwin effect found in the optical and UV emission lines.

Publications

Some parts of the work contained in this thesis have been, or are due to be, published in the following papers:

Page, K.L., Turner, M.J.L., Reeves, J.N., O'Brien, P.T. & Sembay, S., 2003, **“Serendipitous Active Galactic Nuclei in the *XMM-Newton* fields of Markarian 205 and QSO 0130–403”**, MNRAS, 338, 1004

Page, K.L., Pounds, K.A., Reeves, J.N. & O'Brien, P.T., 2002, **“The highly variable X-ray spectrum of the luminous Seyfert 1 galaxy 1H 0419–577”**, MNRAS, 330, L1

Page, K.L., O'Brien, P.T., Reeves, J.N. & Turner, M.J.L., 2003, **“An X-ray Baldwin effect for the narrow Fe $K\alpha$ lines observed in active galactic nuclei”**, MNRAS, in press

Page, K.L., Turner, M.J.L., Done, C., O'Brien, P.T., Reeves, J.N., Sembay, S. & Stuhlinger, M., 2003, **“*XMM-Newton* observations of 3C 273”**, MNRAS, submitted

Other publications

Refereed Journals

Porquet, D., Kaastra J.S., Page K.L., O'Brien, P.T., Ward, M.J., Dubau, J., 2003, “**XMM-Newton observation of the Seyfert 1 ESO 198–G24**”, A&A, in press (astro-ph/0302413)

Pounds, K.A., Reeves, J.N., King, A.R., Page, K.L., O'Brien, P.T., Turner, M.J.L., 2003, “**A high velocity ionised outflow and XUV photosphere in the narrow emission line quasar PG1211+143**”, MNRAS, in press (astro-ph/0303603)

Courvoisier, T.J.-L. et al., 2003, “**Simultaneous observations of the quasar 3C 273 with INTEGRAL, XMM-Newton and RXTE**”, A&A Letters, in press (astro-ph/0308212)

Pounds, K.A., King, A.R., Page, K.L., O'Brien, P.T., 2003, “**Evidence of a high velocity ionised outflow in a second narrow line (super-Eddington?) quasar PG0844+349**”, MNRAS, in press (astro-ph/0305571)

Pounds, K.A., Reeves, J.N., Page, K.L., Wynn, G.A., O'Brien, P. T., 2003, “**Fe K emission and absorption features in XMM-Newton spectra of Markarian 766: evidence for reprocessing in flare ejecta**”, MNRAS, 342, 1147

Pounds, K.A., Reeves, J.N., Page, K.L., Edelson, R., Matt, G., Perola, G.C., 2003, “**A simultaneous XMM-Newton and BeppoSAX observation of the archetypal broad line Seyfert 1 galaxy NGC 5548**”, MNRAS, 341, 953

Page, K.L., O'Brien, P.T., Reeves, J.N., Breeveld, A.A., 2003, “**An XMM-Newton observation of the narrow-line Seyfert 1 galaxy Markarian 896**”, MNRAS, 340, 1052

Barcons, X. et al., 2002, “**The XMM-Newton serendipitous survey . II. First results from the AXIS high galactic latitude medium sensitivity survey**”, A&A, 382, 522

O'Brien, P.T., Page, K., Reeves, J.N., Pounds, K.; Turner, M.J.L., Puchnarewicz, E.M., 2001, “**An XMM-Newton observation of the extreme narrow-line Seyfert 1 galaxy Mrk 359**”, MNRAS, 327, L37

Pounds, K., Reeves, J., O'Brien, P., Page, K., Turner, M., Nayakshin, S., 2001, “**An XMM-Newton observation of the luminous Seyfert 1 Galaxy Markarian 509**”, ApJ, 559, 181

Willingale, R., Osborne, J.P., O'Brien, P.T., Ward, M.J., Levan, A., Page, K.L., 2003, “**The X-ray, optical and radio evolution of the GRB030329 afterglow and the associated SN2003dh**”, MNRAS, submitted (astro-ph/0307561)

Pounds, K.A., Reeves, J.N., King, A.R., Page, K.L., 2003, “**Exploring the complex X-ray spectrum of NGC 4051**”, MNRAS, submitted (astro-ph/0310257)

Conference Proceedings

Pounds, K., Page, K., 2003, “**Evidence for massive ionised outflows in (super-Eddington?) AGN**”, in ‘The restless high energy universe’, ed. E.P.J. van den Heuvel, J.J.M. in 't Zand and R.A.M.J. Wijers, Nuclear Physics B Proceedings Supplements, in press

O'Brien, P., Page, K., Turner, M., Done, C., Reeves, J., 2003, “**XMM-Newton monitoring of 3C 273**”, in ‘Quasar Cores and Jets, 25th meeting of the IAU’, Joint Discussion 18, 70

Page, K., Turner, M., Reeves, J., O'Brien, P., Sembay, S., 2003, “**AGN in the XMM fields of Mrk 205 and QSO 0130–403**”, AN, 324, 167

O'Brien, P., Reeves, J., Pounds, K., Page, K., Turner, M., 2003, “**AGN iron lines: the complex picture from XMM-Newton and Chandra**”, in ‘XEUS - studying the evolution of the hot universe’, ed. G. Hasinger, T. Boller, and A.N. Parmer, MPE Report 281, 191

O'Brien, P., Reeves, J., Pounds, K., Page, K., Turner, M., 2002, “**XMM-Newton observations of Type 1 AGN: discs and tori**”, in ‘Workshop on X-ray Spectroscopy of AGN with Chandra and XMM-Newton’, ed. T. Boller, S. Komossa, S. Kahn, H. Kunieda and L. Gallo, MPE Report 279, 77

Reeves, J., O'Brien, P.T., Pounds, K.A., Turner, M.J.L., Page, K., 2002, “**XMM-Newton Observations of PDS 456 and PG 1211+143: Evidence for iron K absorption in the vicinity of the disc?**”, in ‘Workshop on X-ray Spectroscopy of AGN with Chandra and XMM-Newton’, ed. T. Boller, S. Komossa, S. Kahn, H. Kunieda and L. Gallo, MPE Report 279, 175

Page, K., Pounds, K., Reeves, J., O'Brien, P., 2002, **“An *XMM-Newton* observation of the variable Seyfert 1 galaxy 1H 0419-577”**, in ‘Workshop on X-ray Spectroscopy of AGN with *Chandra* and *XMM-Newton*’, ed. T. Boller, S. Komossa, S. Kahn, H. Kunieda and L. Gallo, MPE Report 279, 297

Reeves, J.N., Turner, M.J.L., Pounds, K.A., O'Brien, P.T., Page, K., 2001, **“*XMM-Newton* observations of AGN iron line profiles”**, in ‘New Century of X-ray Astronomy’, ed. H. Inoue and H. Kunieda, ASP Conference Proceedings, 251, 120

Acknowledgements

There are many people who have been incredibly helpful throughout my PhD. Firstly, I wish to thank my two ‘official’ supervisors, Paul O’Brien and Martin Turner, together with ‘unofficial’ ones, James Reeves and Ken Pounds. Although an excess of supervisors can lead to more suggestions for work to do, it also gave me access to more brains to pick!

Thanks must go to my fellow Wednesday-afternoon-tea-makers, Tim, Simon and Alex (the first years these days just don’t understand the delicate nature of biscuit provision...) and all the other post-grads and post-docs who have helped make these three years of research enjoyable. Also Anita – I bet that, when we first started in U3L, you didn’t think we’d still be studying together 14 years later! I’ll miss those lunchtime gossip sessions...

I am very grateful to my mother, for her support and the strategic placing of my papers around her house to look impressive and ‘to blind people with science’! Also my sister, Zoë, whose ops on Dooyoo and Ciao have livened up many a dull morning!

Finally, I dedicate this thesis to Richard, without whom I would still be the Queen Geek of the Foyer.



In memory of my father and grandmother.

Rhoderick William Colin Page (1951-2001)

Hilda Needham (1921-2002)

We dance round in a ring and suppose
While the Secret sits in the middle and knows.

Robert Frost

Contents

1	Introduction	1
1.1	Active Galactic Nuclei	1
1.1.1	What are they and why study them?	1
1.1.2	History	2
1.1.3	The inner regions	3
1.1.4	Observations at different wavelengths	3
1.1.5	Nomenclature	7
1.2	Unification of AGN	12
1.3	X-ray emission from AGN	17
1.3.1	Emission mechanisms	17
1.3.2	The accretion process	19
1.3.3	The hard X-ray spectrum	21
1.3.4	The soft excess	24
1.3.5	Comptonisation and the accretion disc	28
1.4	XMM-Newton	34
1.4.1	Comparison with other X-ray observatories	36
1.4.2	Data reduction and analysis	37
1.5	Aims of this thesis	39
2	Accretion at low luminosity	41
2.1	Narrow Line and Broad Line Seyfert 1 galaxies	41
2.2	Spectral analysis	44
2.2.1	Blackbody parameterisation of the soft excess	47
2.2.2	Features of the soft excess	52

2.2.3	The Comptonisation model	55
2.3	Discussion	56
2.4	Summary	67
3	Accretion at high luminosity	70
3.1	Quasi-stellar objects	70
3.2	Spectral analysis	71
3.2.1	Blackbody parameterisation of the soft excess	74
3.2.2	The Comptonisation model	78
3.3	Discussion	81
3.4	Summary	84
4	Time variability of the soft excess	88
4.1	3C 273	89
4.1.1	Introduction	89
4.1.2	XMM-Newton observations	90
4.1.3	Spectral analysis	92
4.1.4	RGS data	102
4.1.5	Optical and UV data	106
4.1.6	Discussion	107
4.1.7	Conclusions: 3C 273	117
4.2	PKS 0558–504	118
4.2.1	Introduction	118
4.2.2	XMM-Newton observations	118
4.2.3	Spectral analysis	119
4.2.4	RGS data	125
4.2.5	Optical and UV data	127
4.2.6	Discussion	128
4.2.7	Conclusions: PKS 0558–504	134
4.3	1H 0419–577	137
4.3.1	Introduction	137
4.3.2	XMM-Newton observations	139

4.3.3	Spectral analysis	139
4.3.4	Comparison with other observations	140
4.3.5	Discussion	147
4.3.6	Conclusions: 1H 0419–577	151
4.4	Summary	151
4.5	Caveat	153
5	A complete sample of X-ray selected AGN	155
5.1	XMM-Newton observations	158
5.2	Spectral analysis	159
5.2.1	Soft excess and absorbing column density	161
5.2.2	Spectral evolution	164
5.2.3	Spectral curvature	165
5.3	High flux objects	168
5.4	Discussion	171
5.4.1	Absorbing column density	171
5.4.2	Spectral evolution	173
5.4.3	Spectral curvature	174
5.5	Summary	175
6	An X-ray Baldwin effect	176
6.1	XMM-Newton observations	178
6.2	Discussion	185
6.2.1	The broad-line region	186
6.2.2	The molecular torus	191
6.3	Summary	193
7	Summary and discussion of results	194
7.1	The soft excesses in low- and high-luminosity AGN	194
7.2	Time variability of the soft excess	201
7.3	High redshift QSOs	201
7.4	The narrow Fe $K\alpha$ line	202
7.5	Past and future work	203

List of Figures

1.1	The innermost region of an AGN.	4
1.2	An SED of 3C 273.	5
1.3	This plot shows typical optical spectra for the different groups of AGN.	8
1.4	A <i>Chandra</i> image of 3C 273, showing the central nucleus and the jet responsible for the strong radio emission.	11
1.5	A schematic diagram of the unified theory of AGN.	13
1.6	A plot showing how the principal eigenvectors are related for different types of AGN.	15
1.7	A schematic of the features of an X-ray spectrum.	21
1.8	The expected reflection spectrum due to a power-law source illuminating a slab of cold material.	23
1.9	The soft excess for six Seyfert 1 galaxies, measured by <i>XMM</i>	25
1.10	The spectrum for low energy photons being Comptonised by hot electrons.	30
1.11	The top plot shows the blackbody emission from a typical Shakura-Sunyaev (SS) disc. The lower plot illustrates the emission seen if the mass-accretion rate is high enough for advection to become important.	33
1.12	The <i>XMM-Newton</i> payload.	35
1.13	A comparison of the mirror effective areas of recent X-ray observatories.	37
2.1	The soft excess of Mrk 896, an NLS1.	47
2.2	The unfolded spectrum of the blackbody fit to the NLS1 Mrk 896.	52
2.3	The broad-band spectrum of NGC 5548 (MOS data), showing the power-law fitted above 3 keV, extrapolated down to 0.3 keV.	54

2.4	The warm absorber model to the joint MOS 2 and RGS data of NGC 5548.	54
2.5	The broad-band spectrum of Mrk 896 modelled by two Comptonised components and an iron line.	58
2.6	When considering the 0.2–10 keV (observed) energy band, the ‘power-law’ Comptonised component tends to be more luminous than the soft excess.	60
2.7	The extrapolated Comptonisation model for Mrk 896.	60
2.8	Extrapolating the model to lower energies allows the total luminosity of the soft excess to be calculated.	61
2.9	The top plot shows the variation of the ratio of soft excess blackbody to power-law luminosities over the 0.2–10 keV band with total 0.2–10 keV luminosity; the lower plot compares the normalisations of the Comptonised components with the luminosity, both for the Seyfert sample	63
2.10	Plot of soft excess strength against power-law slope over the 2–10 keV rest frame for each Seyfert galaxy.	64
2.11	Plot showing the relative strength of the soft excess in comparison to the two-point optical to X-ray slope, α_{ox} for the Seyfert galaxies.	65
2.12	Investigating the link between the shape of the soft excess and α_{ox} for the Seyferts reveals various correlations. Both the slope and the temperature of the soft excess are anti-correlated with α_{ox} , while the optical depth shows a positive correlation.	66
2.13	Luminous Seyfert galaxies do not, necessarily, have hot soft excesses.	67
2.14	Luminous Seyfert galaxies have bright soft excesses, whether the luminosity is measured over the observed 0.2-10 keV band, or over the extended 0.001-10 keV range.	68
3.1	The soft excess of Q 0056–363 can be well modelled by three blackbody components.	76
3.2	Fitting the X-ray spectrum of Q 0056–363 with two Comptonised components and an iron line.	79
3.3	The variation of the ratio of soft excess to power-law luminosities over the 0.2–10 keV band with total 0.2–10 keV luminosity for the sample of QSOs.	81
3.4	There does not appear to be a relationship between the strength of the soft excess and the 2–10 keV power-law slope for QSOs.	83

3.5	As for the Seyfert sample, the soft excess/power-law luminosity ratio is not correlated with the strength of the Big Blue Bump for the QSO sample.	84
3.6	There is an inverse relationship between the slope of the soft excess and α_{ox} for the QSOs.	85
3.7	Consistent with the Seyfert galaxies, the luminosity of the soft excess is higher in more luminous objects, but the temperature is independent of the total luminosity.	86
4.1	The result of running <i>epatplot</i> on the MOS 2 spectrum of 3C 273 in revolution 96.	93
4.2	To confirm that the broad line is not simply an artifact introduced by varying photon indices, all ten datasets were fitted simultaneously, while allowing the slope to vary. The co-added residuals are shown above, demonstrating the presence of a broad emission feature.	94
4.3	The soft excess of 3C 273 during revolution 94.	95
4.4	An unfolded plot of the blackbody fit to the revolution 94 3C 273 MOS 2 data.	98
4.5	The variation of the individual blackbody luminosities with that of the entire soft excess, for 3C 273.	99
4.6	Agreeing with all the previous data, there is no relationship between the relative strength of the soft excess (compared to the power-law) and the broad-band luminosity for 3C 273. As was found for the QSOs, although not for the Seyferts, there is also no link between the luminosity ratio and the power-law slope.	100
4.7	The best fit Comptonisation model to the MOS 2 3C 273 data from revolution 94.	104
4.8	The plot shows an absorption feature which may be due to O VII He α at zero redshift in the RGS spectrum of 3C 273. . .	105
4.9	The curves show the extrapolation of the 3C 273 X-ray Comptonisation model down to optical energies for input (disc) temperatures of, from left to right, 2, 5 and 10 eV. The top plot assumes the input photons follow a simple blackbody distribution, while the lower one has a disc blackbody as the input to the model.	108
4.10	The soft excess of 3C 273 measured during each observation. .	109
4.11	Over the limited 0.3-10 keV band, the steeper the slope of the soft excess in 3C 273, the less luminous it appears.	110

4.12	The variation of the spectral slope of the soft excess with the number of photons, over the 1 eV–10 keV range, for 3C 273.	111
4.13	The variation of the electron temperature with slope of the soft excess in 3C 273, for fixed values of the optical depth.	113
4.14	An example (rev. 370) of the correspondance between the best fit contours from the X-ray Comptonisation model and the line of constant optical depth for 3C 273.	114
4.15	For an assumed constant optical depth, the Compton cooling of the corona is clear to see in 3C 273.	115
4.16	The fractional variability amplitude of the MOS 2 data over the ten observations of 3C 273.	115
4.17	Although the luminosity of the separate Comptonised components appear to be independent, there is a positive correlation between the photon indices in the spectra of 3C 273.	116
4.18	The measured 3–10 keV photon index may be related to the 3–10 keV flux in 3C 273.	117
4.19	The soft excess of PKS 0558–504, as measured by <i>XMM</i> during revolutions 153 and 34.	120
4.20	An unfolded plot showing the blackbody fit to the soft excess of PKS 0558–504, during revolution 84.	122
4.21	Agreeing with the samples investigated in previous chapters, there is no correlation between the strength of the soft excess and the 0.2–10 keV luminosity (top). In the same fashion as the Seyfert galaxies, it is noted that the stronger soft excesses occur when the 2–10 keV power-law slope is steeper in the spectra of PKS 0558–504.	124
4.22	This absorption feature in the RGS data from the revolution 153 observation of PKS 0558–504 may correspond to zero-redshift O VII He α	127
4.23	An example (rev. 42) of the extrapolation of the X-ray Comptonisation model to lower energies.	129
4.24	As for 3C 273, a (weak) negative correlation between the soft excess slope and the photon flux over the 0.2–10 keV band is found for PKS 0558–504. If, however, the Comptonisation model is extrapolated down to 1 eV, the observed correlation is positive.	130
4.25	The optical depth of the corona in PKS 0558–504 decreases with an increasing number of photons, calculated for the 1 eV–10 keV band.	131

4.26	There is no strong evidence for Compton cooling in PKS 0558–504, with the temperature not dependant on the photon flux. . . .	131
4.27	The plot shows the variation of the temperature and slope of the soft excess, for lines of constant optical depth, in PKS 0558–504.	132
4.28	Superimposing the curve signifying $\tau = 19.5$ on the contour plots allows a range of consistent temperatures to be read off.	133
4.29	Contrary to the result found for 3C 273, setting the optical depth to a constant value does not clearly show a Compton cooling effect in PKS 0558–504.	133
4.30	Although the soft and hard components do not mirror each other precisely, there is a similarity in the variation of the luminosities of the components, particularly during the earlier observations of PKS 0558–504.	135
4.31	From weighted linear regression, there is a slight positive correlation between the luminosities of the hard and soft Comptonised components, but a weak negative correlation between the corresponding slopes of the PKS 0558–504 spectra. . . .	136
4.32	The 2–10 keV band power-law slope is independent of the flux level in PKS 0558–504.	137
4.33	2–10 keV power-law fit to the PN spectrum, extrapolated down to 0.2 keV, showing the soft excess of 1H 0419–577. . .	140
4.34	Unfolded plot of the best fit to the 1H 0419–577 <i>XMM</i> data. .	141
4.35	Plot showing the difference between the unfolded spectra for the <i>XMM</i> , <i>ASCA</i> and <i>ROSAT</i> observations of 1H 0419–577. . .	144
4.36	The plot shows the ratio of the BB and power-law luminosities against both the 0.5–10 keV luminosity and the 2–10 keV photon index. Both show a positive correlation in 1H 0419–577.	145
4.37	Best fit Comptonisation model for the EPIC PN 1H 0419–577 dataset.	147
4.38	This plot shows the soft excess slope plotted against the flux of photons over the 0.5–10 keV and 1 eV–10 keV bands; both show positive correlations for 1H 0419–577.	149
4.39	Comparing the 1H 0419–577 data from <i>ASCA</i> observations in 1996 and <i>XMM</i> in 2000, the electron corona producing the soft excess can be seen to be cooler in the presence of more seed photons. Likewise, the slope at higher energies becomes steeper/softer.	150
5.1	The 2–10 keV luminosities of radio-quiet objects are plotted against redshift.	157

5.2	Plot of 2–10 keV Γ against redshift for each of the 23 sources.	161
5.3	The broad-band spectrum of QSO 0130–403 is best fitted by a power-law of $\Gamma \sim 2.09$ and a broad Fe emission line at 6.6 keV (in the rest frame).	169
5.4	Broad-band spectra for those QSOs with a 2–10 keV flux of greater than 5×10^{-14} erg cm ⁻² s ⁻¹ .	170
5.5	The joint sample of radio-quiet and radio-loud QSOs, from <i>XMM</i> and <i>ASCA</i> respectively.	173
6.1	The decrease in EW of the narrow, neutral iron line with luminosity.	181
6.2	The correlation between luminosity and redshift for the sample of AGN.	182
6.3	Averaging the iron line equivalent widths within luminosity bins clearly shows the X-ray Baldwin effect, even when excluding the radio-loud objects.	184
6.4	The equivalent width of the Fe K α line against the rest frame 2–10 keV photon index.	185
6.5	A comparison of the equivalent width of the narrow Fe K α line and the FWHM and EW of H β .	188
6.6	The equivalent widths of the optical Fe II and X-ray Fe K α lines.	189
7.1	The stronger soft excesses correspond to those objects with the steeper 2–10 keV power-law slopes.	196
7.2	The soft excesses of Seyferts and QSOs have comparable temperatures and strengths.	197
7.3	The soft excesses of QSOs and Seyfert galaxies show the same range of optical depths.	198
7.4	There is no difference in the soft excess slopes between the Seyfert and QSO samples: soft excess Γ is independent of 0.2–10 keV luminosity. Likewise, the steeper slopes do not necessarily correspond to the more luminous soft excesses.	199

List of Tables

1.1	Comparison of recent X-ray satellites.	36
2.1	The Seyfert and Narrow Line Seyfert 1 galaxies covered in this chapter, ordered by right ascension within their separate groups.	44
2.2	The details of the <i>XMM</i> observations performed of the Seyfert sample.	45
2.3	Fits to the Seyfert sample over the 2–10 keV rest frame bands.	49
2.5	Fits to the Seyfert galaxies over the 0.2–10 keV (observed frame) energy band.	51
2.6	The warm absorber <i>xabs</i> fit to the NGC 5548 data.	55
2.7	Comptonisation fits to the broad-band Seyfert spectra.	57
3.1	The QSOs in this sample: radio-quiet then radio-loud QSOs, ordered by RA.	72
3.2	The details of the <i>XMM</i> observations performed of the QSOs.	73
3.3	Fits over the 2–10 keV rest frame bands, for the QSO sample.	75
3.4	Fits over the 0.2–10 keV (observed frame) energy band, for the QSOs.	77
3.5	Values for the warm absorber (or excess neutral absorption) components and absorption edges where required; these were derived from EPIC data.	78
3.6	Comptonisation fits to the broad-band QSO spectra.	80
4.1	The limits on the equivalent widths (EW) of neutral (6.4 keV) and ionised (6.7 keV) iron emission in 3C 273.	94
4.2	Power-law and blackbody fits to the MOS 2 3C 273 spectra.	97
4.3	Comptonisation model fits to the spectra of 3C 273.	103
4.4	Optical and UV magnitudes for 3C 273.	106

4.5	Power-law fits to the 2–10 keV PKS 0558–504 spectra.	121
4.6	The limits on the strengths of narrow (0.01 keV) and broad (0.5 keV) lines (both neutral and ionised) in the PKS 0558–504 data.	121
4.7	Fits to the broad-band (0.2–10 keV) spectra of PKS 0558–504.	123
4.8	Comptonisation fits to the broad-band PKS 0558–504 data.	126
4.9	Optical and UV magnitudes for PKS 0558–504.	128
4.10	Fits to the <i>XMM-Newton</i> data from 2000 December.	141
4.11	Fits to the <i>ASCA</i> , <i>SAX</i> and <i>XMM</i> data.	143
5.1	QSOs with known redshifts in the fields of Mrk 205 and QSO 0130–403.	160
5.2	Power-law slopes over a range of energy bands for the sources in the combined Mrk 205 and QSO 0130–403 fields.	167
6.1	The Type-1 AGN included in this sample, ordered by redshift (left-hand then right-hand columns) within the radio-quiet and radio-loud groups.	179
6.2	The objects in the sample for which broad lines were statistically required.	180

Chapter 1

Introduction

1.1 Active Galactic Nuclei

1.1.1 What are they and why study them?

Active Galactic Nuclei are the brightest continuously emitting objects in the Universe, reaching bolometric luminosities of 10^{40} – 10^{48} erg s⁻¹. Active galaxies often appear as star-like sources, but show partly non-thermal spectra; the non-stellar emission is concentrated in the very centre of the galaxies, leading to the name *Active Galactic Nuclei*, or AGN. This strong nuclear emission is now thought to be due to matter in an accretion disc falling into a super-massive black hole (SMBH) of $\sim 10^6$ – 10^9 M_⊙ (Lynden-Bell 1969), though see below for earlier ideas.

Because AGN are so luminous, they can be observed out to very high redshifts; at the time of writing, the most distant quasar (Section 1.1.5) is at $z = 6.28$ (Brandt et al. 2002; Mathur, Wilkes & Ghosh 2002). This makes them excellent probes of the early Universe, since $z = 6$ corresponds to a look-back time of almost 95% of its age, and should further our understanding of the evolution of the Universe as a whole. The intergalactic medium can also be well studied, by looking at the absorption lines in the spectra of distant quasars, as can gravitational lensing effects. The huge masses of the central black holes, and the corresponding extreme gravitational fields, allow the investigation of General

Relativity; for example, as discussed later, some AGN show very broad, skewed iron line profiles in their X-ray spectra, suggesting that they are formed close to a spinning black hole (Wilms et al. 2001).

1.1.2 History

Although it is now generally accepted that AGN have central black holes, this was not always the case. Alternative suggestions have included bursts of star formation, leading to multiple supernova explosions (Colgate & Cameron 1963), supermassive stars, giant pulsars or spinars – rapidly rotating, self-gravitating objects – (Hoyle & Fowler 1963), collections of quarks (Burbidge & Burbidge 1967), *white* holes (Ne’Eman 1965) or even matter-antimatter annihilation (Burbidge 1956). All that was initially known was that AGN were extremely bright and yet the region emitting this radiation had to be very small, because of the rapid time-variability. Lynden-Bell (1969) showed that nuclear reactions (i.e., stars) could not produce the energy required; accretion, however, is one of the most efficient processes in the Universe – more than an order of magnitude more so than nuclear burning – and would be able to power the observed luminosities.

The optical/UV emission lines in the spectra of AGN are found to show substantial velocity broadening, indicating that, if these Doppler shifts are due to gravity, then the central object must be massive and compact; a black hole would fit the bill perfectly. As final support for this theory, the jets observed in radio-loud AGN tend to be well collimated; this is most easily explained by the presence of a single, possibly rotating body at the centre.

It is now thought that all galaxies, both normal and active, probably contain central SMBHs (e.g., Kormendy 1988; Ford et al. 1994; Bertola et al. 2003). More specifically, it is certain that the Milky Way contains a black hole. Previous measurements of stellar velocities (Eckart et al. 2002; Genzel et al. 2000; Ghez et al. 1998; Eckart & Genzel 1996), combined with X-ray emission and flaring from the Galactic centre (Baganoff et al. 2003,b) indicated that the central mass was very likely to be a black hole. This was confirmed by Schödel et al. (2002). By tracing $2/3$ of the orbit of the star closest to

Sag. A* (the compact radio source and what was a black hole *candidate* at the centre of our Galaxy), Schödel et al. calculated that the central point mass of the Milky Way was $(3.7 \pm 1.5) \times 10^6 M_{\odot}$. This can no longer be described by a dark stellar cluster, or a ball of degenerate fermions; it is definitely a black hole.

Even if all galaxies do possess SMBHs, it is unknown whether all nuclei pass through an active stage in their lives, or if some are quiescent, due to a lack of material to feed the black hole.

1.1.3 The inner regions

Figure 1.1, taken from Collin & Huré (2001) shows a schematic view of the innermost regions of an AGN, for a typical $10^8 M_{\odot}$ black hole, accreting at $0.1 \dot{M}_{Edd}$ (where \dot{M}_{Edd} is the Eddington accretion rate; see later). The middle panel shows the region where the optical emission is thought to originate, while the UV, EUV and X-ray components are formed in the hotter areas, closer in to the black hole. The central-most region (left-hand panel) is where the putative hot corona, suggested for the Comptonisation models (see Section 1.3.5), would exist. The standard model of accretion discs (Keplerian orbits, optically thick) is likely to break down at small radii, because of thermal instabilities. Again, at large distances (right-hand panel), the theory must be modified because the vertical structure of the disc becomes important. Gravitational instabilities lead to higher random velocities, which may cause the disc to fragment into clouds (e.g., Shore & White 1982). This clumpy disc may become geometrically thick and might stretch out to the molecular torus suggested by unification models (as discussed below). See Collin & Huré (2001) and their references for more details.

1.1.4 Observations at different wavelengths

AGN emit energy over the whole electromagnetic (EM) spectrum, from radio waves right up to γ -rays. Figure 1.2 plots the average spectrum of 3C 273 over all wavebands as an example; this is known as a Spectral Energy Distribution, or SED. The following sections give a brief overview of these energy bands.

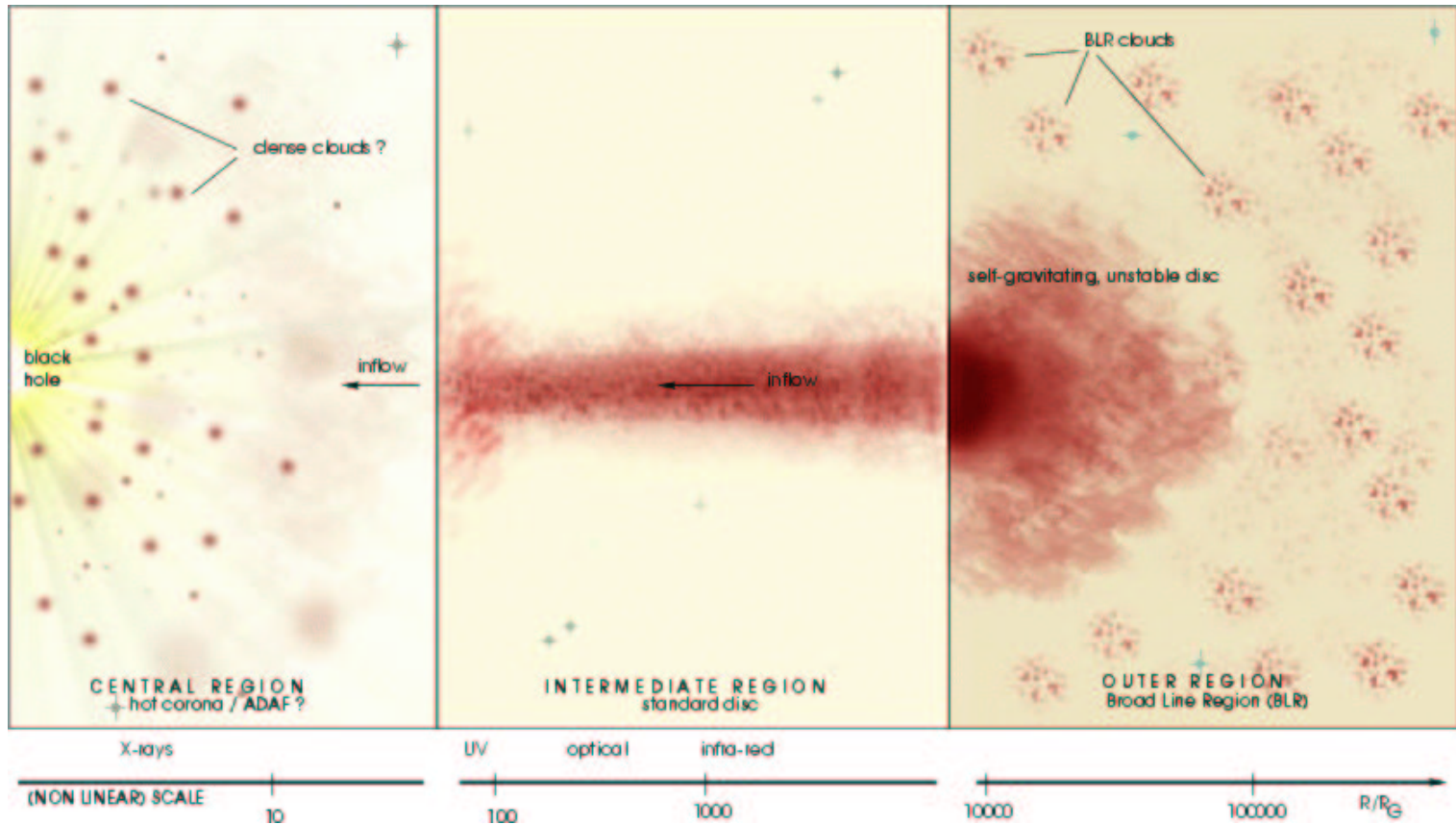


FIGURE 1.1. The innermost region of an AGN, taken from Collin & Huré (2001), from the central black hole out to the Broad Line Region, showing how the accretion disc is likely to change.

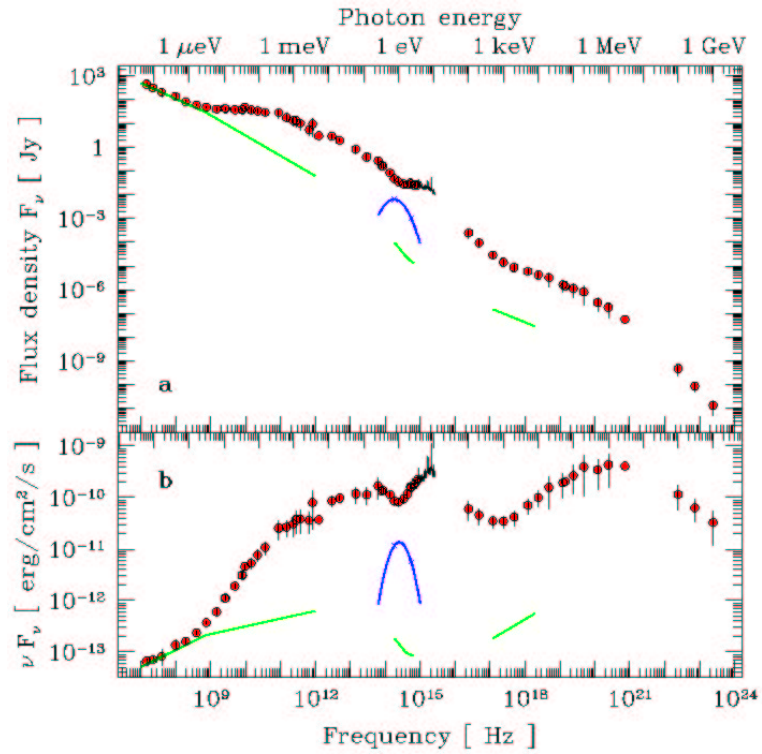


FIGURE 1.2. An SED of 3C 273, taken from Türler et al. (1999); (a) plots the flux density, F_ν , data and (b) the νF_ν representation. The green line signifies the contribution from the jet, while the blue parabola suggests emission from the host galaxy.

Radio observations

It is found that some ($\sim 10\%$) AGN are strong radio sources, while others have much weaker emission at radio wavelengths. The usual definition of radio-loudness is that R , the radio (5 GHz) to optical (B -band) flux ratio, is $\gtrsim 10$. Early studies suggested a bimodal distribution: there appear to be few ‘radio-intermediate’ AGN, with most being either strongly radio-loud or showing very little in the way of radio emission. This bimodality is, however, no longer certain; although some surveys do find a definite separation between RL and RQ objects (e.g., Ivezić et al. 2002), more and more are concluding that there is a continuous transition between the two types, with the apparent dichotomy due to selection effects (Cirasuolo et al. 2003; Hewett, Foltz & Chaffee 2001; White et al. 2000). The radio spectrum takes the form of a power-law and is thought to be formed

through Synchrotron radiation (Jones, O’Dell & Stein 1974; see also Section 1.3.1).

Infrared observations

The origin of the IR continuum in AGN is not yet entirely certain. One suggestion is that the IR emission is an extension of the radio power-law, due to the Synchrotron Self-Compton process. However, there is growing evidence that the emission is almost all thermal in nature and is likely to be linked to absorption/emission from dust. There is a bump in each spectrum at wavelengths longer than $\sim 1 \mu\text{m}$, which would coincide with emission from dust at $\lesssim 2000 \text{ K}$, around the expected temperature for grains in the nuclear regions. Also, the IR continuum seems to vary in the same manner as the optical/UV emission, but with a time delay corresponding to the light travel-time between the central, compact optical/UV-emitting region and the much more distant dust grains (e.g., Clavel, Wamsteker & Glass 1989).

Optical and UV observations

AGN were first identified at optical wavelengths, with Edward Fath at the Lick Observatory noting that NGC 1068 showed strong emission lines in its spectrum, in 1908. It wasn’t until 1943 that Carl Seyfert realised there was a distinct group of such objects with spectra dominated by strong nuclear emission lines. These spectra showed two different types of optical lines, with the permitted emission lines (e.g., the Balmer series of hydrogen) sometimes appearing to be broader. The narrow lines correspond to both permitted (e.g., hydrogen and helium) and forbidden (e.g., carbon, nitrogen, neon, oxygen) transitions. When considering the continuum, rather than the lines, the dominant feature in the optical/UV spectrum is a broad ‘hump’, known as the Big Blue Bump (BBB). This is thought to be thermal emission, very likely from the accretion disc surrounding the black hole (e.g., Shields 1978; Malkan & Sargent 1982). The soft X-ray excess, which will be discussed later, has been suggested to be the Comptonised tail of this BBB.

X-ray and γ -ray observations

At the higher energy end of the EM spectrum, AGN are also observed in the X-ray and γ -ray regime, with all being luminous X-ray Sources (Elvis et al. 1978). The X-rays may come from the inner regions of the accretion disc, or possibly a hot corona above the accretion disc (Haardt & Maraschi 1991; see Section 1.3.5 for more details), while the very high-energy γ -rays are thought to be produced by inverse-Compton scattering of photons off the highly energetic electrons within the jet (Zhang & Cheng 1997). Both X-ray and γ -ray spectra are, to a first approximation, power-law-like [i.e., $F(\nu) \propto \nu^{-\alpha}$; often written in terms of Γ , where $\Gamma = \alpha + 1$; Γ is the photon spectral index, while α is the energy index], although not necessarily with the same spectral index. At higher energies, around 40 MeV or so, most sources show a sharp spectral turnover (Collmar, Schönfelder & Zhang 2002).

1.1.5 Nomenclature

AGN are sub-divided into smaller groups, based mainly on their optical properties and luminosities. These classifications are briefly summarised below, with Figure 1.3 showing typical spectra for the different types of AGN.

- Seyfert galaxies were originally classified by Carl Seyfert (Seyfert 1943). These are radio-quiet objects and have high central surface brightness, although the host galaxy is still clearly detectable; they tend to be spirals, with massive galactic bulges and the presence of an interstellar medium. Since their original discovery, the classification has evolved such that they are also spectroscopically identifiable by the presence of high-ionisation emission lines. Seyfert galaxies are, themselves, divided into two groups – Seyfert 1s and Seyfert 2s (Sy1s and Sy2s) – as was first realised by Khachikian & Weedman (1974).
 - Type-1 Seyfert galaxies are those with highly ionised, broad permitted lines, together with narrow forbidden lines. The narrow lines come from low-density, low-ionisation gas, in the so-called Narrow-Line Region (NLR), and

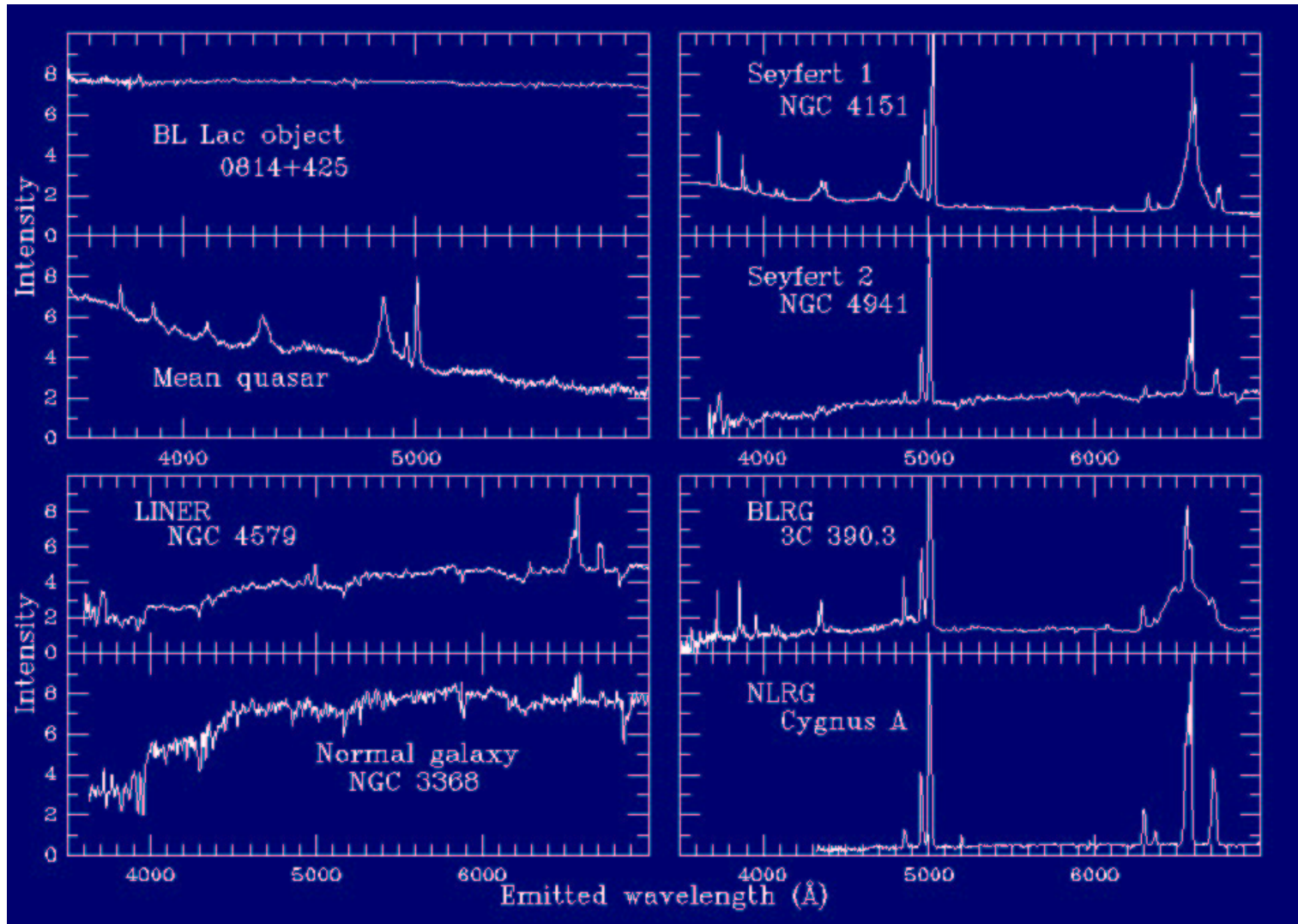


FIGURE 1.3. This plot shows typical optical spectra for the different groups of AGN. The spectra have been redshift corrected, so the lines shown are at their rest frame wavelengths. The Type-1 objects show both broad and narrow lines, while Type-2 AGN have narrow profiles only. Taken from Bill Keel's website, at <http://www.astr.ua.edu/keel/agn>, based at the University of Alabama.

have FWHM of a few hundred km s^{-1} (i.e., still broader than those lines observed in non-active galaxies). Because the density in the NLR is low, transitions are not collisionally de-excited, and so the radiative transitions (and, hence, the forbidden lines) are observed. The broad lines have widths Doppler-broadened up to 10^4 km s^{-1} . The Broad Line Region (BLR) is located closer in to the black hole, shown by both the increased width of the lines, and the higher ionisation state; since only permitted lines are seen, the BLR is thought to be the denser of the two regions, with $n_e \gtrsim 10^9 \text{ cm}^{-3}$, compared to $\sim 10^3\text{--}10^6 \text{ cm}^{-3}$ for the NLR. There are certain objects, known as Narrow Line Seyfert 1 galaxies, which do show the broad lines (c.f. Type-2 galaxies; see below), but they are narrower than in the typical broad-line Seyfert 1s. NLS1s are thought to have high accretion rates and, very probably, small black hole masses; see, e.g., Bian & Zhao (2003). This will be discussed below.

- Type-2 Seyfert galaxies differ from the Type-1 objects by showing only the narrow lines. They have an $[\text{OIII}]\lambda 5007$ to $\text{H}\beta$ ratio of < 3 (Shuder & Osterbrock 1981); Seyfert 2s also tend to show weaker Fe II (or higher ionisation iron) emission lines than their Seyfert 1 counterparts. The precise origin of the differences between Seyfert 1 and 2 type galaxies is not certain; however, as discussed in Section 1.2, it is likely to be mainly an orientation effect.
- Quasars (Schmidt 1963) are the most luminous of the AGN family, with a bolometric magnitude, $M_{bol} < -23$, and can now be seen out to redshifts of more than $z \sim 6$. Originally, the term QSO (Quasi-Stellar Object) was used for the radio-quiet objects in this class, with ‘quasar’ being the abbreviated form of ‘Quasi-stellar Radio Source’. However, both are now accepted as general terms, covering radio-loud and radio-quiet objects. QSOs are basically brighter versions of Seyfert galaxies, where only the nucleus is observed, as a star-like point-source (hence the term *Quasi-Stellar Object*); the host galaxy itself remains undetected and can be > 100 times fainter than the central nucleus. The majority of QSOs are found to be radio-quiet (RQQs)– the radio emission of RQQs is not non-existent, but is

about 100 times less than that of the radio-loud quasars (RLQs). Quasars are FR-II objects, as defined in the section on radio galaxies, below. Figure 1.4 shows an X-ray image of the quasar 3C 273.

- Blazars, encompassing BL Lacs (named after the first object in the class, identified in the direction of the constellation of Lacerta, the lizard) and optically violent variables (OVVs), are another member of the AGN family. These objects show no (BL Lacs) or only very weak (OVVs) emission lines and are all radio sources, with BL-Lacs being FR-I low-luminosity sources and OVVs corresponding to FR-II objects. They are rapidly variable at all wavelengths – they can vary by as much as $\Delta m \gtrsim 0.1$ magnitudes in one day (Peterson 1997) – and strongly polarised in the optical. OVVs and BL Lacs are thought to be viewed down the radio jet, such that the emission is relativistically beamed; this is backed up by the fact that blazars do not have visible radio lobes. Blazar spectra are purely power-law continua, with no thermal component.
- LINERs - Low Ionisation Nuclear Emission-Line Region galaxies - are the least luminous of the classifications. They were first identified by Heckman (1980) and are, in fact, very common, possibly existing in nearly half of all spiral galaxies (Ho, Filippenko & Sargent 1994). LINERs show only weak nuclear activity, with most of their emission coming from starlight. The emission line spectra indicate the existence of a non-stellar continuum, although this has yet to be observed directly (Netzer 1990). The observational difference, in the optical region, between LINERs and Seyfert 2-type galaxies lies in the relative strength of certain low-ionisation lines, with Heckman's definitions being that the [OII] $\lambda\lambda 3727, 3729$ lines are stronger than the [OIII] $\lambda 5007$ line, [OI] $\lambda 6300$ /[OIII] $\lambda 5007 \lesssim 0.33$ and [NII] $\lambda 6584/H\alpha \gtrsim 0.6$.
- Radio Galaxies are thought to be the radio-loud analogues of Seyfert galaxies (which do not show strong radio emission). As for Seyferts, there are two optically-defined groups - the narrow-line radio galaxies (NLRGs) and the broad-line counterparts (BLRGs). Although radio galaxies are considered, in some senses, to be

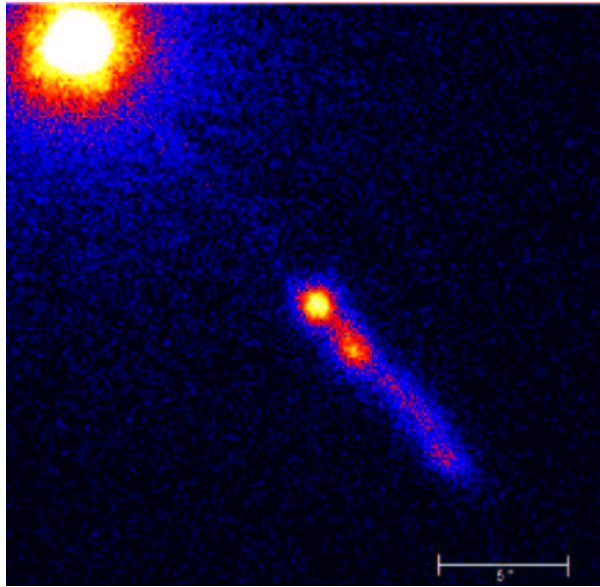


FIGURE 1.4. A *Chandra* image of 3C 273, showing the central nucleus and the jet responsible for the strong radio emission. A five arcsec scale bar is shown at the bottom right. (Credit for image: NASA/CXC/SAO/H. Marshall et al.)

radio-loud Seyferts, they typically occur in elliptical galaxies, rather than spirals. The radio lobes in these galaxies are powered by a jet of particles and emit non-thermal, synchrotron radiation (e.g., Blandford & Rees 1974). Radio galaxies are also sub-divided into classes dependent on the appearance of their radio lobes; these differences were first described in Fanaroff & Riley (1974). Fanaroff-Riley Class I (FR-I) are those objects which are brightest in the centre, with the surface brightness decreasing outwards; they are also the weaker radio sources. FR-II sources show limb-brightening, i.e. are brighter further away from the core. The lobe-dominated FR-II objects contain both NLRGs and BLRGs. FR-I only seem to show weak, narrow lines, but Antonucci (1993) suggests that this is simply due to the starlight from the host galaxy ‘drowning out’ the broader emission lines.

As a final note to this section, Starburst galaxies should be mentioned. These are galaxies in which the star-formation rate is much higher than average. They contain many young stars and are more energetic than normal galaxies, although are not as luminous as AGN. They show strong IR emission, due to the heating of dust by UV emission from the young stellar population. Starbursts may be formed through the merger of

galaxies. Although not AGN as such, much work has been done on the connection between the groups. It has been suggested that Starbursts may evolve into AGN, with the central cluster of stars collapsing to form a black hole (Weedman 1983; Norman & Scoville 1988). Alternatively, circumnuclear star-forming regions have been found in several Sy2 galaxies (e.g., Mauder et al. 1994; Heckman et al. 1997), implying that it is possible for the two phenomena to co-exist.

1.2 Unification of AGN

The simplest model of AGN comprises a central, massive black hole, surrounded by an accretion disc. At a greater distance from the black hole is the BLR and, even further out, the NLR; these are not coplanar with the disc and are probably ‘clumpy’, consisting of dense, optically thick clouds within a hot, confining medium (e.g., Carroll & Ostlie 1996; Fig. 1.1).

The main scheme for the unification of the different types of AGN relies on orientation effects (see Antonucci 1993 and references therein). Antonucci & Miller (1985) discovered that NGC 1068, a classical Sy2, showed very broad Sy1-like Balmer lines when viewed in polarised light. Similar Sy2s were later discovered (e.g., Miller & Goodrich 1990), leading to the idea that Seyfert 1 and 2 galaxies are essentially identical, but viewed from different angles. It was suggested that some kind of obscuring material – a torus – surrounds the BLR, such that, from certain orientations, it is hidden from view, and a Type-2 galaxy is seen. Hot electrons outside the active nucleus scatter the light from the BLR, allowing the broad lines to be observed in polarised light. Figure 1.5 shows a schematic diagram for such a unification model.

The above model, based *solely* on orientation effects, does not, however, account for differences in radio-loudness, for example; why should some objects possess strong radio jets, while others do not? Neither does it explain why QSOs appear very similar to Seyfert galaxies, only much more luminous.

It has been suggested (e.g. Wang, Biermann & Wandel 2000) that the fundamental

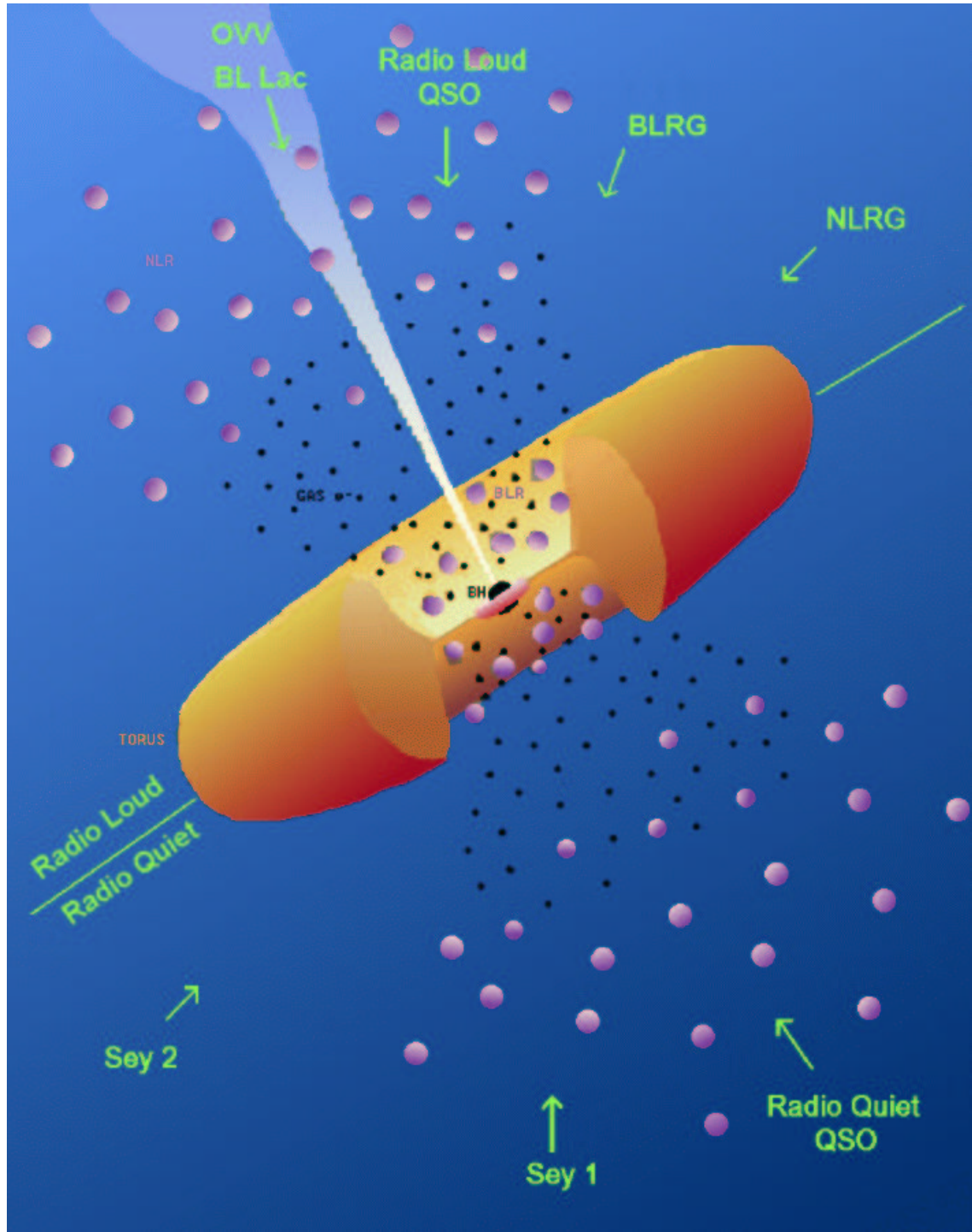


FIGURE 1.5. A schematic diagram of the unified theory of AGN. Taken from the April section of the *BeppoSAX* 1999 calendar on the ASI Science Data Centre webpages <http://www.asdc.asi.it/bepposax/calendar/> (adapted from Urry & Padovani 1995)

difference between QSOs and Seyferts is one of accretion rate, with the QSOs accreting at a higher value. It should be noted that there are very few Type-2 QSOs known, leading to the suggestion that the torus increases in opening angle with increasing luminosity. This could also help to explain why more luminous objects show much weaker narrow iron lines than the fainter Seyferts. (This topic will be investigated in Chapter 6.) As for the strength of the radio emission, one possibility is differences in the angular momentum of the central black hole (Punsly & Coroniti 1990), such that the rotating, Kerr black holes form radio-loud objects, while the Schwarzschild variety produce the radio-quiet counterparts. Boroson (2002), based on work done previously (Boroson & Green 1992), suggests that it is the black hole mass and the Eddington ratio which determine the differences between radio-quiet and radio-loud QSOs; NLS1s and broad absorption line (BAL) QSOs are also included. They investigate the correlations between various optical measurements for a large sample of QSOs in the Bright Quasar Survey (BQS), finding two correlations to be the strongest; these are referred to as principal components, or eigenvectors and are known as PC1 and PC2; PC1 shows an inverse correlation between the strengths of two emission lines, FeII and [OIII] (or $H\beta$), while PC2 is dominated by a luminosity-HeII anti-correlation. The most popular explanation (Boroson & Green 1992) is that PC1 depends primarily on L/L_{Edd} (L_{Edd} being the Eddington luminosity, which is proportional to M) and PC2 on the accretion rate ($\propto L$). Plotting PC2 against PC1 leads to a striking difference between radio-loud and radio-quiet objects, probably due, at least in part, to differences in the black hole mass (with RLQs being associated with the more massive black holes; see also Laor 2000a). Figure 1.6, taken from the 2002 paper by Boroson (his figure 7) summarises the findings. Meier (2002) also discusses the grand unification of AGN, concluding that more work is required to refine any scheme involving the spin and accretion rates of black holes.

To conclude this section on the unification of AGN, the differences between Broad and Narrow Line Seyfert 1 galaxies will be discussed. It has been suggested that NLS1s may be accreting at a high rate in relation to their black hole mass. Pounds, Done & Osborne (1995) analysed an object known as RE 1034+39, discovering that it possessed a very soft X-ray spectrum which could be mainly modelled as thermal emission, with the

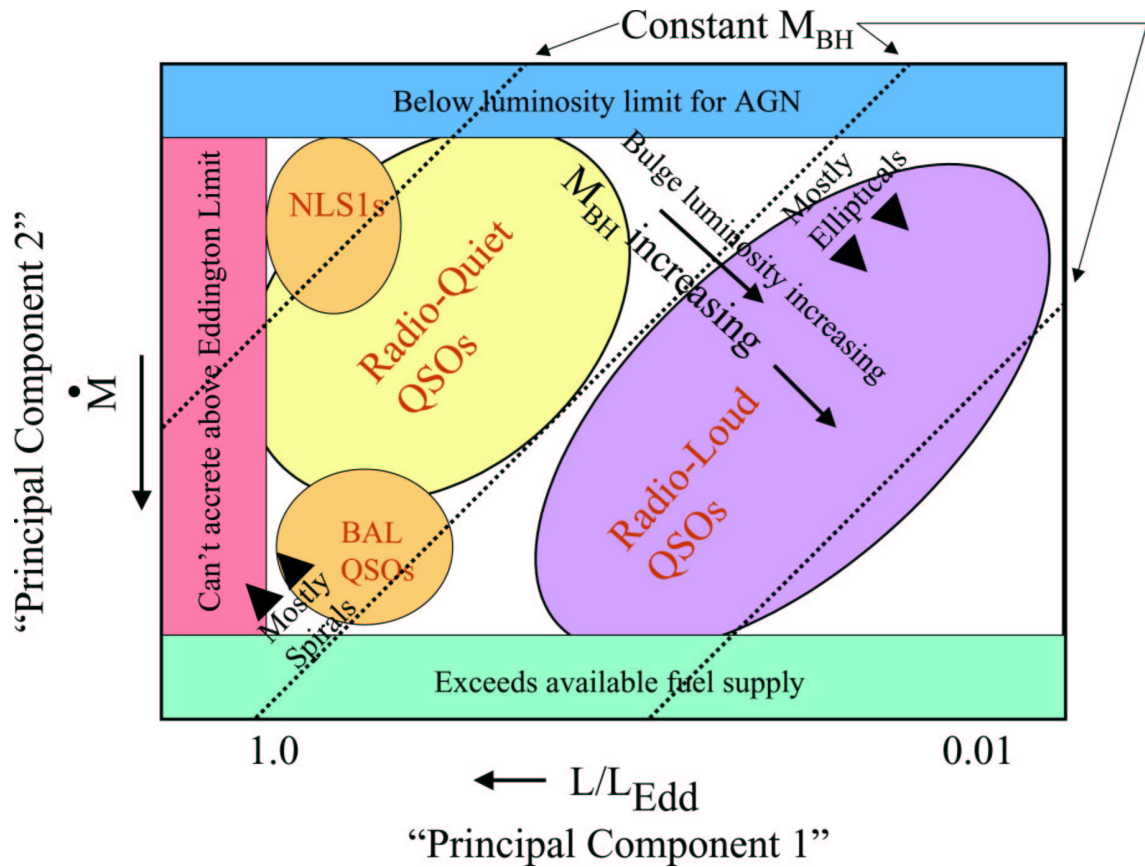


FIGURE 1.6. A plot showing how the principal eigenvectors are related for different types of AGN; taken from Boroson (2002). The plot demonstrates how the mass accretion rates and luminosities, as a fraction of Eddington, of QSOs – both radio-quiet and radio-loud – and NLS1s are linked.

underlying power-law being substantially weaker. Pounds and co-workers note the remarkable similarity between the spectrum of this object and the ‘high’ state X-ray spectra of Galactic black hole candidates (GBHCs), such as Cyg X-1 (Tanaka 1990). The spectra of GBHCs are generally described as being in either ‘low’ or ‘high’ states: the high state consists of a strong thermal (BB) component ($kT \sim 1$ keV), together with a steep photon index of ~ 2.2 – 2.7 ; the low state is purely a power-law, with Γ being much harder, ~ 1.7 (Esin et al. 1998). The high spectral state is generally the more luminous of the two (Nowak 1995). GBHCs are occasionally found in other states (Esin et al. 1998), termed ‘intermediate’ (with both spectral shape and luminosity between the high/low values), ‘very-high’ (luminosities close to Eddington values) and ‘quiescent/off’ (very low X-ray flux). The change in spectral state is thought to be due to a change in accretion rate, with

the ‘high’ state spectra likely to be produced when the rate is close to Eddington. By analogy to these GBHCs, Pounds, Done & Osborne (1995) theorised that the very soft spectra of NLS1s could be linked to an increased accretion rate. They consider that a high accretion rate could cause an intense soft X-ray flux; these photons could then lead to Compton cooling of the electrons in the hard photon source, producing the steep spectrum found at higher energies; see also Haardt & Maraschi (1991). The high accretion rate can explain the narrowness of the optical emission lines as well: the position of the BLR depends on the balance between the gravitational attraction of the black hole and the ionisation power of the radiation. For a higher accretion rate, the ionising strength increases, meaning that the line-forming regions are positioned at a greater distance from a black hole of a given size (Wandel 1997). Thus, the clouds are not moving as rapidly and so the Doppler-broadening is not as strong. ‘Normal’, or Broad Line Seyfert 1s, on the other hand, with their lower accretion rates (for approximately the same, though possible slightly larger, size of black hole compared to the NLS1s), have more centralised BLRs and, so, broader optical lines.

An alternative model for the narrowness of the permitted lines in NLS1s suggested that geometrically thick accretion discs were being viewed face-on (Puchnarewicz et al. 1992; Brandt & Gallagher 2000). However, indirect evidence for small black hole masses in NLS1s was provided through variability analysis. Based on work with the *ROSAT* PSPC, Boller, Brandt & Fink (1996) pointed out that NLS1s frequently show rapid X-ray variability over short timescales, which implied the presence of small, low mass black holes; Leighly (1999) found similar results from *ASCA* data. Hayashida (2000) and Bian & Zhao (2003) find that their respective samples of NLS1s do possess relatively low black hole masses. Various authors (Puchnarewicz et al. 2001; Comastri et al. 2001; Laor 2000a) find that the mass accretion rate for NLS1s seems to lie within the $0.3 \lesssim \dot{m} \lesssim 1.0$, where \dot{m} is the fraction of the Eddington accretion rate. Nicastro (2000) finds that a wind driven by radiation-pressure leads to the FWHM of the broad component of $H\beta$ being lower when the accretion rate is higher, as is seen in NLS1s. Also, Czerny et al. (2001) obtain black hole masses using power density spectra. These data indicate that $\log(M_{BH}) \sim 7.5$ for BLS1s (Broad Line Seyferts), with $L/L_{Edd} \lesssim 5\%$.

For NLS1s, the corresponding values are $\log(M_{BH}) \sim 6.5\text{--}8.2$, with luminosities up to $\sim 40\%$ L_{Edd} (Janiuk, Kuraszkiewicz & Czerny 2001). Finally, in a set of recent conference proceedings, Wandel (2003) considers the relation between the SMBH in AGN and their host galaxies. The data gathered for this paper shows the differences between the masses found for NLS1s, BLS1s and QSOs, with NLS1s tending to have the least massive black holes and QSOs the most massive. All these findings lend support to the theory proposed by Pounds, Done & Osborne (1995), with NLS1s having relatively low mass black holes, but high accretion rates.

As an aside, there is a train of thought which considers that NLS1s may be AGN in an early stage of their evolution (Grupe 1996; Mathur 2000). Various facts support this theory, including the assumed low black hole mass (at such high accretion rates the black holes should grow quickly over time), super-Solar metallicities (signifying rapid star formation, associated with an early phase of galactic evolution) and NLS1s being bright IR emitters (again, a parallel with young, star-forming systems); see Mathur (2000) and references therein.

1.3 X-ray emission from AGN

1.3.1 Emission mechanisms

There are various different processes which lead to the production of X-rays, which form characteristic spectral shapes. Some of these are discussed below.

Bremsstrahlung

Bremsstrahlung, a German word meaning ‘Braking radiation’, is associated with the deflection of charged particles by the Coulomb fields of nuclei. Classically, a charge which is accelerated or decelerated radiates; the amplitude of the radiation is proportional to Zze^2/m , since Newton’s second law tells us that acceleration, $a = F/m$ and the Coulomb force states that:

$$F = \frac{1}{4\pi\epsilon_0} \frac{Q_1 Q_2}{r^2} = \frac{1}{4\pi\epsilon_0} \frac{Zeze}{r^2} \quad (1.1)$$

where Z is the charge on the (massive) nucleus and z that of the moving particle; r is the separation of the charges and ϵ_0 is the permittivity of free space (8.85×10^{-12} F m⁻¹). Therefore, Bremsstrahlung, also known as free-free radiation, varies inversely with the square of the mass (intensity is proportional to the square of the amplitude), so electrons radiate more strongly than protons for example.

Bremsstrahlung is an optically thin, thermal process and, thus, depends on the whole volume of the particles involved. As the opacity increases, the radiation becomes thermal (blackbody-like); the strength of optically thick, blackbody emission depends on the surface area of the emitter, rather than the total volume. In AGN, Bremsstrahlung could originate in the hot, ionised gas which is postulated to exist in the vicinity of the central engine.

Synchrotron Radiation

When charged particles move relativistically in the presence of magnetic fields, non-thermal Synchrotron radiation is emitted; the non-relativistic form is known as Cyclotron radiation. Beaming effects concentrate the emitted radiation field along the forward direction, leading to a distribution lying within a cone of half-angle $1/\gamma$, where $\gamma = (1 - v^2/c^2)^{-1/2}$ for a velocity v . Assuming the electron energy spectrum is a power-law, Synchrotron radiation also results in one, where the spectral index (α) is related to the particle distribution index (p) by $\alpha = (p-1)/2$ (Rybicki & Lightman 1979). It is thought that radio-jets in AGN may emit Synchrotron radiation.

If the photons emitted by the spiralling electrons then interact with those same relativistic particles they gain energy through inverse Comptonisation; this is known as Synchrotron Self-Comptonisation.

Comptonisation

Under the original definition, the term Comptonisation involves electrons scattering from high energy photons and, thus, gaining energy. In Astronomy, however, Comptonisation often really means *Inverse* Comptonisation – that is, photons gaining energy from interactions with energetic electrons. In this thesis, the term Comptonisation always refers to the inverse process. As is discussed in more detail in Section 1.3.5, Compton scattering can be either saturated or unsaturated, depending on the environment. In AGN the process is expected to be unsaturated and leads to a power-law spectrum over a limited energy range.

1.3.2 The accretion process

As mentioned in Section 1.1.2, accretion onto a black hole is a likely method for powering an AGN. Matter tends to form a so-called accretion disc around objects such as black holes, so that its initial angular momentum can be dispersed. This occurs via viscous drag: assuming the system is Keplerian, differential rotation will occur, with the material closest to the black hole moving more quickly than the distant matter; the velocity at a radius r is given by:

$$v_{Kep} = \left(\frac{GM}{r} \right)^{\frac{1}{2}} \quad (1.2)$$

Thus, particles from an inner region will interact with those in the next region out (although, of course, there are no strictly defined bands), feeling a drag force. This causes the particles to move inward (the other alternative is for them to speed up again, but this requires an input of energy) towards the centre of the gravitational field. This is similar to the way in which the orbits of manmade satellites gradually decay over time, due to the drag of the Earth's atmosphere. As the particles fall inward, angular momentum is transferred outward through the accretion disc. As well as causing the inward movement of material, viscous drag dissipates heat, increasing the temperature of the accretion disc.

The disc can then emit thermal photons, which are observed in the optical/UV band due to the range of temperatures produced.

The energy released through accretion is that due to the loss of potential energy, i.e.

$$E_{acc} = \frac{GMm}{r} \quad (1.3)$$

giving the accretion luminosity to be

$$L_{acc} = \frac{dE_{acc}}{dt} = \frac{GM\dot{M}}{r} \quad (1.4)$$

where m is the mass of the inward-falling particle, \dot{M} the mass accretion rate and M the mass of the central, accreting body. This is the maximum possible energy gain of the particle; in fact, only half of this accretion energy is extracted, since the particle is actually orbiting the central object, rather than in free-fall. From the Virial Theorem – which states that, for a stable, self-gravitating distribution, the magnitude of the potential energy is equal to twice that of the kinetic energy – the remaining half of the potential energy is radiated as heat, within a narrow boundary layer.

Although accretion is a highly efficient process, there is a maximum luminosity that such systems can reach; this is known as the Eddington Limit, or Eddington Luminosity (Eddington 1925) and occurs when the radiative force is equal and opposite to the gravitational attraction. The limit is given by

$$\frac{\sigma_T L_{acc}}{4\pi r^2 c} = \frac{GMm_H}{r^2} \quad (1.5)$$

$$\Rightarrow L_{Edd} = \frac{4\pi GMm_p c}{\sigma_T} \approx 1.26 \times 10^{38} \frac{M}{M_\odot} \text{ergs}^{-1} \quad (1.6)$$

where $m_H = m_p + m_e \approx m_p$ and σ_T is the Thompson scattering cross-section.

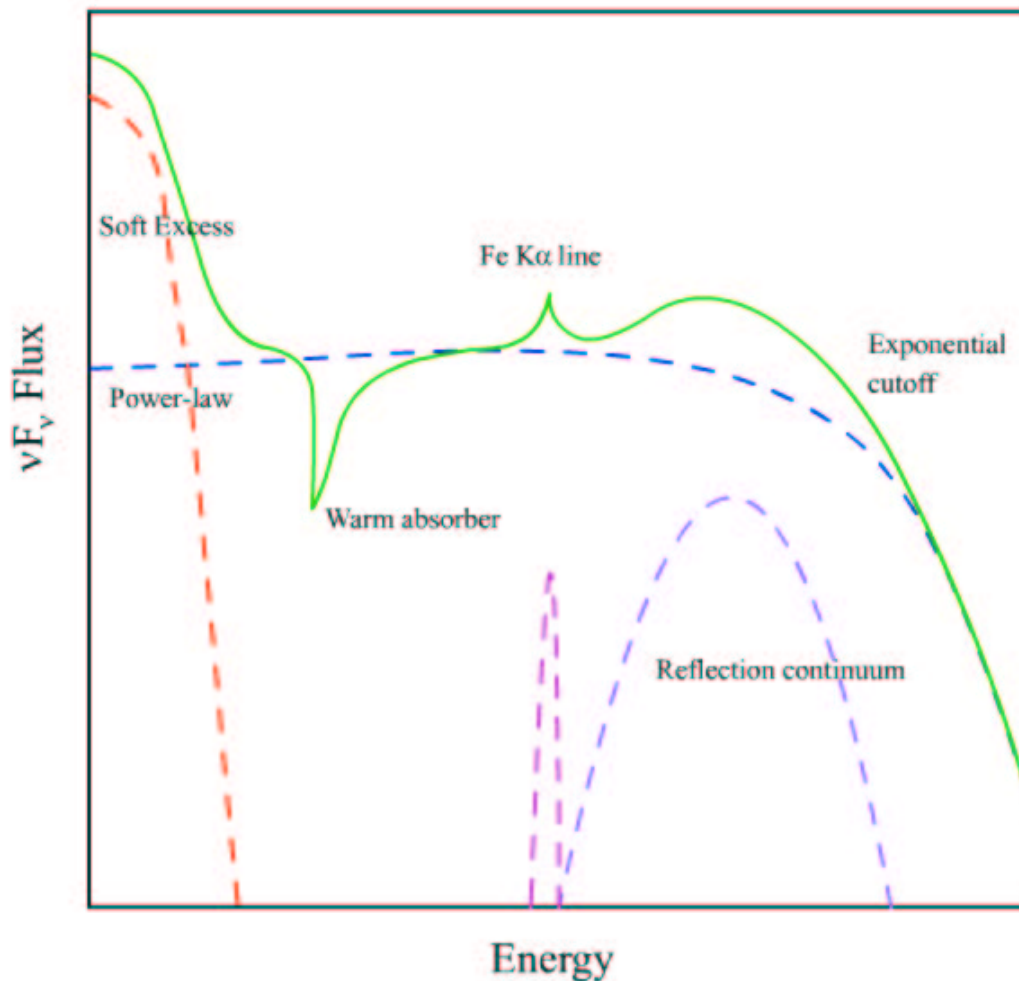


FIGURE 1.7. A schematic of the features of an X-ray spectrum. Based on a figure in Fabian (1998)

1.3.3 The hard X-ray spectrum

As mentioned previously, AGN are characterised by strong X-ray emission (Elvis et al. 1978; Tananbaum et al. 1979). To a first approximation, the X-ray spectrum can be described as a power-law, extending out to very high energies (up to 300 keV from the *Compton Gamma Ray Observatory*; Johnson et al. 1993). The spectrum at higher, γ -ray energies is also a power-law, but generally with a different photon index.

Upon closer inspection, it is found that there tend to be other features superimposed upon this X-ray power-law (Figure 1.7).

The most striking of the deviations at higher energies is generally an emission line around 6.4 keV, which corresponds to Fe $K\alpha$ fluorescence (Figure 1.8). These lines were first identified by *Ginga* observations (Pounds et al. 1989; Pounds et al. 1990; Nandra et al. 1991; Nandra & Pounds 1994), with cold (neutral) iron forming the emission at 6.4 keV through to hydrogen-like iron emitting around 6.9 keV. More recently, the lines have sometimes been found to have more than one component: a broad line, together with a very narrow (unresolved by *XMM*; $\sigma < 10$ eV) core (e.g., O’Brien et al. 2001a; Reeves et al. 2001). It is thought that the broader of the lines (FWHM $\sim 5 \times 10^4$ km s⁻¹) is probably formed through reflection from the surface of the accretion disc; the central energy of the line gives an indication of the ionisation state of the disc. The line is broadened due to a combination of the rotation of the accretion disc (it is sometimes possible to distinguish the ‘blue’ and ‘red’ peaks, although the blue edge is enhanced relative to the red by relativistic beaming), the transverse Doppler effect and the gravitational redshift due to the black hole.

The narrow component, however, is generally found to have an energy close to 6.4 keV and is likely to arise from neutral material, much more distant from the black hole. This material could possibly be located in either the putative molecular torus or the Broad Line Region. This is discussed in more detail in Chapter 6.

Wherever fluorescent emission lines occur, a corresponding absorption edge is theoretically expected to exist, at a slightly higher energy: the ion first absorbs a photon of the energy required to excite an inner-shell (K) electron (~ 7.1 keV for neutral iron); as an electron from the $n = 2$ shell drops down to fill the hole left behind in the innermost shell, a photon with an energy equal to that of the difference between the shells (~ 6.4 keV for neutral Fe) is emitted. In this way, both an edge and an emission line should be observed. Such features have been identified in some spectra (e.g., Gondoin, Orr & Lumb 2003; Porquet et al. 2003; Pounds et al. 2003c), although the limited *XMM* mirror aperture at these energies often means that the edges are hard to detect.

Through co-adding *Ginga* spectra of nearby Sy1s, Pounds et al. (1990) discovered a flattening of the spectrum at energies above ~ 10 keV. When hard X-rays enter a slab of cold material (here the accretion disc), they are either Compton down-scattered by

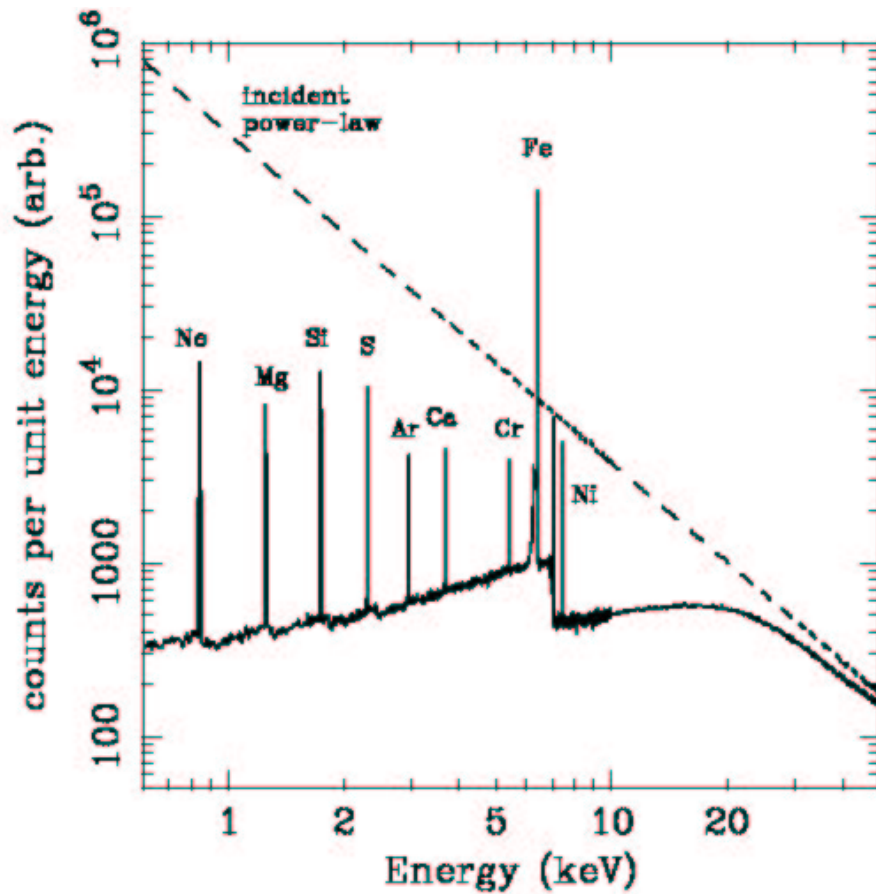


FIGURE 1.8. The expected reflection spectrum due to a power-law source illuminating a slab of cold material. Monte Carlo simulation from Reynolds (1996). The Fe emission line is by far the strongest feature.

free and bound electrons, or photoelectrically absorbed; such absorption is followed by either fluorescent line emission (see above) or Auger de-excitation, wherein the photon is destroyed. Photoelectric absorption is energy dependent, which leads to most of the softer X-ray photons being absorbed, while the harder ones are generally scattered back out of the disc. This ‘Compton reflection hump’ flattens the overall spectrum; this led to a steepening of what was originally thought to be the typical underlying AGN spectral slope, from 1.7 to 1.9 (Nandra & Pounds 1994). This form of reprocessing of the X-ray continuum was predicted and discussed by Lightman & White (1988) and Guilbert & Rees (1988).

1.3.4 The soft excess

At low energies, $\lesssim 2$ keV, most AGN show an up-turn, away from the extrapolation of the high energy power-law; this is known as the soft excess and was first seen in the Seyfert galaxy Mrk 841 by Arnaud et al. (1985). The excess emission was then found to be a common feature in *EXOSAT* observations by Turner & Pounds (1989). Subsequent *ROSAT* observations confirmed this feature by showing that the spectral slopes over the 0.1–2.4 keV band were steeper than the typical value at higher energies (Walter & Fink 1993). If the value of the absorbing column density is allowed to vary when fitting spectra, then a value less than the Galactic column can indicate a soft excess (e.g., Zhou & Yu 1992).

The precise origin of this soft excess is unknown, but theories have circulated over the years. A passing idea was that the feature was not actually an *excess*, but rather the spectrum should be modelled with a steeper slope which would then be modified by an absorbing column; however, *BeppoSAX* and *XMM* spectra have helped to remove ambiguities and it is now more certain that the soft emission is a real phenomenon. Figure 1.9, taken from Pounds & Reeves (2002), shows how the shape of the soft excess can vary, implying that the lower luminosity objects can show a combination of emission and absorption from ionised gas at the lower energies.

The alternatives for the production of the soft excess emission come under two headings: direct, thermal emission from the accretion disc, due to the release of gravitation energy via viscosity, or reprocessed radiation from the interaction of the hard, primary X-rays with the surface of the accretion disc.

Fitting the observed X-ray soft excesses with one or more blackbody components, to model direct thermal emission, is nicely simple and works very well for most spectra. However, a relationship between the temperature of the accretion disc and the black hole mass can be derived as follows:

$$\text{Schwarzschild Radius, } R_{sch} = 2GM/c^2 \Rightarrow R \propto M$$

$$\text{area of disc, } A = 4\pi R^2 \Rightarrow A \propto R^2 \propto M^2$$

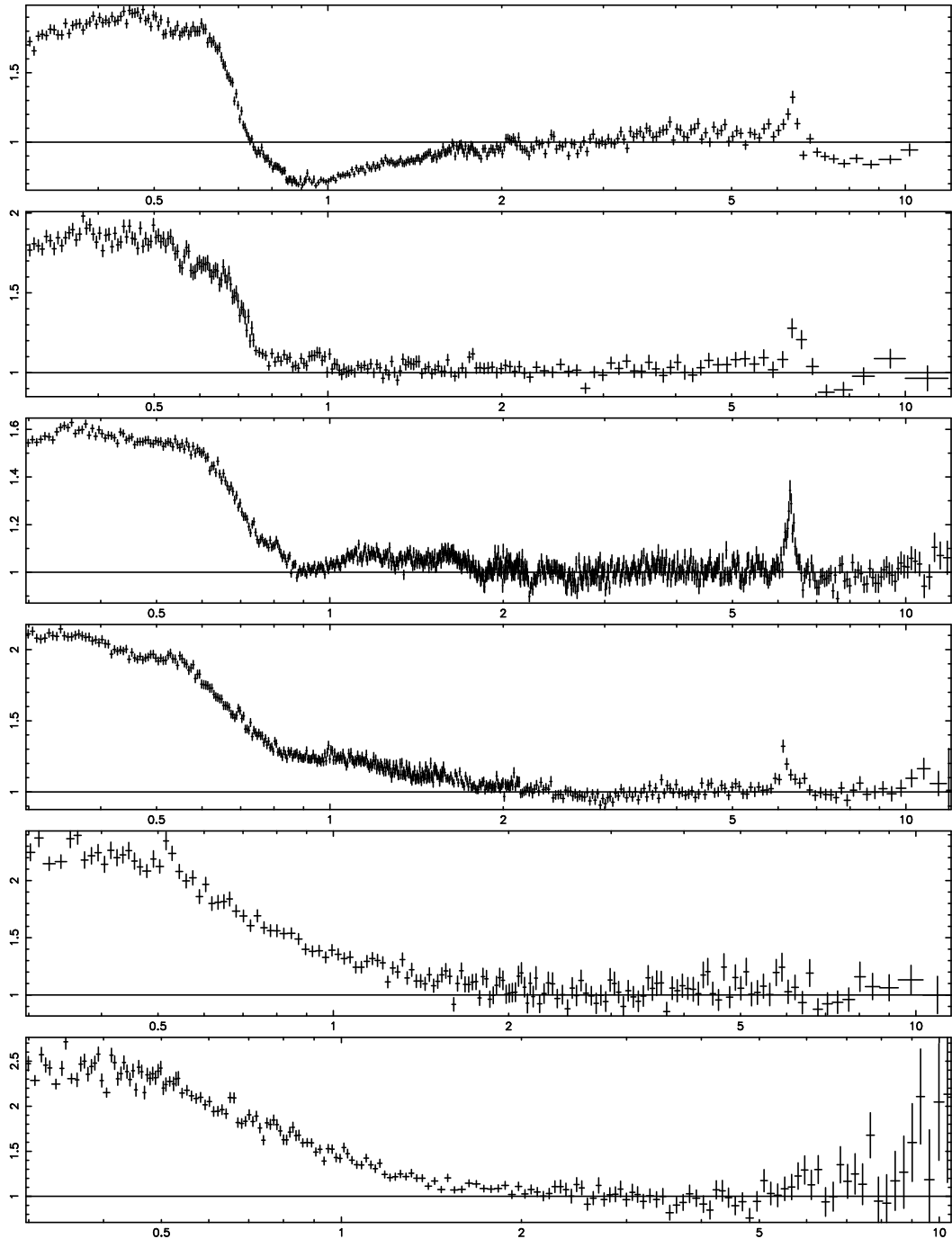


FIGURE 1.9. The soft excess for six Seyfert 1 galaxies, measured by *XMM*. The ordinate shows the ratio of the data points to a power-law fitted over the 2–12 keV range, while the abscissa is the photon energy in keV, in the observed frame of reference. From top to bottom, in order of increasing 2–10 keV luminosity, are MCG-6-30-15, Mrk 766, NGC 5548, Mrk 509, 1H 0419-577 and PKS 0558-504. Taken from Pounds & Reeves (2002)

The Stefan-Boltzman law tells us that the luminosity of an object, L , is given by $L = e\sigma AT^4$, where e is the efficiency relative to a blackbody; i.e., $L \propto AT^4 \Rightarrow L \propto M^2T^4$.

However, the gravitational potential energy released upon accretion is $\Delta E_{acc} = GMm/R_*$ so, differentiating, gives that $L_{acc} \propto M\dot{M}$.

Thus, $L \propto M\dot{M} \propto M^2T^4$ (from previous expression)

Rearranging, gives the relationship: $T \propto (\dot{M}/M)^{1/4}$.

More precisely, (from, e.g., Shakura & Sunyaev 1973; Peterson 1997):

$$T(r) \sim 6.3 \times 10^5 \left(\frac{\dot{M}}{\dot{M}_{Edd}} \right)^{1/4} M_8^{-1/4} \left(\frac{r}{R_{sch}} \right)^{-3/4} K \quad (1.7)$$

where \dot{M} is the mass accretion rate, \dot{M}_{Edd} is the Eddington accretion rate, M_8 signifies the mass of the central black hole in units of $10^8 M_\odot$ and R_{sch} is the Schwarzschild radius, $2GM/c^2$. Hence, the temperature expected for the inner-most part of the accretion disc ($r = 3 R_{sch}$), for a $10^6 M_\odot$ black hole radiating at $0.5\dot{M}_{Edd}$, is ~ 60 eV; similarly, the temperatures are even lower for more massive black holes (~ 10 eV for $M_{BH} \sim 10^9 M_\odot$; Laor & Netzer 1989). Unfortunately, when modelling the total soft excess, temperatures of over ~ 500 eV can be found (e.g., O'Brien et al. 2001b), which implies that the primary emission from the disc is not hot enough to form the observed excess. Alternatively, determining the luminosity of the blackbody component from the measured temperatures and using the Stefan-Boltzmann law of $L = \sigma AT^4$ for an area, $A = \pi r^2$, the radii come out consistently less than the Schwarzschild radius (see, e.g., Vaughan et al. 2002), implying again that the temperatures are too high for simple BB emission.

It is generally agreed that the optical/UV emission of AGN, seen mainly as the Big Blue Bump, is due to thermal radiation from the accretion disc (e.g., Malkan & Sargent 1982); emission from the disc at one temperature would not form a broad enough signature to account for both the blue bump in the optical and the soft X-ray excess (Courvoisier et al. 1987), though. However, with an added boost from inverse Comptonisation, the disc photons could lead to the soft emission (Pozdniakov, Sobol & Sunyaev 1976; Sunyaev & Titarchuk 1980; Czerny & Elvis 1987; see also Section 1.3.5).

It should be mentioned that there is an alternative theory for the production of the optical continuum, this being optically thin free-free emission (e.g., Antonucci & Barvainis 1988; Barvainis 1990, 1993), rather than photons from a geometrically thin, but optically thick accretion disc. However, Kriss (1994) states that the recombination radiation should lead to strong X-ray spectral features, much stronger than any observed.

The soft excess has, in the past, been modelled with a second power-law component (e.g., Turner & Pounds 1989), however with instruments which are sensitive at the lower X-ray energies, such as *XMM*, the soft excesses tend to show curvature (e.g., Page et al. 2003a).

Another theory was that the soft excess is dominated by a blend of soft X-ray lines, such as iron L-shell, oxygen and neon K-shell emission (e.g., Turner et al. 1991). Although this may be the case for some objects, there are others for which the soft excess appears smooth, with little, or no, indication of lines (e.g., Page et al. 2003a; Turner et al. 2001). Weaver et al. (1995) found that the soft excess in NGC 2110 was best modelled in terms of blended Fe-L emission and appeared to originate from an extended region. They suggest many possible theories, including that a hot, outflowing wind is the cause of the extended X-ray emission. This is, however, a Seyfert 2, so may not be relevant for Type-1 AGN. In general, the rapid variability in the soft X-ray region implies that most of the soft excess must be produced in the inner regions of the AGN (e.g., Ulrich, Maraschi & Urry 1997; Mushotsky, Done & Pounds 1993 and references therein). Two objects (MCG-6-30-15 and Mrk 766; Branduardi-Raymont et al. 2001) have been found possibly to show a soft excess consisting of relativistic lines, but this does not appear to be a common occurrence.

If the accretion disc is strongly ionised, then reflection from the disc surface can enhance the emission at low energies. Incorporating ionised disc reflection models, such as those described by Ballantyne, Ross & Fabian (2001) or Nayakshin, Kazanas & Kallman (2000), can not only account for the finite-width ionised iron line, but also adds to the soft emission. Although this reflection component can sometimes produce the entire observed soft excess (e.g., Czerny & Życki 1994; Reeves et al. 2001), more usually additional components are still required, but they may be fewer in number (e.g., O'Brien et

al. 2001a) or less strong (e.g., Page et al. 2003a).

Cheng & Zhang (1996) proposed a so-called ‘synchro-curvature’ model, which combines synchrotron radiation (which assumes a straight, uniform magnetic field) with a formula for curvature of the field lines. According to Xia & Zhang (2001), this mechanism can model the whole of the spectrum of NGC 5548, without the need for a separate soft excess component. Before any conclusions can be drawn, however, it needs to be determined for certain whether the soft and hard X-rays have the same point of origin or are completely separate components.

Piro, Matt & Ricci (1997) studied the soft excess with *ROSAT* and *Ginga*, finding that, for their sample of 17 objects, no model fits every spectrum satisfactorily; they find a combination of BB emission, ionised warm absorber and reflection from ionised material is required to fit all of the spectra, although the blackbody fit is the most successful of the three. They, therefore, conclude that the soft excess phenomenon is likely to vary from source to source. Whether or not this is the case, it is clear that there remains a lot of work to be done in the area of soft excesses.

1.3.5 Comptonisation and the accretion disc

The Compton y -parameter (Rybicki & Lightman 1979; Sunyaev & Titarchuk 1980) gives an indication of the strength of the interaction between the photons and electrons. It is defined as being:

$$(average\ fractional\ energy\ change) \times (mean\ number\ of\ scatterings)$$

and is given (for non-relativistic electrons) by:

$$y = \frac{4kT}{m_e c^2} \text{Max}(\tau, \tau^2) \quad (1.8)$$

where τ is the optical depth, and kT the temperature, of the electron corona [$\text{Max}(\tau, \tau^2)$ represents the mean number of scatterings in the medium, where τ corresponds to an optically thin medium and τ^2 to an optically thick one]; m_e is the electronic mass

(= 0.511 MeV/c²). The photon index of the power-law-like part of the spectrum is then given by

$$\Gamma = \left(\frac{4}{y} + \frac{9}{4} \right)^{1/2} - \frac{1}{2} \quad (1.9)$$

If $y \gg 1$, the Comptonisation becomes saturated. For a set temperature, it can easily be seen that, as the value of y increases, so, too, does the optical depth of the system. In this limit, almost all the photons will interact and a Wien spectrum (of the form $\nu^3 e^{-h\nu/kT}$) is produced, with the final temperature of the photons being close to that of the electron population.

If the y -parameter is low, the energy of the photon distribution is not increased by much. That is, most photons do not interact with the electrons, so the final spectrum is a modified BB spectrum. The intermediate regime, where $y \sim 1$, is known as unsaturated Comptonisation. Here, a power-law spectrum is formed over a limited range; this drops off exponentially for $E \gtrsim 4kT$. The resulting spectral index is that given by Equations 1.8 and 1.9 above. Subsequently, for high temperatures, the cut-off is not always observable with the current X-ray observatories. Figure 1.10 is taken from Sunyaev & Titarchuk (1980; their figure 5), and shows the expected shape of a Comptonised spectrum; they define $\gamma = 4/y$. Hence, a low value of γ (i.e., high y) tends towards a Wien-like spectrum; for a higher γ /lower y , a power-law, followed by an exponential cut-off, can be seen.

As mentioned previously, thermal photons from the accretion disc are not considered to be hot enough to form the soft X-ray excesses observed. A more physically acceptable model involves the Compton interaction of the relatively cool disc photons with hot electrons, most likely located in a corona above the accretion disc. Interactions with the electrons lead to the up-scattering of the input photons, increasing their energy such that their temperatures become consistent with those measured for the soft excess emission. An added advantage of the Comptonisation model is that it can be extended to explain the higher energy spectrum as well, since it not only broadens the spectrum through up-scattering of the photons, but also forms the pseudo-power-law described above. A two-temperature Comptonisation distribution thus allows the formation of both the soft

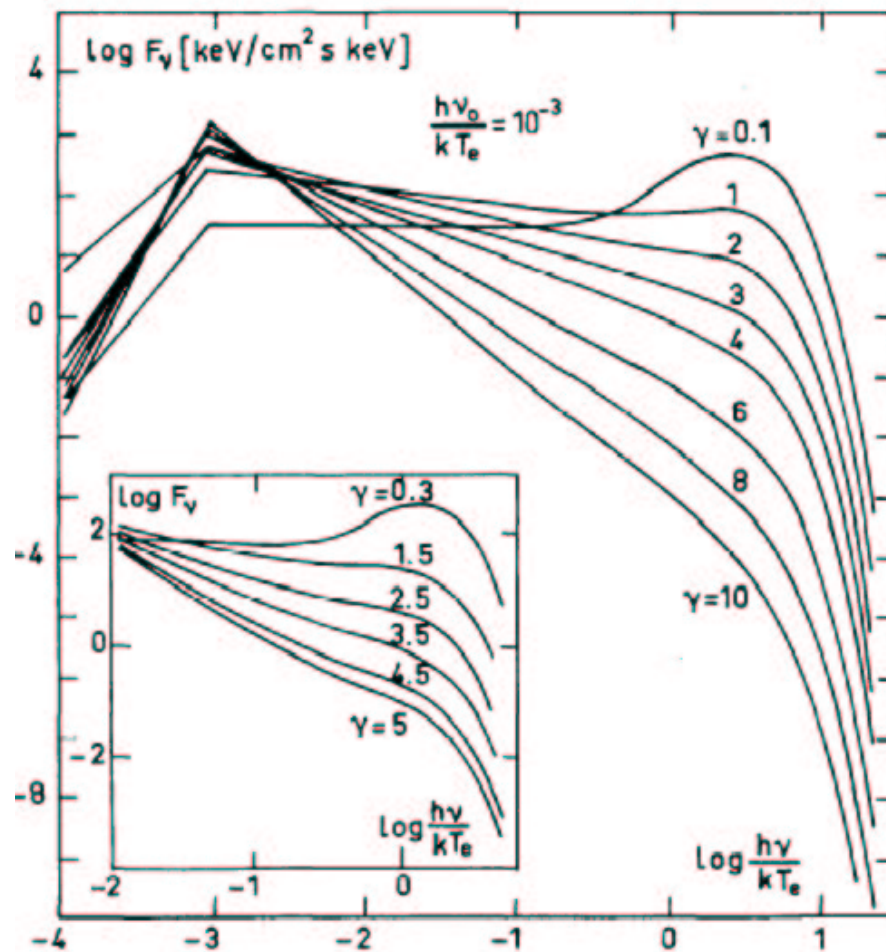


FIGURE 1.10. The spectrum for low energy photons being Comptonised by hot electrons. $\gamma = 4/y$; from Sunyaev & Titarchuk (1980)

excess and the harder power-law slope; the method is described below. There is also likely to be a disc-corona feedback mechanism, due to the re-absorption of the hard coronal X-rays by the accretion disc (e.g., Haardt & Maraschi 1991).

It is found that such a two-temperature model fits many AGN X-ray spectra very well (e.g., Petrucci et al. 2000; O'Brien et al. 2001b; Page et al. 2002; Page et al. 2003a). Such a model has two populations of electrons at different temperatures; the cooler distribution up-scatters photons from the disc to produce what is seen as the soft excess. The spectral shape is only power-law-like over a small energy range, so the overall spectrum looks like a broader version of a blackbody. The hotter electrons provide more of an energy boost, leading to a spectrum which appears as a power-law over a much wider energy band.

The hotter electron distribution must obviously contain a very large amount of energy. It is postulated that these electrons are heated by magnetic flares (e.g., Galeev, Rosner & Vaiana 1979; Nayakshin 2000a; Merloni & Fabian 2001; Liu, Mineshige & Shibata 2002; Liu, Mineshige & Ohsuga 2003) in active regions. The magnetic flare model produces a power-law spectrum, reflection and an Fe $K\alpha$ line, as generally observed in typical AGN spectra. As the accretion rate increases, this model allows the disc to gain an ionised skin, which can help to explain why there is a lack of reflection features in distant quasars (e.g., Reeves 1999; Vignali et al. 1999), together with the X-ray Baldwin effect in the *broad* lines (see Chapter 6).

However, although the double-Comptonisation model fits the data well, some of the fundamentals are still in question. For example, how is the theorised corona of hot electrons formed? In the following sections, a number of suggestions are outlined. (The corona currently in question is that which forms the soft emission, rather than the hotter one which leads to the high-energy continuum.)

Over-heated disc model

A relationship between the temperature of the disc and the mass-accretion rate was given previously, as Equation 1.7:

$$T(r) \sim 6.3 \times 10^5 \left(\frac{\dot{M}}{\dot{M}_{Edd}} \right)^{1/4} M_8^{-1/4} \left(\frac{r}{R_{sch}} \right)^{-3/4} K$$

This shows that, for a high accretion rate, the temperature of the disc will increase; that is, for $\dot{m} > \dot{m}_{cr}$ (where \dot{m}_{cr} is equal to the inverse of the radiative efficiency of the disc, η , often ~ 0.1), the temperature rises sharply ($\dot{m} = \dot{M}c^2/L_{Edd}$, where L_{Edd} is the Eddington luminosity given in Equation 1.6; Beloborodov 1998). Eventually, such temperatures are reached that the disc will become mainly ionised. At this point, the opacity of the disc decreases, since only free-free interactions can contribute to τ . This lower optical depth means that the energy in the disc cannot be radiated as efficiently and is not reprocessed into Planckian radiation; the emission is no longer of blackbody form. This leads to the over-heating of the disc close in to the black hole and the formation of

a corona of hot electrons. The hot corona then Comptonises the disc photons to produce the soft excess observed; see Beloborodov 1998 for more details.

Hybrid thermal/non-thermal electron distribution

As mentioned previously, it is thought that the hard-energy tail of the X-ray spectrum may come about through Comptonisation of the disc photons by a (probably) non-thermal electron distribution, while the soft excess will require a much cooler Comptonising environment; generally these are considered to be two separate regions. However, what if these two distributions were to be located in the same region? If both thermal (i.e., following a Maxwellian energy distribution) and non-thermal electrons/ions were to exist together, would the non-thermal component undergo energy-exchanging interactions with the thermal electrons, so becoming coupled and, essentially, part of the Maxwellian distribution? If this interaction timescale is shorter than that for other processes, then the distribution will thermalise. If, however, other processes are more rapid, then a hybrid thermal/non-thermal distribution will result, with different temperatures for the separate components; see Coppi 1999 and Janiuk & Czerny 1999 for more in-depth discussions.

This hybrid distribution has been used to model GBHCs and also AGN. For example, Vaughan et al. (2002) apply the method to Ton S180, finding similar results as those for the high/soft state of Cyg X-1 (Gierliński et al. 1999).

Advection-dominated accretion

If the accretion disc is particularly hot (more likely for Seyfert galaxies than QSOs, since $T \propto M^{-1/4}$ and Seyferts probably have lower black hole masses), then we may see the direct emission from the disc at the lower X-ray energies (Wang & Netzer 2003). At a high fraction of the Eddington mass-accretion rate, the Shakura-Sunyaev (SS) model (Shakura & Sunyaev 1973) breaks down; that is, not all of the energy released through viscosity can be radiated locally. If the cooling timescale is greater than the accretion one (due, for example, to a very high optical depth; Abramowicz et al. 1988), then some

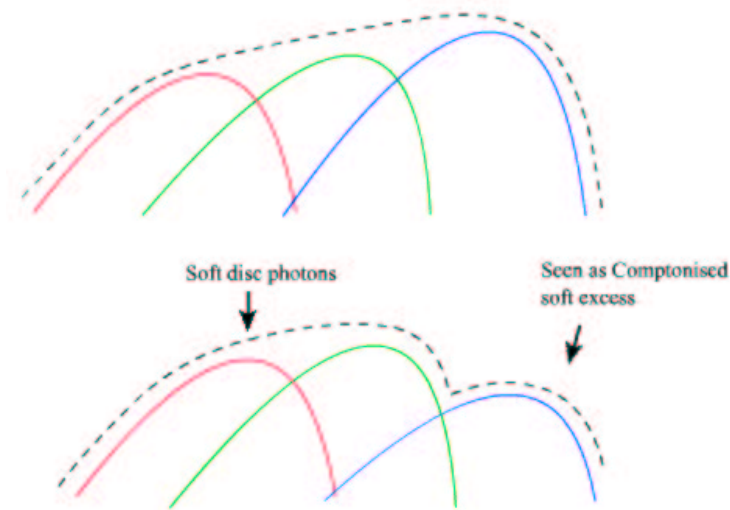


FIGURE 1.11. The top plot shows the blackbody emission from a typical Shakura-Sunyaev (SS) disc. The energy/temperature increases from left to right, with the red curves signifying the coolest component and the blue curves, the hottest. The lower plot illustrates the emission seen if the mass-accretion rate is high enough for advection to become important. This can make the spectrum appear to be that of emission from a cooler disc, with a Comptonised component (the hottest, blue curve), rather than emission from a hot SS disc where some energy has been advected inside the event horizon of the black hole. Artwork by R.J. Owen.

of the energy will be advected inside the event horizon of the black hole, so being, effectively, lost. This produces a disc spectrum but with the top of the highest temperature component missing (see Figure 1.11). This can appear to be the Comptonised tail of lower-temperature disc emission, rather than a higher-temperature component with a portion taken out of it. See Abramowicz et al. (1988) and Narayan & Yi (1995) for more details on advection-dominated accretion flows (ADAFs) in slim discs.

Ionised skin

Assuming that there are magnetic flares above the disc, leading to the observed power-law tail of the spectrum, then the radiation from the flares could lead to the formation of ‘hot-spots’ on the disc; i.e., irradiation results in an ionised skin, which is hotter than the rest of the accretion disc. This hot layer then Comptonises the disc photons, forming the

soft excess (Di Salvo et al. 2001).

Alternatively, the regions of the disc heated by the flares could thermalise the radiation; this would then be emitted as a blackbody spectrum with a temperature higher than that of the mean disc emission (Haardt, Maraschi & Ghisellini 1994).

1.4 XMM-Newton

The vast majority of the data for this thesis were obtained from the satellite *XMM-Newton*. The *XMM* (X-ray Multi-Mirror) observatory (Jansen et al. 2001) was launched on 1999 December 10, the first commercial launch of an Ariane-5 rocket. The satellite is the second of ESA's 'Cornerstone' missions and is expected to have an operational lifetime of ten years. The 48-hour orbit of *XMM* is highly elliptical, moving between a perigee of 7 000 km and a southern apogee of 114 000 km, and is inclined at 40° to the equator. This ellipticity optimises the time the satellite can obtain data, both in being outside the Van-Allen radiation belts and in avoiding frequent passages through the Earth's shadow.

XMM comprises three Wolter type-1 telescopes, with an EPIC (European Photon Imaging Camera) instrument in the focal plane of each. Two of the cameras contain seven MOS CCDs each (Turner et al. 2001), while the remaining camera has 12 PN (back illuminated) CCDs (Strüder et al. 2001). The telescopes containing the MOS cameras are also fitted with Reflection Grating Spectrometer (RGS) components (den Herder et al. 2001), which divert some of the light, leaving the MOS instruments with only 44% of the incident flux; these RGS instruments perform medium resolution spectroscopy. Finally, there is the OM (Optical Monitor; Mason et al. 2001), which allows simultaneous optical/UV observations of the X-ray targets, over the range 1700–6000 Å. The MOS and PN cameras each have a field of view of 30 arcmin diameter, while the OM covers 17×17 arcmin.

Of the EPIC instruments, the PN has the best high energy response, making it particularly useful for investigating the Fe $K\alpha$ emission around 6.4 keV. It also has a quick

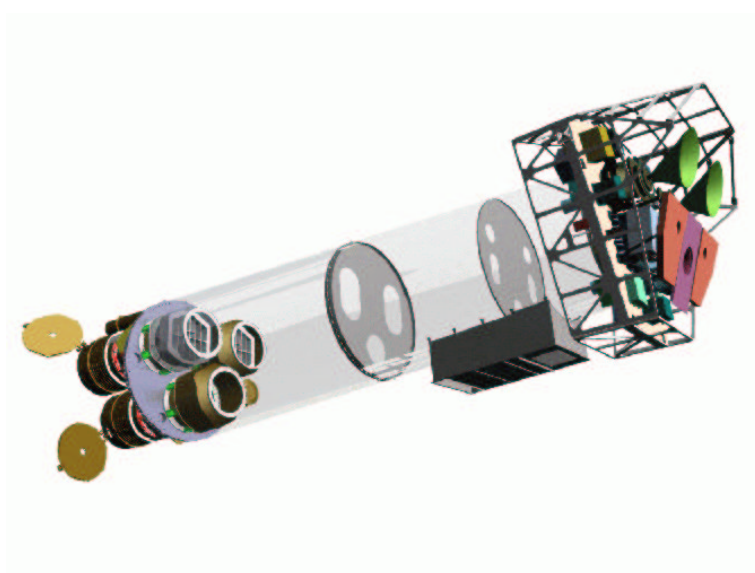


FIGURE 1.12. The *XMM-Newton* payload, taken from Jansen et al. (2001). The green cones at the right-hand side are the radiators for the EPIC MOS cameras, while the PN and RGS radiators are shown in violet and light blue, respectively. The OM telescope is almost obscured from view, but can just be seen as a dark cylinder towards the left of the image.

read-out rate (73.4 ms, c.f. 2.6 s for MOS, for full-frame – see below), which helps it to deal with higher count-rates without running into problems with so-called ‘pile-up’. Pile-up occurs when more than one photon hits the CCD in the same (or a neighbouring) pixel before the charge has been read out. This causes a problem, in that two low-energy photons are then identified as a single high-energy one; this distorts the X-ray spectrum, tending to flatten the overall shape. To help prevent such problems, there is the option to use the CCDs in large- or small-window mode, rather than the full-frame, since this allows a quicker read-out of the charge. Although MOS is more prone to pile-up, it does have better charge-transfer efficiency than the PN, together with better energy resolution. Pile-up effects had to be dealt with when fitting the *XMM* spectra of 3C 273 (Section 4.1) and PKS 0558–504 (Section 4.2) and, so, is discussed in more detail in Section 4.1.2.

The EPIC instruments have three filters consisting of different thicknesses of aluminium, which are used to filter out the optical light. The thin and medium filters are formed of 400 and 800 Å of aluminium, respectively; the thick filter has 1100 Å of Al, together with 450 Å of tin. For fields with little stray starlight, the thin filter can be

Table 1.1. Comparison of recent X-ray satellites. Data taken from the *XMM* Science Operations Centre webpage, <http://xmm.vilspa.esa.es>. ^a HEW stands for Half Energy Width, which is the diameter of the circle within which half the photons fall.

satellite	energy range (keV)	mirror PSF HEW ^a (arcsec)	mirror effective area at 1 keV (cm ²)
<i>XMM-Newton</i>	0.15–15	15	4650
<i>Chandra</i>	0.1–10	0.5	800
<i>ROSAT</i>	0.1–2.4	7	400
<i>ASCA</i>	0.5–10	174	350

chosen, leading to a better soft X-ray response. There is also the option to have use the open setting, with no filter at all, or the closed position, which has an effective filter of 1.05 mm of Al and is used solely for calibration purposes.

1.4.1 Comparison with other X-ray observatories

Observing in the X-ray band is a very important part of Astrophysics, due to the many high-energy processes which occur throughout the Universe; because of its wide energy bandpass (0.2–12 keV), coupled with the largest effective collecting area of any focusing telescope to date (4650 cm² at 1 keV; 1000 cm² at 10 keV) and good angular resolution, *XMM-Newton* is one of the best instruments to perform X-ray astronomy, with a flux detection limit of $\sim 1.4 \times 10^{-15}$ erg cm⁻² s⁻¹, over the 2–10 keV band (Hasinger et al. 2001). In comparison, *Chandra* has a smaller Point Spread Function (PSF) (and, hence, better angular resolution), but the effective area of its mirrors is much less. Figure 1.13, taken from http://heasarc.gsfc.nasa.gov/docs/xmm/about_overview.html, compares the effective areas for *XMM*, *Chandra*, *ROSAT* and *ASCA*; the detector efficiencies have not been included. This clearly shows that *XMM* has, by far, the largest mirror effective area. Table 1.1 also lists the effective areas, together with PSFs and energy ranges for the same satellites.

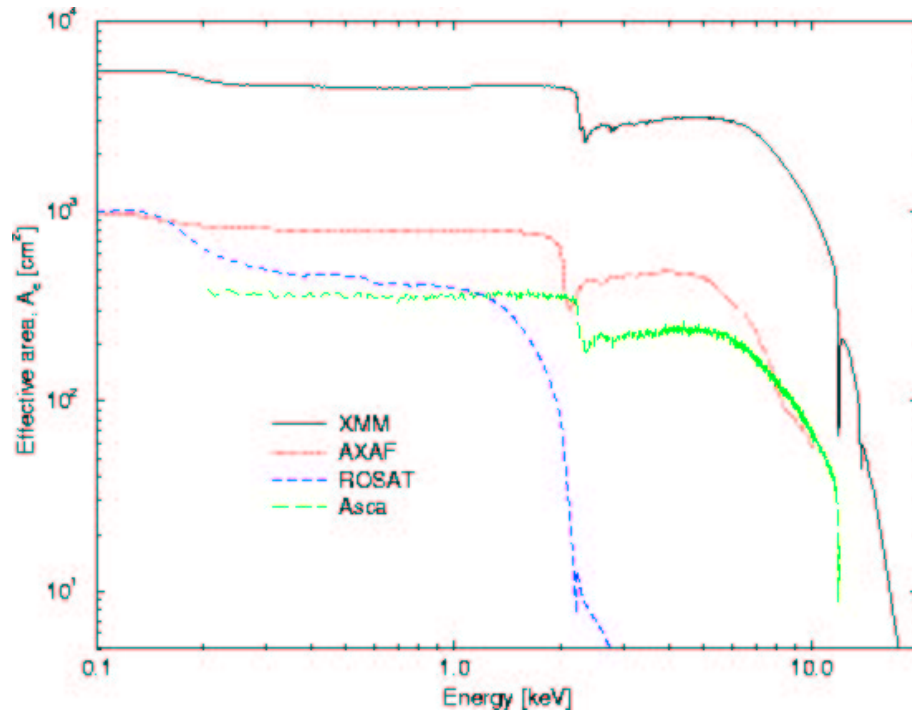


FIGURE 1.13. A comparison of the mirror effective areas of recent X-ray observatories, taken from the HEASARC *XMM-Newton* webpage (http://heasarc.gsfc.nasa.gov/docs/xmm/about_overview.html). *AXAF*, standing for the *Advanced X-ray Astrophysics Facility*, was the original name for the *Chandra X-ray Observatory*.

1.4.2 Data reduction and analysis

The *XMM* data have all been processed using *emchain* and *epchain* (for MOS and PN respectively) within the SAS (Science Analysis Software); the event-lists were further filtered using XMMSELECT, choosing patterns 0–12 for MOS and 0–4 (single- and double-pixel events) for PN, except in the event of pile-up, when pattern zero events only are used. The spectra were extracted using circular regions, with the same region off-set each time to obtain a corresponding background spectrum. These spectra were then grouped, using the FTOOL command *grppha*, to a minimum of 20 counts per bin, to facilitate the use of the χ^2 minimisation technique, before using the XSPEC software package to analyse them. Throughout this work, H_0 is taken to be $50 \text{ km s}^{-1} \text{ Mpc}^{-1}$, $q_0 = 0$ and $\Lambda = 0$. Errors are given at the 1σ level, unless otherwise stated.

When fitting spectra which are derived from a point source close to the centre of the

CCD chip, ready-made ‘canned’ response matrices can be used, rather than running the SAS commands *rmfgen* and *arfgen*. These are merged combinations of *rmfs* (redistribution matrix functions) and *arfs* (ancillary response functions), so just one file is required. However, if the sources are extended (not the case for the objects covered in this thesis), or are not all close to the centre of the CCD (particularly likely for serendipitous sources), then *arfgen* needs to be run for each object, to correct for vignetting effects and the encircled energy fraction. At this point, either *rmfgen* can be utilised, or canned CCD-only redistribution matrices (i.e. *rmf* not *rsp*) obtained from the *XMM* website. The energy resolution of the PN chips changes as one moves out from the centre, due to charge transfer effects; to take this into account, PN *rmfs* are provided at intervals of 20 rows, with Y0 being used for rows 1-20 (furthest from the centre), up to Y9 for the central objects. For example, *e pn_ff20_sdY9_qe.rmf* should be used with *arfgen* for a central source (Y9), extracted for patterns 0-4 (*sd* = singles and doubles) in a full-frame (*ff*) image. Note that, for pure redistribution matrices, the type of filter (thin, medium or thick) is not included; this becomes part of the generated *arf*. For MOS, the relevant responses are *m1_r5_all_15.rmf* and *m2_r5_all_15.rmf* (*all* meaning the spectra were extracted for patterns 0–12).

There are now updated *rmfs* for all observations, with the MOS files being time-dependent (due to changes in the instruments since launch). These *must* be used for observations which occurred after the MOS chips were cooled, in 2002 November, but should not lead to large differences for the earlier observations. Such updates are required due to the improved understanding of the quantum efficiency, spectral redistribution and Charge Transfer Inefficiency. More details on all the response matrices and updates can be found at <http://xmm.vilspa.esa.es/ccf>.

The Comptonisation model used to fit the soft excesses is *thCompfe* (Życki, Done & Smith 1999). This is more complex than the integrated XSPEC model *comptt* (Titarchuk 1994), in that it takes into account the roll-off of the power-law at low energies, due to the input photon distribution. Since it is uncertain whether disc photons are directly Comptonised by the hotter electron distribution, or whether some first interact with the cooler population, before being Comptonised a second time, the temperature of the photons

producing the power-law was always left free. The Comptonising electron temperature, however, was set to 200 keV. The temperatures are determined from the energy of the roll-over of the spectrum, which occurs at $\sim 4kT$. It is expected that the power-law-producing electrons have very high temperatures, leading to a roll-off well outside the *XMM* energy band, [the *Compton Gamma Ray Observatory* has observed breaks in the spectra of some Seyfert galaxies between 50–300 keV (Johnson et al. 1993)] so the arbitrarily large value of 200 keV was chosen. Throughout this work, the *hotter* Comptonised component refers to that which forms the power-law observed at the higher energies; the *cooler* component produces the soft excess emission.

Although for certain objects allowing the disc temperature (i.e., the original input photon temperature) to be free lead to a constrained value, this is unlikely to be accurate, since the temperature is expected to be too cool to be visible over the *XMM* bandpass. Hence, Equation 1.7 was used to provide an estimate. The black hole mass was estimated by assuming a bolometric luminosity of $10 \times$ the 0.2–10 keV value and taking this to be the Eddington value. For those objects with a measured black hole mass, the values were compared and found to be similar. The accretion rates are, naturally, more uncertain, but values of $0.01 \dot{M}_{Edd}$ for Sy1s (e.g., Pounds et al. 2003b) and $0.5 \dot{M}_{Edd}$ for NLS1s and QSOs (e.g., Janiuk et al. 2001) were assumed. The temperatures were then calculated for a radius of $3 R_{sch}$ which corresponds to the inner-most (and, therefore, hottest) stable radius about the black holes; this value was then rounded to the nearest 5 eV. It should be noted, though, that the outcome of the *thComp* model-fitting does not depend strongly on the temperature of the disc photons, provided kT_{bb} is not so high that a blackbody at that temperature would distort the X-ray spectrum above ~ 0.2 keV.

1.5 Aims of this thesis

The previous sections have described briefly what is currently known about AGN, in particular over the X-ray band. This thesis aims to try and understand how the soft X-ray excess is produced and what parameters of the AGN affect it, by considering samples of both low- and high-luminosity objects. These AGN have been observed and analysed

consistently, to provide samples which can be easily compared with each other. The wide range of luminosities/black hole masses may lead to a better understanding of how the accretion rate affects the soft excess if, indeed, it does so.

Chapter 2 covers Type-1 Seyfert galaxies, the relatively low luminosity AGN, while Chapter 3 deals with the high luminosity QSOs. Following these chapters, which analyse many different objects, Chapter 4 concentrates on three objects which have been observed a number of times by *XMM* and other X-ray satellites. This allows an analysis of the variation of the soft excess over time. Chapter 5 then investigates a sample of relatively distant radio-quiet QSOs. Chapter 6 covers the apparent Baldwin effect observed in the narrow iron lines identified in *XMM* data. This ties in with the previous work by investigating the differences between low- and high-luminosity objects. Finally, Chapter 7 summarises all the work and presents the conclusions which can be drawn.

Chapter 2

Accretion at low luminosity

2.1 Narrow Line and Broad Line Seyfert 1 galaxies

As introduced in Chapter 1, Seyfert galaxies represent the lower-luminosity ($M_{bol} > -23$), radio-quiet section of the AGN family, being more powerful than LINERS, but less so than QSOs. The boundary between bright Seyfert galaxies and the less-luminous QSOs is not hard and fast. For this thesis, the classifications from NED – the NASA/IPAC Extragalactic Database¹ – have been assumed. (A ‘rough and ready’ calculation of the absolute magnitudes of the objects found the mean value for the Seyfert sample to be ~ -21 , while the QSO mean magnitude was -24).

As with all AGN, Seyfert galaxies show strong X-ray emission, which can exhibit rapid variability over 1000s seconds (Mushotsky et al. 1993). The UV and optical continua also vary, but over periods of days (e.g., Edelson, Pike & Krolik 1990), while the IR emission varies only a little, over timescales of months (Edelson & Malkan 1987). The speed of these changes indicates that the X-rays must be produced in the innermost regions of the nucleus, while the other emission originates further out.

Only Type-1 objects – that is, those which show both forbidden and (broader) permitted lines – are being considered in this work. Osterbrock (1981) introduced intermediate classifications, with the notation Sy1.5, 1.8 and 1.9, where the strength of the broad line

¹NED is operated by JPL, under contract with NASA

component decreases as the numerical suffix increases. There is also a subsection of Sy1s, known as NLS1s; there are a number of observational differences between NLS1s and other Seyfert galaxies, mostly based on their optical spectra. The main characteristic of NLS1s is that they have particularly narrow Balmer lines, these being only slightly broader than the forbidden lines ($H\beta \lesssim 2000 \text{ km s}^{-1}$; Osterbrock & Pogge 1985); in this respect they are somewhat similar to Seyfert 2 galaxies, which only show narrow lines in their optical spectra. However, NLS1s also show an $[OIII]/H\beta$ ratio of > 3 , which is one of the distinguishing features of Type-1 AGN (Shuder & Osterbrock 1981). The third property is the frequent presence of strong FeII (or higher ionisation iron) emission lines; again, these are more usually seen in Seyfert 1 galaxies than in Seyfert 2s. When considering the X-ray band, observations with *ROSAT* found that NLS1s tended to have steep 0.1–2.4 keV X-ray slopes, leading to soft X-ray luminosities which are higher than can be explained by the reprocessing of the hard X-ray continuum. That is, if a hard X-ray source illuminates cool material – i.e., the accretion disc – the radiation which re-emerges from the disc will not be sufficiently strong to account for the total observed soft luminosities. This indicates that these objects may have strong soft excesses. They also have increased variability in the soft X-ray region, with doubling timescales as short as a few minutes (Boller, Brandt & Fink 1996). Brandt, Mathur & Elvis (1997) showed, using *ASCA* data, that NLS1s also have steeper 2–10 keV spectra than their Broad Line Seyfert 1 (BLS1) counterparts; this was later confirmed by Leighly (1999).

Liu et al. (2002) extend the disc-corona Comptonisation model (see Section 1.3.5) to the inner regions of the AGN. They state that, for high accretion rates, Compton cooling in the corona is very strong. This is, then, consistent with NLS1s having both a higher \dot{M} and a correspondingly steeper spectral slope.

To recap what was covered in Chapter 1, the X-ray spectra of Seyfert galaxies (both BLS1s and NLS1s) can be broken down into the following components:

- an under-lying power-law component; this dominates over the 2–10 keV (rest frame) band
- an emission line, usually close to 6.4 keV, signifying the presence of neutral (cold)

iron; there may be a combination of narrow and/or broad lines

- at lower energies, $\lesssim 2$ keV, the soft excess, which reveals itself as an upturn in the spectrum, away from the extrapolated power-law

The main aim of this thesis is to analyse the soft excess emission. The optical/UV continua of AGN are thought to be the thermal emission from the accretion disc; such a component would not be hot (or broad) enough directly to account for the temperature of the soft X-ray excess, so the alternative model of inverse Comptonisation is considered, whereby some of the disc photons interact with hotter electrons, thus gaining enough energy to explain the soft excess. In order to try and identify what does affect the properties of the soft excess, two separate samples of AGN have been analysed. This chapter concentrates on Seyfert 1 and Narrow Line Seyfert 1 galaxies, which, as stated above, are at the lower-luminosity end of the AGN family and, to some extent, are generally at relatively low redshifts. (This is something of a selection effect, since it is obvious that the brighter objects will be more easily visible at greater redshifts/distances.)

It might be expected that, if the soft excess were simply the high-energy tail of the accretion disc emission, then those objects with larger accretion rates and smaller black hole masses would possess hotter soft emission (Ross, Fabian & Mineshige 1992; see also Equation 1.7). However, Leighly (1999) found that the temperature of the soft excesses measured in that sample of NLS1s was close to constant, even though the objects covered a wide range of luminosities. As discussed in that paper, more sophisticated accretion disc models may be able to explain this constancy of temperature. Shimura & Takahara (1993) solve the equations, finding that at \sim Eddington accretion rates, the temperature is only weakly dependent on the black hole mass; this is due to the optical depth becoming independent of the central mass. This (lack of) variation in the temperatures will be investigated in the forthcoming chapters, as will any dependence of the soft excess strength on luminosity or spectral slope.

Table 2.1 lists the objects in this chapter, together with their position, classification, redshift and Galactic absorption. The AGN are a combination of proprietary observations

Table 2.1. The Seyfert and Narrow Line Seyfert 1 galaxies covered in this chapter, ordered by right ascension within their separate groups. RA and Dec. are given in Equinox 2000 coordinates.

Object	RA	Dec.	classification	redshift	Galactic N_H (10^{20} cm^{-2})
Mrk 335	00h06m19.5s	+20d12m10s	NLS1	0.026	3.99
Mrk 359	01h27m32.5s	+19d10m44s	NLS1	0.017	4.79
Mrk 1044	02h30m05.4s	-08d59m53s	NLS1	0.017	3.50
Mrk 766	12h18m26.5s	+29d48m46s	NLS1	0.013	1.71
Mrk 493	15h59m09.6s	+35d01m48s	NLS1	0.031	2.11
Mrk 896	20h46m20.9s	-02d48m45s	NLS1	0.026	3.89
Fairall 9	01h23m45.8s	-58d48m20s	Sy1	0.047	3.19
ESO 198-G24	02h38m19.7s	-52d11m32s	Sy1	0.046	3.13
1H 0419-577	04h26m00.8s	-57d12m00s	Sy1	0.104	2.03
NGC 4593	12h39m39.4s	-05d20m39s	Sy1	0.009	2.31
IC 4329a	13h49m19.2s	-30d18m34s	Sy1	0.016	4.42
NGC 5548	14h17m59.5s	+25d08m12s	Sy1	0.017	1.69
Mrk 841	15h04m01.2s	+10d26m16s	Sy1	0.036	2.34
ESO 141-G55	19h21m14.1s	-58d40m13s	Sy1	0.036	5.09
Mrk 509	20h44m09.7s	-10d43m25s	Sy1	0.034	4.40
Mrk 926	23h04m43.4s	-08d41m08s	Sy1	0.047	3.60

and public ones obtained from the online *XMM* Science Archive². The details of the observations (date, length, *XMM* mode, etc.) are given in Table 2.2.

2.2 Spectral analysis

The MOS 1, MOS 2 and PN spectra were extracted as explained in Section 1.5: a circular region (radius ~ 40 arcsec, although the exact size depended on where the target was positioned relative to the chip gaps) was centred on the source to produce the spectrum, before off-setting the same region slightly to obtain a background region. Only the spectra of IC 4329a suffered from pile-up (see Section 1.4), so all other spectra were extracted with patterns 0–12 for MOS 1/2 and 0–4 for PN (corresponding to sin-

²http://xmm.vilspa.esa.es/external/xmm_data_acc/xsa/index.shtml

Table 2.2. The details of the *XMM* observations performed of the Seyfert sample; the exposure time was taken from the headers of the spectral files. ^a The revolution number of the *XMM* orbit in question; ^b SW – Small Window, LW – Large Window, FF – Full Frame. Timing mode observations were not used; ^c error in proposal coordinates, so only PN data were obtained; ^d observations were co-added for analysis.

Object	start date (rev. ^a)	exposure time (ks)			mode ^b			filter		
		MOS 1	MOS 2	PN	MOS 1	MOS 2	PN	MOS 1	MOS 2	PN
Mrk 335	2000-12-25 (192)	33.7	33.7	28.4	LW	LW	FF	medium	medium	medium
Mrk 359	2000-07-09 (107)	3.9	3.9	2.5	SW	SW	LW	medium	medium	medium
Mrk 1044	2002-07-23 (480)	7.8	7.8	5.5	SW	SW	SW	medium	medium	medium
Mrk 766	2001-05-20 (265)	–	125.2	89.8	Timing	SW	SW	thin	medium	medium
Mrk 493	2003-01-16 (568)	18.4	18.4	13.7	SW	SW	LW	medium	medium	medium
Mrk 896	2001-11-15 (355)	10.4	10.4	7.2	LW	LW	FF	medium	medium	medium
Fairall 9	2000-07-05 (105)	28.7	28.7	27.7	LW	LW	FF	medium	medium	medium
ESO 198–G24	2001-01-24 (207)	22.9	23.1	15.6	FF	FF	FF	medium	medium	medium
1H 0419–577 ^c	2000-12-04 (181)	–	–	5.7	–	–	SW	–	–	medium
NGC 4593	2000-07-02 (103)	–	14.1	9.5	Timing	FF	SW	thin	medium	thin
IC 4329a	2001-01-31 (210)	12.7	12.7	9.9	LW	LW	FF	medium	medium	medium
NGC 5548 ^d	2001-07-09 (290)	–	82.8	65.1	Timing	SW	SW	medium	medium	thin
	2001-07-12 (291)	–	29.2	26.1	Timing	SW	SW	medium	medium	thin
Mrk 841	2001-01-14 (201)	–	13.3	9.5	Timing	SW	SW	thin	thin	thin
ESO 141–G55	2001-10-09 (336)	53.2	53.3	0	FF	FF	FF	medium	medium	medium
Mrk 509	2000-10-25 (161)	25.2	24.1	29.5	SW	SW	SW	thin	thin	thin
Mrk 926	2000-12-01 (180)	–	10.3	7.3	Timing	SW	SW	thin	thin	thin

gles/double/triples/quadruples for MOS and just singles/doubles for PN).

A consistent model was applied to each background-subtracted spectrum: first, as is conventional, a simple absorbed power-law was fitted, to the joint MOS+PN data, over the 2–10 keV (rest frame) energy band. While the soft excess (at low energies) and iron-lines/reflection components (at high energies) can make the definition of the power-law index complicated, in this thesis the traditional 2–10 keV band is taken to give a nominal power-law; this allows comparison with previous observations. The summed data, over the total length of the observations, were used, since there were no significant variations in count-rate for any of the objects, and the Galactic absorbing column in the direction of each object was determined from the *FTOOL nh*, which uses data from Dickey & Lockman (1990). Section 1.3.3 discusses the fact that AGN often show evidence for an emission line corresponding to iron around 6.4 keV. Hence, an intrinsically narrow ($\sigma = 10$ eV, corresponding to the resolution of *XMM*) line at ~ 6.4 keV was added to each fit, whether or not it was statistically required; occasionally it was necessary to fix the line energy at 6.4 keV, to obtain a sensible result. If the line improved the fit by 99% or more ($\Delta\chi^2 > 6.6$ for one degree of freedom, since the width was kept constant), the equivalent width (EW) and the 90% error are stated; if the line was insignificant, the 90% upper limit is given. The resulting power-law slopes and line data are given in Table 2.3 and Chapter 6 analyses the line data in more detail. Additional (generally broader) Gaussian components were included where statistically necessary; such broad lines are likely to be due to reflection from the accretion disc and are discussed in Chapter 1. Emission lines should, theoretically, be followed by a somewhat higher energy absorption edge, as discussed in Section 1.3.3; if such a feature improved the fit, the value is given in Table 2.4. The possible presence of a Compton reflection feature (see Chapter 1) was also investigated; only NGC 5548 required such reflection, though, with $R \sim 0.87$ (Table 2.4).

The last column of Table 2.3 gives the values of the two-point optical to X-ray spectral index, α_{ox} , which is defined as

$$\alpha_{ox} = \frac{\log \frac{f_{\nu(2keV)}}{f_{\nu(2500A)}}}{\log \frac{\nu(2keV)}{\nu(2500A)}} \quad (2.1)$$

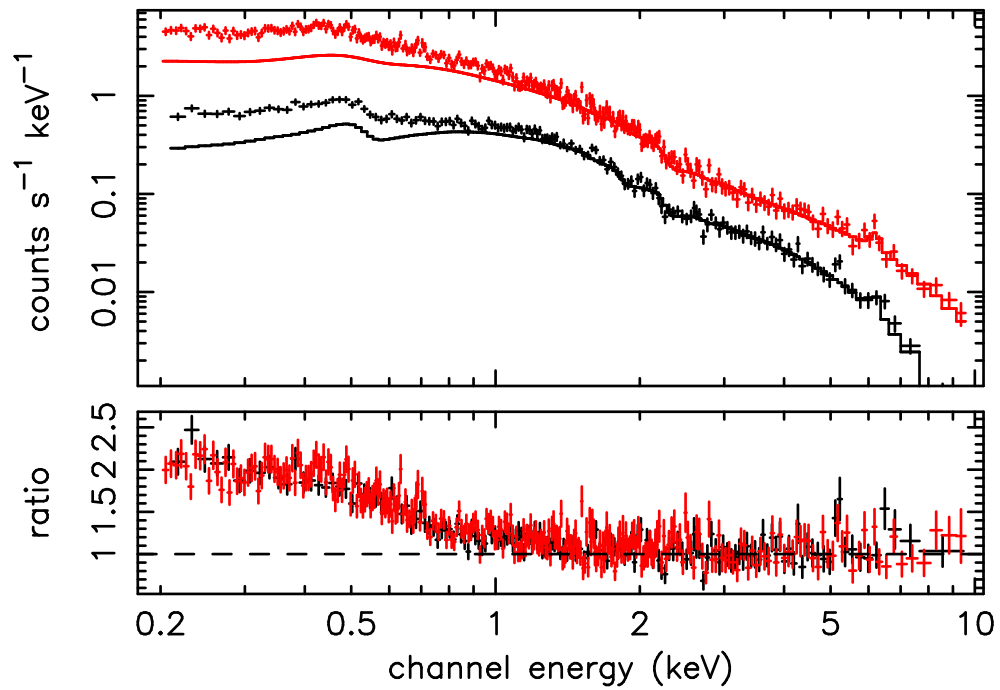


FIGURE 2.1. The soft excess of Mrk 896, an NLS1. MOS is shown in black, PN in red.

Since a literature search did not reveal measurements of α_{ox} for every object in this sample (or, indeed, for the QSOs in Chapter 3), each value was calculated for consistency, using optical magnitudes taken from NED. The optical continuum is assumed to be a power-law, with spectral index $\alpha = 0.7$; this allows the flux at 2500 Å to be estimated from the V-band magnitude (5500 Å). A steep α_{ox} then signifies that the Big Blue Bump is strong.

2.2.1 Blackbody parameterisation of the soft excess

The 2–10 keV power-law was then extrapolated down to 0.2 keV in the observed frame of reference. For each low-luminosity object, soft excesses (that is, excess flux above the extrapolated power-law) could be clearly seen; Figure 2.1 shows an example.

Although previous missions could not easily distinguish different models for the soft excess due to a lack of band-width and resolution in the low-energy instrumentation, the EPIC instruments on-board *XMM* are improving the situation, showing that there is in-

Table 2.3. Fits to the Seyfert sample over the 2–10 keV rest frame bands; 90 per cent errors are given for the equivalent widths of the lines, or the upper limit, when no line is statistically detected. α_{ox} is the estimated optical to X-ray spectral index, as discussed in the text. ^f frozen; ^a Both MOS and PN spectra piled-up, so single-pixel only (PATTERN=0) events were chosen, see Section 1.4; ^b MOS data only.

Object	2–10 keV Γ	Line Energy (keV)	intrinsic width (keV)	Equivalent width (eV)	2–10 keV luminosity (10^{43} erg s ⁻¹)	χ^2/dof	α_{ox}
Mrk 335	2.24 ± 0.01	6.52 ± 0.04 6.37 ± 0.10	0.291 ± 0.052 0.01^f	210 ± 58 < 39	3.66	1459/1235	1.45
Mrk 359	1.85 ± 0.04	6.44 ± 0.03	0.01^f	168 ± 65	0.66	259/271	1.59
Mrk 1044	2.03 ± 0.03	6.42 ± 0.02	0.01^f	183 ± 59	0.72	326/371	1.37
Mrk 766	2.06 ± 0.01	6.43 ± 0.02 7.04 ± 0.14	0.01^f 1.03 ± 0.11	26 ± 7 455 ± 110	1.47	2206/1927	1.40
Mrk 493	2.17 ± 0.03	6.45 ± 0.05	0.01^f	< 112	1.60	504/480	1.53
Mrk 896	2.04 ± 0.04	6.32 ± 0.04	0.01^f	138 ± 49	0.97	246/263	1.36
Fairall 9	1.82 ± 0.01	6.38 ± 0.01 6.83 ± 0.10	0.01^f 0.51 ± 0.11	98 ± 20 238 ± 82	10.07	1205/1263	1.58
ESO 198–G24	1.75 ± 0.02	6.41 ± 0.02 6.92 ± 0.05	0.01^f 0.01^f	70 ± 20 40 ± 22	9.92	950/970	1.29
1H 0419–577	1.88 ± 0.03	6.4^f	0.01^f	< 85	56.7	325/349	1.42
NGC 4593	1.80 ± 0.01	6.35 ± 0.01	0.01^f	100 ± 18	1.02	1324/1232	1.69
IC 4329a ^a	1.64 ± 0.01	6.40 ± 0.02	0.01^f	40 ± 10	1.11	1595/1536	1.14
NGC 5548	1.67 ± 0.01	6.40 ± 0.01	0.01^f	62 ± 6	4.57	2370/2081	1.42
Mrk 841	1.93 ± 0.02	6.39 ± 0.04	0.01^f	54 ± 26	8.10	871/852	1.43
ESO 141–G55 ^b	1.84 ± 0.10	6.44 ± 0.05 6.71 ± 0.10	0.01^f 0.279 ± 0.099	23 ± 15 98 ± 48	11.88	564/446	1.34
Mrk 509	1.66 ± 0.01	6.30 ± 0.07 6.91 ± 0.06 6.40 ± 0.06	0.128 ± 0.068 0.124 ± 0.093 0.01^f	73 ± 14 36 ± 18 < 36	14.3	1684/1616	1.51
Mrk 926	1.72 ± 0.01	6.36 ± 0.05 6.4^f	0.153 ± 0.066 0.01^f	101^{+258}_{-59} < 36	2.70	891/948	1.20

Table 2.4. The additional absorption components required from fitting the EPIC data. ^a excess absorption; ^b reflection parameter, $R = \Omega/2\pi$

Object	Edge Energy (keV)	τ	N_H^a (10^{22} cm^{-2})	ionisation parameter	R^b
Mrk 766	0.22 ± 0.01	1.61 ± 0.14	0.25 ± 0.05	158 ± 63	—
	0.40 ± 0.01	0.44 ± 0.04	—	—	—
	0.52 ± 0.01	0.42 ± 0.03	—	—	—
	0.70 ± 0.01	0.55 ± 0.04	—	—	—
	0.78 ± 0.02	0.13 ± 0.04	—	—	—
	1.02 ± 0.02	0.10 ± 0.02	—	—	—
	2.17 ± 0.02	0.06 ± 0.01	—	—	—
	7.10 ± 0.03	0.23 ± 0.03	—	—	—
ESO 198–G24	7.26 ± 0.10	0.17 ± 0.05	—	—	—
IC 4329a	0.72 ± 0.01	0.34 ± 0.04	0.30 ± 0.02	—	—
	0.87 ± 0.01	0.20 ± 0.93	—	—	—
	7.37 ± 0.06	0.14 ± 0.02	—	—	—
NGC 5548	0.72 ± 0.01	0.33 ± 0.01	—	—	0.87 ± 0.40
	0.87 ± 0.01	0.25 ± 0.01	—	—	—
	1.27 ± 0.01	0.05 ± 0.01	—	—	—
	1.79 ± 0.02	0.04 ± 0.01	—	—	—

trinsic curvature in the soft excess and that power-law models do not provide acceptable fits (e.g., Page et al. 2003a; Porquet et al. 2003; see also Sections 4.1.3 and 4.2.3). Subsequently, each soft excess was first modelled using a combination of blackbody (BB) components. Even though it was mentioned in the introduction (Chapter 1) that this is not a very physical method, since it is highly unlikely that the soft excess is due to direct thermal emission from the accretion disc, it is a useful parameterisation.

Both warm absorbers and cold, neutral columns of gas in the rest frame of the objects were tried each time, but it was found that this did not generally improve the fits. Some of the spectral fits were improved by the addition of absorption edges, though. Where relevant, these are listed in Table 2.4, together with the iron edges at higher energies. Further details can be found on the warm absorbers of these objects in such papers as Reynolds (1997), Morales & Fabian (2002), Steenbrugge et al. (2003) and Pounds et al. (2003b); see, also, below, for a discussion of Mrk 766 and NGC 5548.

Edges around 0.74 and 0.87 keV tend to be associated with O VII and O VIII respectively; however, individual edges are often very hard to identify, since it is unknown whether the absorbers are neutral, ionised, or if there is an out-flowing wind, which will lead to blueshifted results; see, e.g., Pounds et al. (2003a,d) and Reeves, O’Brien & Ward (2003) for recent results on high velocity, ionised outflows. The RGS instruments would provide a more in-depth study of the absorption (and emission) features present in the soft excess. However, to a first approximation, the soft emission is fairly featureless; the improved resolution provided by the RGS would not affect the overall BB (or Comptonisation; Section 2.2.3) continuum fits and this is discussed in the following section. In fact, Comptonisation serves to broaden and smear narrow disc features (Sunyaev & Titarchuk 1980), which helps to explain the lack of strong emission lines found in most AGN, although this doesn’t take into account any absorption that occurs away from the area of Comptonisation.

It was found that the number of BBs required for the best-fit model varied between one and three, with temperatures between ~ 20 and 400 eV; Table 2.5 lists the results for the best fits (Fe $K\alpha$ line energies and widths were frozen to the values found over the 2–10 keV band), while Figure 2.2 shows an unfolded plot of a typical soft excess. In Table 2.5 the temperatures of the blackbodies have been loosely grouped into cool, medium and hot columns. There is obviously not a specific cut-off between the components, so arbitrary boundaries were chosen. It should be noted, however, that the temperatures of the individual blackbodies are well determined and distinct. The coolest component is < 70 eV, while the hottest is > 200 eV. The ‘medium’ BB is always present and is always the strongest of the components, with F-test values of a few hundred for a decrease of two degrees of freedom. Since $F > 2.3$ corresponds to a probability of 90% for two parameters, this component is very strongly required. The other BBs are not quite as strong, but still significant, with F-values of $\gtrsim 10$ –15, with sometimes the ‘hot’ component being stronger than the ‘cold’ one, and vice versa.

Table 2.5. Fits over the 0.2–10 keV (observed frame) energy band. The soft excess has been modelled by a variable number of BB components. ^a BB temperature; ^b over the 0.2–10 keV (observed) band.

Object	Γ	kT ^a (keV)	kT ^a (keV)	kT ^a (keV)	total ^b lum. (10 ⁴⁴ erg s ⁻¹)	total ^b BB lum. (10 ⁴⁴ erg s ⁻¹)	BB/ Γ lum. ratio ^b	χ^2/dof
Mrk 335	2.05 ± 0.03	0.066 ± 0.001	0.144 ± 0.003	0.403 ± 0.013	1.69	0.79	0.89	2320/1707
Mrk 359	1.74 ± 0.06	—	0.120 ± 0.003	0.310 ± 0.026	0.17	0.05	0.44	755/740
Mrk 1044	1.89 ± 0.07	0.044 ± 0.003	0.115 ± 0.003	0.333 ± 0.024	0.36	0.21	1.40	920/842
Mrk 766	2.11 ± 0.02	—	0.125 ± 0.007	0.247 ± 0.017	0.65	0.23	0.55	3795/2392
Mrk 493	2.17 ± 0.03	0.031 ± 0.009	0.115 ± 0.007	0.198 ± 0.009	0.80	0.33	0.69	1117/944
Mrk 896	2.03 ± 0.04	—	0.084 ± 0.003	0.224 ± 0.022	0.33	0.10	0.41	698/715
Fairall 9	1.77 ± 0.02	—	0.112 ± 0.002	0.310 ± 0.015	2.20	0.30	0.16	1784/1727
ESO 198–G24	1.73 ± 0.03	—	0.125 ± 0.006	0.297 ± 0.021	2.07	0.25	0.14	1645/1532
1H 0419–577	1.88 ± 0.04	0.031 ± 0.002	0.110 ± 0.005	0.252 ± 0.030	18.2	5.9	0.48	734/706
NGC 4593	1.69 ± 0.02	—	0.099 ± 0.001	0.369 ± 0.009	0.24	0.06	0.35	2217/1704
IC 4329a	1.71 ± 0.01	—	0.070 ± 0.005	0.267 ± 0.013	2.73	0.72	0.36	3172/2011
NGC 5548	1.74 ± 0.01	—	0.130 ± 0.004	0.306 ± 0.015	0.88	0.11	0.14	4172/2537
Mrk 841	1.84 ± 0.03	0.038 ± 0.004	0.107 ± 0.002	0.275 ± 0.010	2.75	1.12	0.69	1580/1314
ESO 141–G55	1.63 ± 0.03	0.061 ± 0.008	0.139 ± 0.006	0.395 ± 0.014	2.70	0.69	0.34	686/561
Mrk 509	1.60 ± 0.01	0.018 ± 0.005	0.108 ± 0.001	0.326 ± 0.009	2.94	0.66	0.29	2869/2107
Mrk 926	1.71 ± 0.02	—	0.126 ± 0.005	0.307 ± 0.027	5.45	0.58	0.12	1441/1414

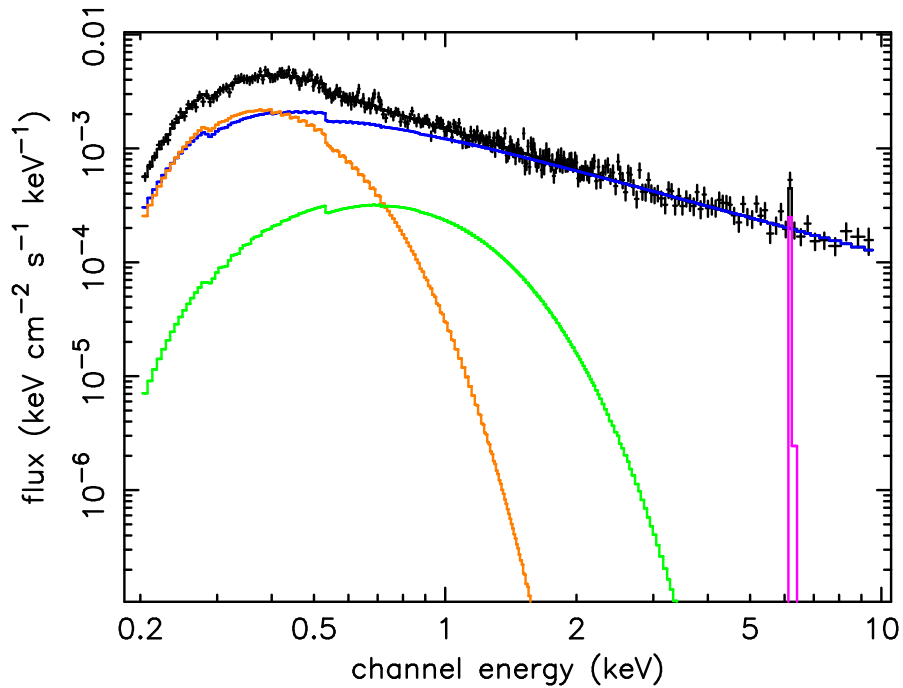


FIGURE 2.2. The unfolded spectrum of the blackbody fit to the NLS1 Mrk 896. For clarity, the PN data only are shown. The (blue) power-law has a spectral index of ~ 2.04 ; the narrow iron line, at 6.32 keV, has an EW of ~ 138 eV. The orange BB temperature is ~ 84 eV, the green one, ~ 224 eV.

2.2.2 Features of the soft excess

As mentioned above, the soft excess in this work is generally being modelled as a smooth continuum. However, if data from the high-resolution RGS instrument are analysed in detail, it is sometimes found that there are emission and/or absorption features apparent in the spectrum. Investigating these ‘humps and bumps’ gives an indication of the kind of elements found in the vicinity of the AGN, forming the constituents of any warm absorber or cold neutral gas present. If the lines are blue-shifted from their rest frame energies, then the presence of some form of out-flowing wind is suggested.

Analysing RGS data within XSPEC is a good first step: a quick look allows strong features to be found and modelled, although determining the actual ion – both the element and its ionisation state – has to be done manually. SPEX (Kaastra, Mewe & Raassen 2002), on the other hand, is a spectral analysis package which allows physical warm absorber models to be fitted to the data. There are two distinct models within SPEX:

the *slab* and *xabs* models. *Slab* considers the absorption edges and lines for each individual ion, while *xabs* is a grid photo-ionisation model, where the total column density, ionisation parameter and elemental abundances are given. Both models include outflow and broadening velocities; see Kaastra et al. (2002) for more details. Alternatively, the *xstar* code (Kallman et al. 1996) calculates a grid of ionised absorber models, which can then be used within XSPEC; this is very similar to *xabs* within SPEX.

Unfortunately, unless the features are particularly strong, long RGS observations of relatively bright sources are required to produce a spectrum worthy of a detailed investigation. Of the sources in this thesis, the RGS spectra of NGC 5548 (Steenbrugge et al. 2003; Pounds et al. 2003b), PG 1211+143 (Pounds et al. 2003a), PG 0844+349 (Pounds et al. 2003d) and PDS 456 (Reeves et al. 2003) have been analysed using the SPEX package or the *xstar* code. As an example of such work, the final fit for NGC 5548 is summarised below, the author of this thesis having worked on the paper by Pounds et al. (2003b).

NGC 5548

NGC 5548 shows clear evidence for absorption features superimposed on the soft excess (Figure 2.3). A detailed study of these data was reported by Steenbrugge et al. (2003) and, following on from this, Pounds et al. (2003b) performed a joint fit between the EPIC MOS 2 (MOS 1 was in Timing mode) and RGS data.

Figure 2.4 shows the joint fit to the data using the SPEX model *xabs*; the values for the warm absorber components are listed in Table 2.6. It should be noted that neon and sulphur are overabundant by unphysical values; this was also found for the fit to the RGS data alone, as discussed in Steenbrugge et al. (2003). Setting the values to the Solar abundance produced as good a fit statistically. It was found that the rather complicated resultant model could be simplified to a number of absorption edges (see Table 2.1); hence, ignoring the complexities of emission/absorption features when fitting the soft excess as observed by EPIC – and simply including the occasional absorption edge to improve the χ^2 slightly – is easily justified.

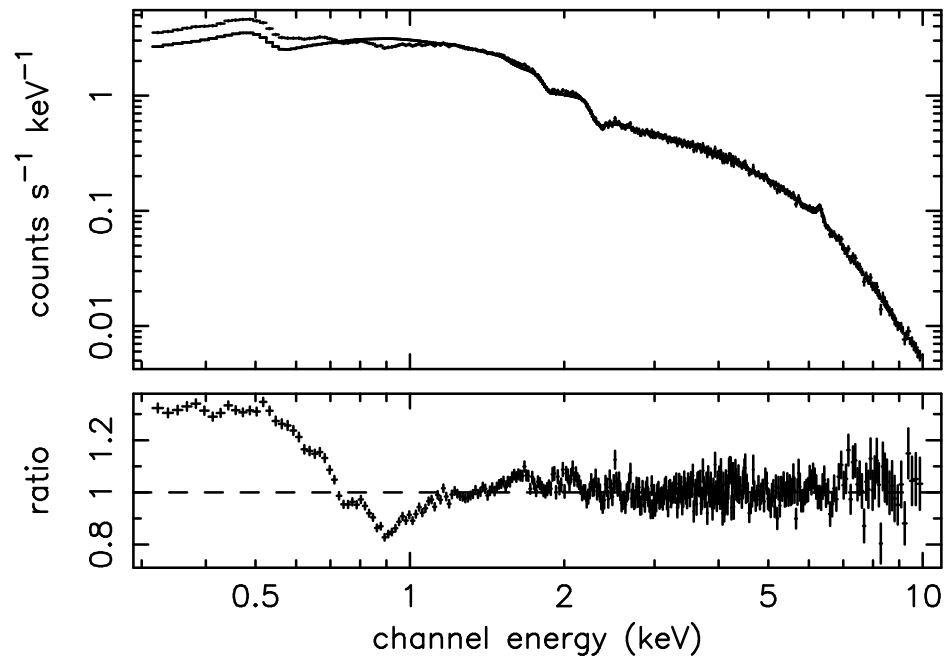


FIGURE 2.3. The broad-band spectrum of NGC 5548 (MOS data), showing the power-law fitted above 3 keV, extrapolated down to 0.3 keV. There is clear evidence for absorption superimposed on the soft excess emission.

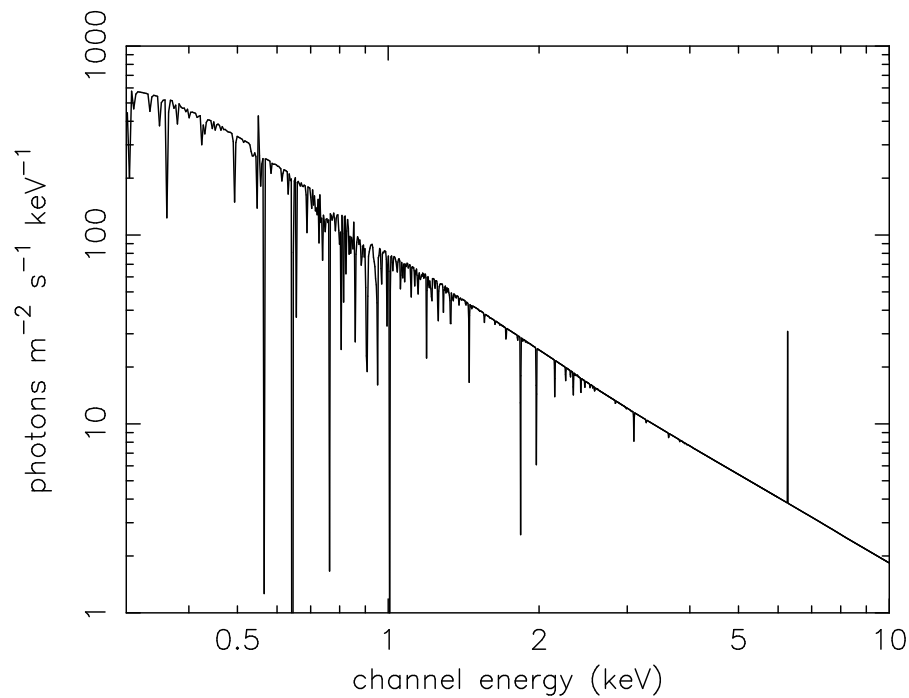


FIGURE 2.4. The warm absorber model to the joint MOS 2 and RGS data. The underlying continuum was modelled with a power-law and blackbody component, determined from the fit to the MOS data only.

Table 2.6. The warm absorber *xabs* fit to the NGC 5548 data. The continuum was modelled with a power-law and two blackbodies; the turbulence velocity (i.e., that which broadens the lines) was set to zero. ^a abundances are relative to oxygen, which is kept at the Solar value.

Component	1	2	3
N_H (10^{20} cm^{-2})	47.70	1.40	33.07
$\log \xi$ (erg cm s^{-1})	2.69	0.40	1.98
outflow velocity (km s^{-1})	-606	-512	-707
abundances ^a			
C	0	3.89	0.67
N	1.94	3.88	0.04
Ne	2.62	37.99	0
Na	0	0	3.91
Mg	0.86	0	0
Si	1.36	0	0
S	0.31	103.72	0.68
Ar	4.04	0	0
Fe	0.72	14.68	0.19

Mrk 766

As for NGC 5548, Mrk 766 has an extremely complex soft spectrum, with features that can either be explained by relativistic emission lines or a dusty warm absorber (Branduardi-Raymont et al. 2001; Lee et al. 2001; Mason et al. 2003; Turner et al. 2003). Such a detailed model is beyond the scope of this thesis and, so, the soft features have been simply modelled by a warm absorber and individual absorption edges where required.

2.2.3 The Comptonisation model

As discussed in Chapter 1, Comptonisation of the disc photons is a possible method for the production of the soft excess, together with the high-energy power-law shape. The model used here is the *thComp* model (Życki et al. 1999) as previously described in

Chapter 1, Section 1.5. The broad-band spectrum of each object was fitted with a double Comptonisation model, to cover the whole 0.2–10 keV energy band; this consisted of a low-temperature (usually $kT \sim 0.1\text{--}0.4$ keV) electron cloud to fit the soft excess, together with a high temperature one, with kT set to 200 keV. As explained in Section 1.5, this temperature is fixed because it will be too high to be measured over the *XMM* bandpass. The value is calculated from the exponential roll-over point of the power-law, which occurs at $4kT$, where kT is the energy of the electron population; since the hotter electrons are expected to have temperatures well above 10 keV, this cut-off will not be observed in the *XMM* data. It was found that this model led to excellent fits for most of the objects, as is shown in Table 2.7 and Figure 2.5. Also given in the table are the photon indices obtained from the earlier 2–10 keV fits (first given in Table 2.3). Comparing these with the values formed through Comptonisation, it can be seen that the values are very similar. In all but three of the cases, the *thComp* value for the slope is slightly steeper than the simple power-law fit to 2–10 keV, although this is not a large difference when the errors are taken into account.

By allowing the temperature of the photons which act as the input to the Comptonisation process forming the power-law to be free in the model, it is clear that these photons are much hotter than those directly emitted from the accretion disc. This implies that, if this model is correct and self-consistent, the photons first interact with the cooler, soft-excess-forming electrons, before progressing to the hotter population. In one case (NGC 4593), the power-law input-photons appear to be at a higher temperature than the soft excess itself. This seems highly unlikely, but is a very strong indication that it is not the thermal photons from the disc which directly form the power-law.

2.3 Discussion

Both the multiple-BB and Comptonisation models provide good fits to the broad-band spectra for these Broad and Narrow Line Seyfert galaxies, although the Comptonisation model provides the more satisfactory, physical explanation for the processes occurring. However, it should be noted that, for those objects with soft excesses best fitted with

Table 2.7. Comptonisation fits to the broad-band Seyfert spectra. Hotter (power-law) electron temperature set to 200 keV. The penultimate column restates the photon index found by fitting a simple power-law+Gaussian model to the 2–10 keV band for comparison. ^a soft excess component; ^b power-law component; ^c optical depth; ^f frozen

Object	COOLER COMPTONISED COMPONENT ^a			HOTTER COMPTONISED COMPONENT ^b		2–10 keV Γ	χ^2/dof
	input photon temperature ^f (eV)	electron temperature (keV)	τ^c	input photon temperature (keV)	Γ		
Mrk 335	15	0.173 ± 0.009	21 ± 2	0.052 ± 0.015	2.23 ± 0.10	2.24 ± 0.01	2403/1709
Mrk 359	60	0.150 ± 0.017	34 ± 7	0.089 ± 0.025	1.93 ± 0.03	1.85 ± 0.04	768/738
Mrk 1044	50	0.148 ± 0.030	25 ± 4	0.144 ± 0.035	2.09 ± 0.02	2.03 ± 0.03	980/844
Mrk 766	40	0.241 ± 0.014	17 ± 2	0.132 ± 0.059	2.14 ± 0.01	2.06 ± 0.01	3781/2394
Mrk 493	40	0.147 ± 0.024	46 ± 8	0.081 ± 0.005	2.32 ± 0.02	2.17 ± 0.03	1244/946
Mrk 896	50	0.412 ± 0.152	12 ± 3	0.374 ± 0.078	1.97 ± 0.10	2.04 ± 0.04	707/715
Fairall 9	10	0.131 ± 0.015	35 ± 32	0.073 ± 0.058	1.87 ± 0.01	1.82 ± 0.01	1804/1726
ESO 198–G24	10	0.345 ± 0.124	15 ± 6	0.096 ± 0.041	1.81 ± 0.02	1.75 ± 0.02	1667/1532
1H 0419–577	10	0.199 ± 0.019	20 ± 2	0.089 ± 0.037	1.93 ± 0.02	1.88 ± 0.03	760/707
NGC 4593	20	0.103 ± 0.004	66 ± 5	0.192 ± 0.010	1.87 ± 0.10	1.80 ± 0.01	2263/1703
IC 4329a	15	0.550 ± 0.290	9 ± 3	0.226 ± 0.020	1.72 ± 0.02	1.64 ± 0.01	3191/2011
NGC 5548	10	0.349 ± 0.019	20 ± 1	0.101 ± 0.006	1.76 ± 0.02	1.67 ± 0.01	4193/2536
Mrk 841	10	0.184 ± 0.007	21 ± 2	0.076 ± 0.023	2.02 ± 0.01	1.93 ± 0.02	1702/1316
ESO 141–G55	10	0.723 ± 0.111	10 ± 1	0.088 ± 0.009	1.68 ± 0.06	1.84 ± 0.10	758/566
Mrk 509	10	0.111 ± 0.016	55 ± 6	0.114 ± 0.066	1.75 ± 0.01	1.66 ± 0.01	3036/2109
Mrk 926	5	0.237 ± 0.033	19 ± 5	0.090 ± 0.034	1.76 ± 0.01	1.72 ± 0.01	1455/1414

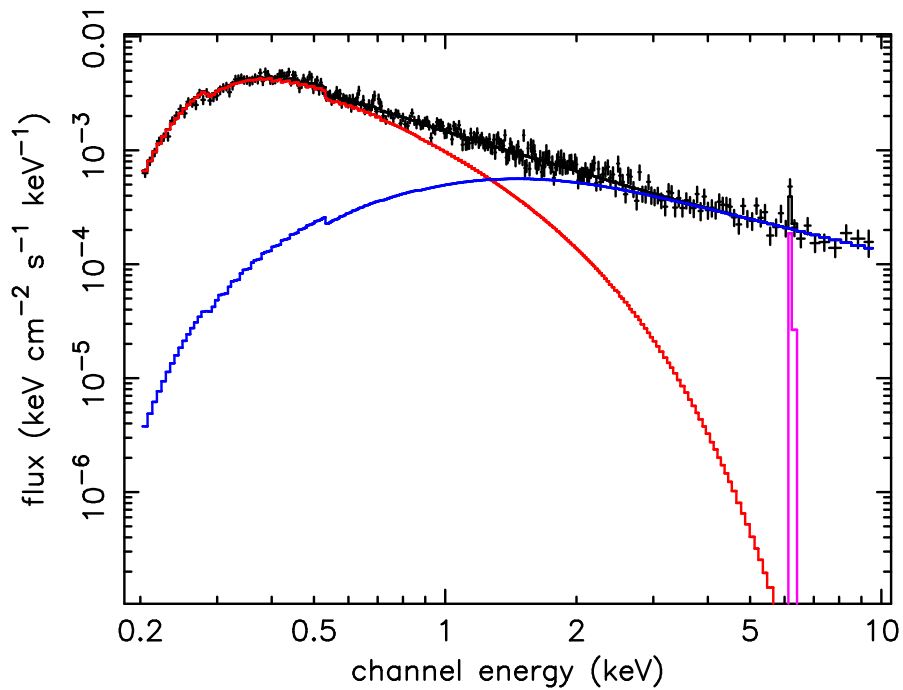


FIGURE 2.5. The broad-band spectrum of Mrk 896 modelled by two Comptonised components and an iron line. The temperature of the cooler, soft-excess component is $kT \sim 0.412$ keV, with an optical depth of ~ 12 . The hotter component has a spectral index of $\Gamma \sim 1.97$.

three BB components, deleting the third still results in a statistically better fit than for the double Comptonisation model. It is difficult to imagine how there could be two or three areas emitting blackbody radiation at different temperatures, whereas the Comptonisation model seems somewhat ‘neater’ and easier to explain. It must be borne in mind, though, that these models are simply parameterisations, and a ‘means to an end’, when it comes to investigating the spectra.

Referring back to Table 2.5, the ratio of the luminosities of the soft excess to the power-law, over the *XMM* observable band of 0.2–10 keV, are given. In general, the power-law has the larger luminosity, although, for the case of Mrk 1044, an NLS1, the soft excess is actually the stronger component. This is also shown for the Comptonisation model in Figure 2.6; the solid line shows the points where the two components would have equal luminosities. Since most of the points lie below the line, it is clear to see that the harder component contains most of the luminosity over the observed 0.2–10 keV

band. (Using this model, it is Mrk 1044, Mrk 896, Mrk 766 and IC 4329a which have more luminous soft excesses than power-law components.) It should be noted, however, that these luminosities are very dependent on the energy band over which they are calculated. If the model fitted is extrapolated to lower energies, then much more of the soft excess will be included; Figure 2.7 illustrates this for Mrk 896; the soft excess peaks around 0.2 keV. It must be cautioned, however, that there are no physical data below 0.2 keV; the extension is purely an extrapolation of a theoretical model. Thus, Figure 2.6 was re-plotted, using the luminosities calculated over the rest frame band of 0.001–10 keV; the plot is shown in Figure 2.8. (The *dummyrsp* command within XSPEC was used to extend the model fitted to the data to energies below the band covered by *XMM*.) Again, the line shown is that of $y = x$; i.e., where the luminosities of the components over the energy band are equal. Now the soft excess luminosities are much more likely to be comparable to, or larger than, the value for the hotter Comptonised component. It should be noted that, although this method gives the total luminosity for the soft excess, it cannot do so for the power-law component, since this extends out to very high energies; assuming this power-law is actually due to Comptonisation, there will, eventually, be a roll-over, but this cannot be constrained without the addition of very high energy data – e.g., archive data from the PDS instrument which was onboard *BeppoSAX*. Hence, it is not logical to extend the model higher than 10 keV, since the maximum energy would be purely an arbitrary value. However, because of the slope of the power-law, its contribution to the luminosity generally decreases at higher energies. Taking Mrk 896 as an example again, extrapolating the response matrix up to 500 keV, while keeping the the temperature of the hotter component at 200 keV, the 0.001–500 keV luminosity is found to be only approximately double that over the 0.001–10 keV band. Hence, over the entire range of soft to hard X-ray energies (~ 1 eV up to hundreds of keV), the power-law will be somewhat stronger than the values quoted here, so may always dominate the soft excess value.

To try and identify if there is a link between the relative strength of the soft excess and the luminosity of the object, Figure 2.9 was plotted. The strength of the soft excess is defined as being the ratio of the de-reddened luminosities of the blackbodies to the power-law, over 0.2–10 keV. Using the blackbody parameterisation was simply for con-

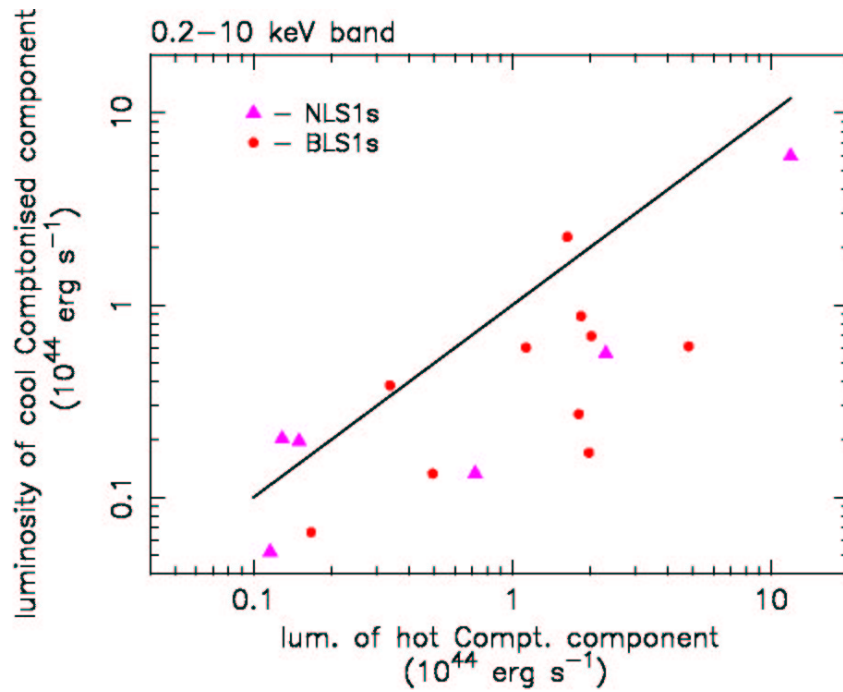


FIGURE 2.6. When considering the 0.2–10 keV (observed) energy band, the ‘power-law’ Comptonised component tends to be more luminous than the soft excess.

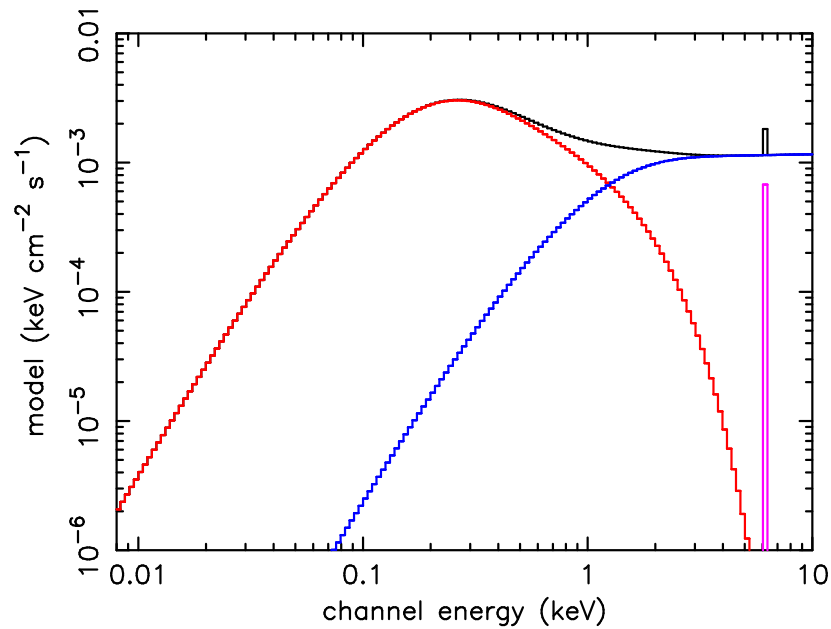


FIGURE 2.7. The extrapolated Comptonisation model for Mrk 896. Using *dummysp*, the model fitted over the 0.2–10 keV *XMM* band can be extended to much lower energies. This allows more of the theoretical soft excess to be included, since the emission actually peaks ~ 0.2 keV.

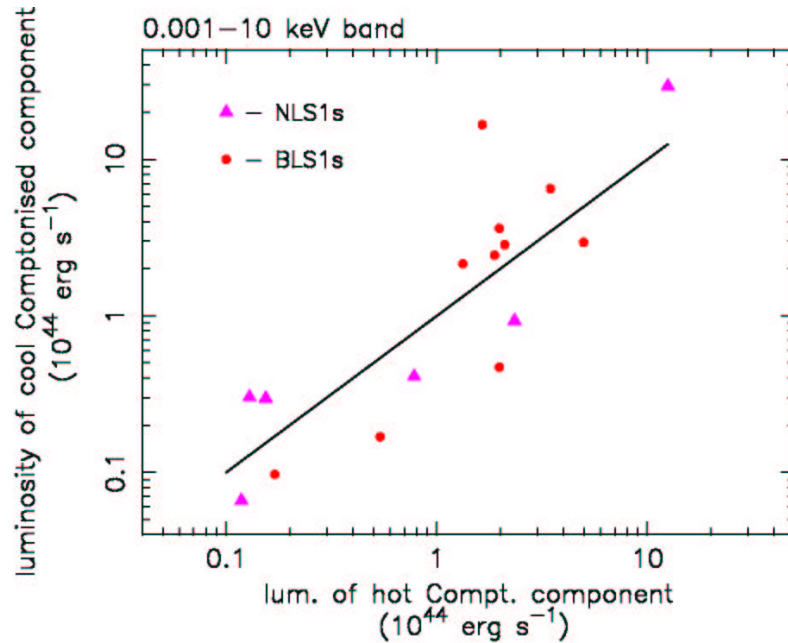


FIGURE 2.8. Extrapolating the model to lower energies allows the total luminosity of the soft excess to be calculated. The energy range used was 0.001–10 keV, for both the soft excess and the hotter component. The solid line shows where the luminosities of the two components are equal.

venience; the strength could have been defined using the Comptonisation model instead, either as the ratio of the luminosities of the cool and hot components, or as a ratio of the normalisations of these parameters, which have units of photons $\text{cm}^{-2} \text{s}^{-1}$ at 1 keV (Życki, private communication). Taking the ratio of the normalisations of the power-law and BB components is not so straight forward, since there is usually more than one BB to consider and the normalisation units are different for the power-law and BB components. The ratio of the normalisations of the *thComp* components is plotted against the broad-band luminosity in the lower panel of Figure 2.9.

Since this is a comparison, the actual energy range chosen is not overly important, so long as the band used remains constant. The abscissa of Figure 2.9 is the total 0.2–10 keV (de-reddened) luminosity of each object. The plot shows a large amount of scatter, implying that there is no close correlation between the strength of the soft emission and the X-ray luminosity. Using a simple Spearman Rank (SR) test, it was found that the probability of an inverse correlation with the soft excess/power-law luminosity ratio was

only $\sim 54\%$. It is noticeable that it is generally the NLS1s which have the larger BB/T luminosity ratio, with the mean value for the NLS1s being 0.73, more than double that for the BLS1s (0.31). However, even when considering the NLS1s and BLS1s separately, there is no significant correlation between ratio and the total luminosity. Vaughan et al. (1999) investigate a sample of *ASCA*-observed NLS1s, finding similar soft excess luminosity ratios as presented here. They conclude that NLS1s tend to show strong soft excesses, even with the limited low-energy data provided by *ASCA*.

All further plots use the BB/T luminosity ratio as the definition of the relative strength of the soft excess; however, the correlations were also checked using the normalisation ratio and were found to be in broad agreement.

Figure 2.10 plots the BB/power-law luminosity ratio against 2–10 keV power-law slope. As the slope steepens (i.e., softens), the soft excess becomes stronger in relation to the power-law. This is, to some extent, counter-intuitive: a steeper slope might be expected to ‘eat into’ the soft emission (since, in the BB+power-law model, the power-law continues to low energies without any form of cut-off), decreasing the measured soft excess; however, this is not the result found. As mentioned at the start of this chapter, NLS1s are generally found to have both steep slopes (Brandt, Mathur & Elvis 1997) and strong soft excesses (corresponding to steep spectra over the *ROSAT* band; Boller et al. 1996), possibly due to Compton cooling of the hard electrons by the increased soft flux. Figure 2.10 confirms this previously-found relationship between steepness of slope and strength of soft excess, with an SR correlation of 99.99%; the best fit line through the points has a gradient of 1.66 ± 0.03 , from weighted linear regression. It should be noted that, even when excluding the NLS1 points, the correlation between the strength and slope is still strong, when considering linear regression: 6.06 ± 1.07 . Spearman Rank only gives a probability of 85%, though, which is not significant.

There is a possibility (Chapter 4) that Compton cooling of the corona above the accretion disc may occur. That is, as the soft photons from the disc pass through the Comptonising corona, they gain energy; assuming there is no external heating source, this implies that the coronal electrons must, in turn, become cooler. Naturally, if there is some form of heating source – for example, magnetic flares above the disc – then

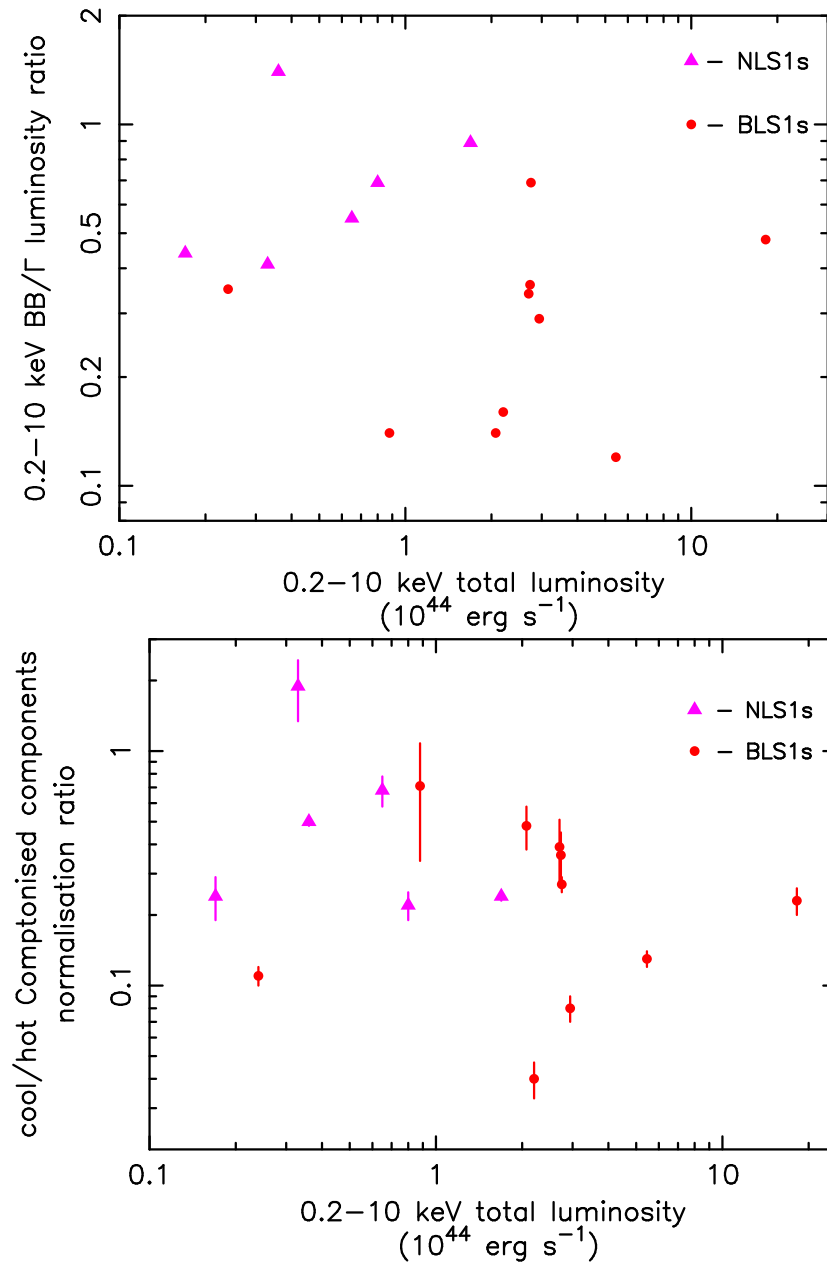


FIGURE 2.9. The top plot shows the variation of the ratio of soft excess blackbody to power-law luminosities over the 0.2–10 keV band with total 0.2–10 keV luminosity; the lower plot compares the normalisations of the Comptonised components with the luminosity

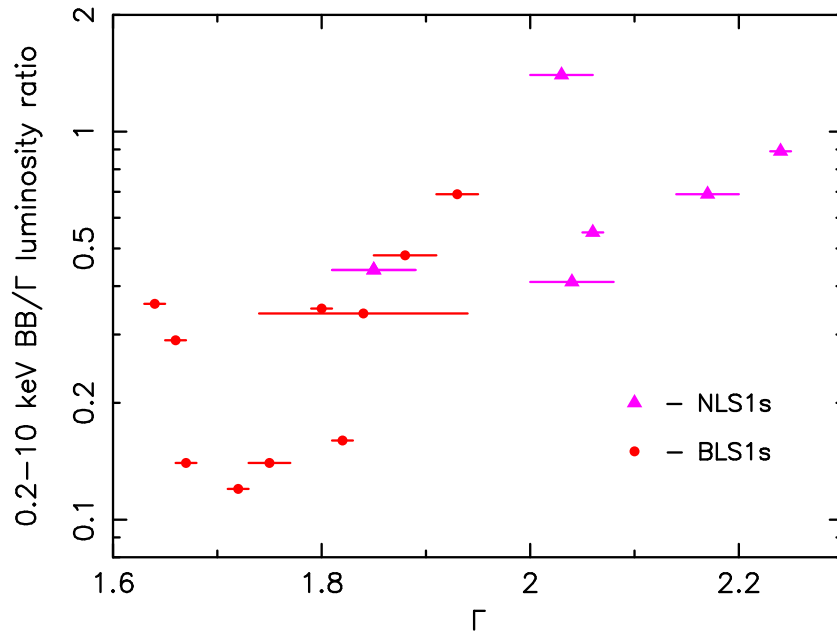


FIGURE 2.10. Plot of soft excess strength against power-law slope over the 2–10 keV rest frame for each object.

the temperature of the corona does not have to decrease and can either stay constant or become hotter, depending on the power of the heat source.

To explore both the possibility of cooling and the link between the soft excess and the Big Blue Bump, the above luminosity ratio was compared to α_{ox} (Table 2.3). This is not the only method which could be used, but seemed the most straight-forward, with a steep value of α_{ox} taken to mean the BBB is strong. From Figure 2.11 there appears to be no correlation between the measurements (SR probability of $< 60\%$ for a positive trend).

Comparing the slope of the soft excess with α_{ox} , however, does reveal an anti-correlation (top of Fig. 2.12): the steepest optical to X-ray slopes occur when the soft excess slope is the flattest ($> 99.9\%$ probability from Spearman Rank). Since $\Gamma \sim 1/(kT\tau^2)^{1/2}$, from Equations 1.8 and 1.9, a trend between the slope and α_{ox} suggests that there may also be correlations with the temperature and/or the optical depth, τ . These are plotted in the lower half of Fig. 2.12. Using the Spearman Rank, the probability of an inverse correlation between the temperature and α_{ox} is 99.99%, while the τ - α_{ox} correlation is

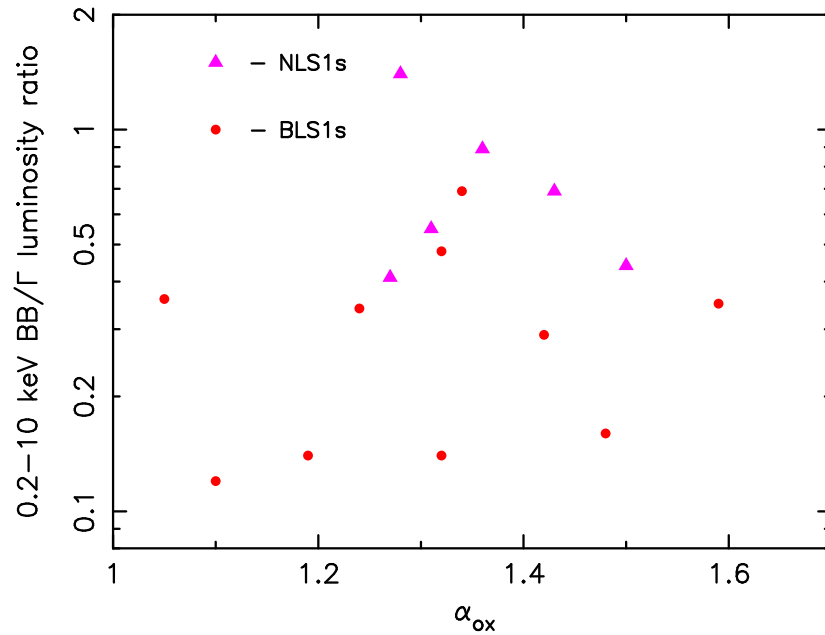


FIGURE 2.11. Plot showing the relative strength of the soft excess in comparison to the two-point optical to X-ray slope, α_{ox} .

significant at $> 99.999\%$. Drawing these results together, it is found that, for a steeper optical to X-ray slope (i.e., in the presence of more optical/UV photons), the slope of the soft excess hardens. This appears to be partly due to a decrease in the temperature of the corona (which could be explained by a Compton cooling effect: more input photons \Rightarrow electrons are cooled) and partly due to an increase in the coronal optical depth. It must be cautioned, however, that the temperature and optical depth are strongly coupled within the *thComp* model. Because of this, the dependency of the overall slope on α_{ox} is the most clear-cut result.

Finally, it was found that a high broad-band (0.2–10 keV) luminosity does not automatically imply a hot corona (Fig. 2.13), but the total luminosity is strongly correlated ($\sim 99.7\%$) with the luminosity of the Comptonised soft excess component (Fig. 2.14) over the 0.2–10 keV range (99.9 % over 0.001–10 keV). This last result relates to Figures 2.6 and 2.8, where it was found that the luminosities of the two Comptonised components increased together. Only if there were some kind of inverse correlation between the low- and high-energy components would the total luminosity not be related to that of the soft excess. These findings are true for both NLS1s and BLS1s, with the NLS1s

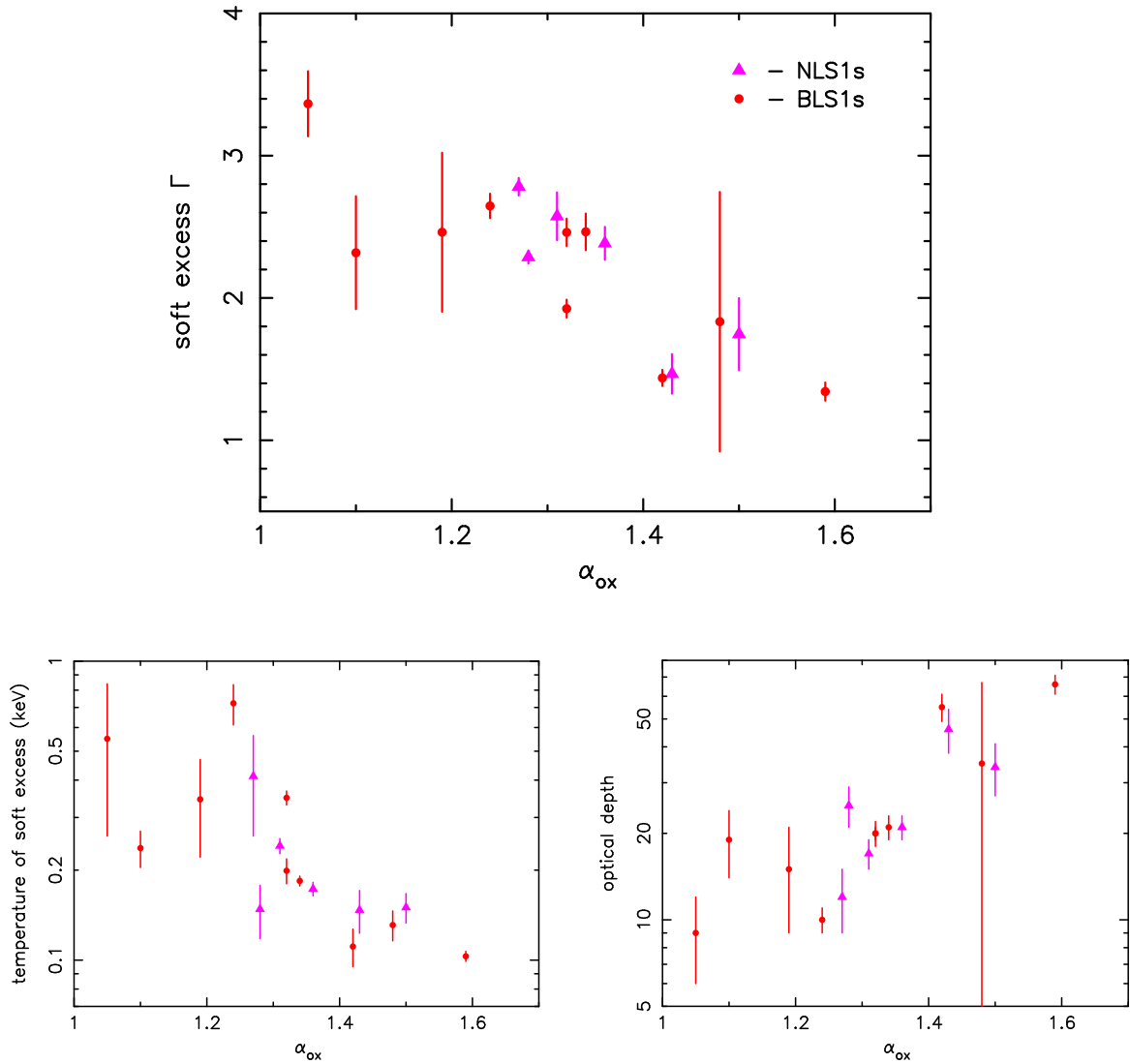


FIGURE 2.12. Investigating the link between the shape of the soft excess and α_{ox} reveals various correlations. Both the slope and the temperature of the soft excess are anti-correlated with α_{ox} , while the optical depth shows a positive correlation.

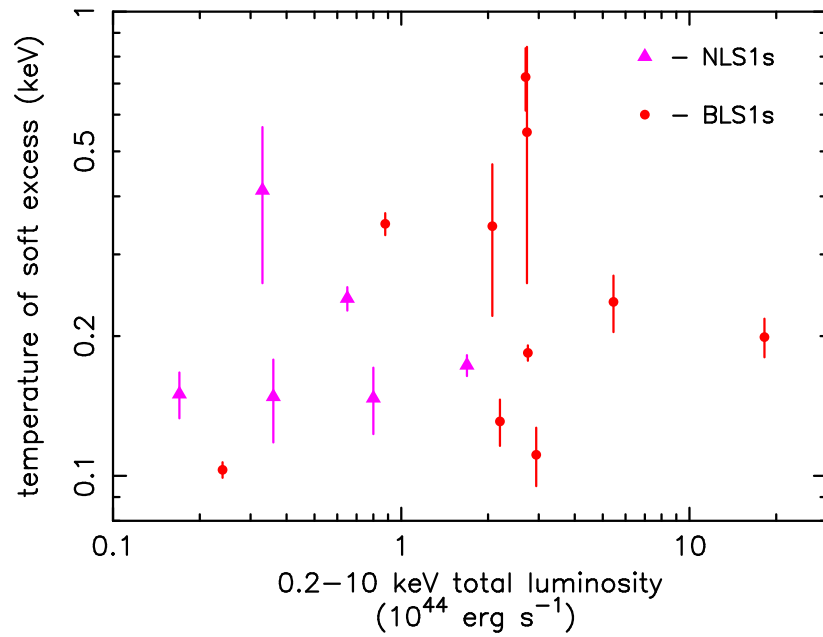


FIGURE 2.13. Luminous Seyfert galaxies do not, necessarily, have hot soft excesses.

generally being the lower luminosity objects.

2.4 Summary

This chapter has investigated the soft excesses of relatively low luminosity AGN, i.e., Narrow Line and Broad Line Seyfert 1 galaxies. Within the group, one difference, in particular, is apparent, namely that the NLS1s tend to show steeper power-law components and correspondingly stronger soft excesses (Fig. 2.10). This is, actually, slightly noticeable within the BLS1s alone: the continuum is steeper when the soft excess is stronger. This may be due to the Compton cooling of the coronal electrons producing the power-law component. As Table 2.7 shows, it is possible, within the framework of the model used, that the photons which act as an input to the hotter (power-law) corona have already been Comptonised to the soft excess temperature. Hence, the more photons there are forming the soft excess, the more there are to interact with, and cool, the more energetic electrons; the cooler the electrons forming the power-law, the steeper (softer) the resulting continuum.

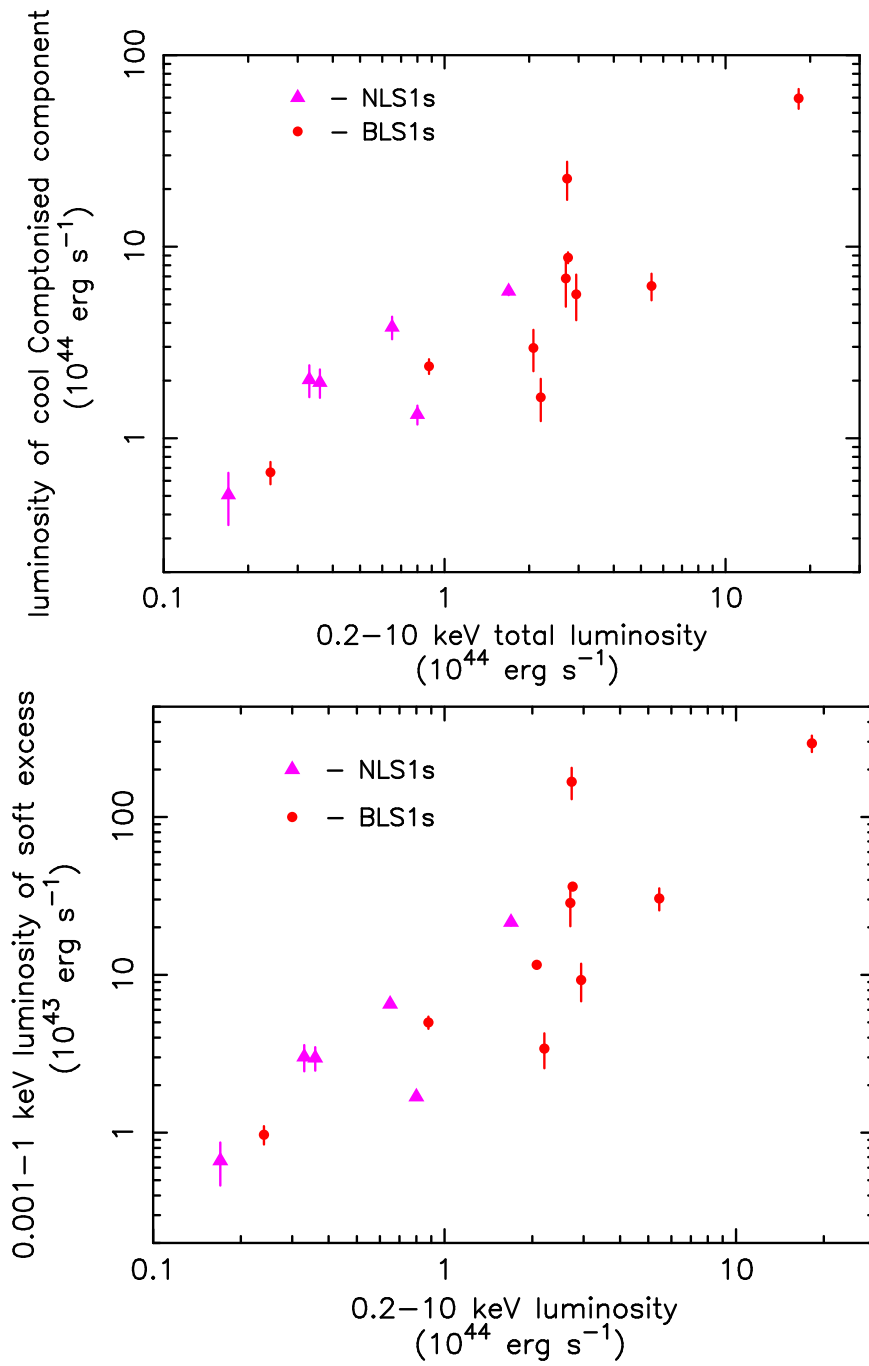


FIGURE 2.14. Luminous Seyfert galaxies have bright soft excesses, whether the luminosity is measured over the observed 0.2–10 keV band, or over the extended 0.001–10 keV range.

Comparing the soft excess parameters with α_{ox} , there is an anti-correlation between the two slopes – the optical to X-ray value and that of the soft excess. This may be, in part, due to the cooling of the coronal electrons, although the optical depth of the corona also seems to vary. The temperature of the soft excess (i.e., the cool Comptonised component) covers only a small range, with a mean value of $kT = 0.143 \pm 0.003$ keV. This constancy of temperature is in agreement with the findings of Leighly (1999).

There is a large scatter in the graph of soft excess strength versus 0.2–10 keV luminosity, implying there is no correlation between the parameters. Likewise, no trend was found with α_{ox} . However, the more luminous sources do have brighter soft excesses, although they may not be the hottest.

When considering the narrow-line and broad-line objects separately, most of the parameters cover the same ranges; as mentioned above, NLS1s have steeper 2–10 keV power-law indices and stronger soft excesses comparative to the power-laws, but the actual properties of the soft excesses – e.g., temperature and optical depth – are very similar to those for the BLS1s. It was suggested in the introduction that the physical difference between these groups of objects is likely to be one of accretion rate. Hence, accretion rate does not seem to be instrumental in altering the parameters of the soft excess. This would seem to imply that the soft excess is somehow fundamental to the intrinsic model of AGN and will be further investigated for the higher-luminosity objects in the next chapter.

Chapter 3

Accretion at high luminosity

3.1 Quasi-stellar objects

QSOs – both radio-loud and radio-quiet – are defined to be the brightest AGN, with bolometric magnitudes of $M_{bol} < -23$, although the *X-ray* emission from radio-quiet AGN is about three times lower than that from their radio-loud counterparts (Zamorani et al. 1981; Worrall et al. 1987). To recap from Chapter 1, radio-loud AGN are defined as being those with $R \gtrsim 10$, where R is the 5 GHz/B-band flux ratio. There may be an actual dichotomy between RL and RQ AGN, whereby the radio-loud objects have larger black hole masses (e.g., Laor 2000a; Laor 2000b; McLure & Dunlop 2001), although whether the change in radio-loudness is continuous or not is still under debate (see Section 1.1.4).

In the early days of AGN research, the extremes of both Seyfert galaxies and QSOs were discovered, leading to a large luminosity gap between the two types. QSOs were not, at first, identified with host galaxies, because their central nuclei were so bright that they appeared star-like, hence the name of *Quasi-stellar* objects. Over time, however, both groups were extended, until the brightest Seyferts were very similar to the least luminous QSOs, leading to the idea that Seyferts and QSOs do, in fact, form a continuous group. QSOs are thought to have more massive black holes than those in Narrow- and Broad-Line Seyfert 1 galaxies (see, e.g., black hole masses given by Kaspi et al. 2000 and McLure & Dunlop 2001), although their accretion rates may be similar to NLS1s

(i.e., high; Boroson 2002), with BLS1s accreting less rapidly.

Initially the soft excess was found to be common in Seyfert galaxies (Turner & Pounds 1989), although the same feature was also frequently found to exist in the spectra of QSOs (Masnou et al. 1992; Saxton et al. 1993). The first detections were in radio-quiet objects (Comastri et al. 1992), but later work also identified soft excess emission in radio-loud AGN (Bühler et al. 1995; Prieto 1996; Schartel et al. 1996). As covered later, in Chapter 5, RLQs have flatter hard X-ray spectra than those measured for the radio-quiet objects (e.g., Wilkes & Elvis 1987; Brinkmann et al. 1997; Reeves et al. 1997). RLQs are also more likely to show intrinsic absorption (e.g., Elvis et al. 1994; see also Chapter 5). Both this hardening of the slope and the existence of an absorbing column may be tied in to the presence of the strong collimated radio jets which make quasars strong radio emitters. However, investigating two radio-loud QSOs in detail (3C 273 and PKS 0558–504, Chapter 4) shows their soft excesses to be very similar to those measured in their radio-quiet counterparts. This implies that the soft excess is probably not related to the jet emission.

As previously discussed, a simple-minded approach might suggest that having a more massive black hole would lead to a cooler accretion disc and, hence, a cooler/weaker soft excess. However, disc theory and the production of the soft excess are not yet well enough understood to draw such conclusions. Chapter 2 covered the soft excesses found in the lower-luminosity Seyferts and NLS1s; here, the same analysis is repeated, but for objects classified as QSOs. The majority of the targets in this sample are radio-quiet, as Table 3.1 shows. Table 3.2 also lists the observation modes of *XMM* for the different QSOs.

3.2 Spectral analysis

As for the Seyfert and Narrow-Line Seyfert 1 galaxies in Chapter 2, the first model fitted to the joint MOS+PN data was a power-law (and Gaussian component), attenuated by Galactic absorption, over 2–10 keV (Table 3.3). Over recent years, it has been found that many AGN show an intrinsically narrow (\sim few eV) emission line around 6.4 keV

Table 3.1. The QSOs in this sample: radio-quiet then radio-loud QSOs, ordered by RA.

Object	RA	Dec.	classification	redshift	Galactic N_H (10^{20} cm^{-2})
UM 269	00h43m19.7s	+00d51m15s	RQQ	0.308	2.30
Q 0056–363	00h58m37.2s	–36d06m08s	RQQ	0.162	1.93
Q 0144–3938	01h46m12.5s	–39d23m05s	RQQ	0.244	1.44
Mrk 1014	01h59m50.2s	+00d23m41s	RQQ	0.163	2.59
PG 0804+761	08h10m58.6s	+76d02m42s	RQQ	0.100	2.98
PG 0844+349	08h47m42.4s	+34d45m04s	RQQ	0.064	3.29
HE 1029–1401	10h31m54.3s	–14d16m51s	RQQ	0.086	6.54
PG 1211+143	12h14m17.7s	+14d03m13s	RQQ	0.081	2.74
Mrk 205	12h21m44.0s	+75d18m38s	RQQ	0.071	2.80
Mrk 1383	14h29m06.6s	+01d17m06s	RQQ	0.086	2.85
Mrk 876	16h13m57.2s	+65d43m10s	RQQ	0.129	2.87
PG 1634+706	16h34m28.9s	+70d31m33s	RQQ	1.334	4.50
PDS 456	17h28m19.8s	–14d15m56s	RQQ	0.184	20.00
PB 05062	22h05m09.9s	–01d55m18s	RQQ	1.770	6.13
MR 2251–178	22h54m05.8s	–17d34m55s	RQQ	0.064	2.70
3 Zw 2	00h10m31.0s	+10d58m30s	RLQ	0.089	5.72
B2 1028+31	10h30m59.1s	+31d02m56s	RLQ	0.178	1.96
B2 1128+31	11h31m09.5s	+31d14m05s	RLQ	0.289	2.02
B2 1721+34	17h23m20.8s	+34d17m58s	RLQ	0.206	3.11

(see Section 1.3.3), corresponding to neutral iron, but that the equivalent width of the line is smaller in the more luminous objects. Chapter 6 combines the measurements of the line EW in the Seyferts (Chapter 2) with the values for the QSOs presented here and discusses the implications for the decrease in strength with luminosity.

The fit to the PG 1211+143 data is complex and based on work published by Pounds et al. (2003a). There is the possible presence of extremely broad emission, which suggests the line may be formed by reflection from the inner-most accretion disc, where relativistic effects have to be taken into account. This was modelled with a *laor* line (Laor 1991), as is conventional. The best fit has a disc emissivity index of $\beta = 5.3 \pm 0.7$, for an inner radius of $2.98 \pm 0.26 R_{sch}$ and inclination angle $55 \pm 3^\circ$. There are also a number of absorption components, detailed in Table 3.5. Because of the broadness of this

Table 3.2. The details of the *XMM* observations performed of the QSOs discussed in this chapter. ^a The revolution number of the *XMM* orbit in question; ^b SW – Small Window, LW – Large Window, FF – Full Frame, EFF – Extended Full Frame; ^c observations were co-added for analysis; ^d MOS 2 SW mode missed the target.

Object	start date (rev. ^a)	exposure time (ks)			mode ^b			filter		
		MOS 1	MOS 2	PN	MOS 1	MOS 2	PN	MOS 1	MOS 2	PN
UM 269	2002-01-04 (380)	20.3	20.3	16.3	LW	LW	FF	medium	medium	medium
Q 0056–363	2000-07-05 (105)	5.3/5.3	5.3/5.3	14.5	LW	LW	LW	thin/thick	thin/thick	thin
Q 0144–3938	2002-06-17 (462)	32.3	32.3	28.1	LW	LW	FF	medium	medium	medium
Mrk 1014	2000-07-29 (117)	10.4	10.4	10.8	LW	LW	FF	medium	medium	medium
PG 0804+761	2000-11-04 (166)	6.7	6.7	0.6	LW	LW	FF	thin	medium	thin
PG 0844+349	2000-11-04 (166)	23.3	23.3	20.2	LW	LW	FF	medium	medium	medium
HE 1029–1401	2000-11-22 (175)	7.1	7.1	5.3	SW	SW	LW	thin	thin	thin
PG 1211+143	2001-06-15 (278)	53.4	53.4	49.6	SW	SW	LW	medium	medium	medium
Mrk 205	2000-05-07 (75)	16.9	16.9	16.4	FF	FF	FF	medium	medium	medium
Mrk 1383	2000-07-28 (116)	5.0	4.9	3.5	LW	LW	LW	thin	thick	thin
Mrk 876 ^c	2001-04-13 (246)	4.2	4.4	3.5	LW	LW	FF	thin	thick	thin
	2001-08-29 (315)	7.2	7.2	2.6	LW	LW	FF	thin	thick	thin
PG 1634+706	2002-11-22 (541)	19.3	19.3	15.7	FF	FF	FF	medium	medium	medium
PDS 456	2001-02-26 (223)	44.0	44.0	38.9	LW	LW	FF	medium	medium	medium
PB 05062	2001-05-24 (267)	34.2	34.2	26.7	FF	FF	EFF	thin	thin	thin
MR 2251–178 ^d	2000-11-29 (179)	–	–	3.5	Timing	SW	SW	medium	thin	medium
3 Zw 2	2000-07-03 (104)	7.5	7.5	10.1	FF	FF	SW	thin	thin	thin
B2 1028+31	2000-12-06 (182)	26.2	26.2	21.5	LW	LW	FF	thin	thick	thin
B2 1128+31	2000-11-22 (175)	23.3	23.3	18.9	LW	LW	FF	thin	thick	thin
B2 1721+34	2001-02-13 (216)	6.9	6.9	4.1	LW	LW	FF	thin	thick	thin
	2001-02-26 (223)	6.3	6.5	3.2	LW	LW	FF	thin	thick	thin

line, the fit was actually extended down to 1 keV, to model the full residuals. This is only one of two possible fits discussed by Pounds et al. (2003a); the other model includes a low ionisation absorber, which leads to curvature in the hard band and removes the need for the *laor* line. However, that style of fit requires the use of XSTAR and, since the two models lead to comparable χ^2 values, the relativistic line model is presented here.

3.2.1 Blackbody parameterisation of the soft excess

Extrapolation of the power-law down to 0.2 keV once again revealed soft excesses in the spectra, as Figure 3.1 shows; the BB fits are given in Table 3.4. In Chapter 2 it was found that the Seyfert galaxies investigated did not generally show the presence of an intrinsic warm absorber, although a small number of the fits were improved by the inclusion of individual absorption edges. For some of the QSOs presented here, there was evidence for an additional absorption component as well as individual absorption edges/lines; if required, these are shown in Table 3.5. Where fitting a warm absorber implied that the ionisation of the material was consistent with zero, a neutral component (in the rest frame of the object) was included instead, using *zwabs* within XSPEC. None of the absorbing column densities is particularly large and this, together with the high ionisation values where applicable, would imply that little in the way of emission or absorption features would be expected at low energies. As was mentioned in Chapter 2, it is not necessarily easy to identify the edges or absorption lines, since they could correspond to neutral or ionised material which is either stationary (with respect to the object rest frame) or flowing outwards as a wind; this leads to a large number of possibilities for both the metal and the ionisation state. The best way to deal with these spectra would be to analyse RGS data where available. However, since this thesis is mainly investigating continuum emission, the identifications have not been attempted here. PG 1211+143, PG 0844+349 and PDS 456 are discussed in some detail in Pounds et al. (2003a), Pounds et al. (2003d) and Reeves, O’Brien & Ward (2003) respectively, though; in both of these objects, the presence of a wind is suspected.

As for the lower-luminosity Seyfert galaxies, between one and three blackbody com-

Table 3.3. Fits over the 2–10 keV rest frame bands, for the QSO sample; 90% errors are given for the equivalent widths of the lines, or the upper limit, when no line is statistically detected. α_{ox} , as defined in Chapter 2, is also given. ^a The second line component fitted to PG 1211+143 is a broad *laor* line – see discussion in text. ^f frozen

Object	2–10 keV Γ	Line Energy (keV)	intrinsic width (keV)	Equivalent width (eV)	2–10 keV luminosity (10^{44} erg s ⁻¹)	χ^2/dof	α_{ox}
UM 269	1.69 ± 0.04	6.4^f	0.01^f	<92	4.15	213/198	1.19
Q 0056–363	2.04 ± 0.03	6.32 ± 0.06 6.46 ± 0.15	0.235 ± 0.071 0.01^f	235 ± 116 < 110	3.19	351/376	1.16
Q 0144–3938	1.81 ± 0.03	6.45 ± 0.03	0.01^f	149 ± 52	3.33	325/368	1.42
Mrk 1014	2.23 ± 0.08	6.40 ± 0.09	0.01^f	< 400	1.05	153/157	1.48
PG 0804+761	2.25 ± 0.06	6.63 ± 0.20 6.34 ± 0.11	0.912 ± 0.258 0.01^f	990 ± 280 < 123	4.18	255/289	1.18
PG 0844+349	2.19 ± 0.02	6.51 ± 0.08 6.39 ± 0.84	0.370 ± 0.091 0.01^f	330 ± 101 < 38	0.81	704/754	1.49
HE 1029–1401	1.97 ± 0.02	6.64 ± 0.10 6.4^f	0.370 ± 0.110 0.01^f	258 ± 100 < 30	3.68	597/557	1.37
PG 1211+143 ^a	1.79 ± 0.02	6.43 ± 0.04 7.07 ± 0.22	0.01^f see note ^a	37 ± 24 854 ± 270	0.81	1217/1164	1.52
Mrk 205	1.74 ± 0.02	6.38 ± 0.04 6.81 ± 0.13	0.01^f 0.239 ± 0.169	78 ± 29 122 ± 62	1.36	559/602	1.42
Mrk 1383	2.00 ± 0.03	6.34 ± 0.05	0.01^f	73 ± 41	2.42	475/484	0.89
Mrk 876	1.84 ± 0.03	6.44 ± 0.05	0.01^f	96 ± 59	3.07	429/400	1.35
PG 1634+706	2.07 ± 0.03	6.4^f	0.01^f	<37	209	379/387	1.39
PDS 456	1.87 ± 0.01	6.4^f	0.01^f	< 6	11.81	1268/1210	1.32
PB 05062	1.80 ± 0.01	6.4^f	0.01^f	<20	730	585/579	0.95
MR 2251–178	1.65 ± 0.02	6.43 ± 0.06	0.01^f	< 70	5.42	410/429	1.19
3 Zw 2	1.61 ± 0.02	6.39 ± 0.04	0.01^f	< 94	2.20	499/506	1.29
B2 1028+31	1.76 ± 0.03	6.47 ± 0.11 6.47 ± 0.15	0.466 ± 0.131 0.01^f	259 ± 124 < 65	3.37	475/533	1.22
B2 1128+31	1.83 ± 0.03	6.31 ± 0.15 6.4^f	0.516 ± 0.186 0.01^f	255 ± 110 < 75	9.45	557/541	1.21
B2 1721+34	1.80 ± 0.02	6.42 ± 0.04	0.01^f	65 ± 33	15.17	703/716	1.04

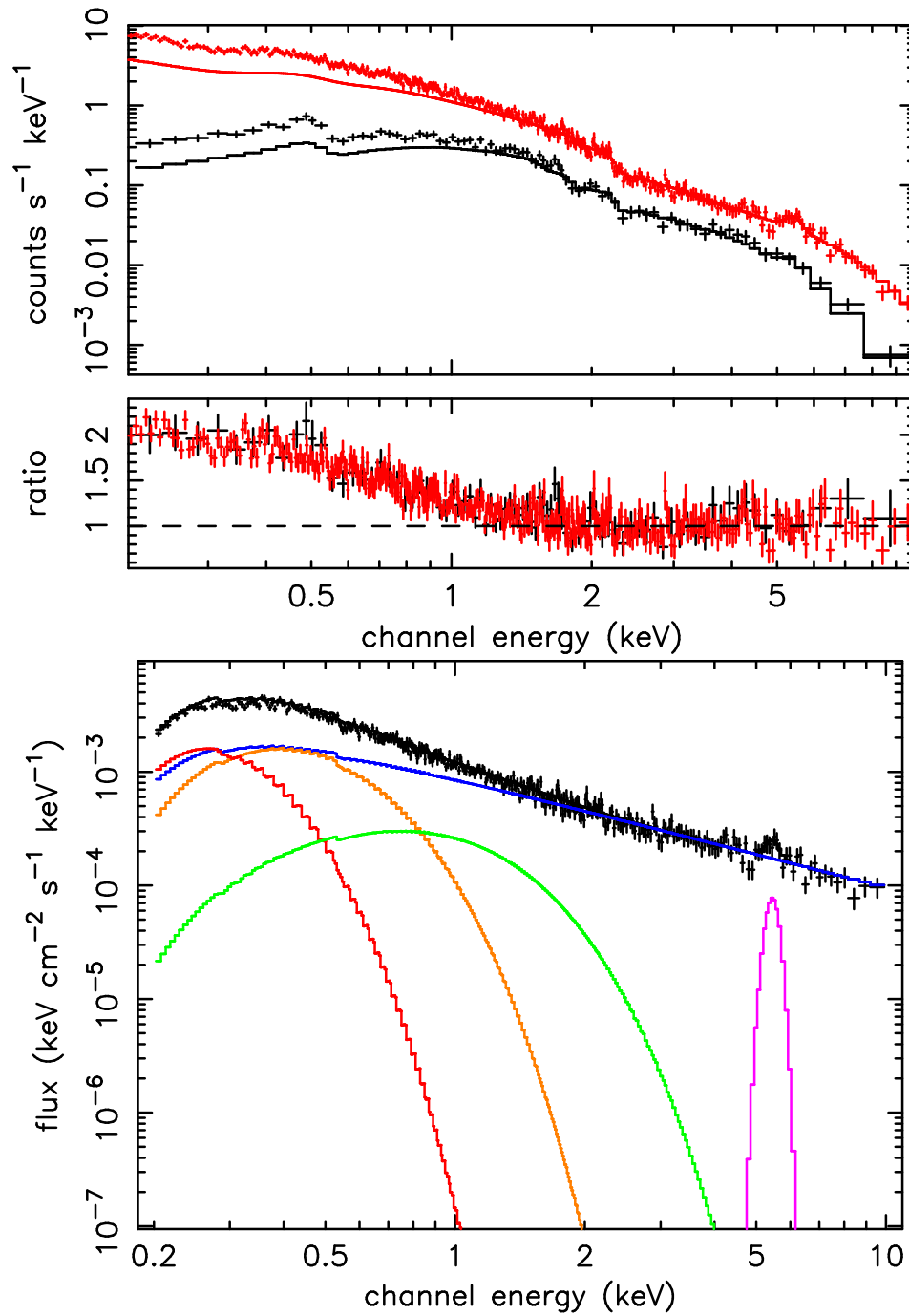


FIGURE 3.1. The soft excess of Q 0056–363 can be well modelled by three black-body components, with temperatures around 60, 125 and 285 eV. In the top plot, the MOS data are in black and PN in red; in the lower plot, PN data only shown.

Table 3.4. Fits over the 0.2–10 keV (observed frame) energy band, for the QSOs. The soft excess has been modelled by a variable number of BB components. ^a BB temperature; ^b over the 0.2–10 keV (observed) band.

Object	Γ	kT ^a (keV)	kT ^a (keV)	kT ^a (keV)	total ^b lum. (10 ⁴⁴ erg s ⁻¹)	total ^b BB lum. (10 ⁴⁴ erg s ⁻¹)	BB/ Γ lum. ratio ^b	χ^2/dof
UM 269	1.60 ± 0.06	—	0.095 ± 0.005	0.305 ± 0.022	9.96	2.53	0.34	520/510
Q 0056–363	1.96 ± 0.05	0.061 ± 0.013	0.124 ± 0.016	0.287 ± 0.039	11.29	3.96	0.54	901/889
Q 0144–3938	1.78 ± 0.05	—	0.111 ± 0.004	0.325 ± 0.036	10.17	3.48	0.52	777/748
Mrk 1014	2.30 ± 0.03	—	0.103 ± 0.006	—	3.91	0.45	0.13	513/506
PG 0804+761	2.22 ± 0.02	—	0.100 ± 0.005	—	13.72	1.13	0.09	741/692
PG 0844+349	2.03 ± 0.05	0.076 ± 0.011	0.129 ± 0.012	0.326 ± 0.028	3.37	1.39	0.70	1282/1209
HE 1029–1401	1.83 ± 0.04	—	0.106 ± 0.002	0.290 ± 0.010	11.74	4.26	0.57	1049/997
PG 1211+143	1.86 ± 0.05	0.047 ± 0.002	0.141 ± 0.010	0.340 ± 0.101	3.87	2.49	1.80	1560/1367
Mrk 205	1.69 ± 0.03	—	0.117 ± 0.008	0.274 ± 0.038	2.72	0.27	0.11	1230/1052
Mrk 1383	1.94 ± 0.04	0.035 ± 0.005	0.106 ± 0.005	0.275 ± 0.021	8.45	2.96	0.54	1094/1031
Mrk 876	1.91 ± 0.02	—	0.103 ± 0.002	—	8.02	1.28	0.19	998/917
PG 1634+706	1.89 ± 0.06	—	0.159 ± 0.016	0.452 ± 0.132	940	380	0.68	638/658
PDS 456	1.93 ± 0.02	—	0.112 ± 0.002	0.330 ± 0.029	131	105	4.09	2401/1637
PB 05062	1.77 ± 0.03	—	0.199 ± 0.024	0.505 ± 0.080	2469	693	0.39	1074/976
MR 2251–178	1.74 ± 0.02	—	0.144 ± 0.006	—	12.25	1.87	0.18	824/768
3 Zw 2	1.56 ± 0.04	—	0.111 ± 0.006	0.281 ± 0.024	5.07	1.45	0.40	1003/947
B2 1028+31	1.69 ± 0.04	—	0.113 ± 0.004	0.288 ± 0.020	7.57	1.42	0.23	1019/1044
B2 1128+31	1.68 ± 0.04	—	0.113 ± 0.004	0.303 ± 0.017	23.25	5.37	0.30	1047/1013
B2 1721+34	1.74 ± 0.03	—	0.114 ± 0.005	0.282 ± 0.025	35.66	6.19	0.21	1294/1222

Table 3.5. Values for the warm absorber (or excess neutral absorption) components and absorption edges where required; these were derived from EPIC data. The temperature of the absorber was set to 1×10^4 K. ^a These values correspond to absorption lines and their equivalent widths, rather than edges/optical depths.

Object	edge/line energy (keV)	τ /EW (eV)	N_H (10^{22} cm $^{-2}$)	ionisation
Q 0144–3938	—	—	0.34 ± 0.07	12 ± 6
PG 1211+143	0.24 ± 0.02	2.44 ± 1.18	0.13 ± 0.04	3.23 ± 2.09
	0.79 ± 0.01	0.59 ± 0.07	—	—
	0.96 ± 0.01	0.46 ± 0.08	—	—
	1.07 ± 0.03	0.20 ± 0.08	—	—
	7.10 ± 0.05	0.36 ± 0.07	—	—
	1.63 ± 0.01^a	17 ± 5^a	—	—
	2.14 ± 0.03^a	12 ± 5^a	—	—
	2.92 ± 0.02^a	29 ± 11^a	—	—
	7.59 ± 0.02^a	106 ± 32^a	—	—
PG 1634+706	—	—	0.45 ± 0.13	—
PDS 456	7.85 ± 0.04	0.31 ± 0.03	0.29 ± 0.03	—
	9.22 ± 0.04	0.69 ± 0.08	—	—
PB 05062	—	—	0.83 ± 0.22	—
MR 2251–178	—	—	0.29 ± 0.03	3.90 ± 1.04
3 Zw 2	—	—	0.07 ± 0.02	—

ponents are required to model the spectrum, varying from a low temperature of ~ 35 eV, up to ~ 500 eV. In Table 3.4, the temperatures are given in three columns of < 80 , 80 – 200 and > 200 eV and, once again, the medium temperature BB component is always present. Starting with a power-law-only fit, the addition of a BB with $kT \sim 80$ – 200 eV improves the fit substantially, with F-test values of $\gtrsim 200$. The decrease in χ^2 for the cool and hot components (when present) corresponds to $F \sim 5$ – 25 (all F values given for a drop of two degrees of freedom).

3.2.2 The Comptonisation model

The *thComp* Comptonisation model, producing both the soft excess and power-law as in Chapter 2, was applied to each spectrum, again leading to generally acceptable fits; see

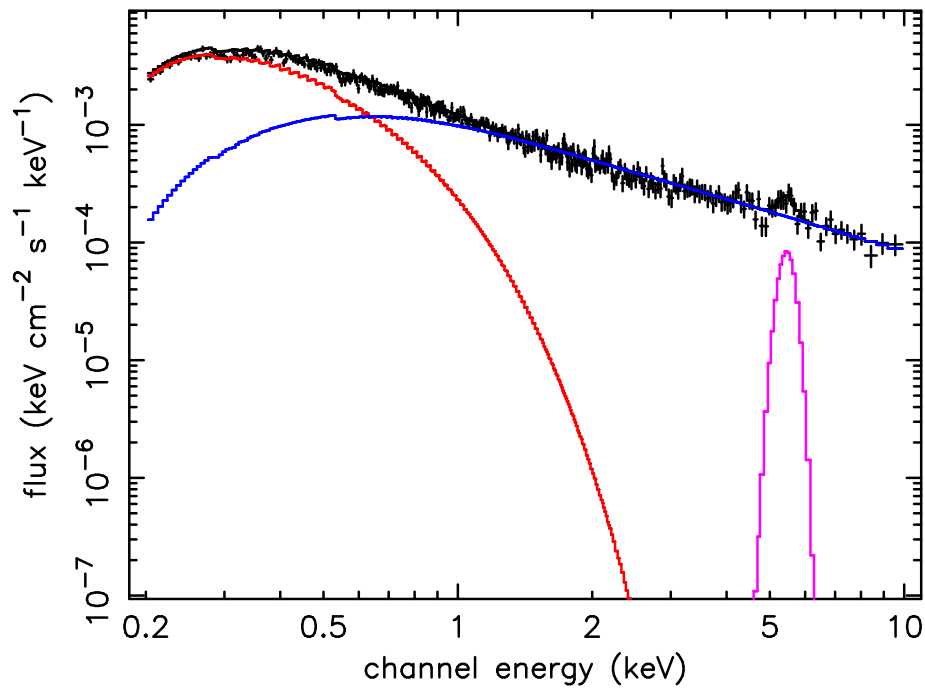


FIGURE 3.2. Fitting the X-ray spectrum of Q 0056–363 with two Comptonised components and an iron line. The narrow line is not plotted, since it is not statistically required.

Figure 3.2 and Table 3.6. As in the previous chapter, allowing the temperature of the photons acting as the input to the hotter Comptonising distribution to vary freely shows clearly that, in this model, the photons producing the power-law tend to be much closer in temperature to the soft excess, rather than the accretion disc itself. This indicates that the photons most probably interact with the cooler of the two electron distributions before reaching the hotter; thus, it appears that, within the framework of this model, as for the lower-luminosity Seyferts, a two-layer Comptonisation model is preferred. The previously determined photon index for the 2–10 keV band (Table 3.3) is listed again in Table 3.6, for comparison with the value determined from the *thComp* model. As was found in Chapter 2 for the Seyfert sample, the slopes tend to be in rough agreement, with the *thComp*-calculated values generally being a little steeper. There are, however, no large differences between the photon indices.

Table 3.6. Comptonisation fits to the broad-band QSO spectra. Hotter (power-law) electron temperature set to 200 keV. Column 7 again gives the photon index found by fitting a simple power-law+Gaussian model to the 2–10 keV band for comparison.^a soft excess component; ^b power-law component; ^f frozen

Object	COOLER COMPTONISED COMPONENT ^a			HOTTER COMPTONISED COMPONENT ^b		2–10 keV Γ	χ^2/dof
	input photon temperature ^f (eV)	electron temperature (keV)	τ^c	input photon temperature (keV)	Γ		
UM 269	20	0.437 ± 0.106	13 ± 3	0.366 ± 0.153	1.61 ± 0.09	1.69 ± 0.04	530/510
Q 0056–363	20	0.171 ± 0.012	23 ± 1	0.173 ± 0.016	2.10 ± 0.02	2.04 ± 0.03	923/889
Q 0144–3938	20	0.116 ± 0.014	66 ± 61	0.092 ± 0.006	1.94 ± 0.02	1.81 ± 0.03	789/750
Mrk 1014	25	0.172 ± 0.017	20 ± 14	0.067 ± 0.136	2.24 ± 0.06	2.23 ± 0.08	511/504
PG 0804+761	25	0.107 ± 0.023	46 ± 14	0.170 ± 0.042	2.25 ± 0.04	2.25 ± 0.06	736/688
PG 0844+349	30	0.123 ± 0.002	34 ± 23	0.063 ± 0.003	2.26 ± 0.01	2.19 ± 0.02	1320/1211
HE 1029–1401	20	0.209 ± 0.034	19 ± 6	0.075 ± 0.078	2.03 ± 0.02	1.97 ± 0.02	1122/999
PG 1211+143	25	0.160 ± 0.010	31 ± 2	0.174 ± 0.077	1.93 ± 0.03	1.79 ± 0.02	1580/1367
Mrk 205	30	0.185 ± 0.044	26 ± 7	0.077 ± 0.015	1.75 ± 0.02	1.74 ± 0.02	1233/1052
Mrk 1383	20	0.531 ± 0.192	11 ± 3	0.542 ± 0.142	1.88 ± 0.11	2.00 ± 0.03	1105/1030
Mrk 876	20	0.114 ± 0.024	47 ± 11	0.180 ± 0.060	1.92 ± 0.03	1.84 ± 0.03	999/914
PG 1634+706	10	0.782 ± 0.123	9 ± 1	0.136 ± 0.089	1.86 ± 0.10	2.07 ± 0.03	641/658
PDS 456	10	0.115 ± 0.019	127 ± 44	0.089 ± 0.070	2.06 ± 0.01	1.87 ± 0.01	2492/1644
PB 05062	5	0.890 ± 0.099	6 ± 5	0.525 ± 0.153	1.78 ± 0.03	1.80 ± 0.01	1076/977
MR 2251–178	20	0.148 ± 0.002	50 ± 34	0.096 ± 0.037	1.75 ± 0.01	1.65 ± 0.02	821/768
3 Zw 2	25	0.443 ± 0.150	11 ± 3	0.422 ± 0.159	1.57 ± 0.06	1.61 ± 0.02	1014/947
B2 1028+31	25	0.262 ± 0.040	19 ± 3	0.084 ± 0.012	1.77 ± 0.04	1.76 ± 0.03	1033/1044
B2 1128+34	15	0.428 ± 0.005	16 ± 0.2	0.619 ± 0.017	1.67 ± 0.03	1.83 ± 0.03	1082/1013
B2 1721+34	15	0.111 ± 0.030	38 ± 14	0.102 ± 0.037	2.08 ± 0.06	1.80 ± 0.02	1300/1220

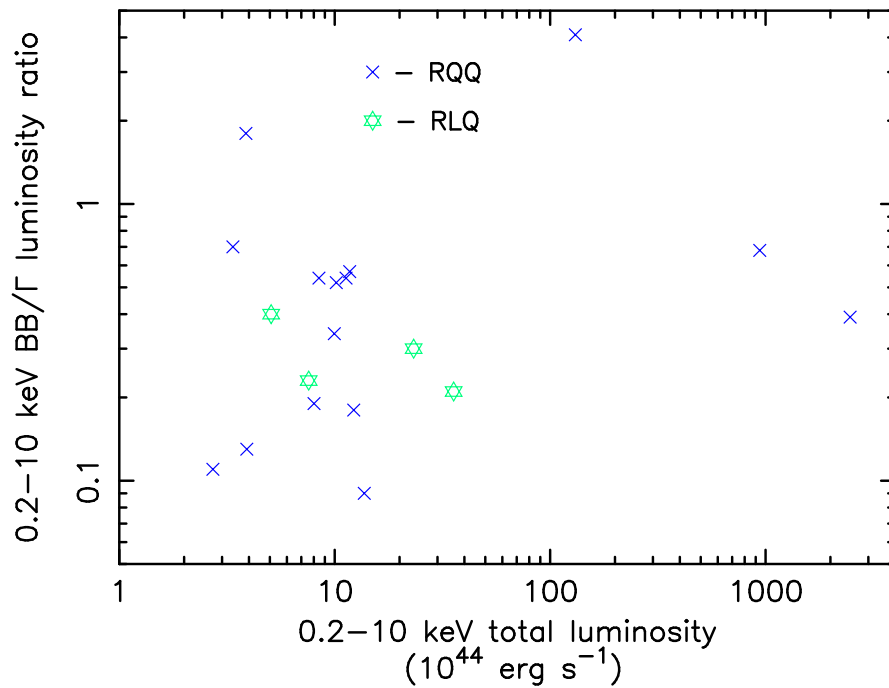


FIGURE 3.3. The variation of the ratio of soft excess to power-law luminosities over the 0.2–10 keV band with total 0.2–10 keV luminosity for the sample of QSOs.

3.3 Discussion

In order to perform a consistent analysis, the same correlations were investigated as for the Seyfert and Narrow Line Seyfert Galaxies in Chapter 2. Figure 3.3 shows that, again, there is no correlation ($\sim 28\%$) between the relative strength of the soft excess and the X-ray luminosity of the object. The two most luminous objects are PG 1634+706 and PB 05062, while the objects with the unusually powerful soft excesses (ratio > 1) are PDS 456 (ratio ~ 4) and PG 1211+143 (ratio ~ 1.8). Both of these latter QSOs are thought to be running at high accretion rates (Reeves et al. 2003; Pounds et al. 2003a), which could be an explanation for the strong soft excesses. However, PG 0844+349 is also thought to be a high accretion rate quasar (Pounds et al. 2003d), but does not show unusually strong soft emission.

While there is a positive correlation between BB/power-law luminosity ratio and the power-law fitted over the 2–10 keV energy band for Seyfert galaxies, no such pattern is observed for QSOs, as shown in Figure 3.4; here Spearman Rank (SR) analysis gives

an insignificant probability of $\sim 50\%$ for such a correlation. In the lower-luminosity objects, it is the Narrow Line Seyfert 1 galaxies which tend to show the strongest soft excesses and the steepest slopes. The lack of such a correlation for the higher-luminosity objects implies that there may not be a high-luminosity ‘equivalent’ of the NLS1s. This is a likely situation, since NLS1s are thought to have relatively low mass black holes; QSOs, on the other hand, generally have more massive central engines, as mentioned at the start of this chapter. QSOs with narrow lines do exist, however, PG 1211+143 being a prime example. This object is sometimes classed as an NLS1, because its luminosity is close to the boundary between Seyfert galaxies and QSOs; however, as is more usual, PG 1211+143 is being included in this sample as a QSO. PG 1211+143 does not show a particularly steep 2–10 keV power-law index, as most NLS1s do; it does, however, have a strong soft excess, it being the second strongest measurement within this sample of QSOs.

If the two objects with $\Gamma = 2.2\text{--}2.3$ (i.e., PG 0804+761 and Mrk 1014) are excluded, there is a positive correlation between the strength of the soft excess and the 2–10 keV slope, with a Spearman Rank probability of 96.4%, agreeing with the results for BL and NLS1s. However, there seems to be no scientific reason for the rejection of the PG 0804+761 and Mrk 1014 data, since they are, in no other way, unusual. Also, PG 0844+349 has $\Gamma = 2.19$, but lies within the group showing the positive trend. Excluding the two objects with the BB/Γ ratios of > 1 (PDS 456 and PG 1211+143) strengthens the correlation even further, to 98.9%. If more QSOs with particularly steep 2–10 keV photon indices were to be found and included in this sample, further conclusions might be possible. Likewise, investigating other QSOs which may be accreting at high fractions of the Eddington rate, as PDS 456 and PG 1211+143 are thought to be, should lead to further understanding of the relationships.

As discussed in Chapter 2, the optical to X-ray slope, α_{ox} (Equation 2.1), can be used as an indication of the strength of the BBB, with a steep α_{ox} meaning that the object has a comparatively strong BBB. As Figure 3.5 shows, however, there is no obvious correlation between the relative strength of the soft excess and that of the BBB (SR $\sim 66\%$); this mirrors the result found for the Seyfert sample. Plotting the slope of the soft excess com-

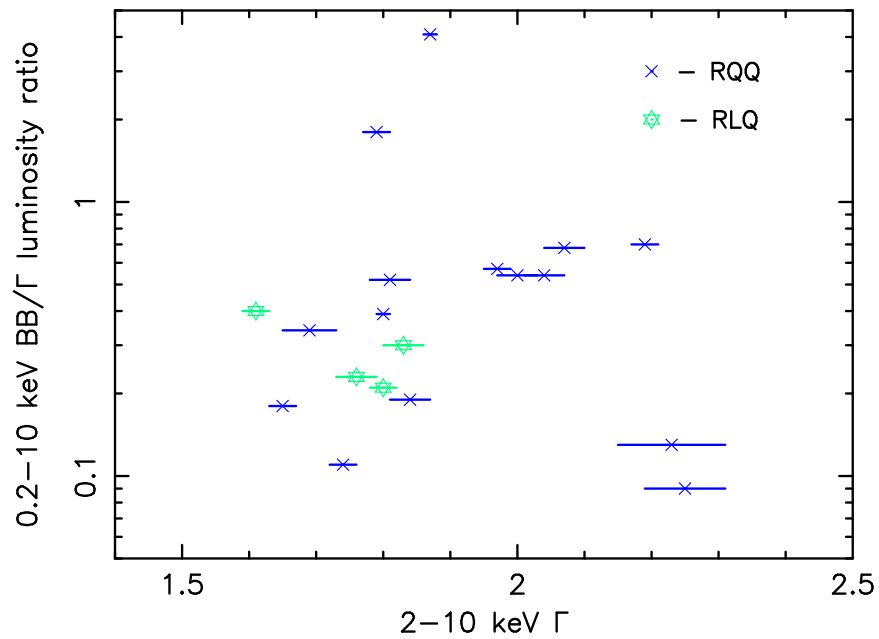


FIGURE 3.4. There does not appear to be a relationship between the strength of the soft excess and the 2–10 keV power-law slope for QSOs.

ponent against α_{ox} (Fig. 3.6) implies there is an inverse trend, as found for the Seyferts (linear regression slope of -1.23 ± 0.13), although the Spearman Rank probability of 61% is not significant. Separating this into the separate kT and τ components shows the same trends as for the Seyfert sample ($kT-\alpha_{ox}$: -52% ; $\tau-\alpha_{ox}$: 73%), although it is noticeable that the Spearman Rank correlations are not statistically significant, whereas the probabilities were strong for the Seyfert sample.

For these more luminous objects, there is still no obvious link (SR = 17%) between the temperature of the soft excess and the luminosity of the QSO: more luminous does not imply hotter (Fig. 3.7). The most luminous QSOs do tend to show the most luminous soft excesses, though. Shown are the soft excess luminosities over 0.001–10 keV, but the correlation is the same for the 0.2–10 keV band as well.

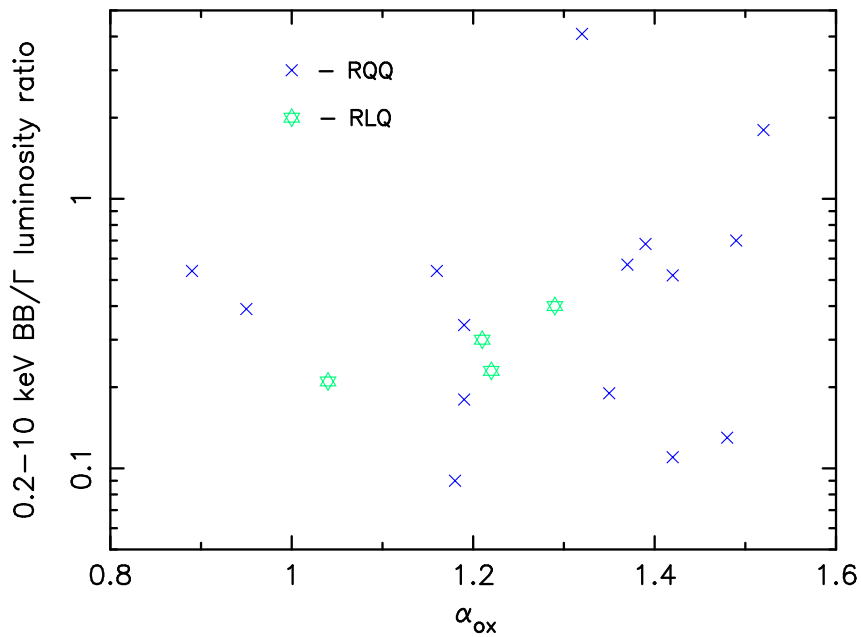


FIGURE 3.5. As for the Seyfert sample, the soft excess/power-law luminosity ratio is not correlated with the strength of the Big Blue Bump for the QSO sample.

3.4 Summary

Following on from Chapter 2, the soft excesses of QSOs – the higher luminosity equivalent of Seyfert galaxies – have been investigated. Due to the restricted sample of radio-loud objects (four out of nineteen), these have not been analysed separately from their radio-quiet counterparts. They are, however, indicated on each plot and, within this limited sample, do not show significantly different properties.

It is found that the relative strength of the soft excess (BB/power-law luminosity ratio) does not depend on the 0.2–10 keV luminosity, α_{ox} or a power-law fitted over the 2–10 keV band. The first two findings are the same as for the lower-luminosity objects, while the lack of correlation between the strength of the soft excess and the softness of the power-law slope indicates that QSOs do not have a direct equivalent of NLS1s. As for the Seyfert active galaxies, there is an indication of an inverse correlation between the soft excess slope and α_{ox} , although this is not very strong for the QSO sample presented here. Again, more luminous soft excesses correlate with the more luminous objects overall. The temperature of the soft excess is, however, again independent of the luminosity.

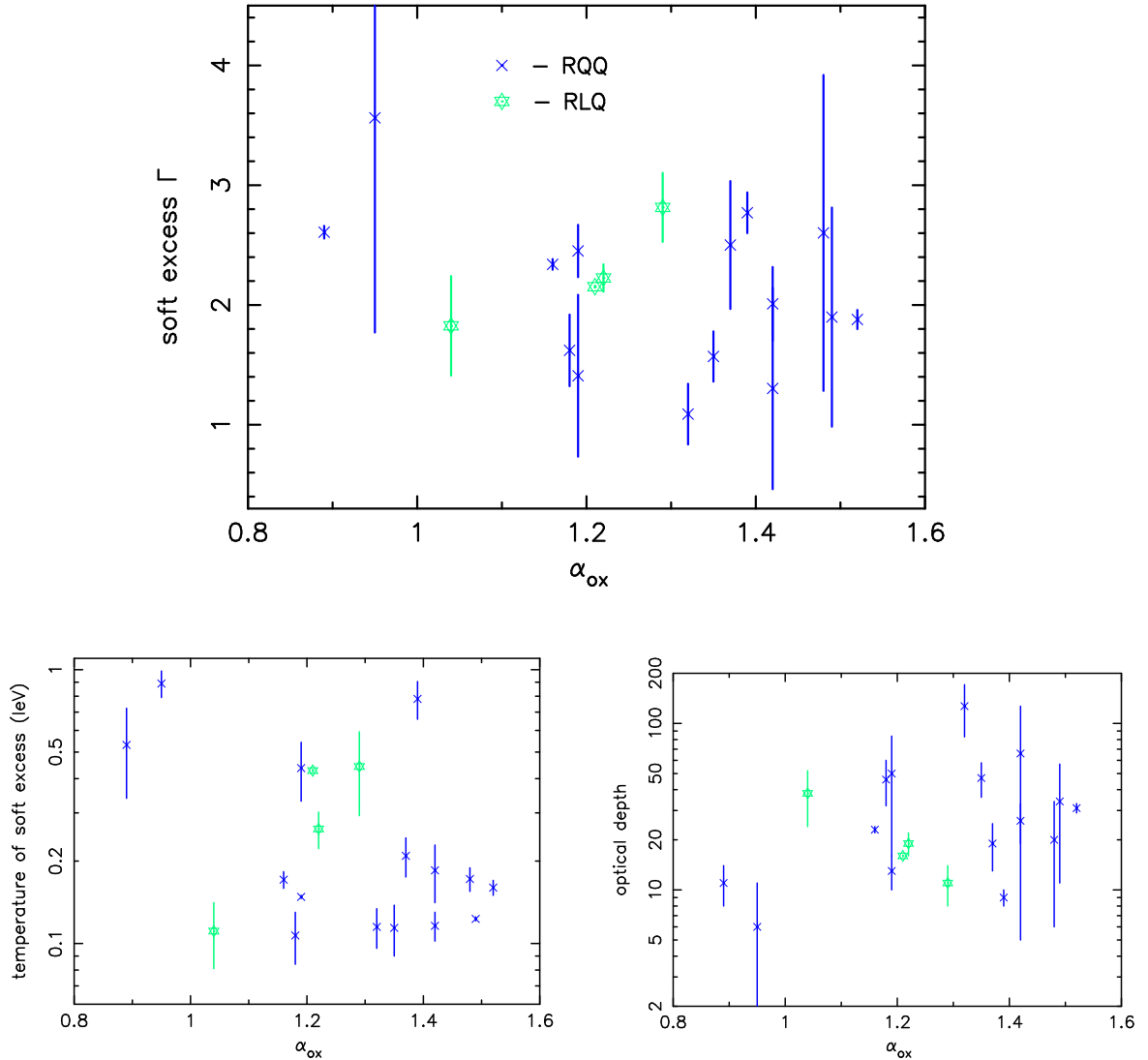
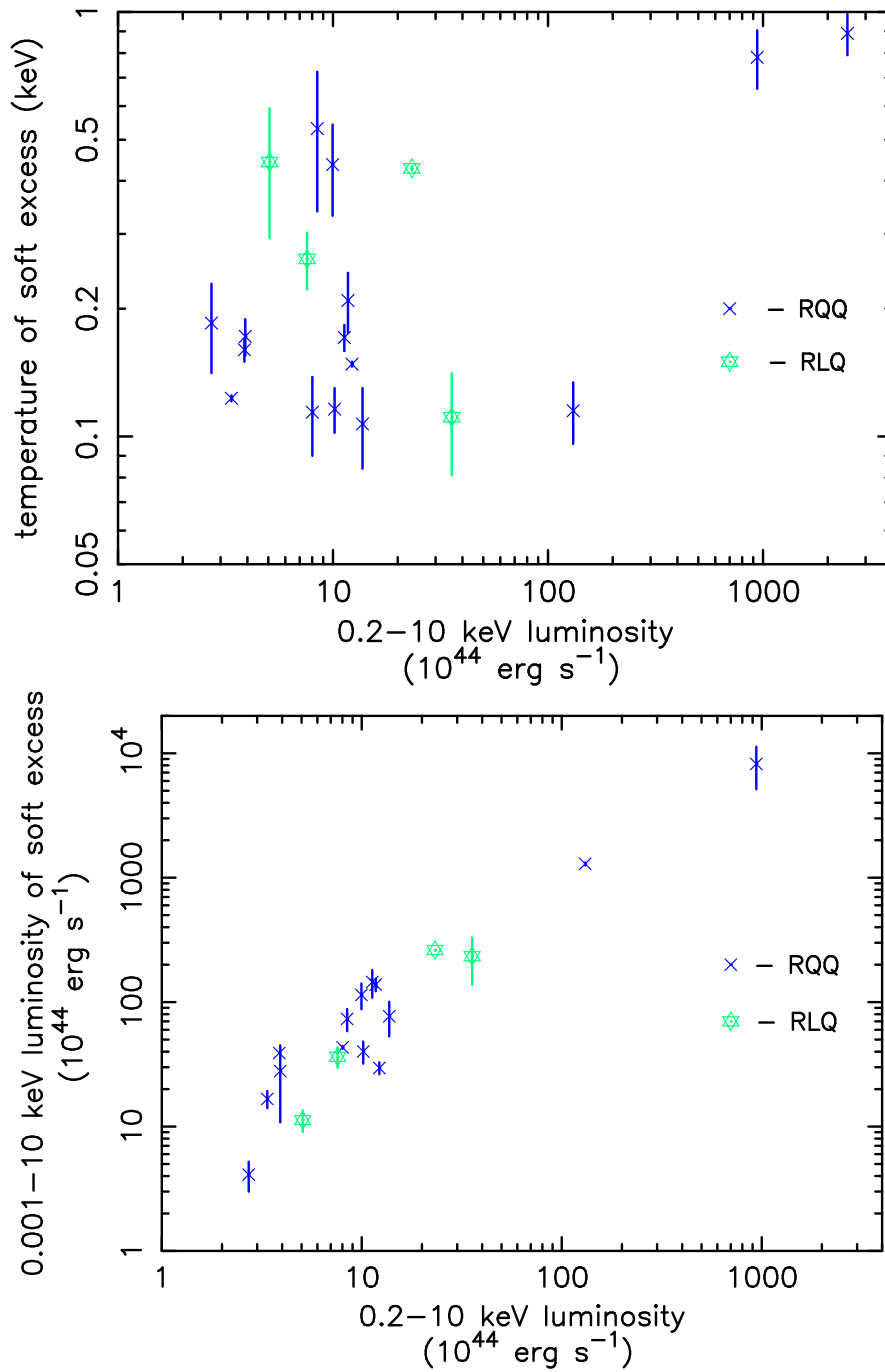


FIGURE 3.6. There is an inverse relationship between the slope of the soft excess and α_{ox} for the QSOs. This may be due to a negative correlation between α_{ox} and the soft excess temperature, together with a positive correlation with the optical depth.



In Chapter 7, the results from this, and the previous, chapter are drawn together, to compare AGN over a wide range of parameter space. Further discussion of these results is left until then.

Chapter 4

Time variability of the soft excess

Although investigating and comparing the soft excesses in different objects allows an in-depth study of the emission in general, it must be kept in mind that AGN cover a wide range of parameter-space, with differing black hole masses, accretion rates etc. If, however, the same source is observed a number of times, information on the time-variability of the soft excess can be obtained, leading to an understanding of the relationship between the different regions of the X-ray spectrum. For example, does the soft excess vary with the harder power-law-like emission? If so, then they are probably formed from the same region within the AGN. If the soft and hard X-rays react in the same way to certain events, but with a time difference, then it is likely that they are formed through the same process, but are separated in space. If there is no apparent link, then the soft excess and hard continuum may be due to independent mechanisms.

This chapter covers three well-known objects which have been observed a number of times in X-rays: 3C 273, PKS 0558–504 and 1H 0419–577. The soft excesses are modelled with both blackbodies and Comptonisation models for each spectrum and the changes over the different observations noted. Section 4.4 summarises the similarities and differences between the objects.

4.1 3C 273

4.1.1 Introduction

3C 273 was the first object positively identified as a quasar, in 1963: the radio source was identified with a magnitude 13, star-like object by Hazard, Mackey & Shimmins (1963) and the redshift measured by Schmidt (1963) to be $z = 0.158$. 3C 273 was later found to be an X-ray source, by Bowyer et al. (1970) and Kellogg et al. (1971), and has been observed with X-ray instruments ever since. Although many more quasars have been discovered since the 1960s, 3C 273 remains one of our nearest neighbours; this, therefore, makes it a prime object to study, over the entire range of the electromagnetic spectrum – see Courvoisier (1998) and references therein. Previous X-ray observations found the high-energy continuum could be fitted by a hard power-law, with a photon index, $\Gamma \sim 1.3\text{--}1.6$ (Turner et al. 1990; Turner et al. 1991; Williams et al. 1992). Observations by *EXOSAT* (Turner et al. 1985) first indicated the existence of a soft excess, at energies $\lesssim 1$ keV; this was subsequently confirmed by further *EXOSAT* observations (Courvoisier et al. 1987; Turner et al. 1990), together with data from *Einstein* (Wilkes & Elvis 1987; Turner et al. 1991), *Ginga* (Turner et al. 1990) and *ROSAT* (Staubert 1992). *BeppoSAX* (Orr et al. 1998) and *ASCA* (Yaqoob et al. 1994; Cappi et al. 1998) have also observed 3C 273. The actual form of the soft excess could not previously be determined, due to lack of precision in the low-energy instruments: power-law, blackbody and thermal Bremsstrahlung models produced equally acceptable fits. The EPIC instruments on-board *XMM-Newton* (Section 1.4) are improving the situation, however, helping to distinguish between different models much more readily.

The soft excess of 3C 273 has been previously found to vary (Turner et al. 1985; Courvoisier et al. 1987; Turner et al. 1990; Grandi et al. 1992; Leach, McHardy & Papadakis 1995); *Ginga* observations (Saxton et al. 1993) found that its fractional variability was larger than that in the corresponding power-law component.

4.1.2 XMM-Newton observations

3C 273 is one of the *XMM-Newton* calibration targets, so is frequently observed by the instruments. At the time of writing, the quasar has been observed in revolutions 94 (2000-06-13), 95 (2000-06-15), 96 (2000-06-17), 277 (2001-06-13), 370 (2001-12-16), 373 (2001-12-22), 382 (2002-01-09), 472 (2002-07-07), 554 (2002-12-17) and 563 (2003-01-05), spanning a time period of two and half years. These data are a combination of public and calibration observations, with the data from revolutions 370 and 373 belonging to Rüdiger Staubert of Tübingen. The ODFs (Observation Data Files) were obtained from the online Science Archive and the data were then processed, and the event-lists filtered, using XMMSELECT within the SAS (Science Analysis Software) v5.4.1, as explained in Chapter 1. The most recent (time-dependent) response matrices were used (e.g., `m21_r7_im_p0_2002-11-07.rmf` for observations using MOS 2 after 2002-11-07), together with an ancillary response function obtained through running *arfgen*.

3C 273 is a very bright object and so systematic errors dominate the statistical ones. Because of this, one camera alone is sufficient to study the object and, to some extent, may even be the better method, since the calibration uncertainties differ between the instruments. It was decided to concentrate the analysis on the data from the MOS 2 camera, for a number of reasons. Firstly, MOS is, at present, thought to be better calibrated than the PN at the softer energies. Also, the MOS 1 camera was in Timing Mode for four of the ten observations. The correlations found for the MOS 2 data were checked against both the MOS 1 and PN values; MOS 1 was always in general agreement with MOS 2, but PN showed some variation. More importantly, perhaps, the PN measurements varied over a much larger range than seen in the MOS instruments. When looking simply at a power-law fit to the 3–10 keV band, each set of data followed the same pattern: MOS 1 showed the flattest slope and PN the steepest (average difference of ~ 0.1), while the MOS 2 slopes lay inbetween, but closer to the PN value (within ~ 0.04 usually) than the corresponding MOS 1 slope. Calibration of the instruments is still ongoing.

Only Small Window Mode observations were utilised, to minimise the pile-up problems. Upon investigation, it was found that the MOS spectra were slightly piled-up, even

with the quicker read-out time from the Small Window. Figure 4.1 shows the output from the SAS task *epatplot*; the lower panel compares the expected fractions of single-, double-, triple- and quadruple-pixel events (solid line) with those actually measured in the spectrum (histogram). It can be seen that a smaller than expected fraction of single events is measured above ~ 1 keV, while the reverse is true for doubles; this is the main signature of pile-up.

The excess double-pixel events are caused by two single photons hitting adjacent pixels and being measured as one event, due to the read-out rate being too slow. If pattern zero (i.e., single pixel events) only are used, then most of the pile-up problems are eliminated. The probability of two photons piling up is independent of their actual energies, since it is only related to the total photon flux: the higher the overall count-rate, the more likely it is that a second photon will strike the CCD before the first is read out. If all double events, both real and pile-up-related, are ignored, then, for *moderate* pile-up, the overall shape of the spectrum will be correct, just with a lower normalisation. (This does, however, mean that the luminosities given throughout this section will be lower than the absolute values, since some of the pattern zero events have been lost to doubles.) The reason why *epatplot* shows a deficit in the pattern zero events is that the predicted fraction (that is, the solid line) is based on the assumption that none of the events are due to pile-up (Molendi & Sembay 2003). If pile-up does occur, this leads to an error in the total number of events, since a piled-up pixel will be recorded as a single photon, rather than the two (or more) lower-energy ones which actually formed it; hence, the *fraction* of all the events expected to be pattern zero is incorrect.

It is also possible that two photons could hit exactly the same pixel before being measured; in this case, the result is a single event, but with the incorrect energy and so would still affect the pattern zero spectrum. This is, however, four times less likely to occur, because of the geometry of the pixels. (Diagonal double-pixel events are only formed through pile-up; these are flagged as such and split into two single pixels by the processing chain.)

Molendi & Sembay (2003) showed, through a comparison with a simultaneous *BepoSAX* observation, that using pattern zero events almost completely eliminated prob-

lems due to pile-up for the *XMM* revolution 277 data; subsequently, this method was used for the MOS camera.

4.1.3 Spectral analysis

Fe K emission

The object of this section is to analyse the soft excess of 3C 273 and to investigate any spectral changes there may be over time. The possible presence of an iron emission line was, however, investigated, by fitting the MOS 2 spectra over the 3–10 keV range with a simple power-law model. On the whole, there is no requirement for an iron line, either narrow or broad, in the individual spectra; the limits on the equivalent widths are given in Table 4.1. The spectra from all ten observations were then co-added, to search for the possible presence of an iron line; this resulted in a spectrum with a total exposure time of almost 230 ks. As Table 4.2 shows, the 3–10 keV spectral index does not vary greatly between observations; this is important, since co-adding spectra with different slopes would lead to curvature and, hence, force a broad residual when fitting a simple power-law model. However, fitting all ten observations simultaneously, while allowing the power-law slope to vary, and then plotting the co-added residuals shows the presence of a broad line very clearly (Fig. 4.2). This shows that the broad feature is not an artifact of the fit.

No narrow line was required ($\text{EW} < 12 \text{ eV}$; $\Delta\chi^2 = 7$ for 1 degree of freedom), but a weak broad line significantly improved the fit ($\Delta\chi^2$ of 45 for 3 degrees of freedom), giving an equivalent width of $114^{+94}_{-45} \text{ eV}$, for $E = 6.80 \pm 0.11 \text{ keV}$ and $\sigma = 0.81 \pm 0.18 \text{ keV}$. The detection of a weak, but broad and ionised, line would appear to support the findings of Yaqoob & Serlemitsos (2000), who detected such a component in *RXTE* and *ASCA* observations of 3C 273.

As in the earlier chapters, after fitting a power-law with Galactic absorption ($N_H = 1.79 \times 10^{20} \text{ cm}^{-2}$) to the 3–10 keV energy band (to avoid the broad soft excess), the fit was extrapolated down to 0.3 keV. There is an obvious soft excess, of which Figure 4.3

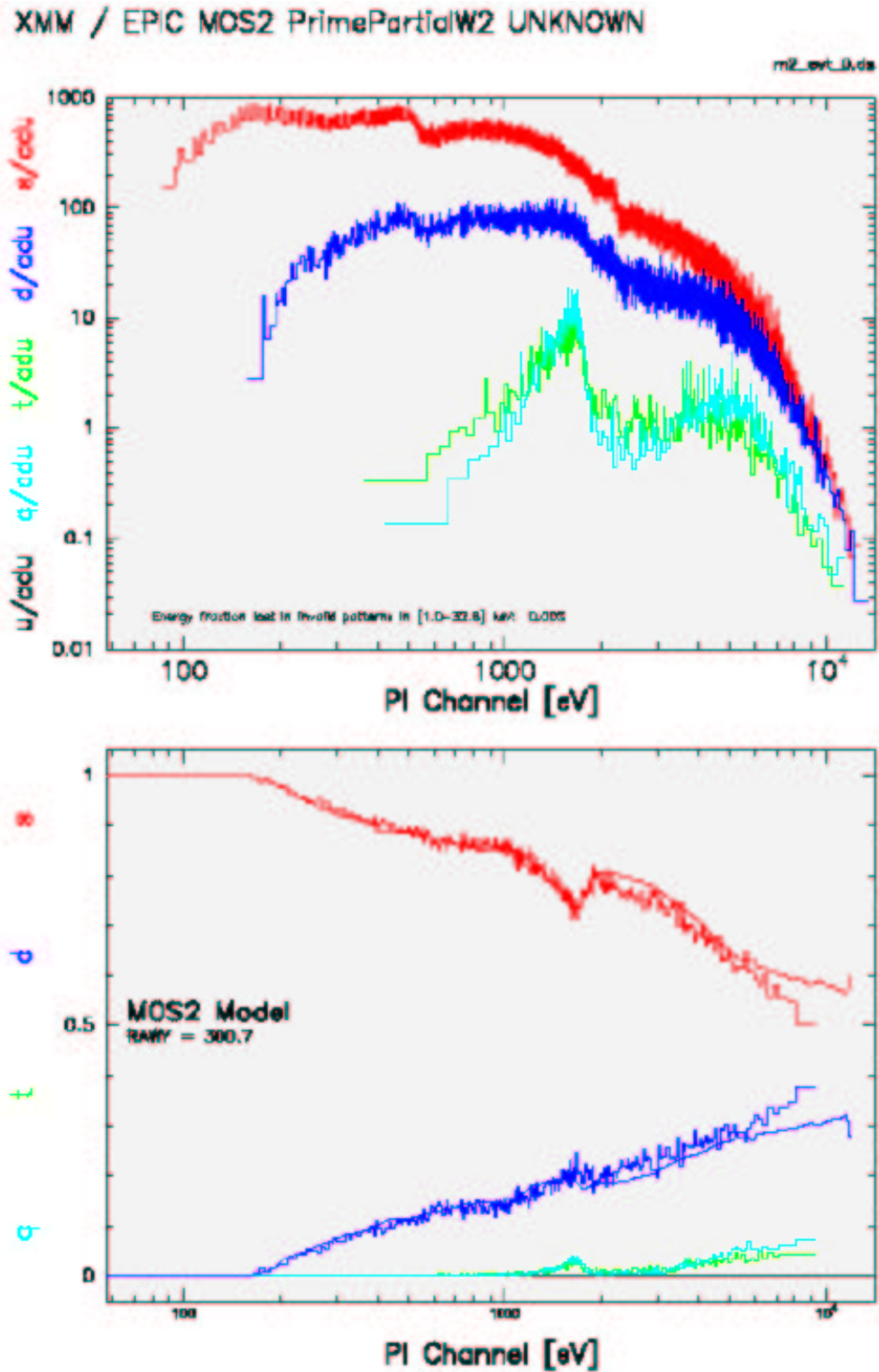


FIGURE 4.1. The result of running *epatplot* on the MOS 2 spectrum of 3C 273 in revolution 96. The top panel shows the counts spectrum for the different pixel-patterns, from single-events up to quadruples. The lower panel indicates the differences between the expected fraction of each pattern and the actual fractions in the total spectrum.

Table 4.1. The limits on the equivalent widths (EW) of neutral (6.4 keV) and ionised (6.7 keV) iron emission in 3C 273. The narrow lines had an intrinsic width of $\sigma = 0.01$ keV, the broad lines, 0.5 keV. Where the line was less than 99% significant, the 90% upper limit is given.

rev.	narrow line	broad line	
	(neutral) EW (eV)	(neutral) EW (eV)	(ionised) EW (eV)
94	< 20	< 73	< 67
95	< 17	< 125	< 138
96	21 ± 10	< 90	< 91
277	14 ± 8	< 64	< 53
370	< 14	< 141	< 192
373	< 30	< 218	< 257
382	< 55	< 201	< 204
472	< 65	< 59	< 46
554	< 18	< 263	< 269
563	< 20	< 85	< 85

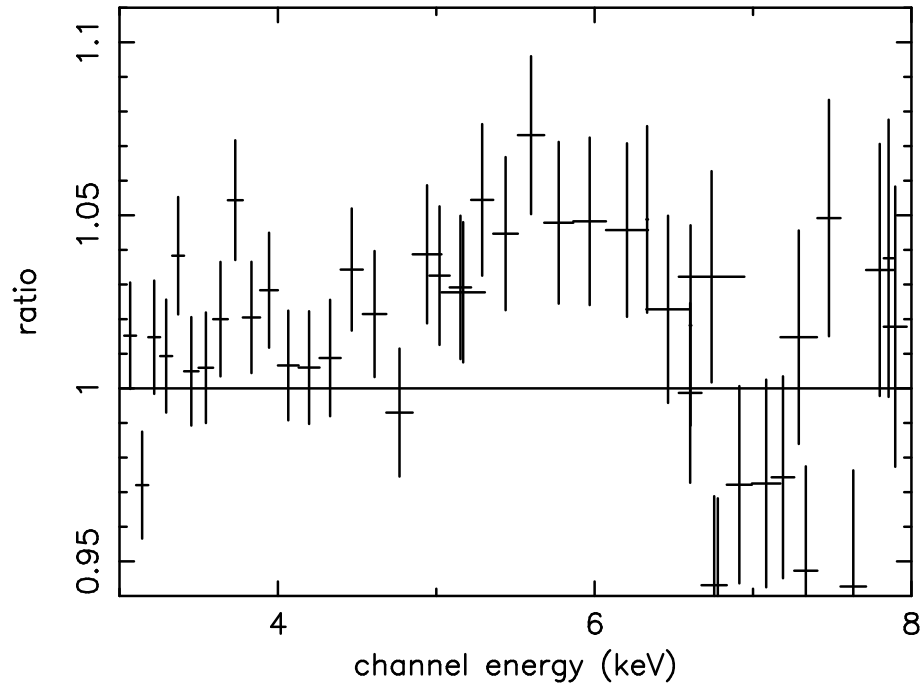


FIGURE 4.2. To confirm that the broad line is not simply an artifact introduced by varying photon indices, all ten datasets were fitted simultaneously, while allowing the slope to vary. The co-added residuals are shown above, demonstrating the presence of a broad emission feature.

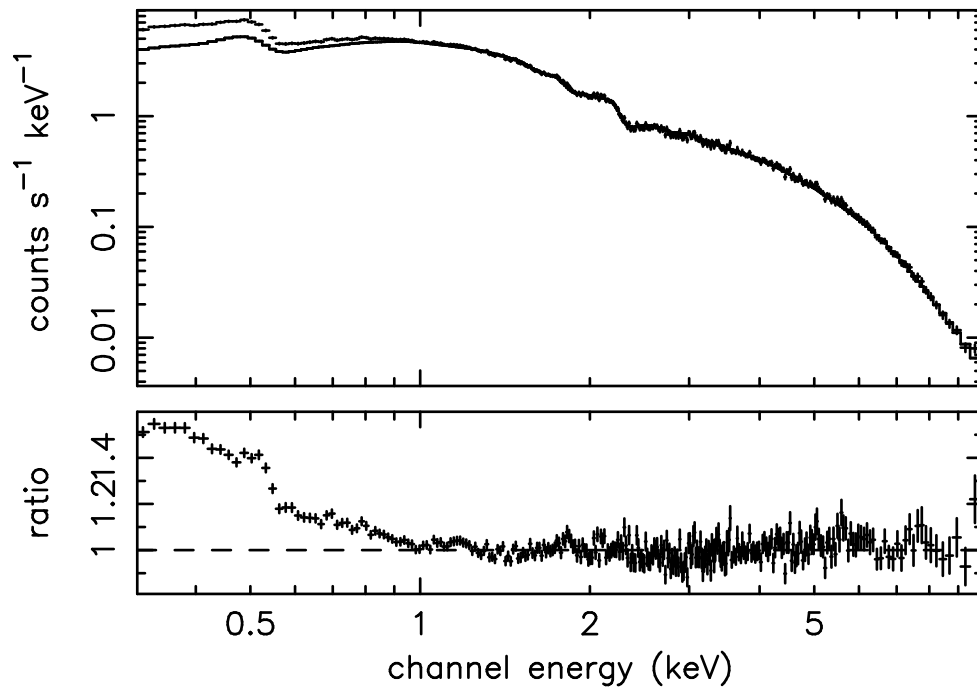


FIGURE 4.3. The soft excess of 3C 273 during revolution 94.

shows an example. (0.3 keV was taken as the lower limit because of uncertainties in the calibration at lower energies, which would decrease the ‘goodness’ of fit significantly in the spectra of 3C 273.)

The soft excess

The soft excess of 3C 273, as observed by EPIC, can be well modelled by multiple blackbody (BB) components. Considering the revolution 94 data as an example, fitting the broad-band spectrum with a power-law together with a single BB component gives an unacceptable fit, with $\chi^2/\text{dof} = 768/574$. Adding a second BB leads to a χ^2/dof value of 749/572; the F-test value for this improvement is 7.26. Adding a third component gives the best-fit value of $\chi^2/\text{dof} = 719/570$, an improvement of $F = 11.9$ over the 2BB model. Each of the remaining observations was best fitted with a flat power-law (generally $\Gamma \sim 1.5\text{--}1.6$) and either two or three BBs. Table 4.2 gives the 3–10 keV power law slopes, together with broad-band BB fits; Fig. 4.4 shows an example of the BB fit. During revolution 277, observations with both the thin and medium filters were performed;

these spectra were fitted simultaneously, leading to the increased number of degrees of freedom seen in the table.

The last column of the table lists the de-reddened luminosities for the models given. These values show 3C 273 to have been at a typical luminosity during each of the observations, c.f. Courvoisier et al. (1987). Any loss in events due to pile-up will effect these values at less than the 5% level (estimated from the *XMM* Users' Handbook). For this investigation, only the relative luminosities are of interest, and variation in pile-up between observations will be negligible.

To investigate whether, as the soft excess changes, all the BB components vary together, a plot was made of the individual BB luminosities against the total luminosity of the soft excess; this is shown in Figure 4.5. It can clearly be seen that the coolest BB component (when present) is by far the most stable – i.e., its luminosity remains close to constant. The increase in the soft excess luminosity is due to the brightening of the two hotter components. It is noticeable that the observation showing the least luminous soft excess (revolution 382) is the only one which does not require the hottest component. Conversely, the cool BB is generally present in the observations with the low luminosity soft excesses, although there is one exception (revolution 373).

To compare with the analysis performed in Chapters 2–3, the ratio of the BB to power-law broad-band luminosities (the ‘strength’ of the soft excess) was calculated (although here the 0.3–10 keV band is used, rather than 0.2–10 keV as for the other objects). This was compared to both the 0.3–10 keV total luminosity and the power-law over the 3–10 keV band. As Figure 4.6 shows, the results are very similar to those found for the QSO sample in Chapter 3: the luminosity ratio is independent of both the total luminosity (SR gives a probability of only 77% for a positive correlation) and the power-law (SR = 55%). As was mentioned in Chapter 3, the first finding – i.e., that the strength of the soft excess does not depend on the overall luminosity – is the same as for the lower-luminosity Seyfert sample. However, when considering the BL/NLS1s, a steeper slope over the hard-energy band correlated with the higher soft excess ratio, indicating that the soft excess photons might be cooling the corona which forms the power-law; the Chapter 3 QSO sample did not show this effect and, as is shown here, neither does

Table 4.2. Power-law and blackbody fits to the MOS 2 3C 273 spectra. The de-reddened luminosities are also given. Note that these are not corrected for loss of events due to pile-up. ^a The ratio of the luminosity of the BB components to the power-law, over the observed 0.3–10 keV energy band.

range (keV)	model	revolution	Γ	kT (keV)	kT (keV)	kT (keV)	χ^2/dof	BB/ Γ lum. ratio ^a	luminosity (10^{46} erg s ⁻¹)
3–10	PL	94	1.645 ± 0.012				427/388		0.74
		95	1.609 ± 0.018				352/341		0.71
		96	1.624 ± 0.013				395/380		0.71
		277	1.601 ± 0.009				833/753		0.85
		370	1.571 ± 0.034				238/253		1.02
		373	1.620 ± 0.035				236/251		1.00
		382	1.713 ± 0.041				210/221		0.76
		472	1.768 ± 0.057				151/154		0.69
		554	1.649 ± 0.038				235/237		0.94
		563	1.748 ± 0.025				256/298		0.76
0.3–10	PL + BBs	94	1.604 ± 0.024	0.082 ± 0.007	0.164 ± 0.021	0.461 ± 0.035	719/570	0.10	1.79
		95	1.614 ± 0.030	0.081 ± 0.013	0.151 ± 0.045	0.408 ± 0.061	576/502	0.14	1.68
		96	1.615 ± 0.028	0.085 ± 0.006	0.177 ± 0.034	0.463 ± 0.083	709/557	0.13	1.69
		277	1.609 ± 0.010	—	0.116 ± 0.001	0.344 ± 0.009	1634/1105	0.13	2.07
		370	1.515 ± 0.046	—	0.132 ± 0.005	0.420 ± 0.019	401/406	0.21	2.42
		373	1.623 ± 0.038	—	0.112 ± 0.007	0.356 ± 0.031	417/404	0.11	2.35
		382	1.758 ± 0.019	0.069 ± 0.013	0.156 ± 0.036	—	410/373	0.09	1.89
		472	1.689 ± 0.064	—	0.112 ± 0.009	0.462 ± 0.038	334/304	0.16	1.76
		554	1.518 ± 0.052	—	0.131 ± 0.004	0.433 ± 0.014	470/389	0.30	2.41
		563	1.743 ± 0.027	—	0.114 ± 0.004	0.340 ± 0.021	453/454	0.14	2.01

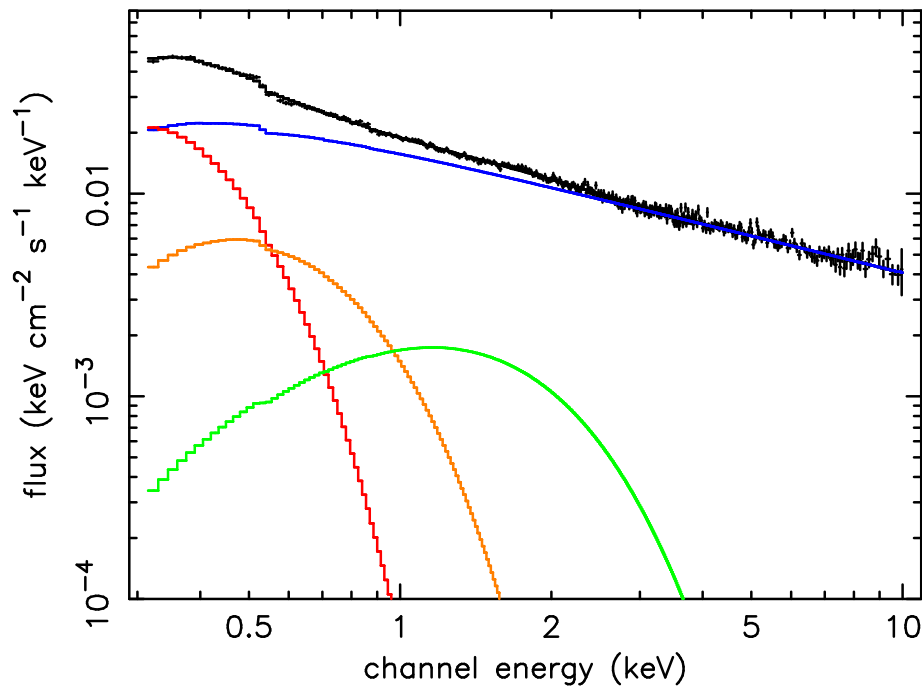


FIGURE 4.4. An unfolded plot of the blackbody fit to the revolution 94 MOS 2 data. The spectrum is fitted by a power-law and three blackbody components, with kT between ~ 80 and 460 eV.

3C 273.

Modelling the soft excess spectrum with multiple blackbodies is probably not physical, but it does point to the soft excess being broad. The *diskbb* command in XSPEC models the accretion disc as emission from multiple blackbody components, working from the temperature at the inner disc radius (see, e.g., Mitsuda et al. 1984; Makishima et al. 1986). However, this method does not succeed in modelling the entire breadth of the emission seen, and was worse ($F = 8.72$; $\Delta\chi^2/\text{dof} = 44/4$ for revolution 94) than the multiple BB fit. An alternative method involves modelling the soft excess with either a second, or broken, power law. However, both of these models were found to be significantly worse fits (the F-test gives improvements of 14.1 and 22.6 for the multiple blackbodies in comparison to the two power-laws and broken power-law respectively, for revolution 94 data; these correspond to $\Delta\chi^2/\text{dof}$ of 71/4 and 114/4 respectively), implying that the soft excess does, indeed, show curvature, rather than a sharp change in slope. To repeat, when using the F-test, a value of $F > 3.0$ (for one parameter) corresponds to

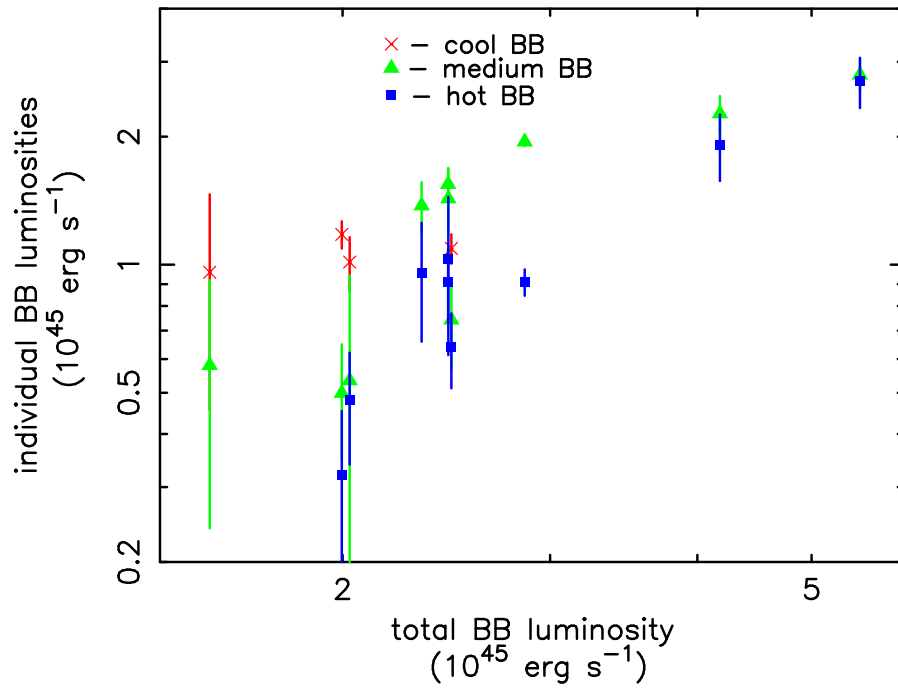


FIGURE 4.5. The variation of the individual blackbody luminosities with that of the entire soft excess. It can be seen that the increasing brightness of the total soft excess is mainly due to the brightening of the hotter two components.

an improvement of $> 90\%$.

As mentioned above, and in previous chapters, although multiple blackbodies parameterise AGN soft excesses very well, the model is not particularly physical. The temperatures for the hotter components are thought to be far higher than can be formed through thermal emission from an accretion disc surrounding a $\sim 10^9 M_{\odot}$ black hole (see, e.g., Liu et al. 2003). A more realistic model for the emission is likely to be Comptonisation: as described previously, thermal photons, emitted from the disc, are upscattered by populations of hot electrons. A two-temperature distribution could then lead to the formation of both the apparent ‘power-law’ at higher energies and the soft excess. Low temperature Comptonised spectra are similar in shape to blackbodies, but are broader; thus, an excess which requires two or three different temperature BBs can easily be modelled by a single Comptonisation component. Relating this to Fig. 4.5, the hotter blackbody components could be thought of as forming this broad component together, while the coolest BB gives an indication of the tail end of the input, disc photons. To in-

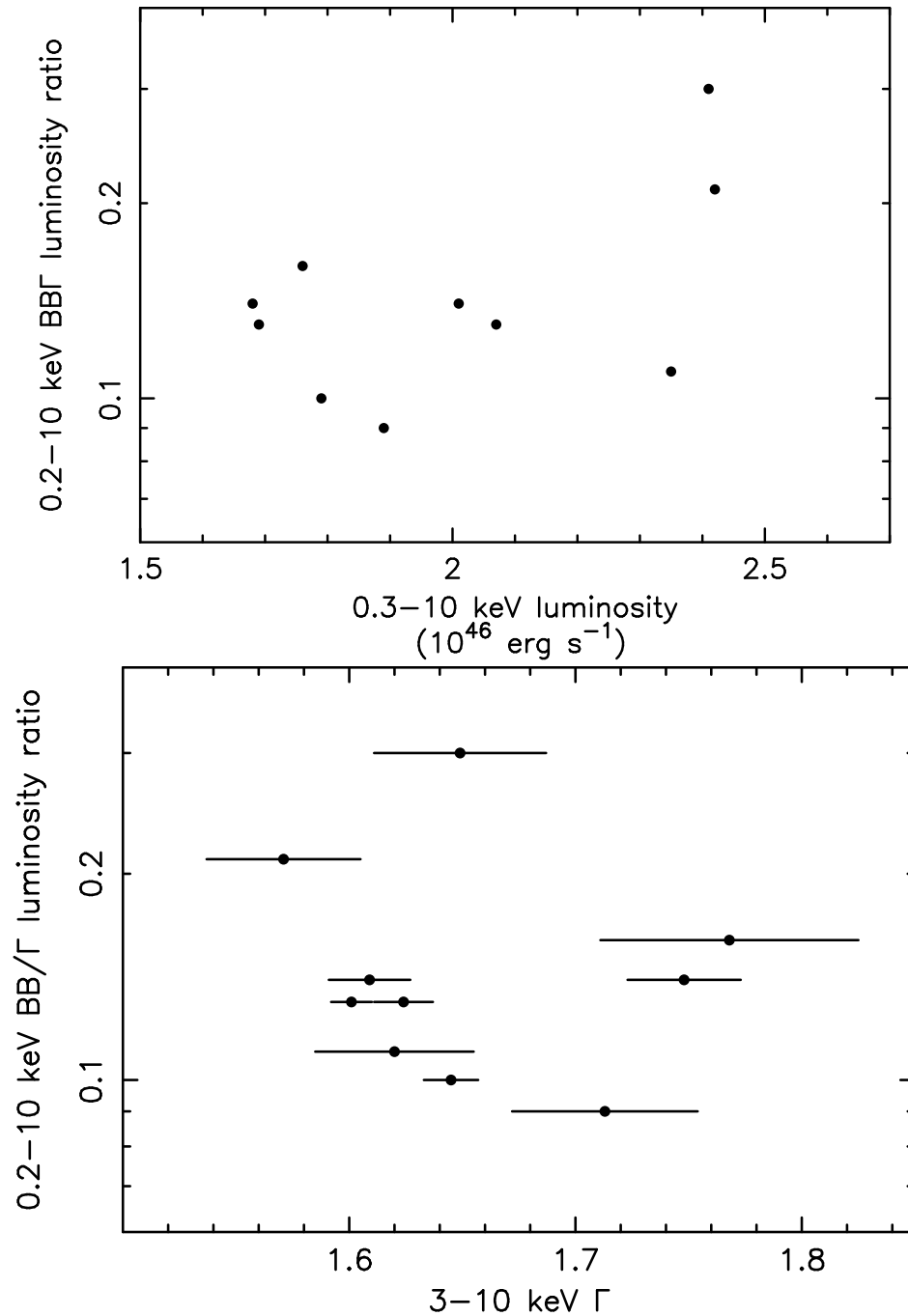


FIGURE 4.6. Agreeing with all the previous data, there is no relationship between the relative strength of the soft excess (compared to the power-law) and the broadband luminosity. As was found for the QSO sample in Chapter 3, although not for the Seyferts in Chapter 2, there is also no link between the luminosity ratio and the power-law slope.

investigate the likelihood of the 3C 273 spectra being formed via this method, the *thComp* Comptonisation model was again used. The temperature of the photons from the disc was set to 10 eV, which is appropriate for thermal emission from a disc surrounding a $10^9 M_{\odot}$ black hole (Courvoisier 1998), accreting at a suitable fraction of the Eddington rate (see Section 4.1.5 and Blaes et al. 2001); these seed photons are assumed to follow a blackbody distribution. The temperature of the hotter distribution was fixed, as usual, at 200 keV. There are two possible geometries for the Comptonisation, as mentioned in Chapters 2 and 3: either (almost) all of the soft photons are initially Comptonised by the ‘soft-excess-producing’ electrons; some would then be further Comptonised by a hotter distribution [possibly formed through magnetic reconnection – see, e.g., Nayakshin (2000a) and Section 1.3.5; these electrons may be non-thermal], to form the observed ‘power-law’. An alternative involves some disc photons being Comptonised to form the soft excess, while others form the higher energy spectrum by directly interacting with the hotter electron population. Since it is not known which process is the more likely, the temperature of the input photons to the hotter component was allowed to vary freely. As Table 4.3 shows, this temperature is generally close to that of the soft excess, implying, within the scope of this model, that, once again, the two-stage process is preferred.

Also given in Table 4.3 is the Compton y -parameter for the soft excess (Section 1.3.5). Recapping from Chapter 1 and Sunyaev & Titarchuk (1980), the y -parameter is given, for an optically thick material of non-relativistic electrons, by Equation 1.8:

$$y = \frac{4kT}{m_e c^2} \tau^2$$

where τ is the Thomson depth and kT the temperature of the electron corona; m_e is the mass of an electron. (The optically thin result is the same except the τ term is not squared.)

If $y \gg 1$, the Comptonisation process is saturated and results in a Wien-like spectrum ($\sim \nu^3 e^{-\nu}$), with the final temperature of the photons close to that of the electron population. For a low y -parameter, the photons tend to pass straight through the corona, emerging at close to their initial temperature (i.e., that of the accretion disc); this pro-

duces a modified BB spectrum. The intermediate regime, where $y \sim 1$, is known as unsaturated Comptonisation. Here, a power-law spectrum is formed over a limited range; this drops off exponentially for $E > 4kT$. From Sunyaev & Titarchuk (1980), the resulting spectral index is given in Chapter 1 by Equation 1.9:

$$\Gamma = \left(\frac{4}{y} + \frac{9}{4} \right)^{1/2} - \frac{1}{2}$$

As Table 4.3 shows, the values of y for the soft excess are all ~ 1 , showing the Comptonisation is unsaturated. The corresponding values for the harder spectrum are slightly larger (1.4–2.4), but still in the unsaturated regime.

Figure 4.7 shows the fit to the data from revolution 94. Although the bandpass of *XMM* only allows the collection of data down to 0.2–0.3 keV, the Comptonisation model used here covers a much broader energy band, down to the 10 eV of the seed photons from the disc. Most of the luminosity of the soft excess lies below the *XMM* band (Figure 4.7 shows that the Comptonisation component is still rising at 0.3 keV) so, as in Chapters 2 and 3, in order to obtain an estimate for the *total* soft luminosity, the model was extrapolated to lower energies using the *dummysp* command in XSPEC, which allows the energy range of the response function to be extended. Calculating the luminosity (and, later, the flux) based on an input temperature of 10 eV is consistent with the data obtained from the Optical Monitor (see below) and does not over-predict the optical/UV flux.

4.1.4 RGS data

To a first approximation, the soft excess of 3C 273 can be modelled as a smooth continuum. However, it has previously been found that some AGN show features in their soft excesses: either relativistic emission lines (Branduardi-Raymont et al. 2001) or a combination of narrow emission/absorption features, sometimes with an absorption trough around 16–17 Å (Sako et al. 2001; O’Brien et al. 2001a; Pounds et al. 2001). The 3C 273 RGS spectrum during revolution 277 was chosen for analysis here, since this had the longest duration, of almost 90 ks. The data were processed using *rgsproc* within

Table 4.3. Comptonisation model fits to the spectra of 3C 273. Input BB temperature fixed at 10 eV; temperature of hotter component fixed at 200 keV. Luminosity calculated for the observed 1 eV–10 keV range.

rev.	COOLER COMPTONISED COMPONENT				HOTTER COMPTONISED COMPONENT			χ^2/dof
	electron temp. (keV)	τ	y-parameter	luminosity (10^{46} erg s $^{-1}$)	input temp. (keV)	Γ	luminosity (10^{46} erg s $^{-1}$)	
94	0.506 ± 0.049	12.1 ± 0.9	0.58 ± 0.02	3.21 ± 0.20	0.442 ± 0.022	1.637 ± 0.024	1.14 ± 0.09	734/572
95	0.450 ± 0.070	12.3 ± 1.4	0.53 ± 0.03	3.51 ± 0.44	0.387 ± 0.032	1.643 ± 0.028	1.13 ± 0.12	583/504
96	0.442 ± 0.055	12.7 ± 1.1	0.55 ± 0.02	3.37 ± 0.32	0.426 ± 0.029	1.646 ± 0.020	1.11 ± 0.10	728/559
277	0.529 ± 0.047	13.4 ± 0.9	0.74 ± 0.01	2.90 ± 0.14	0.632 ± 0.051	1.626 ± 0.021	1.16 ± 0.16	1818/1105
370	0.601 ± 0.148	14.0 ± 2.5	0.92 ± 0.07	2.52 ± 0.35	0.764 ± 0.269	1.549 ± 0.091	1.27 ± 0.78	426/406
373	0.480 ± 0.110	14.7 ± 2.6	0.81 ± 0.08	2.53 ± 0.59	0.549 ± 0.160	1.618 ± 0.062	1.43 ± 0.66	420/404
382	0.458 ± 0.124	12.7 ± 2.6	0.58 ± 0.06	3.76 ± 0.88	0.417 ± 0.081	1.681 ± 0.068	1.21 ± 0.32	407/373
472	0.568 ± 0.246	11.7 ± 3.6	0.63 ± 0.07	2.96 ± 0.64	0.472 ± 0.087	1.728 ± 0.155	1.06 ± 0.34	339/304
554	0.632 ± 0.097	12.9 ± 1.6	0.82 ± 0.06	2.97 ± 0.32	0.564 ± 0.123	1.484 ± 0.121	1.26 ± 0.42	500/389
563	0.499 ± 0.125	14.3 ± 2.6	0.80 ± 0.04	2.78 ± 0.30	0.635 ± 0.184	1.766 ± 0.049	1.07 ± 0.36	473/454

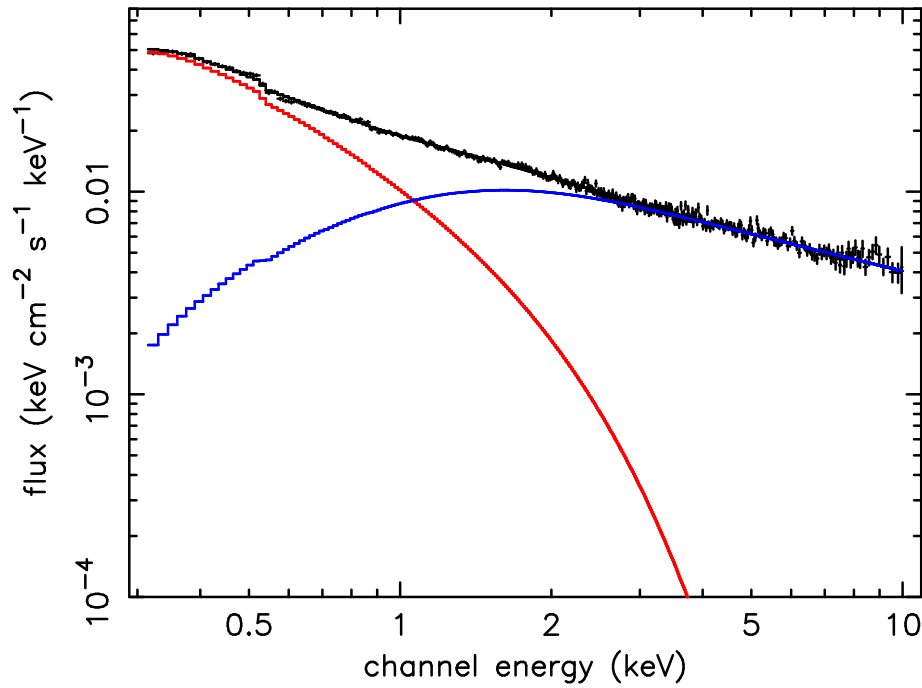


FIGURE 4.7. The best fit Comptonisation model to the MOS 2 data from revolution 94.

the SAS, with *rgsrmfgen* used to provide a response matrix. The resulting spectrum was then investigated in XSPEC. 3C 273 clearly does not exhibit the same spectral shape as that found by Branduardi-Raymont et al. (2001) for MCG $-6-30-15$ and Mrk 766. Upon comparison with the model used for Mrk 359 (O’Brien et al. 2001a), weak, but statistically significant, emission from the triplets of Ne IX and O VII was identified in this RGS spectrum of 3C 273. As for Mrk 359, the individual components cannot be resolved; however, their combined equivalent widths are 3.5 ± 0.9 eV and 1.6 ± 0.6 eV respectively. Only upper limits were obtained for the other features found in Mrk 359, with O VIII Ly α having an equivalent width of $EW < 0.06$ eV (90% upper limit). There is no sign of an Fe M absorption trough ($EW < 0.61$ eV) or absorption edges corresponding to O VII or O VIII. The soft excess is, therefore, not dominated by a blend of soft X-ray lines (Turner et al. 1991).

Fang, Sembach & Canizares (2003) claim to find an absorption feature, in a *Chandra* spectrum of 3C 273, corresponding to the zero-redshift O VII He α (~ 21.60 Å), for which they give an equivalent width of ~ 28 mÅ ($\Leftrightarrow 0.75$ eV). As Fang et al. (2003)

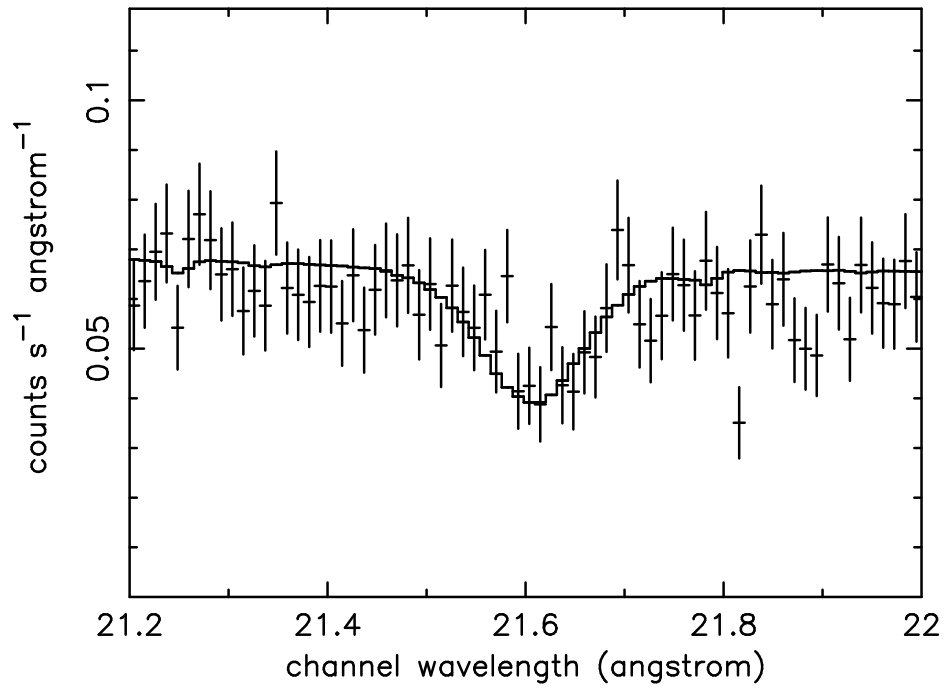


FIGURE 4.8. The plot shows an absorption feature which may be due to O VII He α at zero redshift. The data shown are from the revolution 277 observation

discuss, this is likely to correspond to the detection of warm gas in the local intergalactic medium. Investigating the possibility of absorption in the revolution 277 *XMM* data, a feature is, indeed, found: at a wavelength of $21.62 \pm 0.16 \text{ \AA}$, with a line width of 1 eV, the equivalent width is $\sim 0.88 \text{ eV}$ – similar to the value in Fang et al. (2003). This line is detected at the $> 99.99\%$ level and is shown in Figure 4.8.

Similar zero-redshift absorption is also discussed by Rasmussen, Kahn & Paerels (2003), who analyse both *Chandra* and *XMM* grating data. As well as O VII He α , they identify O VIII Ly α ($\lambda = 18.97 \text{ \AA}$), C VI Ly α ($\lambda = 33.73 \text{ \AA}$) and Ne IX He α ($\lambda = 13.45 \text{ \AA}$). These features are not significantly detected in the data from revolution 277 presented here: O VIII Ly α has an equivalent width of $< 0.79 \text{ eV}$ (detected at $\sim 84\%$ confidence), C VI Ly α has EW $< 0.08 \text{ eV}$ and Ne IX He α , EW $< 0.43 \text{ eV}$. These values are consistent with those given by Rasmussen et al.

Table 4.4. Optical and UV magnitudes for 3C 273.

filter	wavelength (Å)	rev.	rev.	rev.	rev.	rev.	rev.
		94	95	96	277	382	563
		magnitude					
V	5500	12.54	12.60	12.58	12.26	12.67	-
U	3600	11.90	11.94	11.97	11.66	-	-
B	4400	13.24	13.01	12.98	13.10	-	-
UVW1	2910	11.78	12.09	11.81	11.03	-	11.36
UVM2	2310	11.75	11.81	11.77	11.16	-	11.21
UVW2	2120	11.72	11.73	11.74	11.11	-	-

4.1.5 Optical and UV data

For a number of the observations (revs. 94–277, 382 and 563), optical/UV data were obtained from the Optical Monitor (OM; Mason et al. 2001); the remaining orbits had the OM in Grism mode. The magnitudes for the various filters used are listed in Table 4.4.

Blaes et al. (2001) fit an accretion disc model to multi-wavelength 3C 273 data, finding an accretion rate of $4M_{\odot} \text{ yr}^{-1}$. As mentioned above, this led to a disc temperature of 10 eV being used for the X-ray fits presented here, although, in fact, the Comptonisation model is not very sensitive to this value.

If the disc photons are at this representative temperature, then one can consider what would be seen if there were no Comptonising corona and only the direct thermal emission were observed. Taking the disc emission to be characterised by a BB, the resulting peak flux is found to be lower than that predicted by the model in Blaes et al. (2001). That is, more than enough disc photons would be emitted at ~ 10 eV to account for the soft excess spectrum observed, showing that our X-ray Comptonisation fits are consistent with the Blaes et al. accretion disc model.

A lower limit to the temperature of the accretion disc can be roughly estimated by finding the point at which the extension of the X-ray fit would produce a higher optical flux than is observed by the OM. Figure 4.9 plots the extrapolated X-ray Comptonisation model for three different input temperatures (10, 5 and 2 eV). Although the input to the

thComp model has been set to be a simple blackbody throughout this work, it is also possible to use a disc blackbody. This is broader than a single BB and is shown in the lower image of Figure 4.9. For temperatures below 2 eV, the simple model over-predicts the optical flux; the temperature is slightly higher when considering a disc BB. This can, therefore, be taken as a lower limit to the temperature of the photons producing the soft excess.

However, it must be noted that 2 eV is far too low a temperature for an accretion disc such as this. Disc theory is still a very uncertain area, especially at high accretion rates. Collin & Huré (2001) and Collin et al. (2002) find that the optical emission in AGN cannot be accounted for by the standard accretion disc model, concluding that either the disc is ‘non-standard’, or most of the optical luminosity does not come from the accretion disc. A much improved theory of accretion discs is clearly needed, before the relationship between optical and X-ray emission in AGN can be fully understood.

4.1.6 Discussion

Spectral index

As mentioned in the introduction (Section 4.1.1), 3C 273 typically shows a hard spectral index of ~ 1.5 (or flatter). The values found here over the 3–10 keV band (Table 4.2) are noticeably steeper, although this could be due to contamination by the broad soft excess. However, even when considering the broad-band BB fits, the mean spectral index is still relatively steep, with $\Gamma \sim 1.63$. This does not appear to be a calibration problem, though, since Molendi & Sembay (2003) also find $\Gamma \sim 1.63$ for the MECS slope over 3–10 keV (SAX data simultaneous with XMM revolution 277). The hard photon index is known to vary with time, however, (Turner et al. 1990) and it is possible that, during this period, 3C 273 was in a steep index ‘mode’.

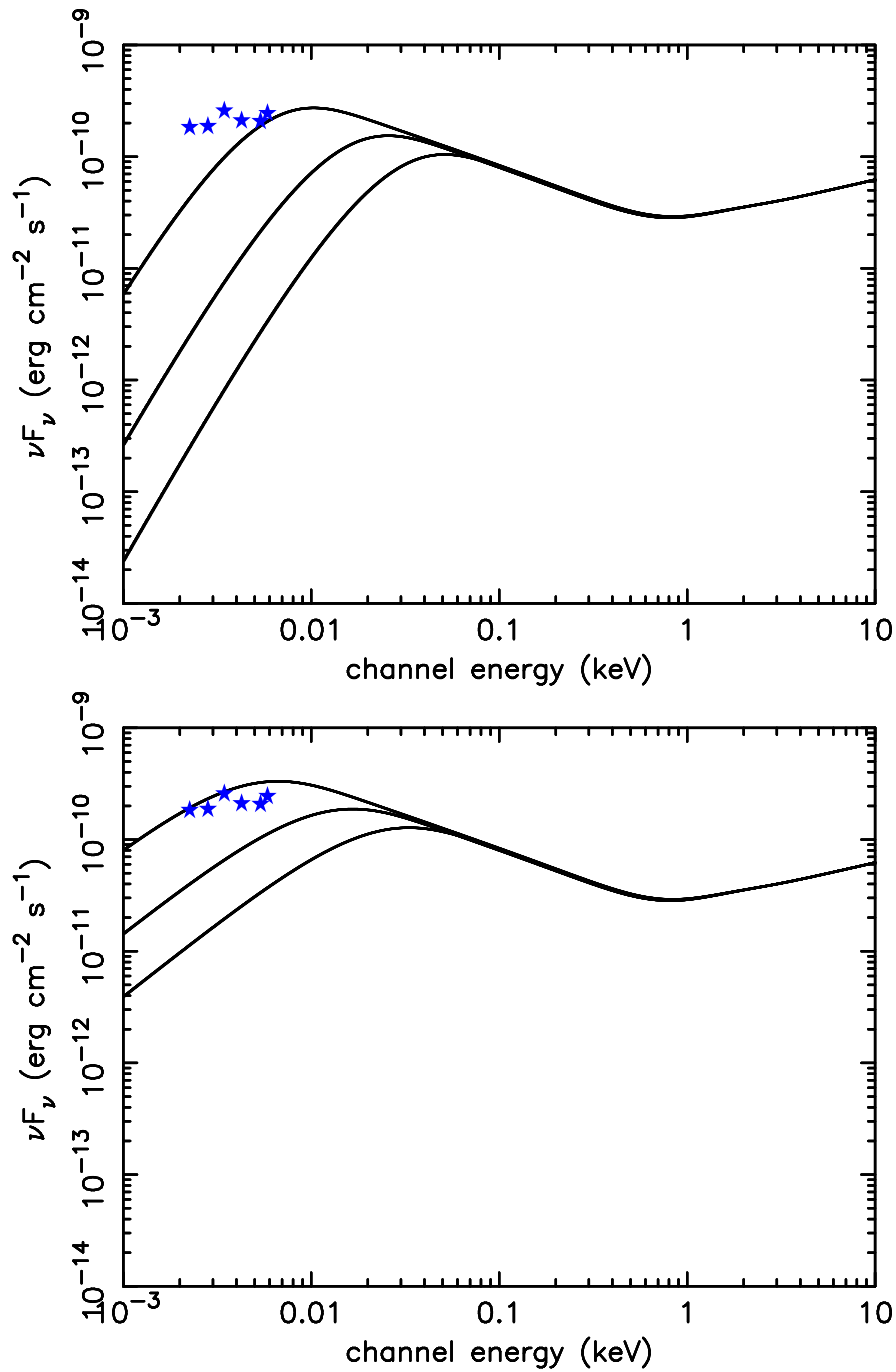


FIGURE 4.9. The curves show the extrapolation of the X-ray Comptonisation model down to optical energies for input (disc) temperatures of, from left to right, 2, 5 and 10 eV. The top plot assumes the input photons follow a simple blackbody distribution, while the lower one has a disc blackbody as the input to the model.

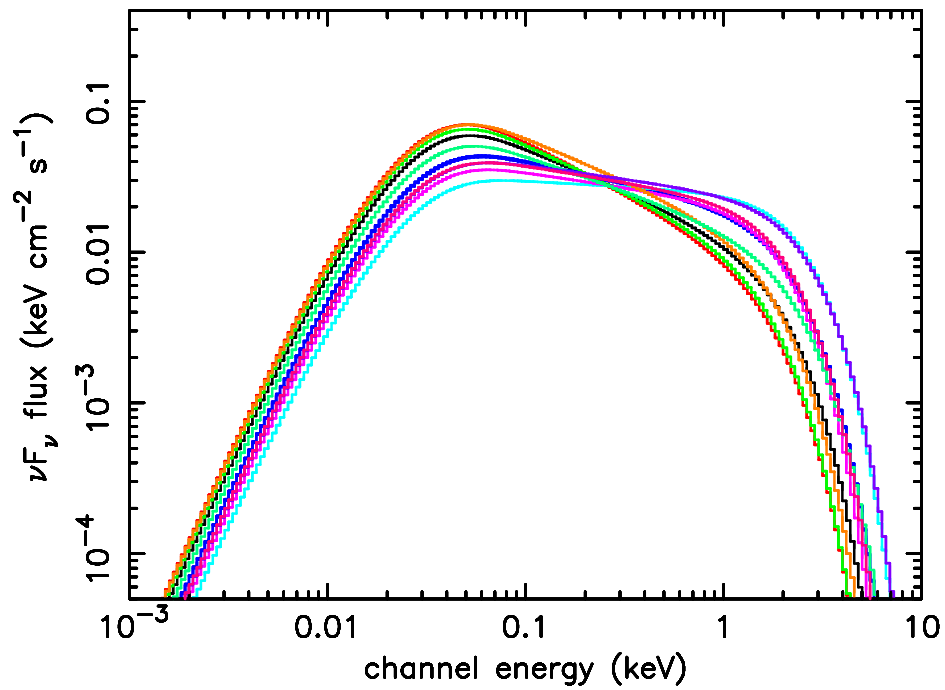


FIGURE 4.10. The soft excess of 3C 273 measured during each observation; the emission appears to pivot about ~ 0.3 keV.

Soft excess

To investigate how the soft excess is changing over time, the model plots for each revolution were overlaid. It was found that the shape of the soft excess appears to pivot; that is, there are times when there are more soft but fewer (relatively) harder photons and times when the reverse is true (Fig. 4.10). Considering the lowest energies (below the ‘pivot point’), the upper-most curve corresponds to the observation with the highest flux of photons; the number of photons then decreases, down to the lowest curve, which has the smallest photon flux.

This result shows up a limitation of the restricted *XMM* energy band. When considering only energies $\gtrsim 0.3$ keV, and fitting the soft excess with blackbodies, it was found that hotter components corresponded to a higher soft excess luminosity (see Fig. 4.5). Hotter blackbodies can be thought of as the slope of the soft excess becoming flatter; this result is also demonstrated in Figure 4.11, which plots the slope of the soft excess against the flux of photons (obtained from the ‘flux’ command within XSPEC), where a higher

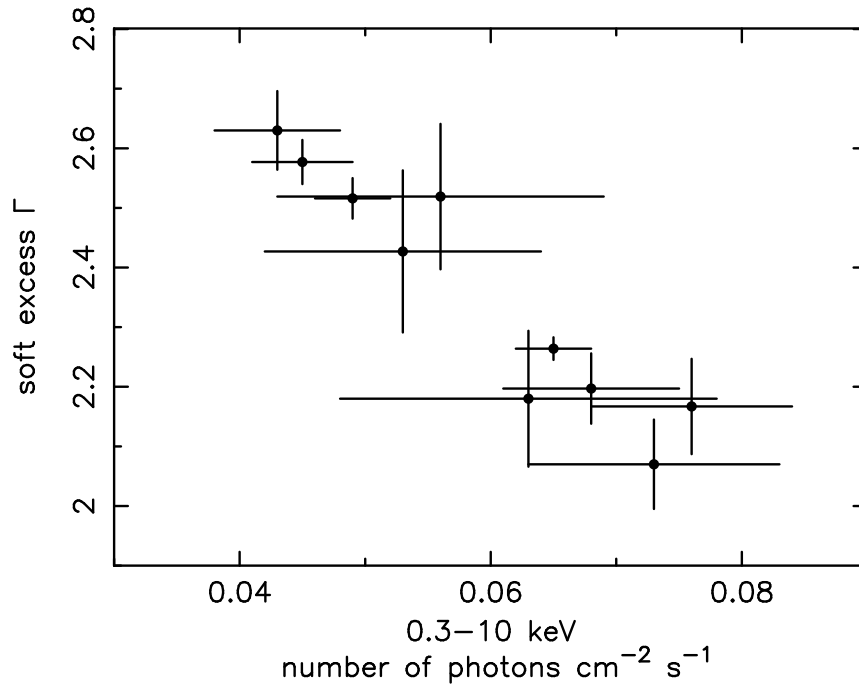


FIGURE 4.11. Over the limited 0.3-10 keV band, the steeper the slope of the soft excess, the less luminous it appears.

number of photons indicates a more luminous soft excess. If, however, the total extent of the soft excess is considered, i.e., down to ~ 1 eV, it is found that the ‘steeper’ soft excesses are, overall, the more luminous, as is shown in Figure 4.12. In the following work, it is assumed that the number of photons within the soft excess is equal (or close) to the number of seed photons from the accretion disc. There is an extremely strong correlation between the slope and 1 eV–10 keV photon flux, with the Spearman Rank probability being $> 99.99\%$.

Figure 4.10 demonstrates that the number of photons in the soft excess (\Leftrightarrow number of seed photons) is varying over time, showing that the accretion disc, itself, is changing. The Spearman Rank gives a 98% negative correlation between the optical depth and number of photons. It is expected that the presence of more seed photons should lead to the cooling of the electrons in the corona and, hence, the soft excess. Both Spearman Rank and weighted linear regression indicate a negative correlation (97%; slope of -0.056 ± 0.034 for the kT-photons data).

Figure 4.12 clearly shows that the presence of more seed photons leads to a steeper

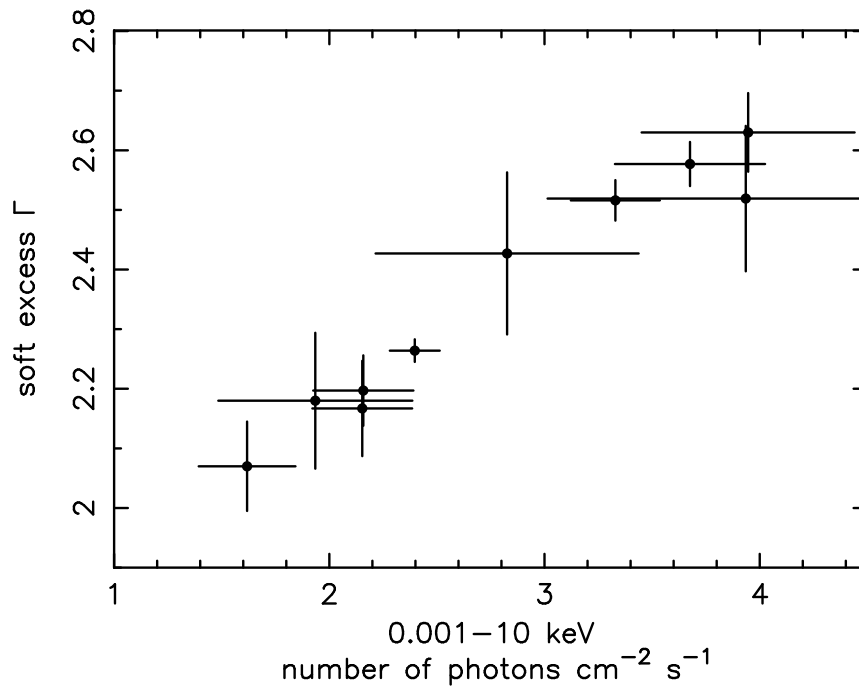


FIGURE 4.12. The variation of the spectral slope of the soft excess with the number of photons, over the 1 eV–10 keV range. This shows that, using the extrapolation of the model, the steeper soft excesses are more luminous.

‘power-law’ for the soft excess. This slope is inversely related to both the optical depth and the temperature of the electrons (Equations 1.8 and 1.9); because the temperature and optical depth are intimately linked within the equation, it is difficult to know for certain whether it is the decrease in optical depth or the cooling of the corona which is the dominant factor in producing the strong correlation observed in Figure 4.12, since the two weaker correlations reinforce each other. The slope and temperature are the variables in the *thComp* routine, rather than the optical depth; this means that it is not straight-forward to fix τ to a constant value, to see if the whole variation observed could be due to Compton cooling. Plots of the electron temperature against soft excess slope were produced for a range of constant optical depths and the actual measurements from the observations over-plotted; the resultant plot is shown in Figure 4.13, with the lower graph showing the line for $\tau = 13.3$, which passes through all but one of the error bars. Assuming that the optical depth does remain constant between the observations, and taking $\tau = 13.3$ as that constant value, the line corresponding to this optical depth was

overlaid on the contour plots of the electron temperature against soft excess slope from the best fit models to the X-ray data. The temperatures of the electrons at the 95% confidence level were then read off, this being the lowest level at which the $\tau = 13.3$ line agreed with all ten observations. An example of the plot is given in Figure 4.14.

Figure 4.15 plots the temperatures (assuming $\tau = 13.3$) against the number of photons and very clearly shows the Compton cooling effect, with a Spearman Rank probability of $> 99.99\%$ and a least-squares fit of -0.12 ± 0.02 . The data are consistent, therefore, with the temperature of the corona above the disc responding to a change in the seed photon flux. That is, the Comptonising region could simply be reacting to the variations in the accretion disc, rather than the electron population changing of its own accord. It must be noted, however, that it is by no means certain that the optical depth remains constant. All that can be definitely concluded is that the product of the temperature and optical depth decreases in the presence of more seed photons.

What these plots show is that the soft excess of 3C 273 seems to pivot between observations, varying between bright-and-soft and faint-and-hard flux states. The soft excess temperatures measured here are low enough such that only part of the soft excess can be observed over the *XMM* band. Hence, the soft excess only appears to be bright when soft if the model is extrapolated down to lower energies.

To try and determine how the regions producing the soft and hard X-rays are linked, various figures were plotted. Figure 4.16 shows the fractional (rms) variability as a function of energy, after the Poisson noise has been accounted for (Edelson et al. 2002). This implies that, over the ten observations, both the hard and soft bands vary by approximately 15%, with very little difference between them. Figure 4.17 shows, in the top plot, the luminosities of the two Comptonised components, and implies that there is no correlation between the hard power-law and soft X-ray luminosities, with Spearman Rank giving a probability of only 62% for an inverse correlation, and linear regression giving a slope which is consistent with zero. However, comparing the photon indices found through the Comptonisation fits (lower plot), there does appear to be a positive correlation, with linear regression giving a value of 0.12 ± 0.02 and Spearman Rank, $\sim 96\%$.

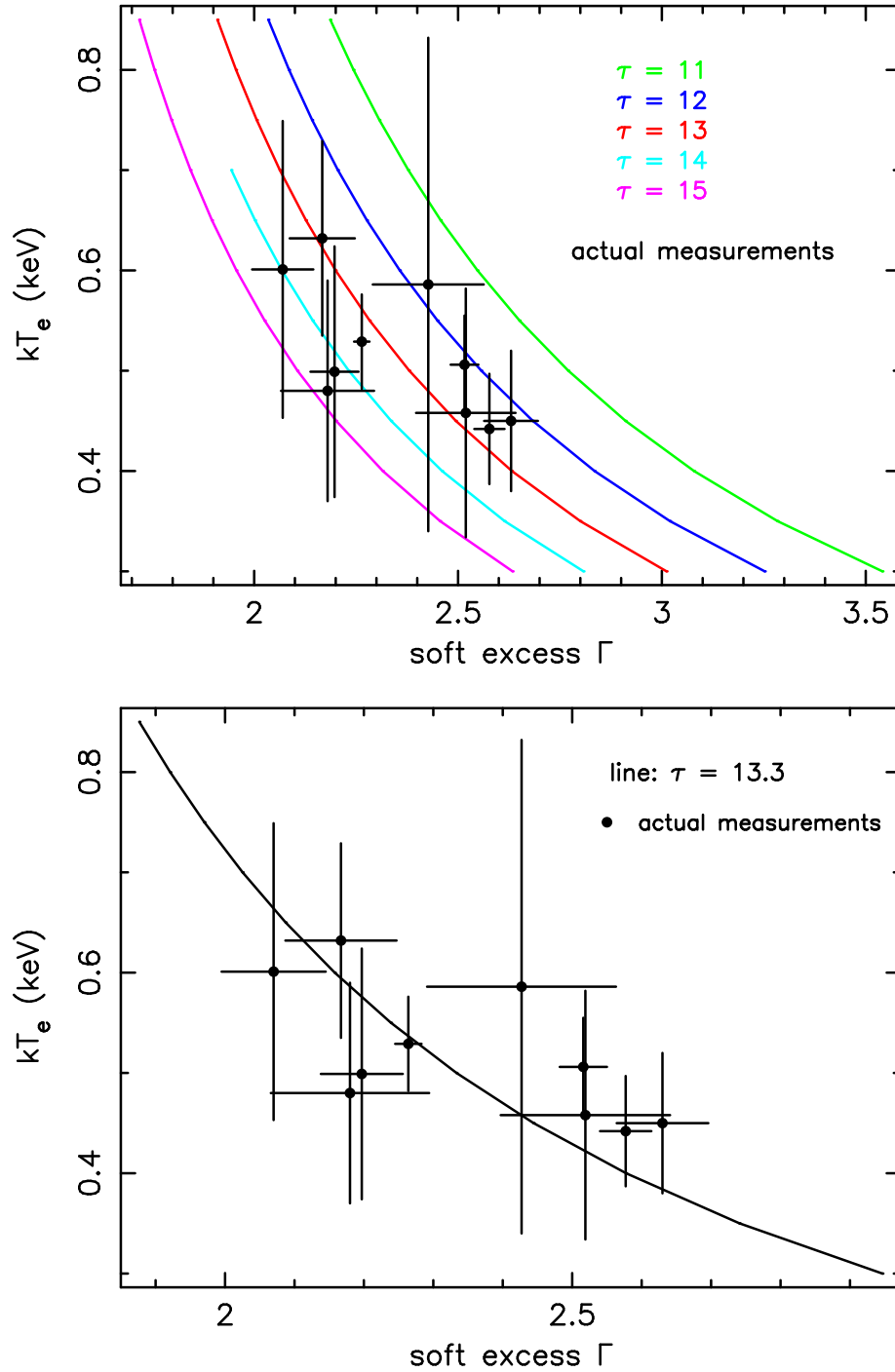


FIGURE 4.13. The variation of the electron temperature with slope of the soft excess, for fixed values of the optical depth. The actual measurements from the observations of 3C 273 are plotted as the individual points. The lower window shows the line where $\tau = 13.3$, which fits the data well.

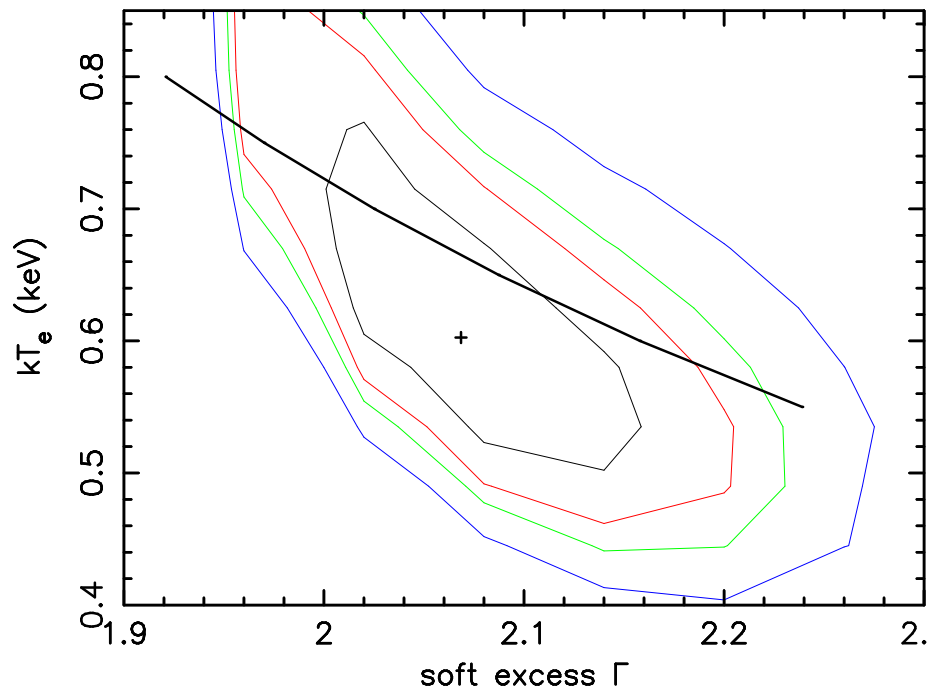


FIGURE 4.14. An example (rev. 370) of the correspondance between the best fit contours from the X-ray Comptonisation model and the line of constant optical depth. The contours shown are those for 68, 90, 95 and 99% confidence.

This second result indicates that there may be a link between the components, and is consistent with our finding that the photons producing the Comptonised power-law are likely to have first interacted with the soft excess corona. That is, when the soft excess is brighter/steeper, there is a possibility for more photons to interact with the hotter electrons, thus cooling them slightly and, hence, softening the power-law. If this is the case, then the harder X-ray band is not purely dominated by the relativistic jet, since the disc photons are affecting it.

Using a simple power-law model (Table 4.2), there is a weak inverse connection between 3–10 keV Γ and the power-law flux over the same energy band (Figure 4.18). Spearman Rank gives a probability of 91%, while least squares fitting gives a slope of -0.028 ± 0.008 . The relationship between the slope and flux of 3C 273 has been found to vary. Turner et al. (1990) found that the parameters were independent, when considering *Ginga* data between 1983 and 1988; this was also found from *RXTE* measurements from 1996-1997 (Kataoka et al. 2002). However, from 1999-2000, Kataoka et al. found

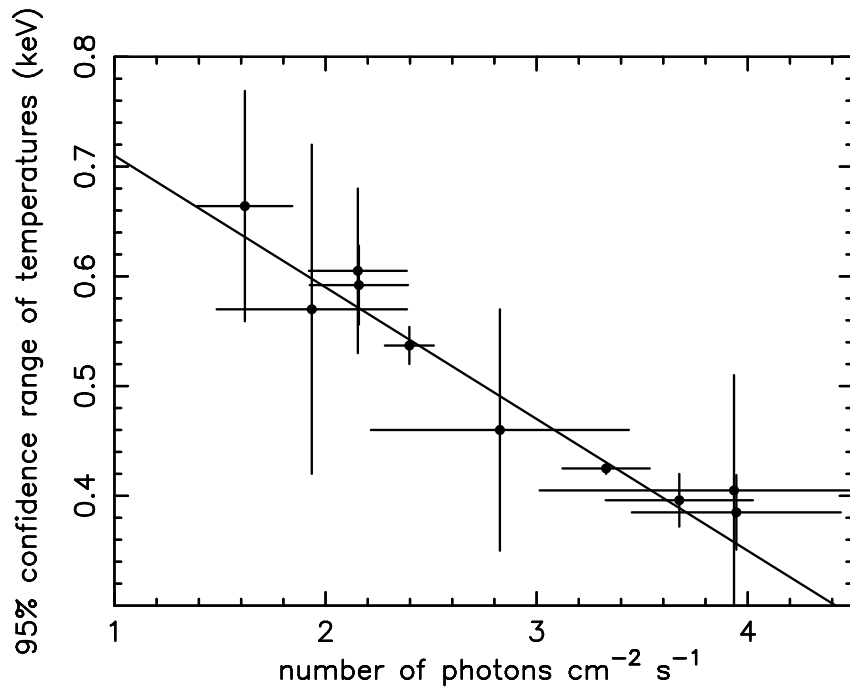


FIGURE 4.15. For an assumed constant optical depth, the Compton cooling of the corona is clear to see. The line shows the weighted linear regression fit of -0.12 ± 0.02 .

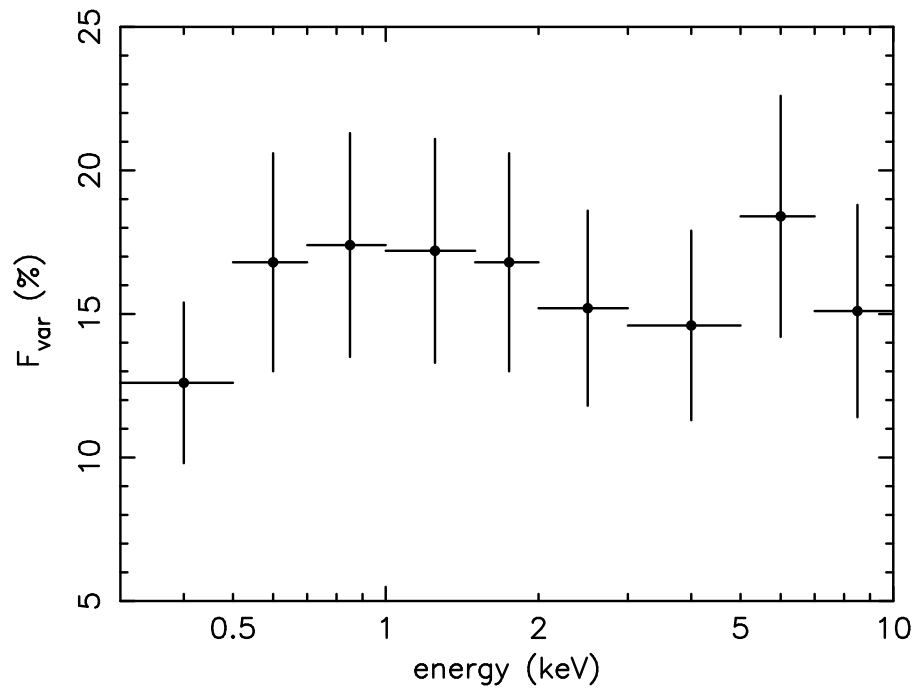


FIGURE 4.16. The fractional variability amplitude of the MOS 2 data over the ten observations of 3C 273.

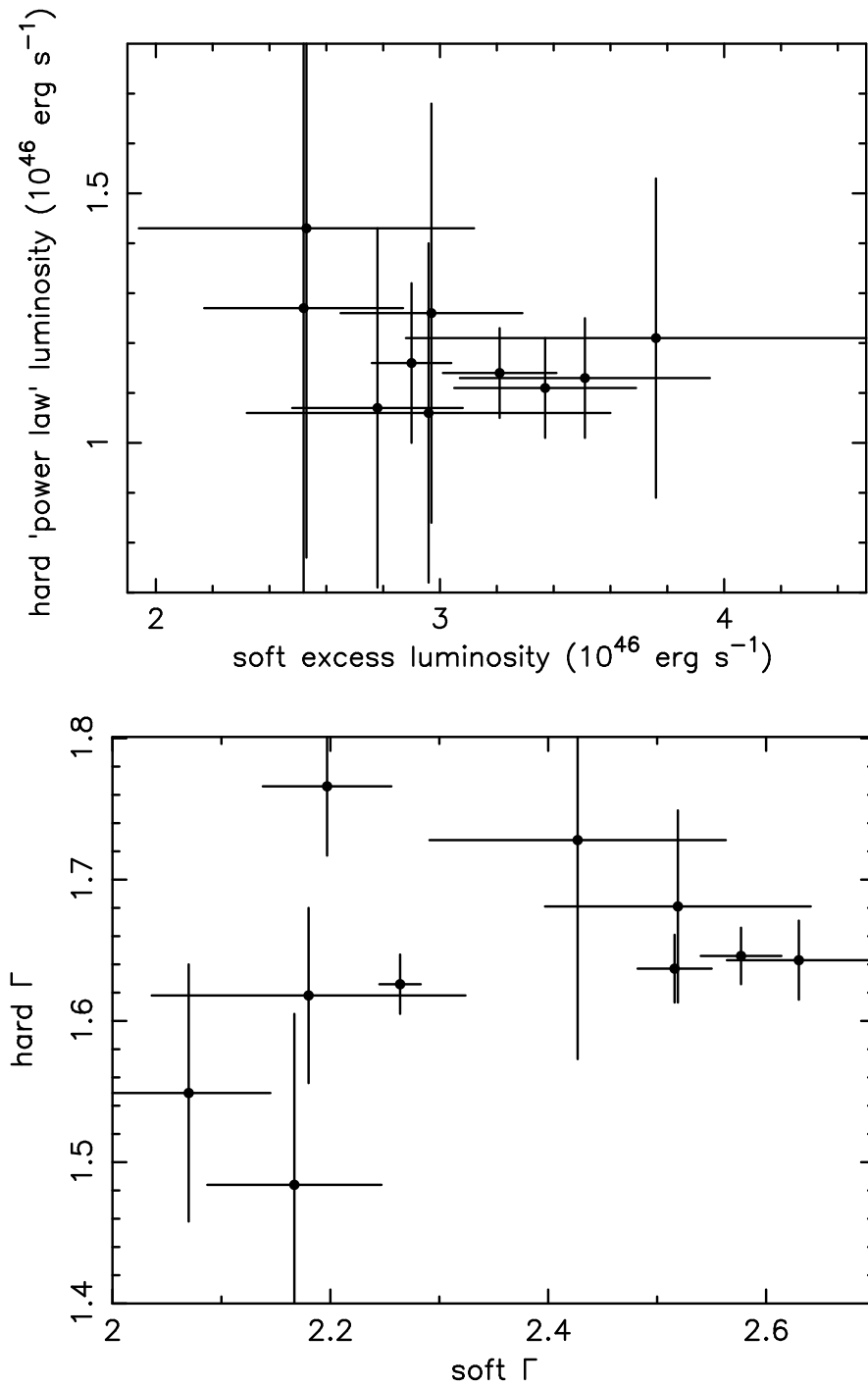


FIGURE 4.17. Although the luminosity of the separate Comptonised components appear to be independent, there is a positive correlation between the photon indices.

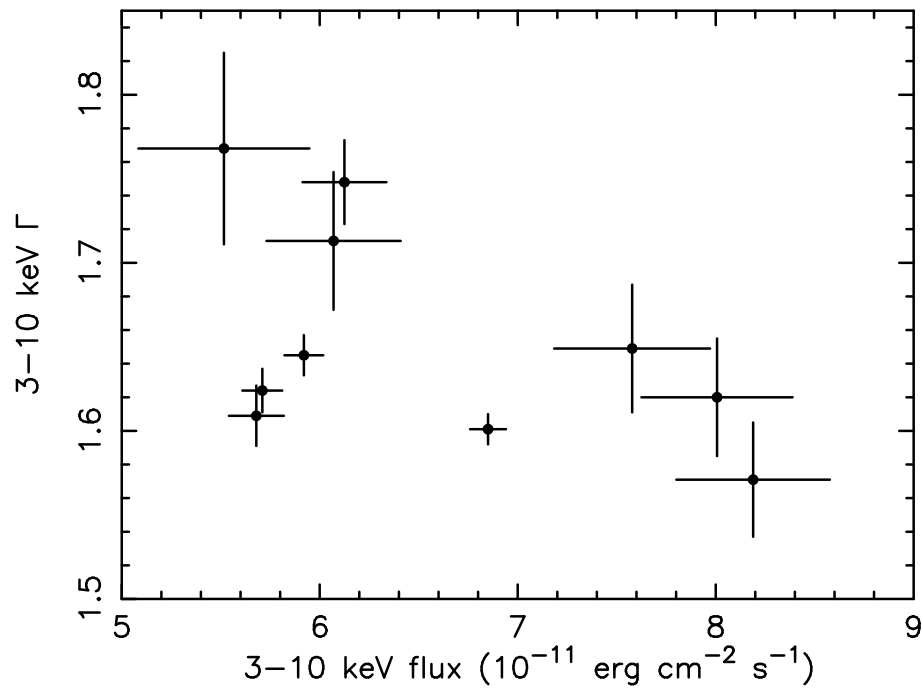


FIGURE 4.18. The measured 3–10 keV photon index may be related to the 3–10 keV flux.

that the slope became *softer* when the flux level increased, the opposite of our findings.

4.1.7 Conclusions: 3C 273

The *XMM* spectrum of 3C 273 has been investigated. It is found that the soft X-ray spectrum is dominated by a strong soft excess below ~ 2 keV. This can be well modelled by a simple blackbody parameterisation, but more likely arises through thermal Comptonisation of cool (UV) disc photons in a warm (400-500 eV) corona above the surface of the accretion disc. The soft excess appears to pivot around ~ 0.3 keV, with the soft X-ray spectrum becoming steeper when it is brighter. It is also found that the hard power-law slope appears to become steeper as the soft excess does, while the 3–10 keV spectral index is hardest when the flux over that band is highest. These spectral changes are all consistent with a model in which the increase in disc photon flux in the unobservable EUV range Compton-cools the populations of coronal electrons responsible for both the soft excess and the hard power-law component above 3 keV.

The detection of a weak, broad, ionised iron line is also confirmed; this presumably originates in the ionised accretion disc. However, the line is only significantly detected though co-adding all of the MOS 2 observations present in the *XMM-Newton* archive.

4.2 PKS 0558–504

4.2.1 Introduction

PKS 0558–504 is a low redshift, luminous quasar, with $z = 0.137$ and $M_v \sim -24.5$. It is radio-loud, although not strongly so, with $R \sim 27$ (Siebert et al. 1999). PKS 0558–504 is quite unusual in that, although it is radio-loud, the Balmer lines are quite narrow (FWHM = 1500 km s^{-1} ; Remillard et al. 1986), making it similar to a Narrow Line Seyfert 1. (NLS1s tend to be radio-quiet; Schartel et al. 1996). The X-ray emission is known to be variable, with *Ginga* observing a 67% increase in three minutes (Remillard et al. 1991). However, no such rapid flares were found by *XMM* (Gliozzi et al. 2001) or the *ROSAT* HRI (Gliozzi et al. 2000), although persistent variability was identified. *ASCA* (Wang et al. 2001) again found short timescale flares, occurring over a matter of minutes.

O’Brien et al. (2001b) investigated the X-ray spectrum of PKS 0558–504 during the *XMM-Newton* revolutions 42 and 84 (2000-03-01 and 2000-05-24) and found it to show a strong soft excess. No strong Fe $K\alpha$ emission was identified and, together with the high luminosity of the source, this implies that the accretion disc is likely to be fully ionised.

4.2.2 XMM-Newton observations

PKS 0558–504 has been re-observed a number of times by *XMM*, in revolutions 153, 283 and 341 (2000-10-10, 2001-06-26 and 2001-10-19), which allows an investigation of the variability of the soft excess. The object was also observed very early on in the mission (revolutions 30 and 32), but these old datasets are extremely hard to process and, so, were ignored for the current work. Only the MOS data were readily accessible

for revolution 42, while only PN data were obtained for the most recent (rev. 341) observation. All ODFs were reprocessed with SAS v5.4.1 for calibration consistency. As for 3C 273, there was an indication of pile-up in the MOS datasets, so pattern zero spectra were produced. For these data, there were no significant differences between the MOS 1, MOS 2 and PN spectra, so joint fits were performed. The discrepancies observed in 3C 273 are likely to be linked to the excellent signal-to-noise in the spectra, leading to calibration uncertainties being extremely obvious; although PKS 0558–504 is bright, 3C 273 is even more so.

4.2.3 Spectral analysis

Fe K emission

The rest frame 2–10 keV energy band was first investigated, fitting a simple power-law to the data, attenuated by Galactic absorption ($N_H = 4.4 \times 10^{20} \text{ cm}^{-2}$). Table 4.5 lists the 2–10 keV power-law slopes, corresponding fluxes and (de-reddened) luminosities. It was found that, while the datasets did not require narrow emission lines (Table 4.6), broad lines were sometimes significant, with the ionised line being statistically preferred. This is similar to the weak, broad, ionised line found through co-adding the 3C 273 spectra. The presence of an *ionised* broad line, rather than a neutral one, is in agreement with Dewangan (2002), who found that steep 2–10 keV slopes, such as PKS 0558–504 shows (Table 4.5), correlate with high central energies for the Fe $K\alpha$ lines, indicating that the AGN with steeper continua have more strongly ionised accretion discs. This situation is most likely to occur at accretion rates close to the Eddington value.

Extrapolating the 2–10 keV power-law fits down to 0.2 keV, a soft excess was observed. For most of the observations, this was obviously strong, but the spectrum for revolution 341 only seems to show a weak excess; this is demonstrated in Figure 4.19.

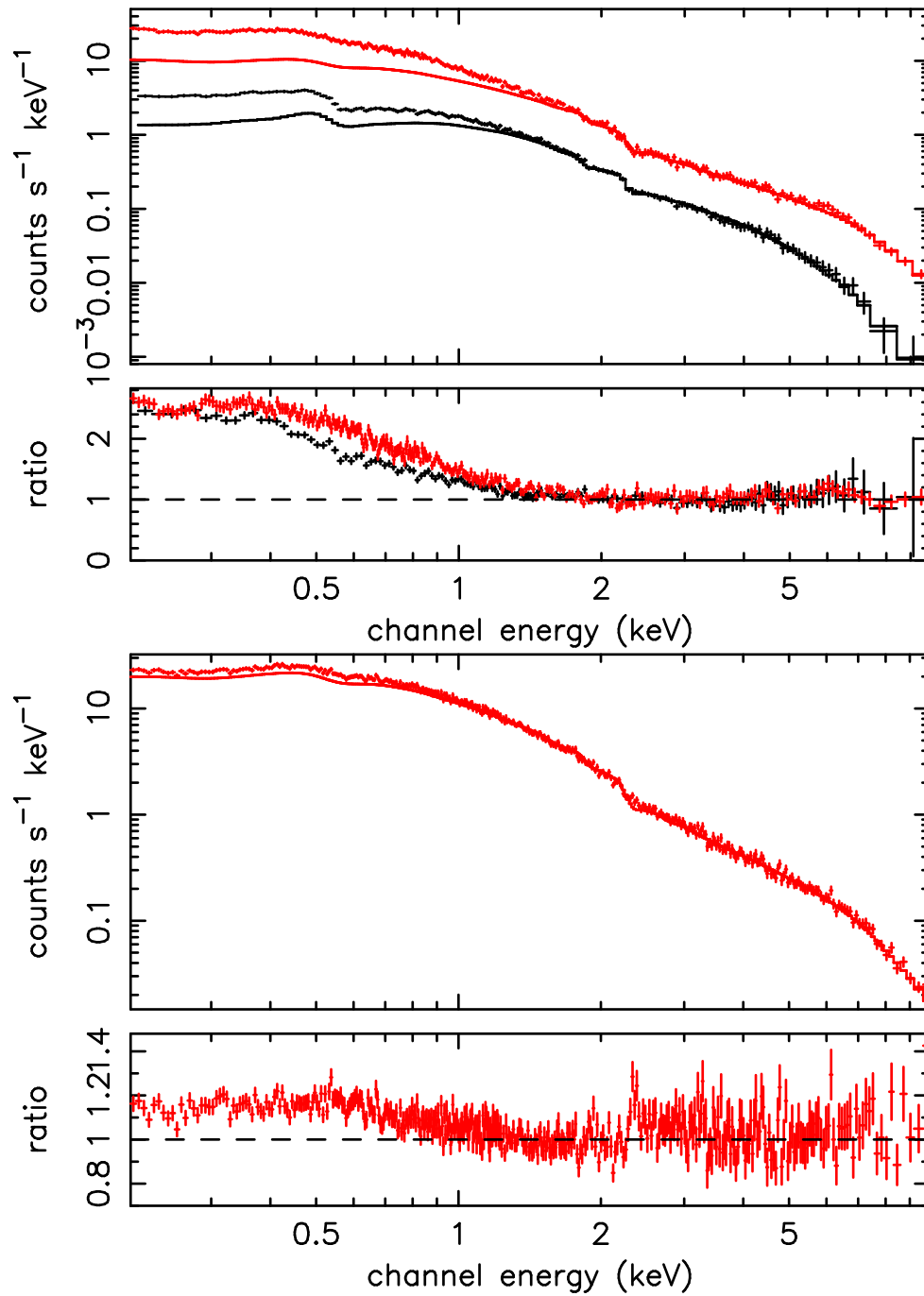


FIGURE 4.19. The soft excess of PKS 0558–504, as measured by *XMM* during revolutions 153 (top) and 341 (bottom). Only PN (red) data were available for the latter revolution.

Table 4.5. Power-law fits to the 2–10 keV PKS 0558–504 spectra.

revolution	Γ	2–10 keV flux (10^{-11} erg cm $^{-2}$ s $^{-1}$)	2–10 keV luminosity (10^{44} erg s $^{-1}$)	χ^2/dof
42	2.42 ± 0.02	1.06	9.84	343/286
84	2.26 ± 0.02	0.86	7.98	790/786
153	2.19 ± 0.02	1.10	10.12	498/706
283	2.14 ± 0.02	0.98	9.02	676/749
341	2.28 ± 0.01	2.09	19.31	787/739

Table 4.6. The limits on the strengths of narrow (0.01 keV) and broad (0.5 keV) lines (both neutral and ionised) in the PKS 0558–504 data. The energy of the neutral components were fixed at 6.4 keV, with the ionised energy being 6.7 keV.

rev.	Narrow Line EW (eV)		Broad Line EW (eV)	
	(neutral)	(ionised)	(neutral)	(ionised)
42	< 59	< 124	478 ± 138	547 ± 155
84	< 35	< 115	227 ± 115	305 ± 127
153	< 45	< 82	193 ± 100	246 ± 108
283	< 45	< 31	< 176	< 204
341	< 22	< 20	< 41	< 60

The soft excess

As has been found for many other AGN, the soft excess of PKS 0558–504 can be well modelled by multiple BB components. In comparison to the flat spectral index found for 3C 273, the slopes measured for PKS 0558–504 tend to be rather steep (see Table 4.5). This, together with the relatively narrow Balmer lines (Remillard et al. 1986), makes the object similar to NLS1s, although more luminous. It is noticeable that the earlier observations require a larger number of blackbodies to parameterise their soft excesses than do the later ones, with the hotter components disappearing over time. Figure 4.20 shows an unfolded plot of the BB fit to the soft excess measured in revolution 84. As well as the power-law slope and BB temperatures, Table 4.7 gives the strength of the soft excess for each revolution, as defined in Chapter 2 – that is, the ratio of the luminosities

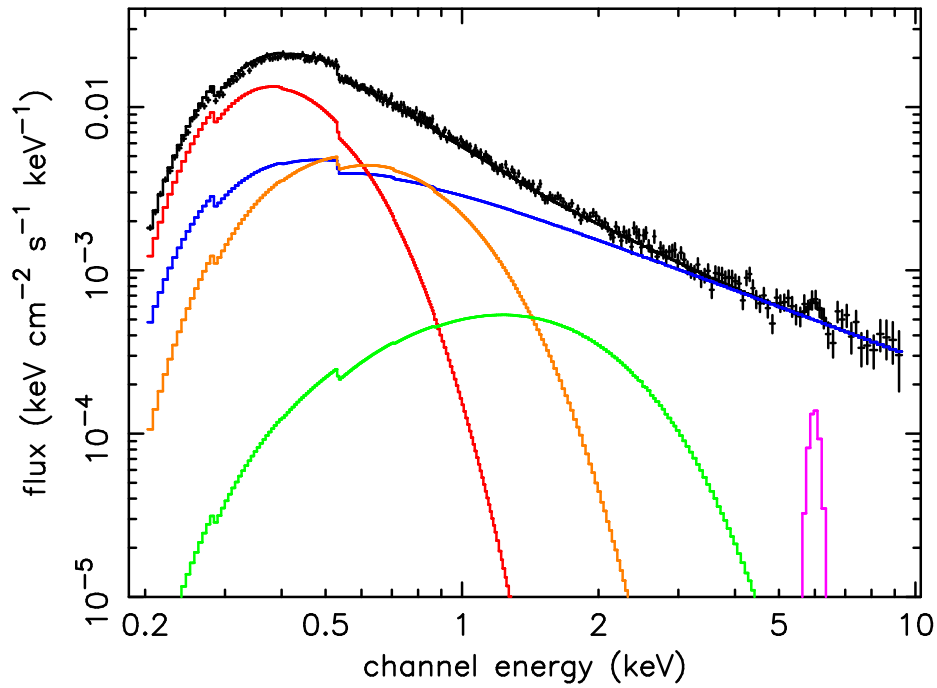


FIGURE 4.20. An unfolded plot showing the blackbody fit to the soft excess of PKS 0558–504, during revolution 84. PN data, only, shown for clarity. The red BB has a temperature of ~ 89 eV, the orange, ~ 188 eV, and the green, ~ 465 eV. The broad, ionised line (EW ~ 305 eV) is also shown.

of the BB and power-law components, over the observed energy range of 0.2–10 keV.

It comes as no surprise that the strength of the soft excess does not correlate with the broad-band luminosity of PKS 0558–504 (Figure 4.21), having found that this was the case for the large samples of Seyferts and QSOs (Chapters 2 and 3), as well as for 3C 273 (Section 4.1.3). Comparing the strength with the 2–10 keV slope, however, shows the same relationship as found for the Seyfert galaxy sample, although not for the QSOs: that is, steeper slopes correspond to stronger soft excesses. This link to the Seyfert sample may, again, be due to the similarity between PKS 0558–504 and the NLS1s. As for the lower-luminosity objects, the correlation may be due to Compton cooling: an excess of photons from the strong soft excess could act to cool the electrons producing the power-law component, thus softening the 2–10 keV slope.

Double/broken power-law and *diskbb* fits were tried to the soft excess, but, again, the resulting fits were not as good as the multiple blackbodies, as Table 4.7 shows. As

Table 4.7. Fits to the broad-band (0.2–10 keV) spectra of PKS 0558–504. ^a 2 individual power-laws; ^b broken power-law fit; ^c disc blackbody; ^d The F-value gives the improvement when fitting the soft excess with multiple blackbodies rather than the present model.

revolution	Γ	kT (keV)	kT (keV)	kT (keV)	0.2–10 keV luminosity (10^{45} erg s $^{-1}$)	BB/ Γ luminosity ratio	χ^2/dof
42	1.69 ± 0.12	0.084 ± 0.003	0.179 ± 0.008	0.437 ± 0.022	5.57	2.42	425/392
84	2.04 ± 0.11	0.089 ± 0.002	0.188 ± 0.009	0.465 ± 0.053	4.39	1.32	1762/1223
153	2.20 ± 0.02	0.085 ± 0.002	0.187 ± 0.006	—	4.96	0.39	1160/1126
283	2.13 ± 0.02	0.088 ± 0.004	0.178 ± 0.009	—	3.45	0.37	1256/1172
341	2.28 ± 0.01	0.135 ± 0.003	—	—	6.97	0.08	1137/1067

revolution	model	Γ	Γ	break energy (keV)	kT (keV)	χ^2/dof	F-value ^d
42	2po ^a	2.91 ± 0.01	0.96 ± 0.14	—	—	572/396	34
	bknpo ^b	2.87 ± 0.01	2.47 ± 0.02	1.45 ± 0.04	—	605/396	42
	diskbb ^c	2.50 ± 0.01	—	—	0.127 ± 0.001	556/396	30
84	2po	3.02 ± 0.01	1.15 ± 0.09	—	—	2141/1227	66
	bknpo	2.95 ± 0.01	2.33 ± 0.02	1.55 ± 0.03	—	2034/1227	47
	diskbb	2.41 ± 0.01	—	—	0.129 ± 0.001	1864/1227	35
153	2po	2.94 ± 0.01	1.34 ± 0.07	—	—	1415/1130	62
	bknpo	2.84 ± 0.01	2.26 ± 0.02	1.56 ± 0.03	—	1331/1130	42
	diskbb	2.36 ± 0.01	—	—	0.128 ± 0.009	1317/1130	38
283	2po	2.78 ± 0.03	1.49 ± 0.08	—	—	1418/1174	76
	bknpo	2.63 ± 0.01	2.15 ± 0.01	1.53 ± 0.03	—	1319/1174	29
	diskbb	2.18 ± 0.01	—	—	0.141 ± 0.001	1292/1174	17
341	2po	2.43 ± 0.02	1.24 ± 0.37	—	—	1248/1067	—
	bknpo	2.41 ± 0.01	2.28 ± 0.01	1.61 ± 0.12	—	1209/1067	—
	diskbb	2.26 ± 0.01	—	—	0.167 ± 0.003	1140/1067	—

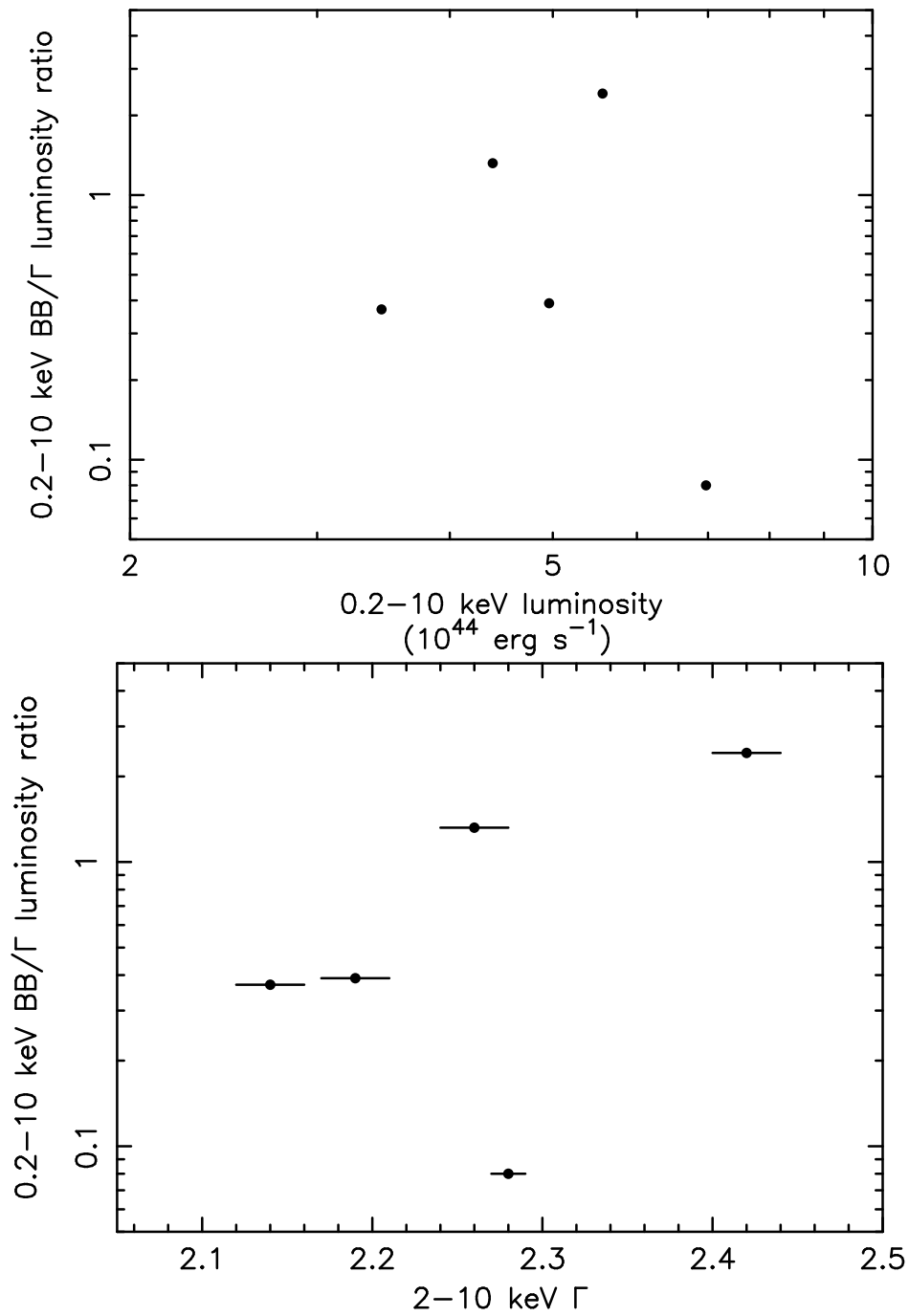


FIGURE 4.21. Agreeing with the samples investigated in previous chapters, there is no correlation between the strength of the soft excess and the 0.2–10 keV luminosity (top). In the same fashion as the Seyfert galaxies, it is noted that the stronger soft excesses occur when the 2–10 keV power-law slope is steeper.

stated previously, when considering the F-test, for one fewer degree of freedom, $F > 3.0$ corresponds to an improvement of 90%; for a larger change in degrees of freedom, the required F value is smaller. It is, therefore, very clear to see that the power-law and *diskbb* models are much worse than blackbodies. It is not possible to provide an F-value for a comparison of the fits to the revolution 341 data, because there is no change in the number of degrees of freedom between these different models. [F is defined to be $(\Delta\chi^2/\Delta\text{dof}) \times 1/(\chi^2_{\nu})$, where χ^2_{ν} is the new reduced χ^2 value.]

The next stage in investigating the soft excess of PKS 0558–504 was to apply the Comptonisation model to the data. The resulting fits are given in Table 4.8 and the values investigated in Section 4.2.6. It is noticeable that the temperatures found for the input photons to the hotter component are much cooler than the temperature of the soft excess. This is at odds with the values found for the objects in Chapters 2 and 3.

4.2.4 RGS data

O’Brien et al. (2001b) found that there was no evidence for intrinsic absorption, either warm or cold, in the revolution 42 and 84 spectra of PKS 0558–504. Since revolution 153 provided a long duration RGS exposure, this spectrum was analysed in the same manner as the earlier ones (Section 4.1.4). The results were consistent, in that there were no significant *rest frame* features to be found, with the neutral O VII and O VIII edges having optical depths of $\tau < 0.1$.

However, although there may not be any features due to absorption in the rest frame of PKS 0558–504, there is significant absorption around 21.6 Å, with an equivalent width of 1.90 ± 0.88 eV, or 71 ± 33 mÅ, for $\sigma = 1$ eV; this is shown in Figure 4.22. Such absorption was found by Fang et al. (2003) in 3C 273, and suggested to correspond to zero-redshift O VII He α ; an absorption line at this wavelength was confirmed in the spectrum of 3C 273 in this work (Section 4.1.4). Rasmussen et al. (2003) also identified this feature in the spectra of Mrk 421 and PKS 2155–304, as well as 3C 273.

If this line is correctly identified as zero-redshift absorption, it is likely to be due to warm gas in the local intergalactic medium, either in a halo around the Milky Way

Table 4.8. Comptonisation fits to the broad-band PKS 0558–504 data. The disc temperature is taken to be 15 eV and the hotter electron population is at a temperature of 200 keV. The luminosities given are for the model extrapolated down to 1 eV.

revolution	COOLER COMPTONISED COMPONENT			HOTTER COMPTONISED COMPONENT			χ^2/dof
	electron temperature (keV)	τ	luminosity ($10^{45} \text{ erg s}^{-1}$)	input temperature (keV)	Γ	luminosity ($10^{45} \text{ erg s}^{-1}$)	
42	0.180 ± 0.020	19.4 ± 2.3	9.98 ± 1.62	0.066 ± 0.007	2.44 ± 0.03	4.51 ± 0.11	543/394
84	0.163 ± 0.009	22.7 ± 1.0	7.48 ± 0.71	0.067 ± 0.005	2.35 ± 0.02	3.12 ± 0.06	1843/1225
153	0.213 ± 0.010	17.5 ± 0.8	11.15 ± 0.89	0.066 ± 0.007	2.22 ± 0.02	3.34 ± 0.08	1226/1128
283	0.195 ± 0.012	20.1 ± 1.5	4.50 ± 0.44	0.068 ± 0.012	2.13 ± 0.01	2.67 ± 0.05	1266/1172
341	0.187 ± 0.025	18.4 ± 2.1	7.39 ± 1.59	0.093 ± 0.017	2.26 ± 0.01	5.99 ± 0.08	1135/1065

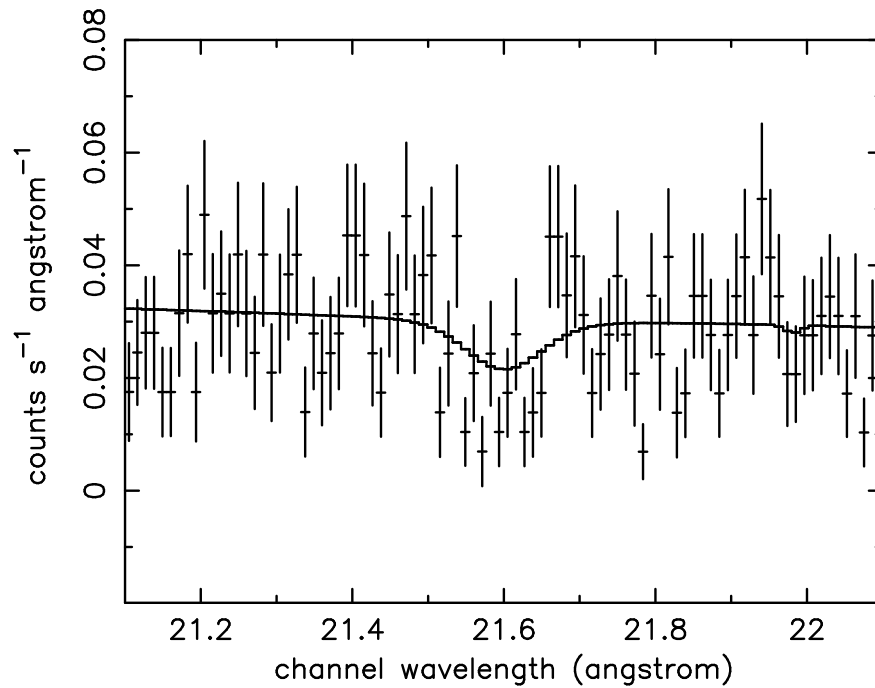


FIGURE 4.22. This absorption feature in the RGS data from the revolution 153 observation of PKS 0558–504 may correspond to zero-redshift O VII He α .

Galaxy (Spitzer 1956), or throughout the Local Group (Kahn & Woltjer 1959). Of these options, Rasmussen et al. (2003) tend toward the second explanation, while Fang et al. (2003) discuss both possibilities, suggesting that the absorption seen may be due to a combination of these sources. Further observations are required to determine the exact location of the gas.

4.2.5 Optical and UV data

Data were obtained from the OM for the first three observations of PKS 0558–504 presented here; Table 4.9 lists the magnitudes measured for each filter. Extrapolating the Comptonisation model to lower energies, it is, again, found that the X-ray model curves over at too high an energy to account for the total optical/UV emission. Figure 4.23 shows a series of curves, corresponding to different input BB temperatures: from left to right the curves represent 3, 4, 5 and 15 eV, where 15 eV was the value used for the fits to the X-ray data. The extrapolation cannot lie above the OM points, otherwise the model

Table 4.9. Optical and UV magnitudes for PKS 0558–504. Where more than one observation occurred for a given filter within a single revolution, the values have been averaged.

filter	wavelength (Å)	rev. 42	rev. 84 magnitude	rev. 153
V	5500	14.94	15.02	—
U	3600	14.05	—	—
B	4400	15.16	—	—
UVW1	2910	13.91	14.05	14.61
UVM2	2310	13.53	—	—
UVW2	2120	13.85	—	—

would over-predict the optical emission; hence, the lowest temperature the accretion disc in PKS 0558–504 can be is ~ 4 eV. The figure shows the data from revolution 42, but the data from revolutions 84 and 153 are consistent with the minimum disc temperature being ~ 4 eV.

4.2.6 Discussion

Soft excess

To investigate how the properties of the soft excess change with the number of input disc photons, Figures 4.24–4.26 were plotted. When investigating the soft excess of 3C 273 (Section 4.1.6), it was found that it was important to differentiate between the luminosity measured over the total *XMM* energy band and that calculated from an extrapolation of the best-fit model to lower energies. Thus, this is the first area investigated for PKS 0558–504.

Fig. 4.24 plots the slope of the soft excess against the flux of photons in both the 0.2–10 (top) and 1 eV–10 keV (bottom) bands. As was found for 3C 273, the correlation

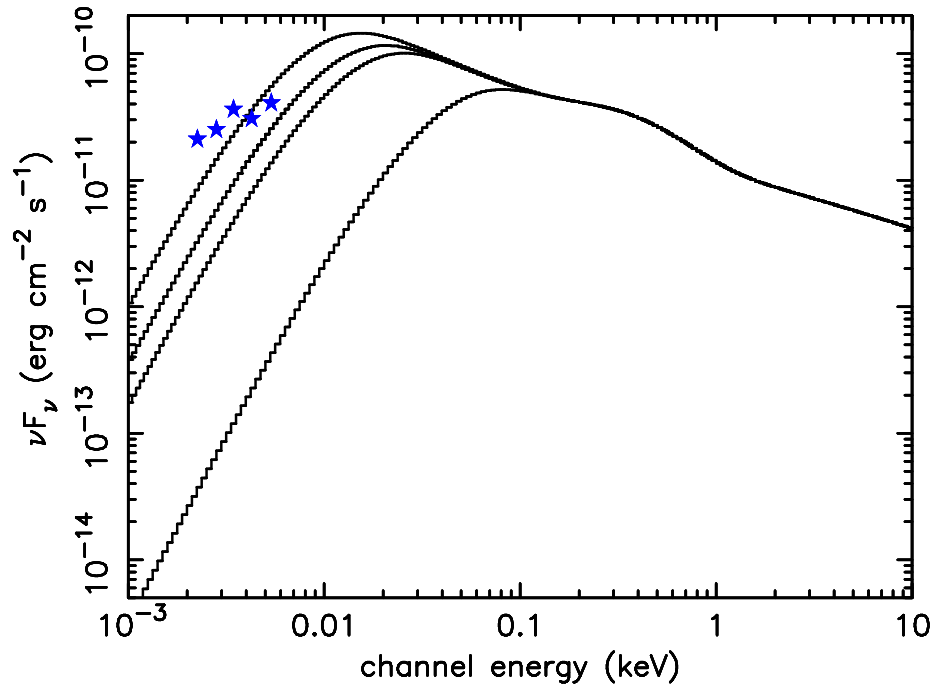


FIGURE 4.23. An example (rev. 42) of the extrapolation of the X-ray Comptonisation model to lower energies. The curves shown represent (from left to right) disc temperatures of 3, 4, 5 and 15 eV.

changes from negative to positive, when extending the energy band used. This is shown in both the linear regression results (-12.26 ± 4.7 for 0.2–10 keV; 0.47 ± 0.15 for 1 eV–10 keV) and the Spearman Rank, although the SR values are not statistically significant probabilities (-13% and 75% respectively). From here on, the energy band considered will be the extended, 1 eV–10 keV, one.

Figure 4.25 again finds that the optical depth appears to drop as more photons pass through the corona, as shown by the weighted linear regression. There is no strong relationship between the temperature of the electrons and the number of seed photons (Figure 4.26; Spearman Rank probability $\sim -52\%$ only). As mentioned when discussing 3C 273, these two values (τ and kT) are intimately linked, through Equations 1.8 and 1.9. As a result of this, the strongest correlation found is when plotting the slope against number of photons (Fig. 4.24), since $\Gamma \propto 1/(kT\tau^2)^{1/2}$.

As previously discussed (Section 4.1.6), it is intriguing to investigate whether the differences in the soft excess can be accounted for simply by a change in temperature,

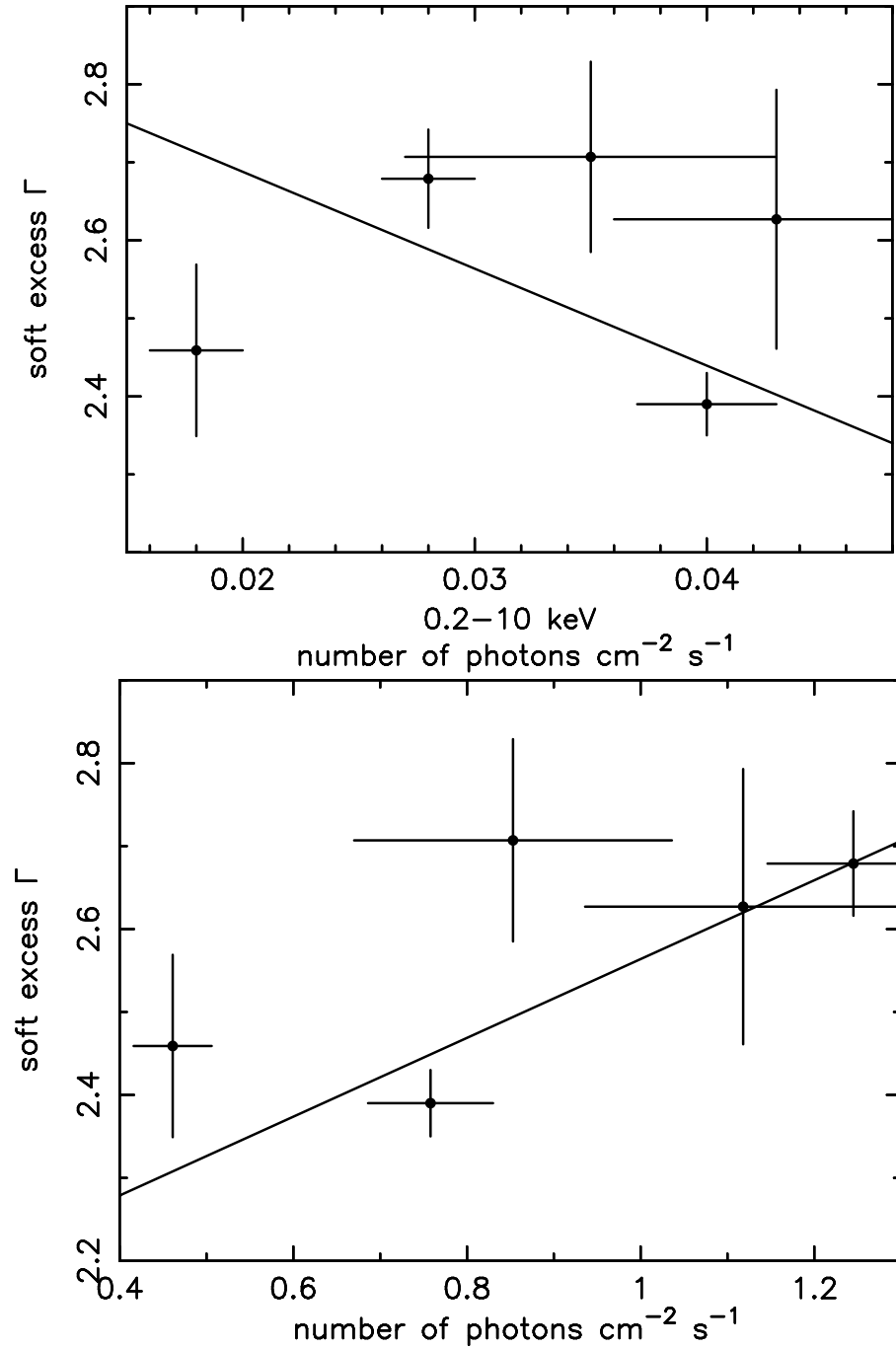


FIGURE 4.24. As for 3C 273, a (weak) negative correlation between the soft excess slope and the photon flux over the 0.2–10 keV band is found. If, however, the Comptonisation model is extrapolated down to 1 eV, the observed correlation is positive. The lines show the best fit weighted linear regression values (see text) to aid the eye.

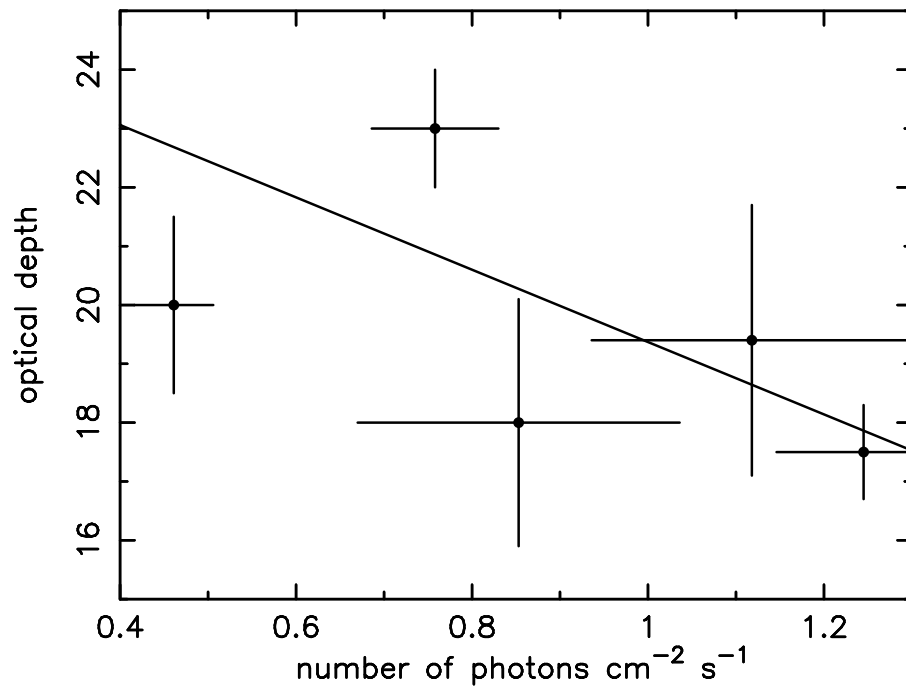


FIGURE 4.25. The optical depth of the corona decreases with an increasing number of photons, calculated for the 1 eV–10 keV band. The best fit regression line has a slope of -6.15 .

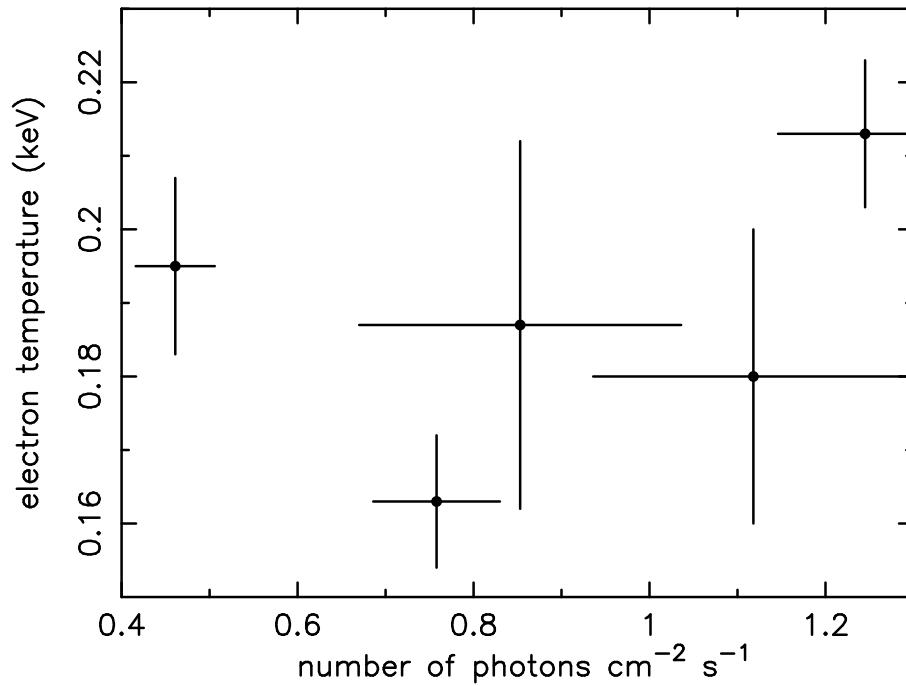


FIGURE 4.26. There is no strong evidence for Compton cooling in PKS 0558–504, with the temperature not dependant on the photon flux.

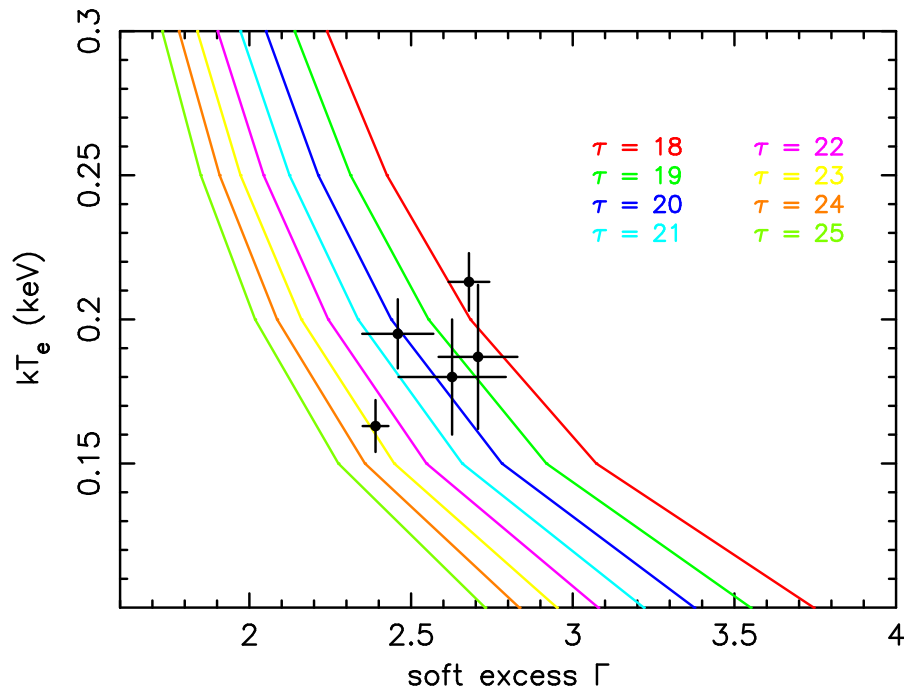


FIGURE 4.27. The plot shows the variation of the temperature and slope of the soft excess, for lines of constant optical depth. The points shown are the actual values obtained from the *thComp* fit to the soft excess of PKS 0558–504 for each revolution of data.

keeping the optical depth constant. To this end, curves of constant optical depth were plotted on kT - Γ axes, and the actual measurements superimposed; this is shown in Figure 4.27. Whereas for 3C 273 (Fig. 4.13) there was a clear value of τ which was consistent, within the error bars, with all the measured points, here it is not quite so obvious. The weighted mean of the measured values is ~ 19.5 , which places the corresponding curve of constant optical depth between the green and blue lines.

If the optical depth is assumed to remain constant, at $\tau = 19.5$, the corresponding range of temperatures can be determined, by overlying the kT - Γ curve formed by keeping the optical depth fixed on the contour plot for each observation. Figure 4.28 shows an example. Reading off where the curve crosses the 95% (green) contour produced the temperature error bars plotted in Figure 4.29; however, this unfortunately does not clarify the results, showing neither a strong cooling nor heating effect. This indicates that the assumption of a constant optical depth may not be suitable for PKS 0558–504, as Figure 4.27 implied.

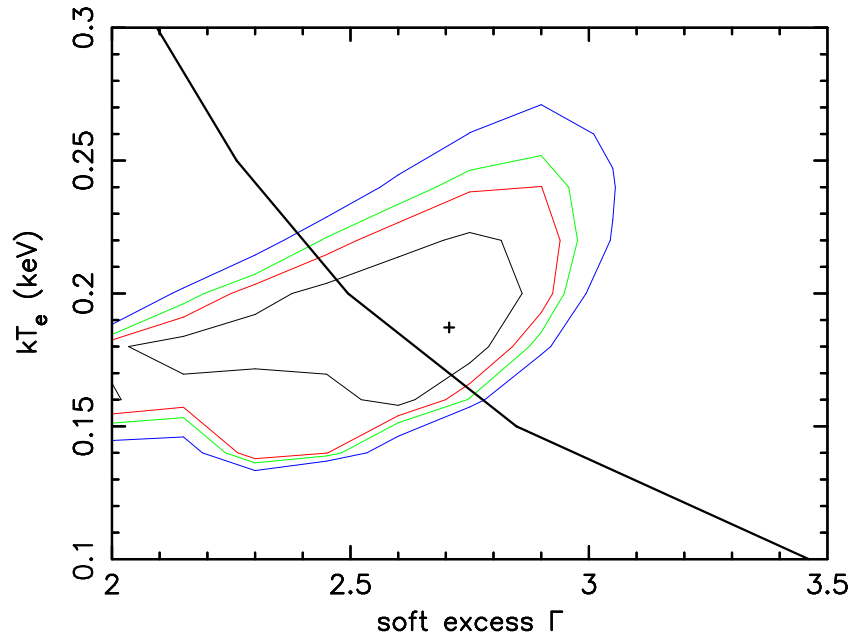


FIGURE 4.28. Superimposing the curve signifying $\tau = 19.5$ on the contour plots allows a range of consistent temperatures to be read off. This plot shows the data from revolution 341, with contours signifying 68, 90, 95 and 99% confidence.

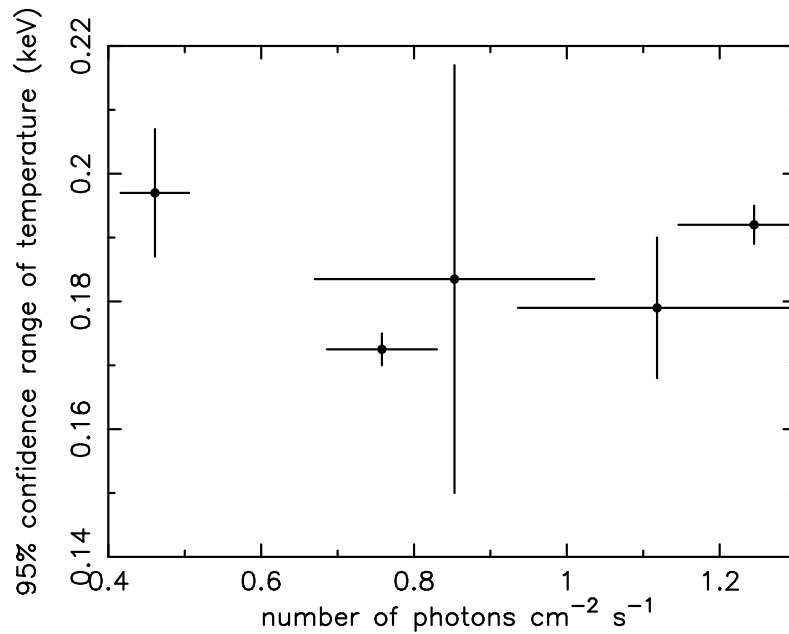


FIGURE 4.29. Contrary to the result found for 3C 273 (Fig. 4.15), setting the optical depth to a constant value does not clearly show a Compton cooling effect.

To investigate the link between the cool and hot Comptonised components, Figure 4.30 was plotted. Although there appears to be some degree of correlation, it can be seen that the soft excess component does not vary exactly with the ‘power-law’ component. It is particularly noticeable that, between revolutions 283 and 341, the soft excess luminosity decreases, but the harder component more than doubles in luminosity. It is this difference which results in the soft excess being very weak during this last observation. An alternative way to compare the two components is by plotting their respective luminosities and slopes against each other; these results are shown in Figure 4.31. Here it is found that there is a weak negative correlation between the slopes (-1.01 ± 0.27 via linear regression; only 13% from Spearman Rank), with the steepest soft excess corresponding to the flatter (harder) continua at higher energies. This is the opposite of what is seen in 3C 273, when the slopes change in the same sense, implying that the hotter electron population may be being cooled. The luminosities are also related, although this time the components vary together (0.59 ± 0.08 ; 39%). Neither of these correlations is statistically significant when considering the Spearman Rank, however. To be certain of either of these relationships, more observations of PKS 0558–504 need to occur, since five is a small sample on which to be basing deductions.

To conclude the comparison with 3C 273, it is noted that the 2–10 keV photon index does not depend on the flux over that same band, as shown by Figure 4.32. This independence has been found for 3C 273 in the past (Turner et al. 1990; Kataoka et al. 2002), although the *XMM* data presented here show the slope hardening as the flux increases.

4.2.7 Conclusions: PKS 0558–504

Spanning a period of just over a year and a half, the soft X-ray excess of PKS 0558–504 has been analysed. It is found that the spectrum can be well modelled by multiple black-body components or by a more physical model consisting of two Comptonisation components, one fitting the soft excess and the other the apparent power-law. It cannot be determined whether the changes observed are due solely to Compton cooling, or if the optical depth of the corona is also changing. It can, however, be concluded that the spec-

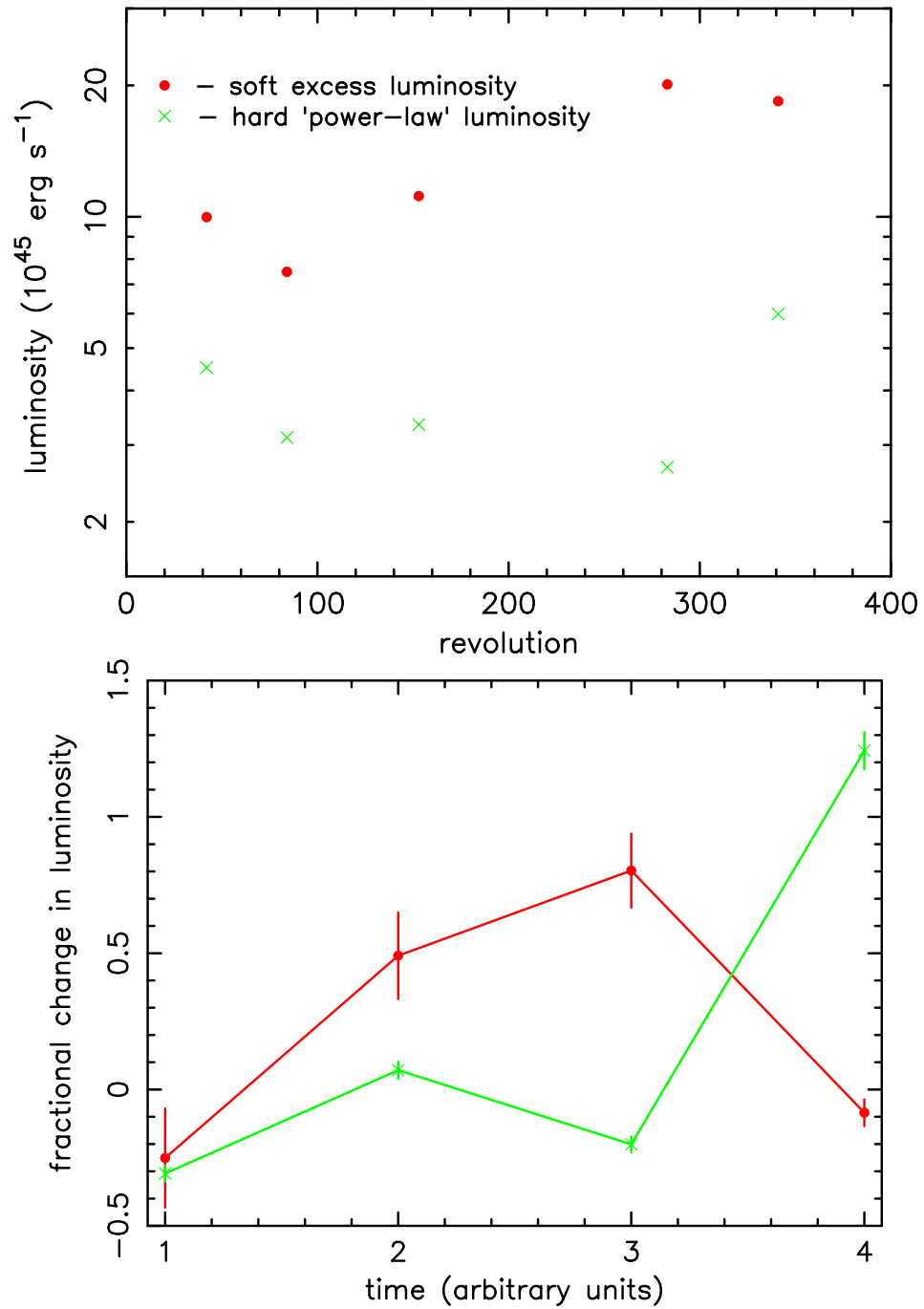


FIGURE 4.30. Although the soft and hard components do not mirror each other precisely, there is a similarity in the variation of the luminosities of the components, particularly during the earlier observations.

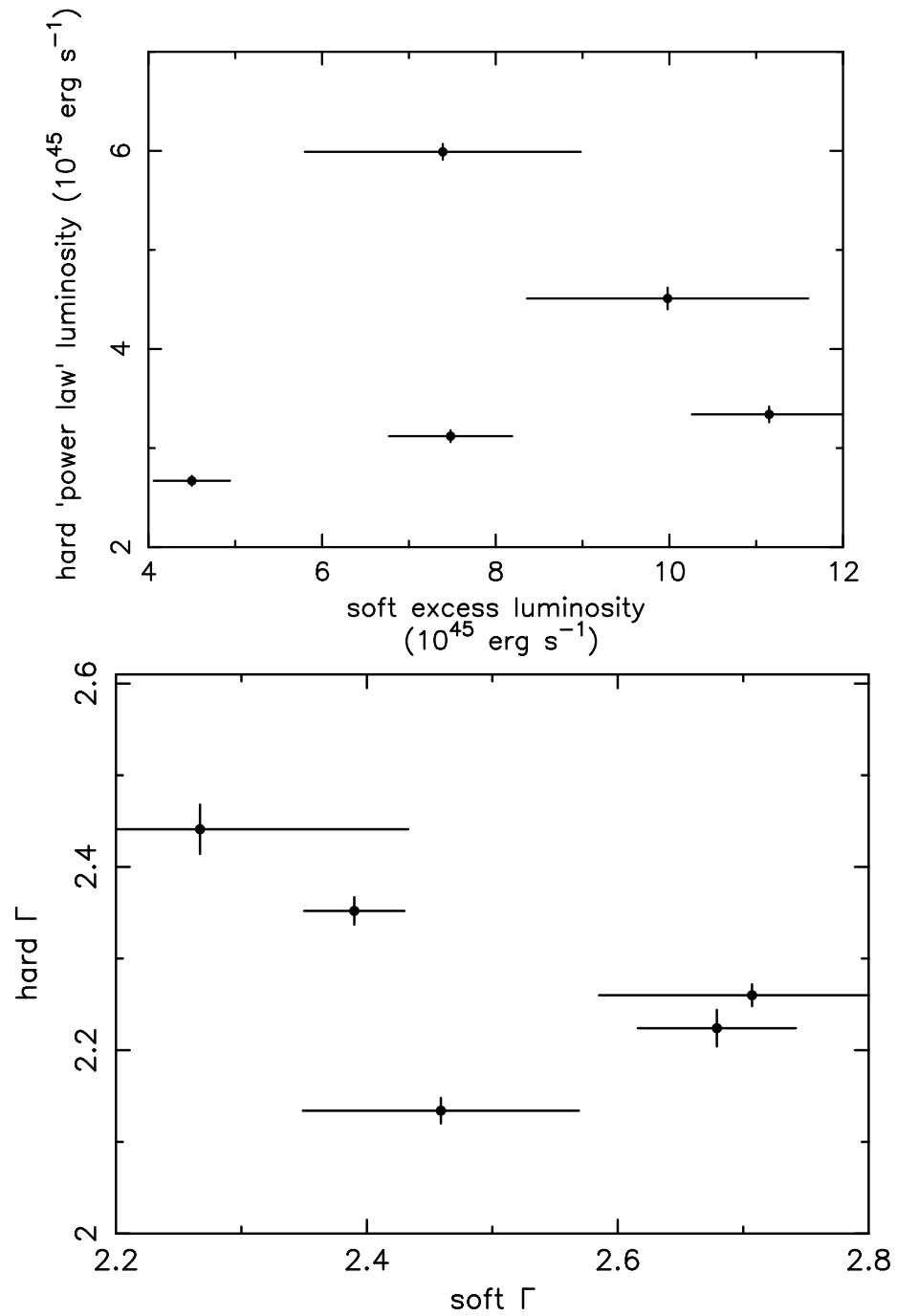


FIGURE 4.31. From weighted linear regression, there is a slight positive correlation between the luminosities of the hard and soft Comptonised components, but a weak negative correlation between the corresponding slopes.

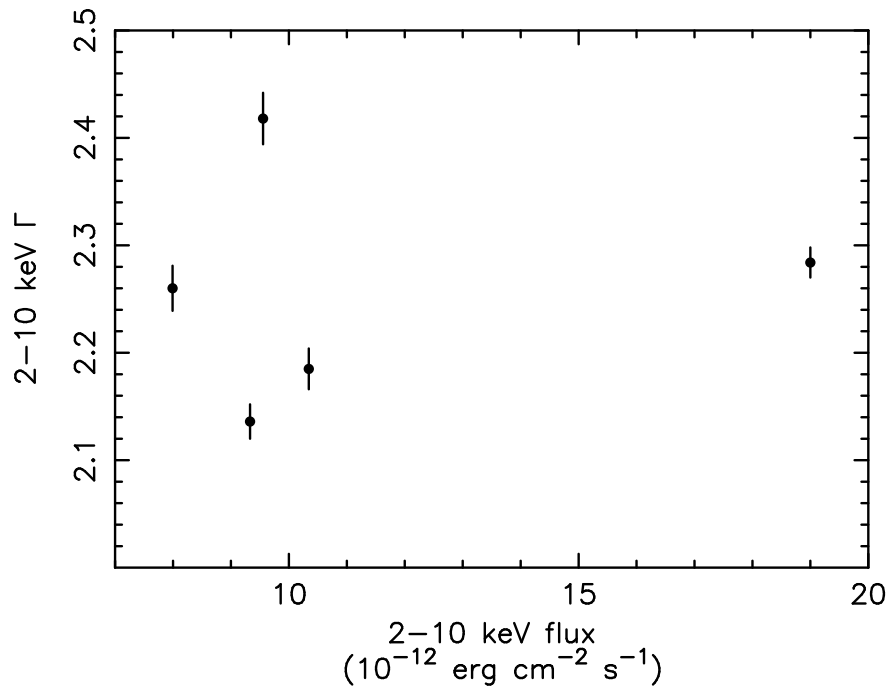


FIGURE 4.32. The 2–10 keV band power-law slope is independent of the flux level.

trum changes between a soft and bright state and a correspondingly fainter and harder one. In this respect, the spectra are very similar to those observed in 3C 273 (Section 4.1).

There is some evidence for a broad, ionised iron line in some of the observations, namely those when the 2–10 keV slope is steepest and, correspondingly, the soft excess is at its strongest. There is, however, no sign of a neutral, narrow line, tying in with the evidence (Chapter 6) that such lines become much weaker in high luminosity objects.

4.3 1H 0419–577

4.3.1 Introduction

1H 0419–577 (also known as LB 1727, 1ES 0425-573 and IRAS F04250-5718) is a radio-quiet Seyfert galaxy, with a $60\mu\text{m}$ flux of 0.18 Jy and an apparent magnitude of 14.1. It is a moderate redshift object ($z = 0.104$) and relatively bright X-ray source, which has been observed over recent years by *ASCA*, *ROSAT* and *BeppoSAX*. 1H 0419-

577 was also one of the brightest Seyfert galaxies detected in the extreme ultra-violet by the *ROSAT* Wide Field Camera (Pye et al. 1995) and *EUVE* (Marshall, Fruscione & Carone 1995). Optical spectra taken over the same period in 1996 as the *ASCA* and *BeppoSAX* X-ray observations (Guainazzi et al. 1998) show 1H 0419-577 to be a typical broad-line Seyfert 1, in accordance with the classification by Brissenden (1989).

As discussed in Chapter 1, over the 2–10 keV band Seyfert galaxies can usually be modelled by a power-law, with photon-index $\Gamma \sim 1.8 - 2$. Below ~ 2 keV a ‘soft excess’ is often reported, although the limited bandwidth and resolution of previous missions have made it difficult to distinguish a soft *emission* component from the effects of absorption by ionised matter. In the case of 1H 0419-577, Turner et al. (1999) did conclude that there is soft emission on the basis of simultaneous *ROSAT* HRI and *ASCA* observations. However, those authors found the 2–10 keV power-law to be unusually flat, with $\Gamma \sim 1.5 - 1.6$, and to extend down to 0.7 keV. The *BeppoSAX* observation of 1H 0419–577 in 1996 September (Guainazzi et al. 1998) also found an unusually flat power-law (over 3–10 keV) of $\Gamma \sim 1.55$, but provided no independent soft X-ray data, due to technical problems with the Low Energy Concentrator Spectrometer (LECS).

The link between the hard X-ray power-law and a soft X-ray emission component is critical in the context of the accretion disc/corona model for AGN, where the hard X-ray emission is explained by Comptonisation of optical/EUV photons from the disc by energetic electrons in an overlying corona (e.g., Haardt & Maraschi 1991). In this model the energy balance between the soft photon flux and the corona then determines the hardness of the spectrum in the 2–10 keV band. As mentioned in Chapter 1, the soft excess may be the Comptonised tail of the Big Blue Bump, representing the thermal emission from an accretion disc surrounding the central black hole (Shields 1978; Czerny & Elvis 1987; Ross & Fabian 1993).

In previous observations of 1H 0419-577, Turner et al. (1999) found evidence for an iron emission line in the *ASCA* data at 6.39 keV, with equivalent width (EW) of 700 ± 400 eV (data from August 1996). A line is not detected in the *SAX* data (Guainazzi et al. 1998), but with a rather high upper limit of ~ 250 eV for the equivalent width.

4.3.2 XMM-Newton observations

The *XMM-Newton* observation of 1H 0419–577 took place on 2000-12-04 and lasted for just over 8 ks. Because of a co-ordinate error, X-ray data were only obtained from the EPIC PN camera.

The PN data were reduced with the *XMM SAS*, following the procedure outlined in Chapter 1, Section 1.5, except that the spectrum was extracted within a box-shaped region of size 20 by 10 pixels, which corresponds to 87×43.5 arcsec; this was due to the close proximity of the source to a chip gap in the CCD.

4.3.3 Spectral analysis

Since no significant changes occurred in the X-ray flux over the 8000 second observation, the summed data were used in modelling the spectrum. First, as usual, a single absorbed power-law (N_H fixed to the Galactic value of $2 \times 10^{20} \text{ cm}^{-2}$) was tried, but found to be a very poor fit across the full 0.2–10 keV band ($\chi^2_\nu = 1409/712$), mainly due to a strong upward curvature in the measured spectrum. Constraining the model to the 2–10 keV band, however, provided a good fit, for a photon-index $\Gamma \sim 1.88$, with $\chi^2_\nu = 325/349$. A Gaussian component was then added to the model, as per the procedure the Chapters 2 and 3, but yielded no significant detection of either a narrow or a broad Fe line. At a rest energy of 6.4 keV (appropriate to neutral iron emission), the equivalent width of a narrow line ($\sigma = 10 \text{ eV}$) was $< 85 \text{ eV}$, while for a broad neutral line ($\sigma = 300 \text{ eV}$; this was chosen to be consistent with the value found by Turner et al. 1999) the upper limit was $< 130 \text{ eV}$. For an ionised line at 6.7 keV the corresponding broad line limit was $< 120 \text{ eV}$. It is noted that these upper limits are consistent with the weak Fe emission lines detected in objects of similar luminosity (Reeves et al. 2001; Pounds et al. 2001).

As found in all the objects in the previous chapters, extrapolating the above 2–10 keV power-law fit down to 0.2 keV revealed a strong and broad (‘hot’) soft excess (Fig 4.33). The soft excess was then modelled as usual by the addition of blackbody emission, the breadth of the excess requiring three blackbody components to match the observed spectrum (Fig 4.34). Details of this fit are given in Table 4.10. The soft excess has no

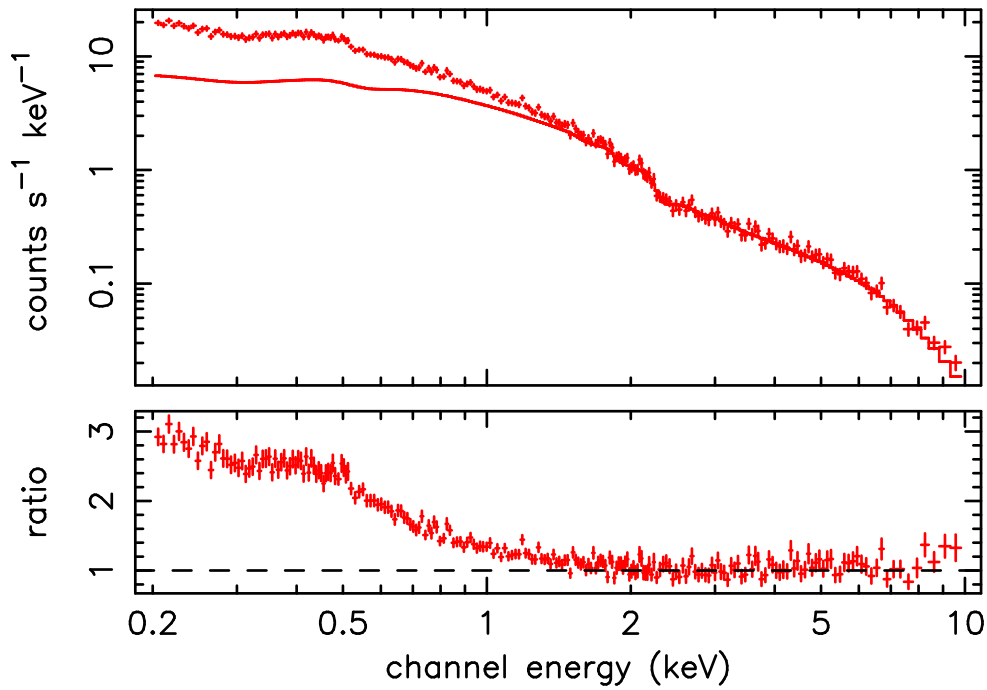


FIGURE 4.33. 2–10 keV power-law fit to the PN spectrum, extrapolated down to 0.2 keV, showing the soft excess of 1H 0419–577.

obvious superimposed absorption features, the limits for the optical depths of the O VII and O VIII edges being $\tau < 0.12$ and $\tau < 0.06$ respectively. A small excess of counts at ~ 0.55 keV could be a calibration residual, although emission from the O VII triplet has been previously identified, close to this energy, in objects of similar luminosity [e.g., Mrk 359 (O’Brien et al. 2001a); Mrk 509 (Pounds et al. 2001)]. Without the benefit of RGS data, this could not be investigated further.

The measured flux of 1H 0419-577 over 2–10 keV was 1.12×10^{-11} erg cm $^{-2}$ s $^{-1}$, corresponding to a luminosity of 5.67×10^{44} erg s $^{-1}$, with a flux of 2.88×10^{-11} erg cm $^{-2}$ s $^{-1}$ over the full 0.2–10 keV band (1.91×10^{45} erg s $^{-1}$), including the strong soft excess.

4.3.4 Comparison with other observations

The *XMM-Newton* spectrum of 1H 0419-577 is, on its own, unremarkable, being very similar in overall continuum shape to the *XMM* observations of comparably high-luminosity Seyfert 1 galaxies (see Chapter 2). However, the spectrum is dramatically different from

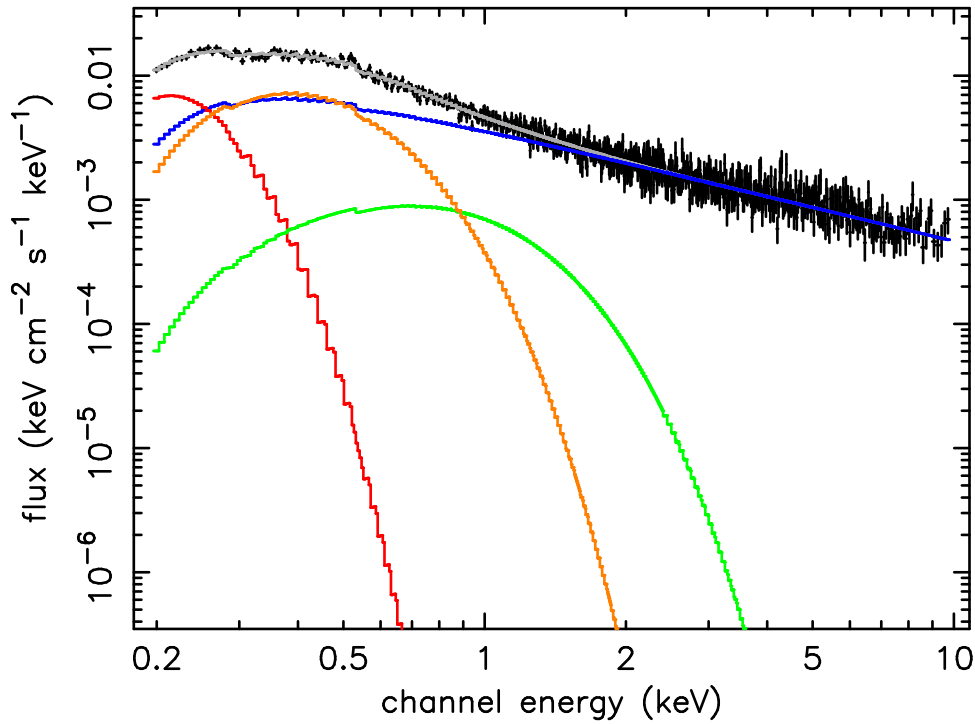


FIGURE 4.34. Unfolded plot of the best fit to the *XMM* data. The model consists of a power-law ($\Gamma = 1.88$) and three blackbody components ($kT = 31$ eV, 110 eV and 252 eV).

Table 4.10. Fits to the *XMM-Newton* data from 2000 December.

range (keV)	model	Γ	kT (keV)	χ^2/dof
2–10	PL	1.88 ± 0.03	—	325/349
0.2–10	PL+BB	2.05 ± 0.01	0.108 ± 0.002	839/710
0.2–10	PL+2BB	1.99 ± 0.02	0.033 ± 0.002 0.121 ± 0.003	767/708
0.2–10	PL+3BB	1.88 ± 0.04	0.031 ± 0.002 0.110 ± 0.005 0.252 ± 0.030	734/706

the several observations in 1996, which show a much flatter 2–10 keV continuum and weaker soft excess. To confirm this spectral change, the data from those previous missions were re-examined consistently, beginning with the *ROSAT* PSPC observation in 1992, then those of *ASCA* in July and August of 1996 (observation numbers 74056000 and 74056010) and in September of that year by *BeppoSAX*. The *ROSAT* HRI also monitored 1H 0419-577 simultaneously with *ASCA*, between 1996 June 30 and September 1. The data from these observations were retrieved from the LEDAS website¹, the Tartarus Database² and the *SAX* homepage³ respectively. Only the data from the SIS instruments on *ASCA* were used.

A power-law plus Galactic absorption was first fitted to the *ASCA* and *SAX* datasets over the 2–10 keV band. In each case the power-law slope was significantly flatter than the *XMM* measurement; details of these power-law fits are given in Table 4.11. It should be noted that the fits here cover the entire 2–10 keV band, whereas Turner et al. (1999) ignored 5.0-7.5 keV within this range, where iron emission would occur if present. If this region is ignored, then the *ASCA* slopes steepen by approximately 0.1, agreeing more closely with those derived by Turner et al. Interestingly, although the slopes are very different, the 2–10 keV flux remains essentially constant between the *XMM*, *ASCA* and *BeppoSAX* observations. This is a point also illustrated in Figure 4.35.

The PN spectrum was then re-fitted over the 0.5–10 keV *ASCA* band, so that the *ASCA* and *XMM-Newton* data could be compared directly. Over this band, the PN data are well fitted with a power-law and only two blackbody components. Each *ASCA* observation was then modelled in this way, with the BB temperatures and relative normalisations frozen to the values determined from the *XMM* data, since the soft excess is not well constrained for the *ASCA* datasets (Table 4.11). The 0.5–2 keV flux is a factor of ~ 3 higher in the *XMM-Newton* observation and the power-law is much steeper ($\Delta\Gamma \sim 0.4$). The power-law slope and soft excess change in the same sense, but to a lesser degree, between the two *ASCA* observations, with the soft flux increasing by 42% from July to August 1996 according to the model, in excellent agreement with the $\sim 40\%$ increase in

¹<http://ledas-www.star.le.ac.uk>

²<http://tartarus.gsfc.nasa.gov>

³<http://www.asdc.asi.it/bepposax>

Table 4.11. Fits to the *ASCA*, *SAX* and *XMM* data. ^f BB components frozen to PN values, with normalisations tied to the same ratio

mission	range	model	Γ	kT (keV)	χ^2/dof	flux ($\text{erg cm}^{-2} \text{s}^{-1}$)
<i>ASCA</i> (1996 July)	2–10 keV	PL	1.35 ± 0.05	—	162/134	9.32×10^{-12}
<i>ASCA</i> (1996 Aug.)	2–10 keV	PL	1.42 ± 0.06	—	91/140	1.13×10^{-11}
<i>SAX</i> (1996 Sept.)	2–10 keV	PL	1.63 ± 0.04	—	140/111	1.15×10^{-11}
<i>XMM</i>	0.5–10 keV	PL+2BB	1.87 ± 0.03	0.093 ± 0.006 0.225 ± 0.020	661/650	2.20×10^{-11}
<i>ASCA</i> (1996 July)	0.5–10 keV	PL+2BB	1.32 ± 0.03	0.093^f 0.225^f	222/185	1.27×10^{-11}
<i>ASCA</i> (1996 Aug.)	0.5–10 keV	PL+2BB	1.53 ± 0.03	0.093^f 0.225^f	143/191	1.61×10^{-11}

count-rate recorded by the *ROSAT* HRI data (Turner et al. 1999).

Since only the data from the MECS instrument onboard *BeppoSAX* were available, BB components could not be constrained for that observation. The power-law slope is 1.63 ± 0.04 , implying that the slope was continuing to soften, as hinted at between the *ASCA* observations.

To compare the flux between *ROSAT* and *XMM*, a simple power-law was fitted to the two datasets, over the range 0.2–2.0 keV, with N_H fixed to the Galactic value. For *ROSAT*, $\Gamma \sim 2.94$, while the PN slope was slightly less steep, at $\Gamma \sim 2.46$. This corresponds to a flux over the 0.2–2 keV band of $3.42 \times 10^{-11} \text{ erg cm}^{-2} \text{ s}^{-1}$ for *ROSAT*, compared to $1.76 \times 10^{-11} \text{ erg cm}^{-2} \text{ s}^{-1}$ as measured by *XMM*. It must be stressed that a single power-law is not a good fit to either the *ROSAT* or *XMM* data, both of which show evidence for a more complex soft excess. It has been noted by a number of authors (e.g., Turner 1993; Iwasawa, Brandt & Fabian 1998) that the *ROSAT* PSPC spectral indices are up to 0.4 steeper than those found from other missions. Allowing for these uncertainties,

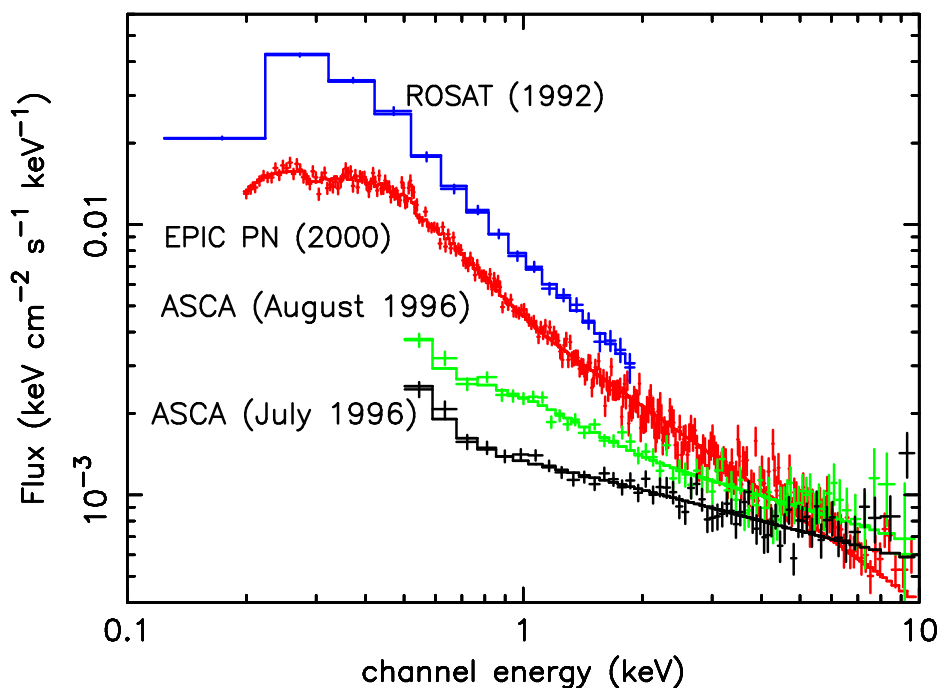


FIGURE 4.35. Plot showing the difference between the unfolded spectra for the *XMM*, *ASCA* and *ROSAT* observations. The model used was a power-law and 2 BBs. It can clearly be seen that the *ROSAT* and *XMM* datasets have steeper power-law slopes and stronger soft X-ray emission than the *ASCA* observations.

it is considered that the *ROSAT* PSPC observation of 1992 is consistent with the soft excess at that time being as strong as in the 2000 December *XMM-Newton* observation.

Tying this work in with the investigation in Chapters 2 and 3, together with the previous sections on 3C 273 and PKS 0558–504, the BB-power-law luminosity ratio was determined; here, the band used is 0.5–10 keV, because of the limitations enforced by the narrower *ASCA* bandpass. This ratio is plotted against both the 0.5–10 keV luminosity and the 2–10 keV photon index in Figure 4.36. Contrary to all the previous results, there is a correlation between the BB/ Γ ratio and the broad-band luminosity – the soft excess appears to be stronger when the source is more luminous. The lower plot, showing the ratio against the 2–10 keV power-law slope, also shows a positive correlation, but this is in agreement with the results for the Seyfert sample (of which 1H 0419–577 is a member; Chapter 2) and PKS 0558–504 (Section 4.2.3). It must be noted, however, that three results is far too small a group to base major conclusions on; when more observations of 1H 0419–577 have been obtained, and these plots added to and improved upon, then the possible correlations can be better investigated.

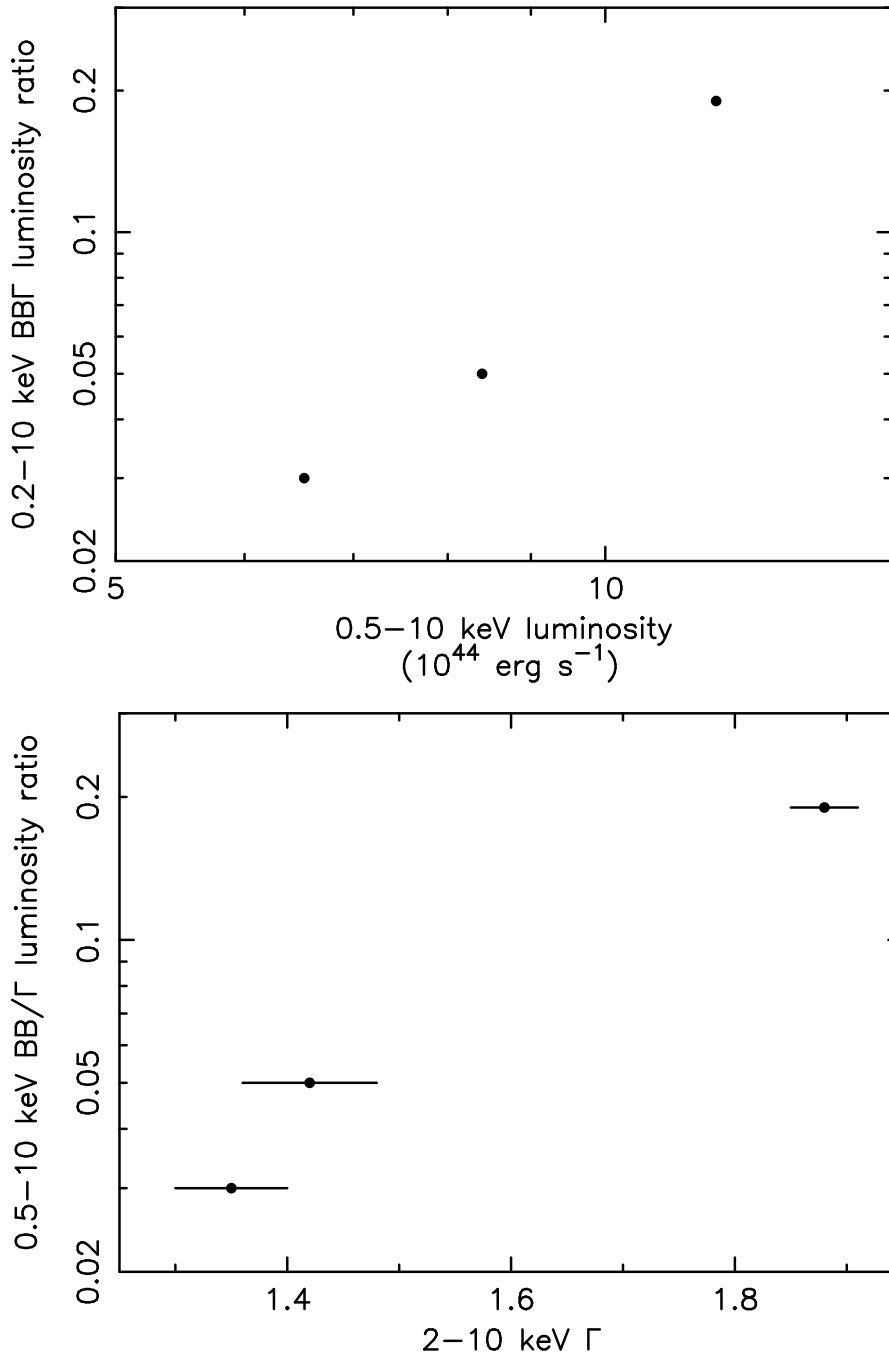


FIGURE 4.36. The plot shows the ratio of the BB and power-law luminosities against both the 0.5-10 keV luminosity and the 2-10 keV photon index. Both show a positive correlation.

The next step was to compare the *ASCA*, *SAX* and *XMM* data to search for neutral iron emission. No evidence for a narrow line ($\sigma = 10$ eV) was found in any of the observations. The July 1996 *ASCA* data gave an equivalent width of < 81 eV, very similar to our *XMM* upper limit. The August *ASCA* and September *BeppoSAX* data yielded upper limits of ~ 140 eV. Broad line fits (width 300 eV) also gave only upper limits of order < 350 eV for the July *ASCA* and September *BeppoSAX* data, while for the August *ASCA* data the fit did show a decrease in χ^2 of 7 for 1 additional degree of freedom (a confidence level of greater than 99%). This line, if real, has an EW of 335 ± 210 eV. Summarising, the August 1996 *ASCA* data suggest that a broad iron line may exist, although none of the other observations detected such emission.

It is known that the low energy response of the *ASCA* SIS has been degrading and that this leads to an underestimate of the soft X-ray flux. In order to estimate the decrease in the low energy efficiency of *ASCA* in the 1H 0419-577 observation, the formula given in the *ASCA* GOF Calibration Memo (Yaqoob et al. 2000), which quotes the effective increase in N_H as a function of time, was used. The net effect of this in the present fits is a change of $\Gamma \sim 0.05$ in the spectral slope. This does not, therefore, alter the conclusions about the change in state of 1H 0419-577 between the *ASCA* and *XMM* observations.

The Comptonisation model

As described above, the spectra of 1H 0419–577 have changed substantially over the years it has been observed. In order to quantify such a change, the *thComp* Comptonisation model was tried. As in previous chapters, photons are up-scattered by thermal electrons characterised by two temperatures, to yield the observed broad soft excess and the harder power law respectively. The temperature for the accretion disc photons was set to 10 eV, which is appropriate for a $\sim 10^8 M_\odot$ black hole; also, the hotter distribution was set to 200 keV as usual. Because the *ASCA* bandpass is not quite as wide as that for *XMM*, it was decided to tie the temperature of the input photons for the hotter (power-law) distribution to the temperature of the cooler (soft excess) electrons. (For the sample of Seyfert galaxies, similar in luminosity to 1H 0419–577, presented in Chapter 2, it was found that the photons forming the input to the hotter Comptonising distribution

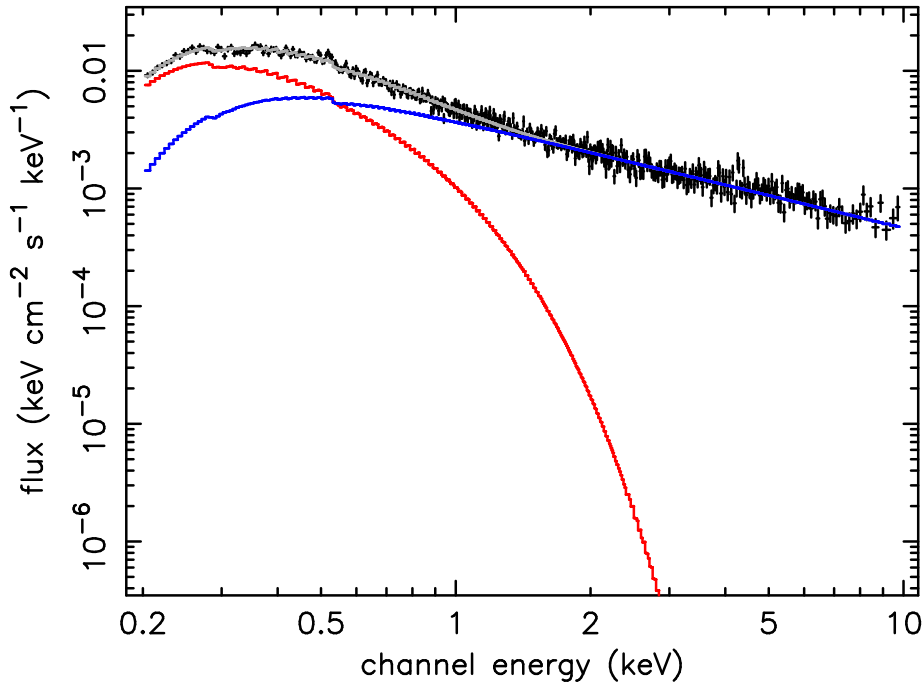


FIGURE 4.37. Best fit Comptonisation model for the EPIC PN dataset. Input photons at 10 eV are Comptonised by electron distributions of ~ 0.155 and 200 keV.

were closer in temperature to the soft excess than the accretion disc.)

For the *XMM-Newton* data an acceptable fit was obtained ($\chi^2_\nu = 1.04$) across the 0.5–10 keV band, with a cooler component of 0.155 ± 0.01 keV ($\tau = 23 \pm 1$), together with a ‘hot’ component with slope 1.93 ± 0.019 ; the fit is shown in Figure 4.37. The same double Comptonisation model was then compared with the *ASCA* data from the 1996 July and August observations. The July data were fitted with a soft excess electron temperature of 0.741 ± 0.279 keV and optical depth of 12 ± 4 ; the hard power-law was much flatter than for the PN observation, with $\Gamma = 1.16 \pm 0.15$. The August dataset showed a slightly cooler temperature, of 0.591 ± 0.201 keV ($\tau = 13 \pm 4$; $\Gamma_{hard} = 1.19 \pm 0.21$).

4.3.5 Discussion

Soft excess

In order to compare with 3C 273 and PKS 0558–504, the slope of the soft excess was plotted against the photon flux over both the 0.5–10 keV and the extrapolated 1 eV–

10 keV bands (Figure 4.38). Here it is found that the flux over both energy bands is positively correlated with the slope; that is, the steeper soft excesses are more luminous over both the limited *XMM* bandpass and the extrapolated one. This is somewhat different from the results for 3C 273 and PKS 0558–504, where only the extended band showed a positive correlation, though the over-all effect is the same. This is discussed in Section 4.4 below.

Figure 4.39 plots both the coronal electron temperatures and the high energy power-law for the three observations against the number of photons over 1 eV–10 keV; the effect of Compton cooling can clearly be seen, with an excess of photons corresponding to a cooler soft excess. At the same time, the presence of more soft excess photons means that the hotter electron population is also affected, since these photons form the input to produce the power-law at higher energies.

Broad-band spectrum

This *XMM-Newton* observation of 1H 0419-577 found the source in a bright/soft state. The overall 0.2–10 keV spectrum is very similar to that of other Seyfert galaxies observed with *XMM-Newton* (see Chapter 2), exhibiting a typical 2–10 keV power-law slope and strong soft excess. However, the new observation of 1H 0419-577 contrasts markedly with both *ASCA* and *BeppoSAX* spectra obtained in 1996, where the 2–10 keV continuum was significantly flatter, and the soft excess much weaker. It is suggested that the strong soft excess in this *XMM* observation is the key to the overall spectral change, with increased cooling of the coronal electrons yielding a steeper/softer hard power-law component. Interestingly, it seems possible that this effect was already apparent between the two *ASCA* observations a month apart in 1996, with an increase in the *ROSAT* HRI flux of at least 40%, and the best fit 2–10 keV power-law slopes increasing from 1.35 ± 0.05 to 1.42 ± 0.06 (see also Turner et al. 1999). If the 2000 December spectral state is considered ‘normal’ for a BLS1 then, in the framework of the disc/corona model, the unusually flat/hard 2–10 keV continuum in the 1996 observations can be attributed to a lack of soft photons (‘photon starved’ Comptonisation).

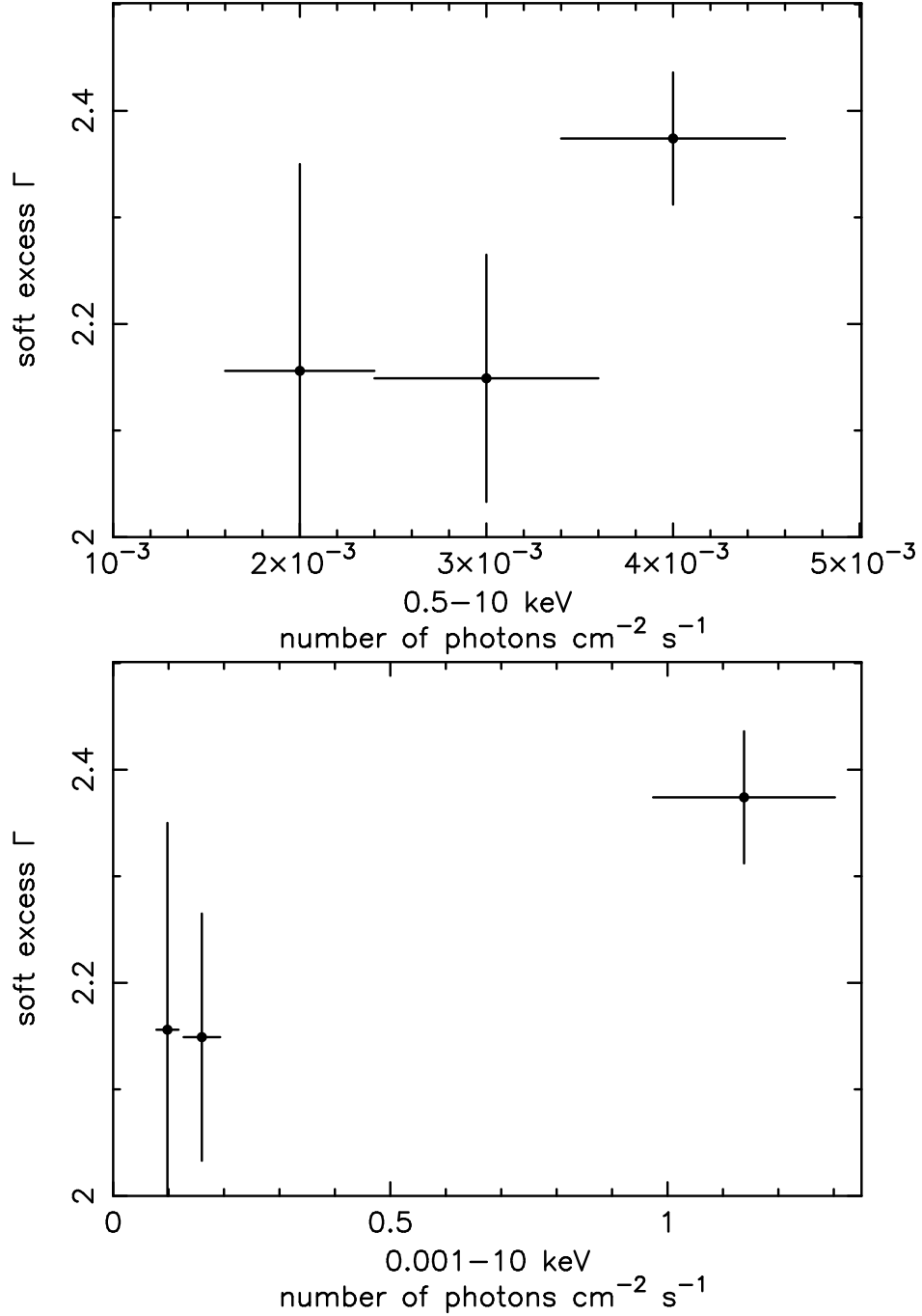


FIGURE 4.38. This plot shows the soft excess slope plotted against the flux of photons over the 0.5–10 keV and 1 eV–10 keV bands; both show positive correlations.

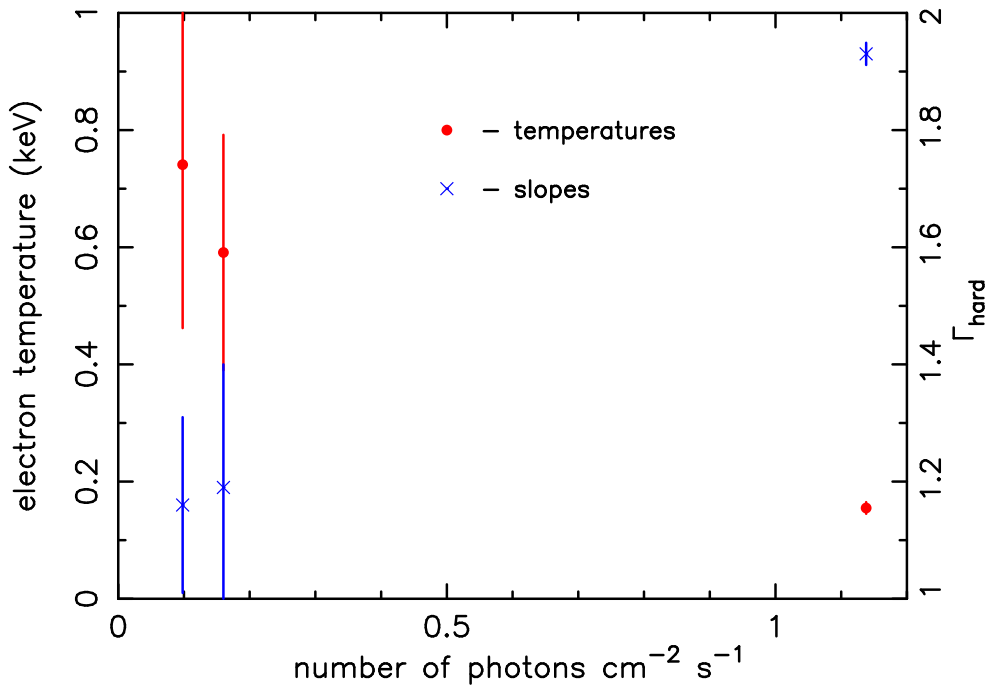


FIGURE 4.39. Comparing the data from *ASCA* observations in 1996 and *XMM* in 2000, the electron corona producing the soft excess can be seen to be cooler in the presence of more seed photons. Likewise, the slope at higher energies becomes steeper/softer.

While the individual parameters should not be taken too literally, since there is a close coupling of temperature and optical depth, the Comptonisation fits support the view that the cooling of the Comptonising electrons, between the 1996 and 2000 observations of 1H 0419-577, follows an increase in photon flux; this also causes the steepening/softening of the power-law over 2–10 keV, due to a cooling of this hotter electron population as well. This is consistent with the much stronger soft X-ray flux detected in the *XMM-Newton* observation and is similar to the results found for 3C 273 and PKS 0558–504.

Finally it is noted that the relatively short exposure of the *XMM* observation means that the limits on the Fe K lines are not very severe. However, it might be expected that any broad line would be weakened if the disc had an optically thick, ionised skin, as the Comptonisation model suggests.

4.3.6 Conclusions: 1H 0419–577

A measurement of the X-ray spectrum of the luminous Seyfert 1 galaxy 1H 0419-577 with *XMM-Newton* has shown it to have a strong soft excess and ‘normal’ power-law slope. A comparison with archival data shows the 2–10 keV continuum to have been much flatter in 1996, together with a far weaker soft excess. The broad-band spectrum can be parameterised by two or three blackbody components; alternatively, a two-temperature Comptonisation model describes the *XMM-Newton* observation well, with the hard continuum seen by *ASCA* in 1996 explained as being due to ‘photon starving’ of the hotter electron component. Comparing the luminosity of the soft excess with the slope defining it, the emission is at its brightest when the slope is steepest, as for 3C 273 (Section 4.1) and PKS 0558–504 (Section 4.2).

No iron line was found, but the upper limits are consistent with the Fe-K emission found in *XMM-Newton* observations of objects of similar luminosity (see Chapter 2).

4.4 Summary

This chapter has studied how the soft excesses of three objects – 3C 273, PKS 0558–504 and 1H 0419–577 – vary over time. Although, at the time of writing, only a single *XMM* observation of 1H 0419–577 has been analysed, the resulting spectrum has been compared to previous *ASCA*, *ROSAT* and *BeppoSAX* data. (During the AO-2 series of observations, *XMM* is conducting a monitoring campaign of 1H 0419–577, to investigate the changes presented here.) There are multiple *XMM* observations of both 3C 273 and PKS 0558–504 (ten and five, respectively), allowing an in-depth study of the soft excess using data from just one X-ray observatory.

Of these three objects, 3C 273 is the most luminous (0.3–10 keV luminosity of $\sim 2 \times 10^{46}$ erg s⁻¹), with the 0.2–10 keV luminosity of PKS 0558–504 being $\sim 5 \times 10^{45}$ erg s⁻¹ and 1H 0419–577 being almost an order of magnitude fainter again, at $L_{0.5-10} = 6 \times 10^{44}$ erg s⁻¹. 3C 273 and PKS 0558–504 are both classed as radio-loud quasars, while 1H 0419–477 is a Broad-Line Seyfert 1 galaxy (and, hence, radio-quiet).

All three objects have strong soft emission, which – as was found in Chapters 2 and 3 for larger samples – can be well fitted as either a combination of different temperature BBs or by a Comptonisation model. Each object shows some evidence for the existence of Compton cooling of the soft excess, possibly combined with a decrease in optical depth in 3C 273 and PKS 0558–504. The overall effect is that the soft excess slope becomes steeper.

For the brighter two objects it is found that the energy range over which the flux is measured affects the outcome of the correlation with the slope of the soft excess. When calculating the photon flux over the limited *XMM* bandpass, be it 0.2–10 or 0.3–10 keV, flatter/harder slopes correspond to the more luminous soft excesses. Upon extrapolation down to 1 eV, however, which includes the total extent of the soft excess model, it is found that the luminosity is higher for the *steeper* slopes. For 1H 0419–577 it is also found that the steeper soft excesses are more luminous, although this is found for both the 0.2–10 keV and the 1 eV–10 keV bands.

The change in energy of the ‘pivot point’ (below which the steep-soft correlation is observed) may be simply an artifact linked to the shape of the Comptonised component. Also, there are only three spectra being compared here. The correlation between soft excess slope and flux needs to be investigated for many more objects, covering a wide range of luminosities, to discover whether there really is a point about which the soft excess luminosity appears to pivot and, if there is, how its energy depends on the object in question. In order to do this, repeated *XMM* observations of various objects need to be performed.

Whatever the outcome of this further investigation, the fundamental result here appears to be that, when taking into account the full range of the soft excess model, the steeper components are more luminous. Since $\Gamma \sim 1/(kT \tau^2)$, the steeper slopes are likely to be due – at least in part – to the cooling of the Comptonising electrons.

If the luminosity of a given object changes, then it is probable that this is due to the accretion rate altering, since $L_{acc} = GM\dot{M}/r$, from Equation 1.4; the black hole mass is not likely to change substantially over such short timescales. From Chapters 2 and 3 (Figures 2.14 and 3.7), it is known that the brighter soft excesses are found in the more

luminous objects and, above, it is found that the brighter soft excesses are parameterised with steeper slopes; this softening is likely to be due to a Compton cooling effect. Drawing this together, for a single object, a higher accretion rate leads to a more luminous object; this, in turn, implies the soft excess will be brighter and, hence, steeper, corresponding to a cooler electron population. That is, if the accretion rate of an object increases, the soft excess gets steeper and cooler.

The possible presence of an iron line could not be thoroughly investigated in the spectrum of 1H 0419–577, due to the short duration of the observation. However, neither 3C 273 nor PKS 0558–504 show evidence for strong emission; as is discussed later, in Chapter 6, this is often the case in high luminosity objects such as these.

4.5 Caveat

After the completion of this thesis, ongoing calibration work on the EPIC MOS instruments led to a new response matrix being tested. It was found that, using this updated response, the results for 3C 273 were somewhat altered from those presented here, changing some of the conclusions. A quick check of the PKS 0558–504 and 1H 0419–577 data revealed that the new calibration did not affect those fits substantially. The new work on 3C 273 has been submitted to MNRAS (Page et al. 2003b) and is currently (October 2003) being refereed. The new results, based on the fits with the updated response, are briefly summarised here.

- It was decided that both MOS and PN data should ultimately be used. It is true that the systematic errors will dominate the statistical ones, but it is not known for certain which of the EPIC instruments is ‘more correct’. Hence, the decision was made to perform joint fits, which would – hopefully – help to average out some of the errors.
- The apparent ‘pivot point’ (Figure 4.10) is no longer found. Because of this, there is no longer a positive correlation between the soft excess Γ and the photon flux over 0.001–10 keV (Figure 4.12)

- There is no longer any evidence for Compton cooling. Instead, there is a *slight* positive correlation between temperature and flux, implying that there may be a more complicated link between the disc emission and the energising of the Comptonising electrons. It must be noted, however, that this correlation is not very strong and may just be an artifact of the fitting. Whichever of these results is the case, it can be concluded that the previous evidence for Compton cooling disappears with the new calibration of the MOS instruments.

Chapter 5

X-ray selected AGN

As has already been mentioned, the majority of luminous AGN are found to be radio-quiet (e.g., Kulkula et al. 1998). Since radio-quiet QSOs are, in general, less X-ray luminous than the radio-loud objects, they are more difficult to detect at higher redshifts, so the majority of distant QSOs studied so far in the X-ray band are radio-loud. One method of increasing the number of high- z radio-quiet objects observed is to make use of the field sources in deep observations taken with a sensitive instrument, such as EPIC, on-board *XMM-Newton*. In this chapter, a study of the background field sources from two long EPIC observations is presented; for both fields optical identifications exist, so that the redshift and optical classification of each object are known.

Chapters 2 and 3 investigated the X-ray spectra – in particular, the soft excesses – in two samples of AGN. The Seyfert sample ranges in redshift between $z = 0.009$ and 0.104 , while the QSOs are generally more distant, with redshift values up to 1.77 , although all but two are at $z \lesssim 0.3$. The objects in this third sample tend to be at higher redshifts, with the most distant QSO being at $z = 3.023$. It must be borne in mind, however, that the data quality for these objects is not as good as for the AGN presented in the previous chapters.

What causes the differences between radio-quiet and radio-loud QSOs (RQQs and RLQs) is still not fully understood. Both black hole ‘type’ (i.e., Schwarzschild and the rotating Kerr holes) and mass have been theorised to lead to the radio-quiet/loud

dichotomy (e.g., Punsly & Coroniti 1990; Boroson & Green 1992; this was discussed in Section 1.2) – although the word ‘dichotomy’ may not be the correct term to use, since some surveys have indicated that there may be a continuous transition between the types and the lack of intermediate objects is purely a selection effect (e.g., Cirasuolo et al. 2003; Section 1.1.4). Whether or not the process is understood, there are a number of observational differences between the types, in wavebands other than the radio.

It was once thought that RQQs were only found in spiral galaxies, while the RLQs inhabited ellipticals. However, advances in observing capability now show that as many as 50% of the RQQs discovered may occur in ellipticals (e.g., Véron-Cetty & Woltjer 1990). RLQs, however, are almost exclusively found in bulge-dominated systems; that is, in ellipticals or early-type spirals (Falomo, Kotilainen & Treves 2001).

The *Einstein* IPC (Imaging Proportional Counter) data showed that radio-quiet and radio-loud quasars have different X-ray power-law slopes over the energy range 0.4–4 keV, with the RQQs being steeper (e.g., Wilkes & Elvis 1987). Follow-up with *ROSAT* (Brinkmann, Yuan & Siebert 1997; Yuan et al. 1998) confirmed these findings for the soft X-ray band and *Ginga* (Williams et al. 1992), *EXOSAT* (Lawson et al. 1992) and *ASCA* (Reeves et al. 1997; Reeves & Turner 2000) for the harder X-ray energies. This observed difference in slope ($\Delta\Gamma \sim 0.3$ over 2–10 keV – Lawson et al. 1992; $\Delta\Gamma \sim 0.5$ in the 0.2–3.5 keV band – Wilkes & Elvis 1987) may be due to an extra, hard X-ray component linked to the radio emission of RLQs; i.e., connected with the radio-jets.

Neither *Einstein* (Canizares & White 1989; Wilkes & Elvis 1987) nor *ROSAT* (Yuan et al. 1998) found any indication for excess absorption in radio-quiet QSOs. More recently, *Chandra* has surveyed RQQs out to redshifts of ~ 6.28 , still finding that there is no intrinsic absorption in the X-ray spectra (Bechtold et al. 2003). Yuan et al. (1998) also found that the mean spectral slope of nearby RQQs is consistent with that of more distant ($z > 2.5$) quasars, implying that X-ray spectral evolution may be unimportant in the radio-quiet objects, although Bechtold et al. (2003) find a suggestion – albeit not a strong one – that the most distant QSOs have flatter slopes. Their statistical analysis indicates that the photon index depends on both luminosity and redshift; however, compared to the number of objects observed at $z \lesssim 3$, there are very few results upon which to base

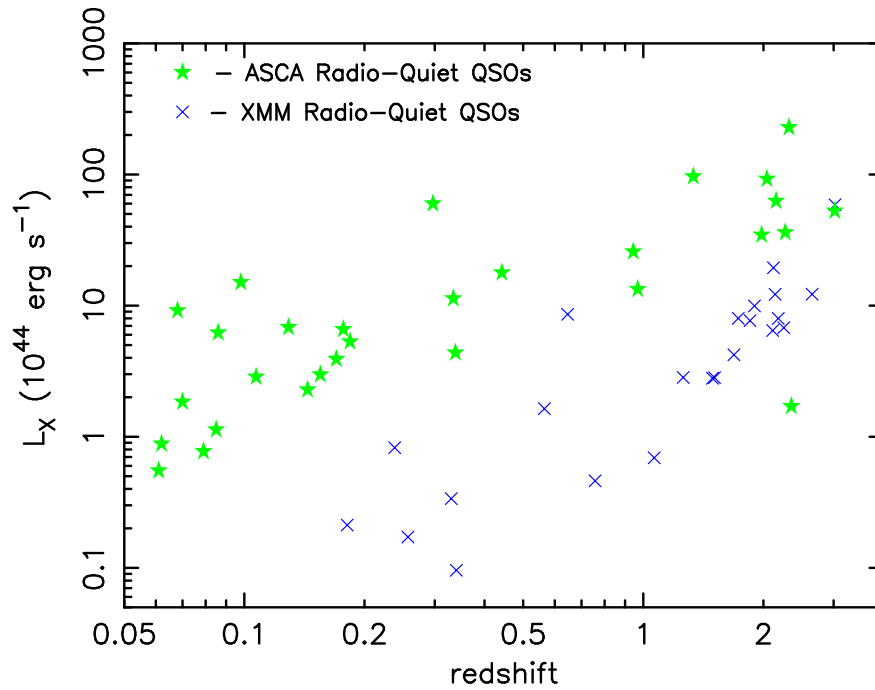


FIGURE 5.1. The 2–10 keV luminosities of radio-quiet objects are plotted against redshift. Measurements marked as stars are taken from Reeves & Turner (2000); crosses are from this work.

a conclusion. As the number of distant QSOs surveyed increases, such correlations will be able to be investigated further.

Because of the effective area of its mirrors (Section 1.4.1), *XMM-Newton* can obtain spectra of fainter objects for a given redshift than could any previous X-ray instrument. This allows the extension of previous surveys of QSOs to include those objects with lower luminosities and to observe a given luminosity at a wider range of redshifts. In this respect, the luminosities of the QSOs presented in this section (median value of $\sim 4 \times 10^{44} \text{ erg s}^{-1}$, mean of $9.66 \times 10^{44} \text{ erg s}^{-1}$; c.f. the mean luminosity of the QSOs in Chapter 3, $5.34 \times 10^{45} \text{ erg s}^{-1}$) are closer to those of the AGN which make up the cosmic X-ray background. Fig. 5.1 shows the luminosity distribution of radio-quiet objects surveyed by *XMM* in this chapter compared with those surveyed by *ASCA* in Reeves & Turner (2000). Comparing these luminosities with those in Chapters 2 and 3, it can be seen that the luminosity range for these RQQs is very similar to that for the Seyfert sample (Chapter 2); they are at the fainter end of the QSO luminosities.

5.1 XMM-Newton observations

The objects in this sample were serendipitously located in the fields of two *XMM* pointed observations: Mrk 205 and QSO 0130–403. The Mrk 205 data are from a calibration observation, in May 2000. There were three separate exposures with both the MOS and PN cameras, each of which lasted for ~ 17 ksec, and these were co-added before spectral analysis was performed. QSO 0130–403 was observed only once, for ~ 37 ksec, in June 2001.

The optical identifications and redshifts for the Mrk 205 field are taken from Barcons et al. (2002), which also quotes X-ray colours and fluxes. For the QSO 0130–403 field, the IDs were taken from the literature (Véron-Véron 1996 catalogue; Iovino, Clowes & Shaver 1996).

In general, one might expect that X-ray-selected targets (such as those in the Mrk 205 field) would show harder spectra than those found through optical observations (i.e., the QSO 0130–403 sample), simply because soft X-ray sources are not as easy to detect, due to Galactic absorption. Comparing both the slopes over 2–10 (rest frame) and 0.2–10 (observed frame) keV for the objects in the two separate fields, a mean difference of $\Delta\Gamma < 0.1$ is found. The actual range of photon indices is also very similar for both of the fields, with the vast majority ($\sim 80\%$) of the spectral slopes lying between $\Gamma \sim 1.6$ –2.4. The similarity in the distributions of indices implies that there is no obvious problem in combining these two fields.

The data obtained allow individual spectral fitting for the quasars in these fields. These spectra are presented and the sample investigated as a whole, to determine whether there is any evidence for evolution, Compton reflection or excess absorption in the rest frames of the objects.

Since the sources were not all close to the centre of the CCDs, *arfgen* was required, as is explained in Section 1.4. Using the *FTOOL* as usual, N_H was found to be $3 \times 10^{20} \text{ cm}^{-2}$ for the Mrk 205 field and $1.9 \times 10^{20} \text{ cm}^{-2}$ for the QSO 0130–403 field.

Of the 23 AGN in this sample, only two (XMMU J013257.8-401030 and XMMU

J013333.8-395554) have actual (upper limit) radio observations, of 0.4 mJy at 5 GHz (Miller, Peacock & Mead 1990). None of the others are detected in the NVSS (NRAO VLA Sky Survey), down to the survey completeness flux limit of about 2.5 mJy. Using this flux limit (and the two actual upper limits), we find that six of the AGN are definitely radio-quiet. Although the remaining seventeen objects could be radio-loud, it is found that (again using the NVSS survey limit) most would only be slightly so, with twelve having $R < 60$.

Statistically, one would expect $\sim 20\%$ of the BLAGN (with X-ray fluxes above 10^{-14} erg cm $^{-2}$ s $^{-1}$) in an *XMM* field to be radio loud (based on studies of sources within the *XMM* observation of the Lockman Hole; private communication, Lehmann 2002); this corresponds to ~ 4 objects in a sample of this size. However, as our survey does not go as deep as 10^{-14} erg cm $^{-2}$ s $^{-1}$, it should be expected that this is an upper limit to the number of radio-loud sources.

5.2 Spectral analysis

As in previous chapters, the spectrum for each source was first modelled using a simple power-law, together with neutral hydrogen absorption fixed at the Galactic value. The majority of sources were seen with both the MOS and PN, although the occasional source would be positioned in one of the chip gaps, or over a bad column. Where both MOS and PN CCDs could be used, joint fits were performed as usual. Table 5.1 lists the redshift (from Barcons et al. 2002 for the Mrk 205 field and NED for the objects around QSO 0130–403), count-rate, flux, luminosity and 2–10 keV (QSO rest frame) spectral slope (all derived from our data) for each of the 23 sources. All but three of the objects in this sample are Broad Line AGN (BLAGN). XMMU J122120.5+751616 and XMMU J122206.4+752613 are classified as Narrow Emission Line AGN (NLAGN) by Barcons et al. (2002), with XMMU J122258.1+751934 tentatively classified as the same. It should be noted that the optical spectrum for this last object is not of high quality and there is, therefore, some uncertainty in the given redshift of 0.257.

Over the 2–10 keV (rest-frame) band, the weighted mean of the photon index for

Table 5.1. QSOs with known redshifts in the fields of Mrk 205 and QSO 0130–403. The luminosities were calculated for $q_0 = 0.5$ and $H_0 = 50 \text{ kms}^{-1}\text{Mpc}^{-1}$ and both flux and luminosity are given over the rest-frame 2–10 keV band. Alternative names for the QSOs in the QSO 0130–403 field are given at the foot of the table. VV96 indicates the Véron-Véron catalogue (Véron-Cetty & Véron 1996); ICS96 is the Iovino, Clowes & Shaver catalogue (1996).

Source ID	z	0.2–10 keV count rate ¹ (10^{-3} s^{-1})	2–10 keV flux (10^{-14} $\text{erg cm}^{-2} \text{ s}^{-1}$)	2–10 keV luminosity ($10^{44} \text{ erg s}^{-1}$)	optical magnitude	2–10 keV rest frame Γ
XMMU J121819.4+751919	2.649	7.39 ± 1.10	1.49	12.20	19.79	2.05 ± 0.41
XMMU J122048.4+751804	1.687	13.01 ± 1.19	3.13	4.22	18.97	1.95 ± 0.36
XMMU J122051.7+752820	0.181	2.95 ± 1.11	1.32	0.21	22.05	1.64 ± 1.37
XMMU J122052.0+750529	0.646	65.75 ± 1.91	41.97	8.59	18.62	1.68 ± 0.10
XMMU J122111.2+751117	1.259	17.83 ± 1.17	2.56	2.83	19.54	2.13 ± 0.30
XMMU J122120.5+751616	0.340	16.28 ± 1.23	1.60	0.10	20.90	1.82 ± 0.44
XMMU J122135.5+750914	0.330	13.78 ± 1.15	5.85	0.34	20.38	1.26 ± 0.26
XMMU J122206.4+752613	0.238	115.2 ± 1.89	36.85	0.83	20.03	1.77 ± 0.77
XMMU J122242.6+751434	1.065	6.05 ± 1.14	0.35	0.69	21.82	2.61 ± 0.36
XMMU J122258.1+751934	0.257	12.86 ± 1.20	7.07	0.17	22.66	1.74 ± 0.29
XMMU J122318.5+751504	1.509	7.72 ± 1.13	1.70	2.82	21.15	1.43 ± 0.29
XMMU J122344.7+751922	0.757	9.87 ± 1.26	1.01	0.46	20.69	1.77 ± 0.59
XMMU J122351.0+752227	0.565	33.81 ± 1.71	10.17	1.64	19.93	1.72 ± 0.17
XMMU J122445.5+752224	1.852	9.68 ± 1.40	3.80	7.68	20.16	2.17 ± 0.36
XMMU J013302.0–400628 ^a	3.023	74.44 ± 1.89	7.63	58.77	17.4	2.10 ± 0.07
XMMU J013257.8–401030 ^b	2.180	17.96 ± 1.42	2.74	7.98	19.2	1.67 ± 0.23
XMMU J013314.7–401212 ^c	1.49	4.82 ± 0.43	1.09	2.80	19.0	2.27 ± 0.58
XMMU J013205.4–400047 ^d	2.12	25.82 ± 1.46	4.57	19.46	20.16	2.05 ± 0.16
XMMU J013348.3–400233 ^e	2.11	2.49 ± 0.37	3.68	6.46	20.3	3.48 ± 1.14
XMMU J013233.2–395445 ^f	1.73	3.14 ± 0.37	5.37	7.99	20.3	1.77 ± 0.38
XMMU J013333.8–395554 ^g	1.90	3.98 ± 0.41	3.52	9.95	19.8	2.21 ± 0.32
XMMU J013408.6–400547 ^h	2.14	17.06 ± 0.13	1.90	12.18	19.56	2.33 ± 0.25
XMMU J013320.4–402021 ⁱ	2.25	4.37 ± 1.06	3.87	6.78	20.5	1.37 ± 0.61

¹ PN count rate, unless MOS data only available.

^a QSO 0130–403; ^b [VV96] J013257.5-401028; ^c [VV96] J013315.2-401203; ^d [ICS96] 012953.4-401612; ^e [VV96] J013348.2-400235;

^f [VV96] J013233.2-395445; ^g [ICS96] 013122.7-401108; ^h [ICS96] 013157.1-402108; ⁱ [VV96] J013320.4-402022

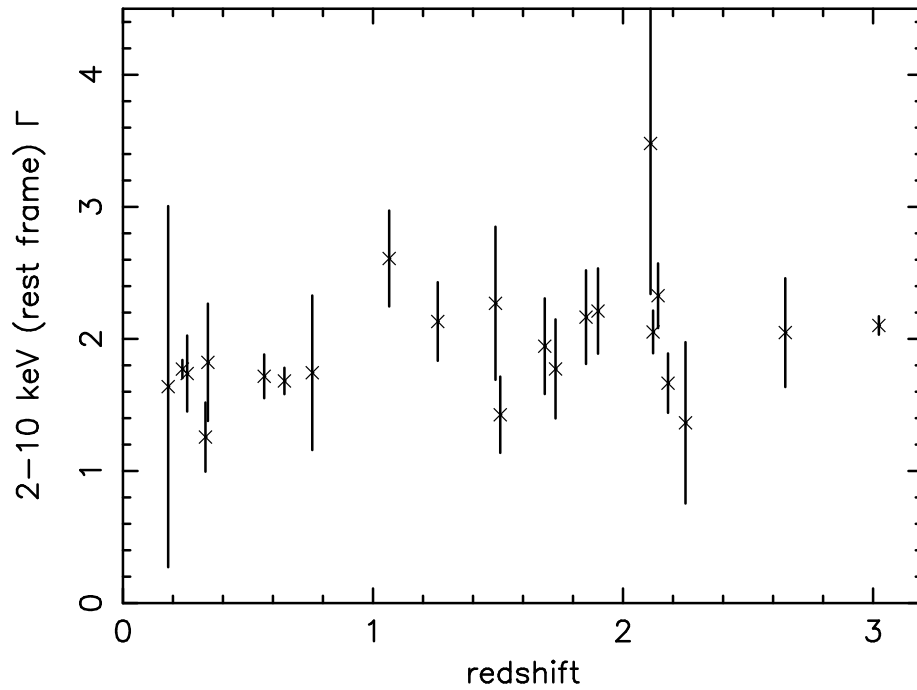


FIGURE 5.2. Plot of 2–10 keV Γ against redshift for each of the 23 sources.

all 23 objects was found to be $\Gamma = 1.89 \pm 0.04$. The dispersion of the slopes from the mean, taking into account the measurement errors, is $\sigma \sim 0.21$ (see Fig 5.2). Using the more rigorous Maximum Likelihood method (Maccacaro et al. 1988), the dispersion was calculated to be 0.29 ± 0.04 . The mean of the 2–10 keV photon index for the RLQs in Reeves & Turner (2000) is given as 1.66 ± 0.04 , while the RQQs had a mean Γ of 1.89 ± 0.05 . It can be seen that the *XMM*-observed radio-quiet objects presented here have a mean slope which is in excellent agreement with the higher flux objects measured by *ASCA* and that the radio-loud *ASCA* objects have a flatter index ($\Delta\Gamma \sim 0.2$), corroborating the known difference between radio-loud and radio-quiet QSOs found in previous surveys.

5.2.1 Soft excess and absorbing column density

For each source, a low-energy blackbody component was added, to see if there was a measurable soft excess; however, it was found that, statistically, only one of the sources required this addition: XMMU J122135.5+750914 was better fitted by the inclusion of

a blackbody component with $kT = 0.152 \pm 0.031$ keV. The luminosity of the soft excess component was $\sim 18\%$ that of the power-law. This is consistent with the relative luminosities calculated for the soft excesses in the Seyfert and QSO samples of Chapters 2 and 3.

Excess absorption in the QSO rest frame was also investigated, using the *zwabs* model in XSPEC to include a component in addition to the Galactic column density. Only three of the sources in the joint fields showed any improvement in the reduced χ^2 , one of which (XMMU J122344.7+751922) then gained an extremely steep ($\Gamma \sim 3.5$) spectral slope, for an excess absorption of $(2.27 \pm 1.06) \times 10^{21} \text{ cm}^{-2}$. The other two objects, both classed as NLAGN, were XMMU J122206.4+752613, with an improvement in χ^2 of 40, for one degree of freedom, for an additional column density of $(6.0 \pm 1.0) \times 10^{20} \text{ cm}^{-2}$ and XMMU J122258.1+751934, showing a decrease in χ^2 of six for one degree of freedom, for $N_H = (1.28 \pm 0.64) \times 10^{21} \text{ cm}^{-2}$. All three of these objects are of low luminosity.

Although the higher redshift objects appeared to show larger upper limits for the absorbing column density, it should be noted that this is likely to be related to the shift in energy bandpass. For an object at $z = 3$, the 0.2–10 keV observed band corresponds to 0.8–40 keV in its rest frame. It is, therefore, obvious that there will be increased difficulty in measuring moderately small absorption related to the softest X-ray photons and, so, a higher upper limit will be found compared to a source of the same flux at a lower redshift.

The photon index was then fixed to a typical value of $\Gamma = 1.9$ (e.g., Nandra & Pounds 1994), to see whether the apparent dispersion in Γ could be explained by excess absorption in the QSO rest frame; i.e., to see if any of the flat spectral slopes were due to the objects being obscured. The model comprised a direct, absorbed power-law, together with a scattered, unabsorbed component (both with $\Gamma = 1.9$). However, for ten of the objects in the sample, this produced a worse fit than that with no obscuration component and only four sources were significantly better-fitted using this model – the two NLAGN which required the *zwabs* column density, together with XMMU J122052.0+750529 and XMMU J122135.5+750914. The obscuring columns found for the NLAGN were

(2.40 ± 0.57) and $(1.75 \pm 1.57) \times 10^{21} \text{ cm}^{-2}$, while the BLAGN objects required (7.73 ± 4.88) and $(17.88 \pm 11.85) \times 10^{22} \text{ cm}^{-2}$ respectively. The remaining nine objects can be equally well fitted by either a simple power-law, or by including the obscured component. It should be noted that the objects with particularly flat spectral indices are all included in this group.

Although, statistically, these nine spectra can be fitted by the inclusion of an obscuring column density, the values for N_H are not well constrained and are entirely consistent with zero. This implies that the more complicated model is not required and that these QSO nuclei are not heavily absorbed, consistent with AGN unification schemes where one should observe a direct line to the nucleus in such objects (i.e., Type-1 AGN). To summarise, there appears to be an intrinsic dispersion in the primary X-ray power-law slopes of these background AGN, which cannot be solely caused by line-of-sight absorption.

In order to try and obtain better statistics for the fits, it was decided to co-add spectra over three redshift ranges ($z < 1$, $1-2$ and > 2) and look at the subsequent continuum shapes. For each grouping, an average background spectrum was produced and the mean redshift calculated. Although co-adding spectra will tend to blur sharp features, such as iron emission lines, this should not be a problem when simply looking at the continuum as a whole.

Only the resulting spectrum for the low-redshift group (mean $z = 0.4$) required excess absorption, with an additional column density of $(2.9 \pm 0.9) \times 10^{20} \text{ cm}^{-2}$ for $\Gamma = 1.83 \pm 0.03$. Such a column would be undetectable at higher redshifts, as it would be shifted out of the *XMM-Newton* bandpass. Even with the better statistics derived from the co-adding of the spectra, there was still no requirement for a soft excess component for either the low- or medium-redshift group, with the luminosity of the soft component being $<6\%$ of the total X-ray luminosity. For the highest-redshift objects, however, a blackbody does improve the fit: a temperature of $kT = 0.214 \pm 0.043 \text{ keV}$ leads to a reduction in χ^2 of 8, for 2 degrees of freedom ($>90\%$ confidence, using the F-test), with the luminosity of the BB component being almost 15% that of the power-law. However, as is discussed below, some of this spectral curvature could be due to reflection.

As an alternative method for identifying curvature due to a soft excess, the lowest-redshift co-added spectrum was fitted with a broken power-law, with the break at 2 keV in the rest frame. Γ was measured to be 1.86 ± 0.10 below the break and 1.82 ± 0.05 above. Hence, there is little softening of the spectrum at lower energies, the upper limit being $\Delta\Gamma < 0.18$; this is consistent with the finding above, that any soft excess present in the low redshift objects is only weak.

It must be noted that there are far fewer counts in each of these spectra than for the objects in Chapters 2 and 3, leading to poorer statistics. A weak (~ 10 – 20%) soft excess will, therefore, be difficult to detect. The lack of strong evidence for such a soft excess component is likely to be attributable to the low count rates in these objects. Also, because of the somewhat higher redshifts, the energy band covered is not as sensitive to the lower temperatures; for example, for an object at $z = 2$, the *XMM* band corresponds to 0.6–30 keV, so cool soft excess components may not be obvious.

5.2.2 Spectral evolution

Fig. 5.2 shows the 2–10 keV power-law indices versus redshift. The dispersion in Γ is clearly visible, but there is no noticeable trend with z . A basic Spearman Rank test to the broad-band photon index versus redshift data implied there was no correlation between the values. This lack of correlation is also noted for the Γ -luminosity data, as would be expected from the tight correlation between L_X and redshift.

Values of the two-point optical to X-ray spectral index, α_{ox} , were measured (Equation 2.1) and the mean calculated to be 1.66 ± 0.04 . For this sample alone, no correlation was found between α_{ox} and redshift. However, previous results from the Bright Quasar Survey (BQS) gave a slightly flatter value of $\alpha_{ox} = 1.56 \pm 0.02$, for unabsorbed QSOs at low redshift (with $z < 0.5$), while the mean slope found by Chandra for the more distant ($z > 4$) objects is somewhat steeper, at 1.78 ± 0.03 (both values from Vignali et al. 2001). Comparing these measurements from the BQS, Chandra and *XMM*, there is an indication that α_{ox} steepens slightly with increasing redshift, with the extreme high redshift QSOs (at $z > 4$) being relatively fainter in the X-ray band, compared to low- z objects. This

agrees with Bechtold et al. (2003), who find that the *Chandra*-detected QSOs at $z > 4$ are more X-ray-quiet than the less distant objects; although redshift and luminosity are strongly correlated with each other, Bechtold et al. find this change in α_{ox} to be more strongly dependent on redshift.

One should be cautious when comparing samples of optically-selected (e.g., BQS) and X-ray-selected objects, since selection biases may lead to complications. However, some studies (e.g., Lamer, Brunner & Staubert 1997) have shown that the differences are not always significant. Likewise, as mentioned in Section 5.1, the differently-selected fields in this chapter show a consistent range of spectral parameters.

5.2.3 Spectral curvature

As discussed in Chapter 1, AGN, as a group, often show ‘reflection’ features, due to back-irradiation of the accretion disc by the hard X-ray flux (Pounds et al. 1990; Nandra & Pounds 1994), the strength of the features depending on the solid angle subtended by the optically thick, reflecting material. The strongest of these features is often an emission line arising from iron fluorescence, at $\sim 6.4\text{--}6.9$ keV, depending on the ionisation state of the material. An absorption edge, located at 7.1 keV (for neutral iron), should also be visible. The individual spectra obtained show no obvious features around this energy range, possibly because of limited signal-to-noise. The Compton reflection hump (which flattens the high energy spectrum) occurs due to the decreasing photo-electric absorption opacity and is expected to peak around 20–40 keV in the rest frame. Because of the high redshift of the objects in this sample, the observed *XMM* energy band extends to up to 30–40 keV in the rest frame and, so, the spectra might be expected to show evidence of the Compton hump.

Neutral reflection models were tried (*pexrav* in XSPEC; Magdziarz & Zdziarski 1995), fixing the exponential energy cut-off at 100 keV and the disc inclination angle at 30° . The strength of the reflection component is given by $R = \Omega/2\pi$, where Ω is the solid angle subtended by the reflector. Upon fitting the AGN individually, only one of the brightest objects, QSO 0130–403, showed evidence for reflection, with χ^2 decreasing by 16 for 1

degree of freedom, corresponding to a probability of $>99.99\%$ via an F-test.

A simpler method, more appropriate to the limited data quality, was to try and identify spectral curvature by measuring the photon index over two distinct energy bands (defined as 0.5–3 keV and 3+ keV in the rest frame of the object) and hence determine the difference between the ‘hard’- and ‘soft’-band values. The values of the slope in all energy bands analysed are shown in Table 5.2. At the foot of each column, the mean value for the photon index in that energy range is given.

If Compton reflection is present, then one would expect the higher-energy spectral slope to be flatter, hence subtracting the soft-band Γ from the harder one would lead to a negative value. Simulations were performed, for an object at the mean redshift of this sample ($z = 1.4$), setting $R = 1$ (corresponding to reflection from the full 2π steradians of Compton thick matter); Γ was then measured over the two energy bands defined above (0.5–3 keV and 3+ keV) and the difference in photon index over the two bands was calculated to be $\Delta\Gamma \sim -0.17$. The weighted mean for the difference in the slopes for our actual spectra was found to be -0.15 ± 0.06 , which corresponds to a reflection component, R , of 0.88 ± 0.35 . The spectral shape for the sample as a whole is therefore consistent with reflection from approximately 2π steradians of optically thick matter, located out of the direct line of sight (such as an accretion disc or molecular torus).

As when investigating the presence of a soft excess and additional absorption, the co-added spectra over three redshift bands were analysed. The photon indices were measured over 0.5–3 keV (rest frame) and 3+ keV energy bands, to compare with the findings above. For the lowest-redshift objects, there was no noticeable change in slope; however, flattenings at the higher-energies of $\Delta\Gamma = -0.25 \pm 0.18$ and -0.30 ± 0.09 were calculated for the middle- and high-redshift groups respectively. This prompted the use of *pexrav*, which indicated the presence of a reflection component (detected at 98% significance), of $R \lesssim 0.9$ for the most distant objects; there was little improvement in the fit for the medium- z group. This is consistent with the result obtained from finding the average change in slope between the soft and hard energy bands for the individual spectra.

In Section 5.2.1, the possibility of a soft excess was discussed. Adding in a blackbody

Table 5.2. Power-law slopes over a range of energy bands for the sources in the combined Mrk 205 and QSO 0130–403 fields.

Source ID XMMU	z	2–10 keV rest frame Γ	0.5–3 keV rest frame Γ	3+ keV rest frame Γ	0.2–10 keV obs. frame Γ
J121819.4+751919	2.649	2.05 ± 0.41	3.36 ± 0.72	2.44 ± 0.45	2.29 ± 0.18
J122048.4+751804	1.687	1.95 ± 0.36	2.21 ± 0.38	1.54 ± 0.32	1.66 ± 0.15
J122051.7+752820	0.181	1.64 ± 1.37	2.37 ± 0.39	4.28 ± 3.04	1.94 ± 0.25
J122052.0+750529	0.646	1.68 ± 0.10	1.83 ± 0.07	1.74 ± 0.15	1.77 ± 0.04
J122111.2+751117	1.259	2.13 ± 0.30	2.08 ± 0.16	1.30 ± 0.33	2.18 ± 0.10
J122120.5+751616	0.340	1.82 ± 0.44	2.34 ± 0.18	1.93 ± 1.04	2.19 ± 0.12
J122135.5+750914	0.330	1.26 ± 0.26	1.91 ± 0.17	1.48 ± 0.50	1.69 ± 0.10
J122206.4+752613	0.238	1.77 ± 0.07	1.50 ± 0.04	1.72 ± 0.13	1.56 ± 0.02
J122242.6+751434	1.065	2.61 ± 0.36	2.19 ± 0.81	-0.73 ± 2.05	2.40 ± 0.52
J122258.1+751934	0.257	1.74 ± 0.29	1.46 ± 0.18	2.00 ± 0.61	1.41 ± 0.09
J122318.5+751504	1.509	1.43 ± 0.29	2.41 ± 0.30	2.30 ± 0.49	2.05 ± 0.15
J122344.7+751922	0.757	1.74 ± 0.59	2.67 ± 0.17	2.24 ± 0.98	2.63 ± 0.13
J122351.0+752227	0.565	1.72 ± 0.17	1.94 ± 0.09	1.39 ± 0.26	1.88 ± 0.05
J122445.5+752224	1.852	2.17 ± 0.36	1.26 ± 0.44	2.08 ± 0.43	1.87 ± 0.16
J013302.0–400628	3.023	2.10 ± 0.07	2.08 ± 0.10	1.90 ± 0.06	1.89 ± 0.03
J013257.8–401030	2.180	1.67 ± 0.23	2.56 ± 0.25	1.91 ± 0.25	1.94 ± 0.10
J013314.7–401212	1.49	2.27 ± 0.58	2.42 ± 0.27	1.53 ± 0.47	2.65 ± 0.17
J013205.4–400047	2.12	2.05 ± 0.16	2.55 ± 0.16	2.21 ± 0.22	2.31 ± 0.08
J013348.3–400233	2.11	3.48 ± 1.14	1.22 ± 1.03	1.47 ± 1.14	2.33 ± 0.41
J013233.2–395445	1.73	1.77 ± 0.38	2.20 ± 0.57	2.54 ± 0.54	1.76 ± 0.19
J013333.8–395554	1.90	2.21 ± 0.32	2.47 ± 0.34	2.59 ± 0.49	2.19 ± 0.15
J013408.6–400547	2.14	2.33 ± 0.25	2.64 ± 0.17	2.10 ± 0.33	2.59 ± 0.10
J013320.4–402021	2.25	1.37 ± 0.61	1.10 ± 1.57	1.49 ± 0.60	1.33 ± 0.31
Mean		1.88 ± 0.04	2.07 ± 0.04	1.87 ± 0.05	1.76 ± 0.01

component to the model for the high- z group gave an acceptable fit, although, statistically, not as good as for reflection. It also seems unlikely that there would be a more clearly detectable soft excess at higher redshifts than the lower- z values, which are more sensitive to any excess at the lowest energies. Nonetheless, a model comprising both a blackbody and a reflection component still improved the fit, giving a $\chi^2_\nu = 142/144$, corresponding to almost 97% confidence for the addition of the reflection component. Thus, there does appear to be an indication of the Compton reflection hump, in the most distant objects.

5.3 High flux objects

Within this sample of AGN are 7 objects with 2–10 keV fluxes of greater than 5×10^{-14} erg cm⁻² s⁻¹. These have spectra with sufficiently good signal-to-noise to allow individual analysis in greater detail.

The central object of the second field, QSO 0130–403 (XMMU J013302.0-400628 in the tables), has the highest *luminosity*, at 5.88×10^{45} erg s⁻¹ (2–10 keV). This is, in fact, more luminous than most of the QSOs considered in Chapter 3, with only PG 1634+706 and PB 05062 having higher 2–10 keV luminosities. QSO 0130–403 was discovered by Smith (1976) on Tololo survey plates and found to be a very blue object, from the optical photometry published by Adam (1985). It has previously been observed in the low-energy X-ray region by the *ROSAT* PSPC (Position Sensitive Proportional Counter), which gave a value of $\Gamma = 1.69_{-0.60}^{+0.71}$, when fixing N_H to the Galactic value (Bechtold et al. 1994).

When fitting the 2–10 keV rest-frame band, the addition of an ionised Fe emission line, with the line width (σ) set to 0.1 keV, decreased χ^2 by 5 for 2 degrees of freedom, which corresponds to a marginal detection at $> 90\%$. (The width of the line could not be well constrained: $\sigma = 0.34 \pm 0.29$ keV.) No narrow component was required, this being in agreement with the findings in Chapter 6 for high luminosity objects. Over the full 0.2–10 keV observed band (corresponding to 0.8–40 keV rest frame), the best fit model consists simply of a power-law ($\Gamma = 2.09 \pm 0.03$) and the emission line, detailed above, at 6.62 ± 0.12 keV, the equivalent width of the line being ~ 200 eV in the rest frame (~ 50 eV observed). There is no requirement for additional column density or a soft excess. The spectrum is shown in Figure 5.3. As discussed earlier in this chapter (Section 5.2.1), the apparent lack of soft excess is likely to be due to the relatively low statistics. For many of the QSOs in the Chapter 3 sample, there was no need for absorption above the Galactic value, as is found here for QSO 0130–403.

As mentioned in Section 5.2.3, there is evidence for neutral reflection in this spectrum, with the 90% confidence range for R being 1.11–3.85; i.e. consistent with reflection from the full 2π steradians of an accretion disc.

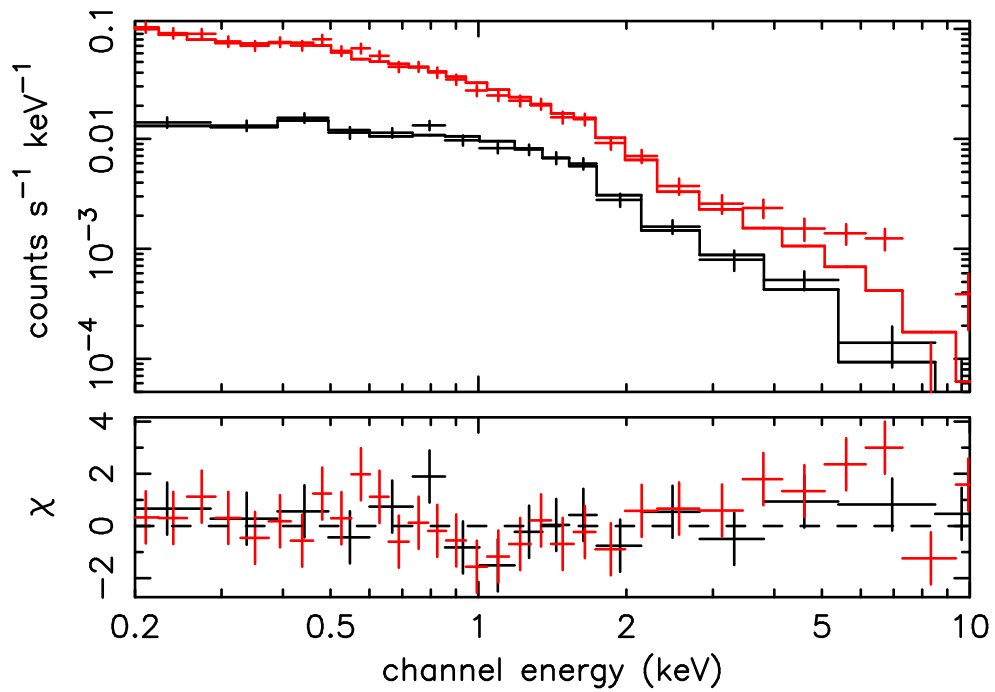


FIGURE 5.3. The broad-band spectrum of QSO 0130–403 is best fitted by a power-law of $\Gamma \sim 2.09$ and a broad Fe emission line at 6.6 keV (in the rest frame). The MOS spectrum is shown in black and the PN in red.

As stated earlier, most of the spectra did not require the presence of a strong soft excess. For each of the high flux objects, a blackbody component was added into the model, with the temperature fixed at 0.1 keV; the 90% upper limit was then calculated for the luminosity over 0.2–10 keV; in general this was found to be $\lesssim 10\%$ of the strength of the power-law. For a low-luminosity QSO, this is a typical value for the relative strength of the soft excess compared to the power-law component (see Chapter 3); thus, the objects in this sample are consistent with other QSOs, where better signal-to-noise in the spectra allow more detailed analysis of the soft excesses.

All the high-flux spectra (Figure 5.4) were systematically fitted to search for the presence of iron lines and reflection. With the exception of QSO 0130–403, neither iron emission nor the Compton reflection hump could be constrained in any of the individual spectra, with 90% upper limits on the equivalent widths of the iron lines lying between 145–650 eV.

It should be noted that two of these bright objects are those classified as Narrow Line

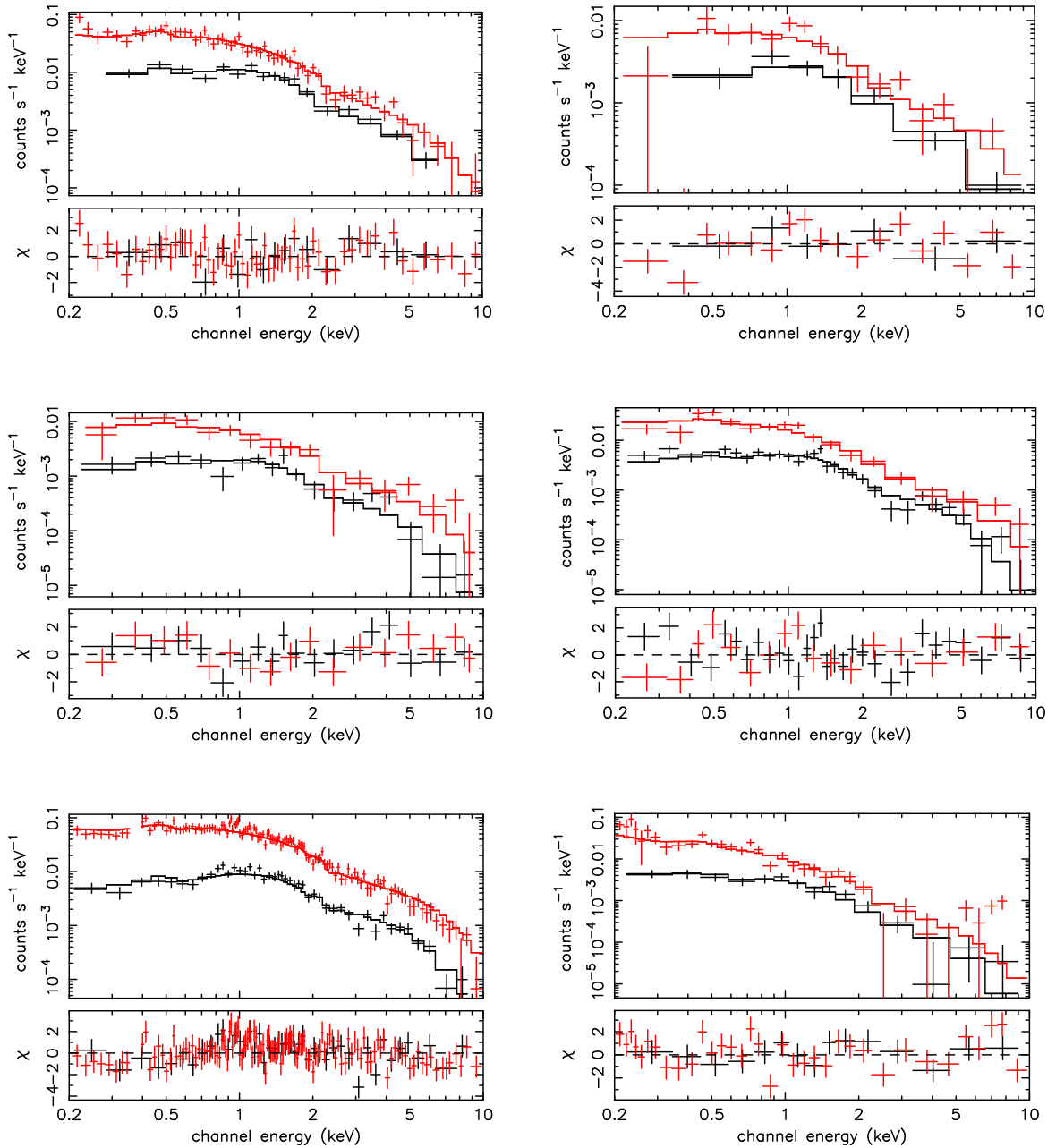


FIGURE 5.4. Broad-band spectra for those QSOs with a 2–10 keV flux of greater than 5×10^{-14} erg cm $^{-2}$ s $^{-1}$. From top to bottom, the objects are XMMU J122052.0+750529, XMMU J122135.5+750914, XMMU J122206.4+752613 in the left-hand column; XMMU J122258.1+751934, XMMU J122351.0+752227 and XMMU J013205.4-400047 on the right.

AGN by Barcons et al. (2002) – XMMU J122206.4+752613 and XMMU J122258.1+751934; this makes them similar to PG 1211+143 (Section 3.3). These are the only two high-flux objects which have measurable excess absorption; the values, however ($\lesssim \text{few} \times 10^{21} \text{ cm}^{-2}$), are not of a large enough magnitude completely to obscure broad-line regions and, hence, explain the narrow-line classification.

The spectrum of Mrk 205 was analysed by Reeves et al. (2001). The fits are repeated here (and are consistent with those presented by Reeves and co-workers) and briefly summarised. Over the 2–10 keV band, the spectral slope of Mrk 205 was found to be 1.74 ± 0.02 . This includes two Gaussian components: a narrow ($\sigma = 10 \text{ eV}$) line at $E = 6.38 \pm 0.04 \text{ keV}$ and a broader ($\sigma = 0.239 \pm 0.173 \text{ keV}$) one at $E = 6.81 \pm 0.13 \text{ keV}$. The broad-band spectrum shows a slight soft excess, and is best fitted by $\Gamma = 1.76 \pm 0.01$ and a blackbody component with $kT = 0.138 \pm 0.005 \text{ keV}$, together with the two emission lines. It is clear that these values for the slopes are consistent with those for the objects in this *XMM* sample.

5.4 Discussion

5.4.1 Absorbing column density

The fits to the QSO spectra implied that the RQQs observed have no additional absorption above that due to our own Galaxy. The flatter spectral slopes for some objects could not be explained by obscuration in the AGN; this agrees with the *XMM* observation of the Lockman Hole (Hasinger et al. 2001; Mainieri et al. 2002), in that these sources are Type-1 AGN, while their intrinsically absorbed objects are mainly Type-2. One possibility is that we are not reaching a low enough ($< 10^{-14} \text{ erg cm}^{-2} \text{ s}^{-1}$) flux level to be measuring spectra of these faint, obscured sources, within these two fields.

However the lack of any absorption above the Galactic value agrees with previous studies of radio-quiet QSOs, e.g., with *Einstein* (Canizares & White 1989; objects with $0.1 < z < 3.5$), *ROSAT* (Yuan et al. 1998; $z > 2$) and *Ginga* (Lawson & Turner 1997; $z < 1.4$). Likewise, the AGN in Chapters 2 and 3 do not tend to require additional

absorption and, indeed, the radio-quiet QSOs in this sample appear to remain unabsorbed up to redshifts of $z \sim 3$.

Radio-loud objects, on the other hand, do tend to show excess absorption (e.g., Elvis et al. 1994; Brinkmann et al. 1997; Reeves & Turner 2000). The data from Reeves & Turner (2000) show an average column density of $1.29 \times 10^{22} \text{ cm}^{-2}$ for radio-loud quasars. For the sample of RQQs in this chapter, a mean of $2.96 \times 10^{21} \text{ cm}^{-2}$ is found for the *upper limits*, which is noticeably smaller.

It is known that the low-energy response of the *ASCA* SIS has been degrading over time (see Yaqoob et al. 2000). The effect of this is an underestimate of the soft X-ray flux, which can show itself as an increase in N_H . In order to check that the differences found between the RLQ and RQQ distributions are not instrument-linked, the measured column densities for a number of objects which have been observed by both *XMM* and *ASCA* were compared. It was found that, within the errors, the instruments agreed; it can, therefore, be assumed that the absorption measured for the Reeves & Turner (2000) radio-loud sample is not due simply to the *ASCA* calibration.

Statistical tests were applied to both the radio-quiet objects from this chapter and the radio-loud ones from Reeves & Turner (2000), to determine whether there was evidence for a difference in population. (There are too few RLQs in Chapter 3 to make any comparison worth while.) Fig. 5.5 shows the column densities against redshift for this combined sample, with the *ASCA*-detected RLQs marked by open stars and the *XMM* RQQs by crosses/arrows.

Due to the overwhelming presence of censored data (that is, upper limit measurements), the ASURV (Astronomy Survival Analysis) software was used (see Feigelson & Nelson 1985). Employing each of the possible two-sample tests, it was found that the probability of the RQQs and RLQs being from the same population was very low: $< 0.01\%$. The Kolmogorov–Smirnov test was also performed on the data, leading to a probability of $\sim 3.4\%$ for the existence of one population only. Other statistical tests were also tried, each method confirming the same result: the radio-quiet QSOs in our sample were found to belong to a different population from the radio-loud objects in Reeves & Turner (2000) – probability of $> 99\%$ in general.

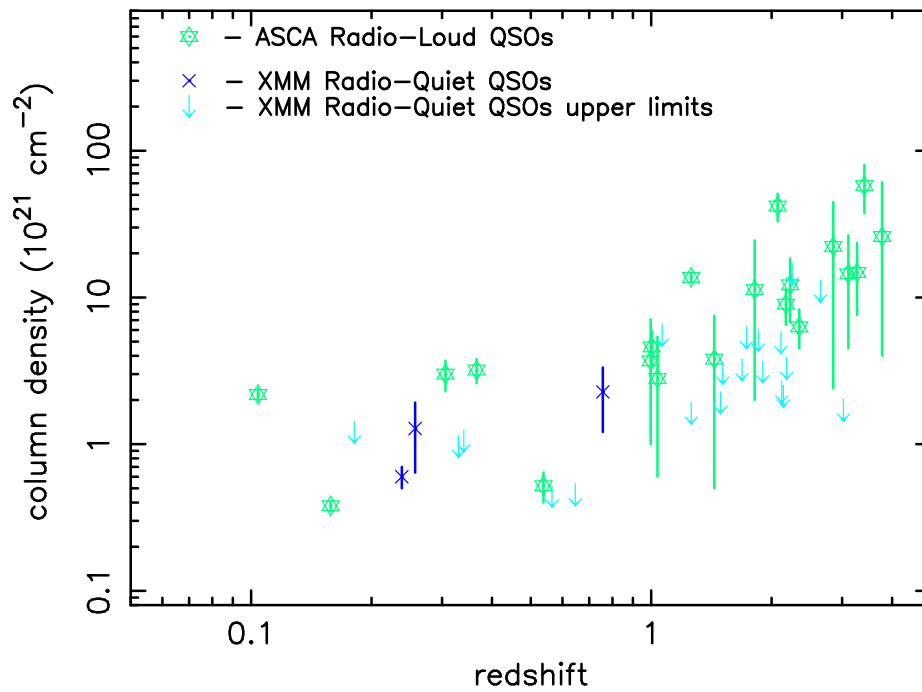


FIGURE 5.5. The joint sample of radio-quiet and radio-loud QSOs, from *XMM* and *ASCA* (taken from Reeves & Turner 2000) respectively.

Summarising, it is found that, although RLQs tend to show excess absorption at high redshifts, radio-quiet objects do not, at least up to $z \sim 3$ – this is also found in the samples of Chapters 2 and 3, where lower redshift objects are investigated. Generally this implies that there is an intrinsic difference in the local environment of the two types of QSO at high redshifts. It must be noted that the situation for radio-quiet QSOs at higher redshifts ($z > 5$) is still unclear; more deep *XMM* observations of individual, bright high-redshift QSOs are required to explore this possibility.

5.4.2 Spectral evolution

The QSOs in this sample all show the same range of continuum photon indices, regardless of luminosity or redshift, over the energy range 2–10 keV. Comparing the slopes over the full 0.2–10 keV range gave the same results.

Canizares & White (1989) also find no evidence for a Γ - z dependence from the *Einstein* data, up to a maximum energy of 4 keV. Likewise, Yuan et al. (1998) found that

the spectral slopes of distant ($z > 2.5$) RQQs were consistent (within the errors) with those of nearby objects; *ROSAT* covered the energy range 0.1–2.4 keV. The *ASCA* data in Reeves & Turner (2000) also showed no significant correlation between photon index and redshift, over a similar energy range to that of *XMM*. The independence of spectral slope and redshift is observed in the higher energy band ($E \gtrsim 2$ keV) of radio-loud objects, too [e.g., comparison between Γ from *EXOSAT* data (Lawson et al. 1992) and *Ginga* (Williams et al. 1992)]. There also appears to be no evolution with redshift of the extreme-ultraviolet spectral slope, for either RL or RQQs (Telfer et al. 2002).

5.4.3 Spectral curvature

For the signal-to-noise of the data presented here, it is not possible to make a conclusive statement on the presence or absence of reflection in the *individual* QSOs in this sample. However, the spectral hardening (where $\Delta\Gamma = 0.2$) that appears to exist for the sample as a whole above 3 keV, is consistent with reflection from 2π steradians of optically thick material, located out of the line of sight.

Past studies (e.g., with *ASCA*, Reeves & Turner 2000) have noted that the strength of the neutral Compton reflection hump, and the associated iron $K\alpha$ line, is considerably lower in the higher-redshift QSOs, than that expected in Seyfert 1 galaxies at low redshift (e.g., Nandra & Pounds 1994). However, the QSO spectra previously obtained above $z = 2$ by *ASCA* were mainly core-dominated radio-loud quasars, where a contribution from the relativistic jet could weaken any apparent reflection features. This does not appear to be the case for the *radio-quiet* AGN found in this sample; the average co-added spectra of these AGN above $z = 2$ appears to indicate the presence of a reflection component with $R \sim 1$, the first time this has been measured for high-redshift QSOs.

Finally it is noted that the reflection may occur from an ionised disc (e.g., Reeves et al. 1997; Eracleous & Halpern 1998; Grandi et al. 2001; Ballantyne, Ross & Fabian 2002). However, the data in this sample show only one significant iron line, located near 6.6 keV; this tentatively suggests that the reprocessing material might be more strongly ionised in some of the higher luminosity AGN, as is observed for instance in the *XMM*-

Newton spectrum of Mrk 205 (Reeves et al. 2001). Such an ionised disc could also explain some of the observed spectral curvature (e.g., O’Brien et al. 2001a; Pounds et al. 2001).

5.5 Summary

The spectra of 23 radio-quiet, high-redshift QSOs have been investigated. It is found that the 2–10 keV photon indices show significant scatter, although there is no obvious trend with redshift. This dispersion in slope is intrinsic and not related to obscuration effects as is thought to be the case for the faint sources constituting the X-ray background. It can, therefore, be concluded that there is no evidence for X-ray spectral evolution of QSOs with redshift or luminosity.

No excess absorption in the rest frame of the radio-quiet QSOs was found. This is in contrast to the additional N_H measured by past studies in high- z , radio-loud quasars and suggests an intrinsic difference could exist in the local environments of the two classes of QSOs. The limited sample of radio-loud objects in Chapter 3 seems to have very similar soft excesses to their radio-quiet counterparts, so the absorption and soft excess components are likely to be unrelated.

Considering the sample as a whole, the spectral slope appears to flatten at $\gtrsim 3$ keV. This indicates the presence of a reflection component from material subtending a solid angle of 2π steradians. This matter could be linked to either the inner accretion disc or a distant molecular torus.

Chapter 6

An X-ray Baldwin effect for the narrow Fe $K\alpha$ line

As the number of AGN surveyed by *XMM-Newton* and *Chandra* increases, it is becoming increasingly apparent that the vast majority show evidence for a narrow (unresolved by *XMM*) line at ~ 6.4 keV, due to emission from neutral iron; recent papers describing such lines include Gondoin et al. (2003a; NGC 3227), Page et al. (2003a; Mrk 896), Pounds et al. (2003c; Mrk 766), Petrucci et al. (2002; Mrk 841), Turner et al. (2002; NGC 3516), O’Brien et al. (2001a; Mrk 359), Reeves et al. (2001; Mrk 205) and many others. In a number of cases (e.g., NGC 3783 – Kaspi et al. 2002; NGC 5548 – Yaqoob et al. 2001) the lines have actually been resolved by *Chandra*, with velocities typically $< 5000 \text{ km s}^{-1}$.

Iron $K\alpha$ emission was first identified as a common feature by *Ginga* (Pounds et al. 1990; Nandra & Pounds 1994); observations by *ASCA* tended to find relatively broad profiles, although re-analysis of some of the data indicates that the lines may be narrower than originally measured (Lubinski & Zdziarski 2001). Very few broad lines have been found in *XMM* data to date, examples being MCG $-6-30-15$ (Fabian et al. 2002b), MCG $-5-23-16$ (Dewangan, Griffiths & Schurch 2003), Mrk 205 (Reeves et al. 2001) and Mrk 509 (Pounds et al. 2001). However, not all these line profiles are the same, with MCG $-6-30-15$ showing a strongly asymmetric line, presumably due to the strong

gravitational forces and high velocity in the inner accretion disc, while the broad component in MCG $-5-23-16$ appears to be symmetrical. Mrk 205 is only well-fitted by a relativistic disc-line model if the disc is strongly ionised, since the broad emission peaks at ~ 6.7 keV. This is not the only conceivable explanation, as Reeves et al. (2001) discuss: the emission could come from a spherical distribution of clouds, rather than the planar accretion disc; alternatively, the broad line may actually consist of a blend of different ionisation narrow lines. The broad line in Mrk 509 is also apparently ionised.

The narrow emission lines observed by *XMM-Newton* and *Chandra* are interpreted as Fe K fluorescence from cold (neutral) matter far from the inner accretion disc. Suggestions for the origin of the narrow line include the putative molecular torus, the Broad Line Region (BLR) or the very outer-most reaches of the accretion disc.

The Baldwin effect is well known for optical/UV emission lines, with Baldwin (1977) first reporting that the EW of the C IV $\lambda 1549$ Å line decreased with increasing UV luminosity. Since then, significant anti-correlations have been found between the luminosity and various other ions, such as N V, He II, C III], Mg II and Ly α (e.g., Tytler & Fan 1992; Zamorani et al. 1992; Green, Forster & Kuraszkiewicz 2001; Dietrich et al. 2002), although the strengths of these correlations is still unclear.

It should be noted that, although the Baldwin effect is generally accepted to be an anti-correlation between equivalent width and luminosity, Green et al. (2001) claim that EW is actually more strongly correlated with redshift for their data. However, Croom et al. (2002) find that, for 12 of the 14 lines tested, the stronger correlation is with absolute magnitude rather than redshift.

Iwasawa & Taniguchi (1993) reported an X-ray Baldwin effect in the Fe K lines found in *Ginga* observations of AGN. They find a strong relationship for their Seyfert sample, but were unable to conclude that it holds for QSOs, due to poor constraints. There is also a Baldwin Effect for the broad iron lines found in the *ASCA* data (Nandra et al. 1997). Such broad lines are thought to be produced through fluorescence of the accretion disc itself. They suggest, based on an earlier paper (Nandra et al. 1995), that this effect is due to the presence of an ionised skin on the accretion disc, with the degree of ionisation increasing with luminosity; see also Nayakshin (2000a,b). Such an ionised

skin is one of the possible methods for the Comptonisation of disc photons to form the soft excess (Section 1.3.5). Nandra et al. (1997) also find that the narrow line core drops in intensity as the luminosity increases, but conclude that the entire Baldwin effect in their data can be attributed to the broader line alone.

When fitting the X-ray spectra of the AGN in Chapters 2, 3 and 4, the presence of iron emission was investigated. The equivalent widths (EWs) of the neutral, narrow lines fitted are here combined with additional results, to investigate the change in strength of the lines with the hard X-ray luminosities of the objects.

6.1 XMM-Newton observations

This sample consists of 53 Type-1 AGN (Table 6.1), these being mainly a combination of proprietary targets and public observations obtained from the online *XMM* Science Archive. A literature search also revealed four more objects for which the relevant data had been published (NGC 5506 - Matt et al. 2001; NGC 3516 - Turner et al. 2002; 1H 0707–49 - Boller et al. 2002; Ton S180 - Vaughan et al. 2002 and Vaughan 2003, private communication).

For the spectra analysed here, the PN data only were used, since the instrument is more sensitive than the MOS cameras at higher energies. (It must, therefore, be noted that some of the values for the equivalent widths given in this chapter are not identical to those in Chapters 2 and 3, which were for MOS and PN together; the differences are only small, however.) For each spectrum, a simple power-law was fitted over the rest frame band of 2–10 keV. If there was evidence for any broadened emission, then a broad Gaussian line was included; see Table 6.2. A narrow ($\sigma = 10$ eV) line was next added and the equivalent width (EW) measured. If the reduction in χ^2 was less than 99% significant, the 90% upper limit was taken for the equivalent width. For the vast majority of the spectra, the energy of such a line was very close to 6.4 keV. For four of the higher luminosity objects, the line energy could not be constrained, with errors much bigger than the actual value. Six of the AGN tended towards ionised lines, although, when taking account of the errors, only two were inconsistent with a neutral origin, these being

Table 6.1. The Type-1 AGN included in this sample, ordered by redshift (left-hand then right-hand columns) within the radio-quiet and radio-loud groups. The luminosities were calculated for the 2–10 keV rest frame and 90% errors/upper limits are given for the rest-frame equivalent widths. ^a Narrow Line Seyfert 1 galaxies; ^b Broad Line Seyfert 1 galaxies; ^c QSOs

object	type	redshift	log[lum. (erg s ⁻¹)]	EW (eV)	object	type	redshift	log[lum. (erg s ⁻¹)]	EW (eV)
NGC 4151 ^b	RQ	0.003	42.27	187 ± 3	PG 0804+761 ^c	RQ	0.100	44.62	< 101
NGC 5506 ^b	RQ	0.006	43.12	70 ± 20	1H 0419–577 ^b	RQ	0.104	44.75	50 ± 44
MCG –6-30-15 ^b	RQ	0.008	42.87	68 ± 15	Mrk 876 ^c	RQ	0.129	44.49	96 ± 59
NGC 3516 ^b	RQ	0.009	42.68	196 ± 22	PG 1626+554 ^c	RQ	0.133	44.40	< 281
NGC 4593 ^b	RQ	0.009	43.07	98 ± 21	PG 1114+445 ^c	RQ	0.144	44.27	120 ± 17
Mrk 766 ^a	RQ	0.013	42.85	45 ± 35	Q 0056–363 ^c	RQ	0.162	44.51	< 159
IC 4329a ^b	RQ	0.016	44.04	30 ± 12	PG 1048+342 ^c	RQ	0.167	44.21	< 191
Mrk 359 ^a	RQ	0.017	42.85	220 ± 74	PDS 456 ^c	RQ	0.184	45.13	< 18
Mrk 1044 ^a	RQ	0.017	42.86	186 ± 61	Q 0144–3938 ^c	RQ	0.244	44.52	152 ± 50
NGC 5548 ^b	RQ	0.017	43.66	59 ± 6	UM 269 ^c	RQ	0.308	44.61	< 99
Mrk 335 ^a	RQ	0.026	43.55	< 54	PG 1634+706 ^c	RQ	1.334	46.34	< 63
Mrk 896 ^a	RQ	0.026	42.99	180 ± 87	PB 05062 ^c	RQ	1.77	46.82	< 61
Mrk 493 ^a	RQ	0.031	43.20	< 101	NGC 3227 ^c	RL	0.004	41.64	191 ± 23
Mrk 509 ^b	RQ	0.034	44.15	85 ± 57	PKS 1637–77 ^c	RL	0.043	43.01	< 95
Mrk 841 ^b	RQ	0.036	43.90	< 83	3 Zw 2 ^c	RL	0.089	44.33	< 84
1H 0707–495 ^a	RQ	0.041	42.52	< 90	PKS 0558–504 ^c	RL	0.137	44.99	< 11
ESO 198–G24 ^b	RQ	0.046	43.92	104 ± 49	3C 273 ^c	RL	0.158	45.91	< 9
Fairall 9 ^b	RQ	0.047	43.97	139 ± 26	B2 1028+31 ^c	RL	0.178	44.53	88 ± 41
Mrk 926 ^b	RQ	0.047	44.42	57 ± 24	B2 1721+34 ^c	RL	0.206	45.53	63 ± 34
Ton S180 ^a	RQ	0.062	43.91	< 64	B2 1128+31 ^c	RL	0.289	44.98	50 ± 39
MR 2251–178 ^c	RQ	0.064	44.73	< 74	S5 0836+71 ^c	RL	2.172	48.11	16 ± 6
PG 0844+349 ^c	RQ	0.064	43.99	< 172	PKS 2149–30 ^c	RL	2.345	47.45	< 40
Mrk 304 ^c	RQ	0.066	43.82	< 115	PKS 0438–43 ^c	RL	2.852	47.39	< 26
Mrk 205 ^c	RQ	0.071	44.11	60 ± 25	PKS 0537–286 ^c	RL	3.104	47.92	< 82
PG 1211+143 ^c	RQ	0.081	43.91	37 ± 24	PKS 2126–15 ^c	RL	3.268	48.03	< 17
HE 1029–1401 ^c	RQ	0.086	44.54	< 105	S5 0014+81 ^c	RL	3.366	47.68	< 17
Mrk 1383 ^c	RQ	0.086	44.38	77 ± 46					

Table 6.2. The objects in the sample for which broad lines were statistically required.
^a The broad line fit to MCG –6-30-15 was based on that by Wilms et al. (2001), which used a relativistic *laor* line, rather than a broad Gaussian. Both the energy and index ($\beta = 4.6$) were frozen at their best fit values from Wilms et al.

object	line energy (keV)	intrinsic width (keV)	EW (eV)
MCG –6-30-15	6.95	see note a	590 ± 62
Mrk 766	6.78 ± 0.19	0.230 ± 0.150	70 ± 30
Mrk 335	6.72 ± 0.14	0.439 ± 0.129	175 ± 50
Mrk 509	6.84 ± 0.14	0.149 ± 0.086	28 ± 20
Fairall 9	6.91 ± 0.141	0.464 ± 0.155	206 ± 90
Mrk 926	6.24 ± 0.15	0.189 ± 0.117	91 ± 35
PG 0844+349	6.47 ± 0.09	0.345 ± 0.117	334 ± 130
Mrk 205	6.86 ± 0.11	0.195 ± 0.151	122 ± 80
PG 1211+143	6.50 ± 0.20	0.120 ± 0.065	240 ± 76
PG 0804+761	7.00 ± 0.36	0.385 ± 0.210	1050 ± 500
Q 0056–363	6.32 ± 0.07	0.218 ± 0.079	260 ± 116
B2 1028+31	6.56 ± 0.09	0.206 ± 0.101	131 ± 110
B2 1128+31	6.41 ± 0.33	0.693 ± 0.437	253 ± 185

PKS 0558–504 and PKS 2126–15. For these objects with unconstrained or ionised line energies, the centre of the line was fixed at 6.4 keV. A neutral reflection component (*pe xrav* in XSPEC; Magdziarz & Zdziarski 1995) was also tried for each spectrum. Only a small number were improved by this addition and, of these reflection parameters, the vast majority were unconstrained. The two objects which gave significant, constrained values were NGC 4151 ($R = 0.52 \pm 0.05$) and MCG –6-30-15 ($R = 1.81 \pm 0.52$); $R = \Omega/2\pi$, where Ω is the solid angle subtended by the reflecting matter. Such a reflection component is evidence for scattering off cool, optically thick matter (e.g., the torus) and will be discussed in more detail later.

Figure 6.1 plots the rest-frame EW against the de-reddened 2–10 keV luminosity. It can clearly be seen that there is a decrease in the EW as the luminosity increases – the ‘X-ray Baldwin effect’. The ASURV (Feigelson & Nelson 1985) package can be used in the presence of censored (upper limit) data. This allows the Spearman Rank (SR) statistic to be applied to the complete dataset, and gives an anti-correlation between

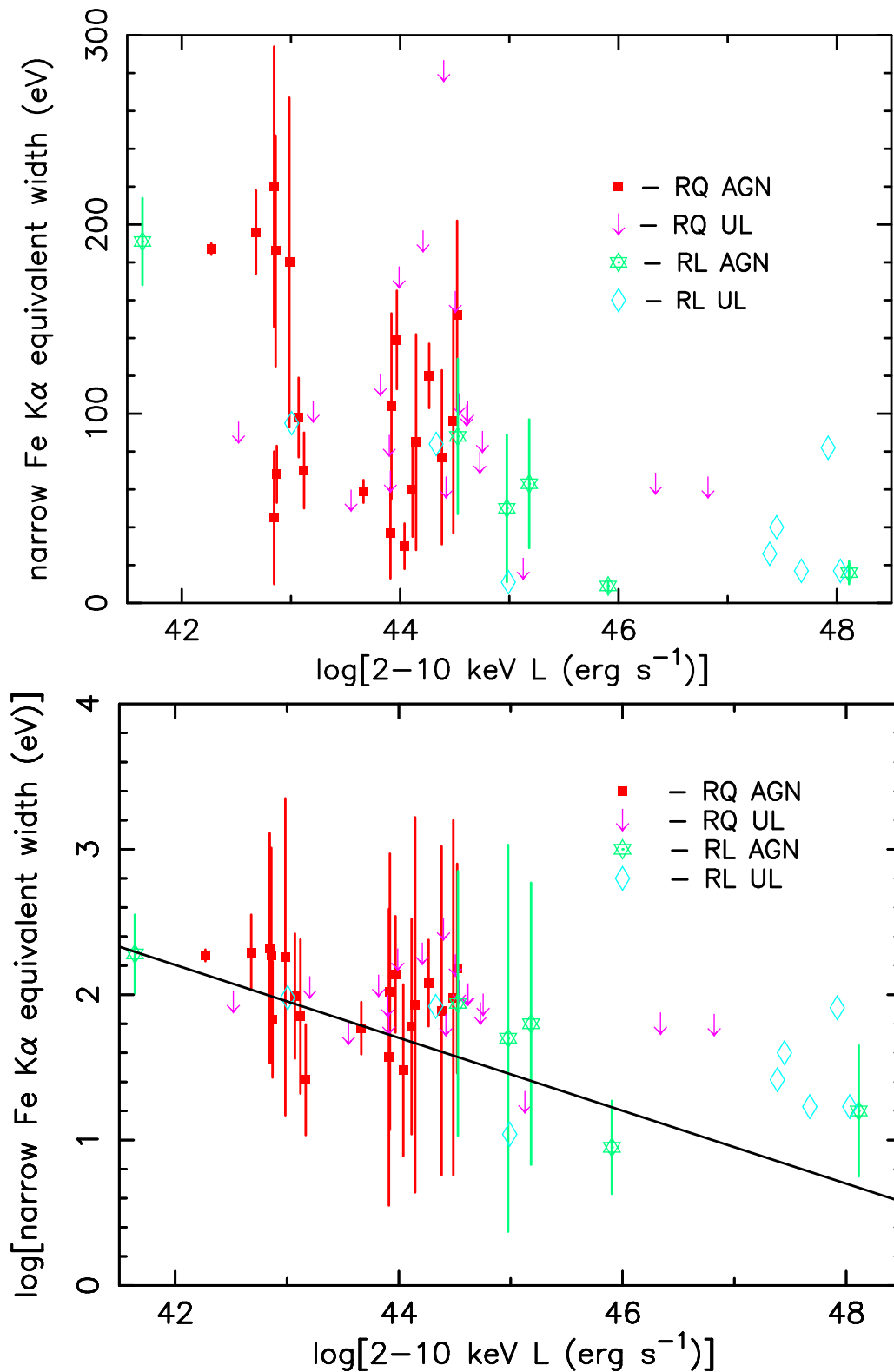


FIGURE 6.1. The decrease in EW of the narrow, neutral iron line with luminosity. Statistically significant measurements are indicated by squares and stars for radio-quiet and radio-loud objects respectively. Arrows and diamonds signify the corresponding upper limits. The line in the bottom plot shows a power-law fit to the data: $\text{EW} \propto L^{-0.25}$.

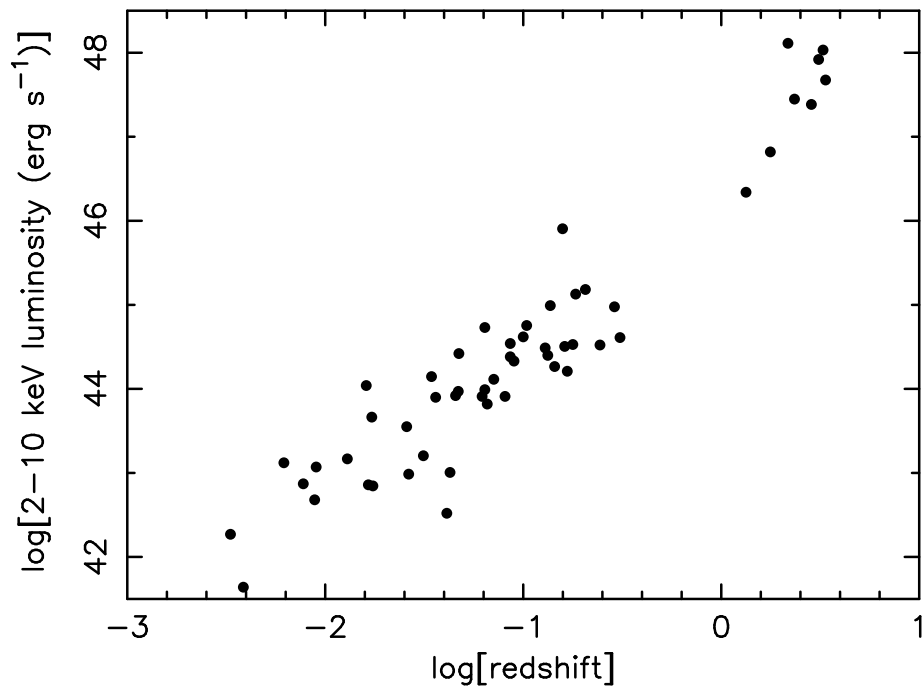


FIGURE 6.2. The correlation between luminosity and redshift for the sample of AGN.

the EW and luminosity of $> 99.99\%$ ($\sim 99.5\%$ if the upper limits are dropped). Due to selection effects, luminosity and redshift are very strongly correlated, as shown in Figure 6.2. Hence, it is often difficult to determine whether the correlation in question is with luminosity or redshift. Using the simple Spearman Rank, a weaker correlation (99%; 79.5% if the upper limits are excluded) was found between the line strength and the redshift. An alternative method for checking involves the Partial Spearman Rank, which gives an indication as to which of the two relationships is stronger. In this case, agreeing with the simple Spearman Rank, the EW-luminosity correlation appears to be the dominant relationship.

Weighted linear regression can be used to find the slope of the best-fit line to the log-log plot of EW against luminosity – that is, the power-law fit. This was performed using two different methods. Firstly the upper limit measurements were completely removed; this gave a value of -0.25 ± 0.05 . The second method used the linear regression option within ASURV; although upper limit values are accounted for, this method does not include the errors on the actual measurements. Using this method, the slope is less steep,

with a value of -0.19 ± 0.04 , but is consistent with the previous result.

As a further check to determine whether the Baldwin effect could be due to evolution, the objects at higher redshifts were progressively removed from the sample. It was found, however, that even considering only those AGN at $z < 0.1$, there still remained an inverse correlation between EW and luminosity which was consistent in magnitude with that found for the complete sample. This implies that the decrease in line strength is predominantly a luminosity-dependent effect.

There is a possible complication in that the highest luminosity AGN tend to be radio-loud, since the average X-ray emission from radio-quiet AGN is about three times lower than that from radio-loud objects (Zamorani et al. 1981; Worrall et al. 1987). The underlying worry, therefore, is that the EW is very low at the highest luminosities because of dilution through beaming effects. However, as Fig. 6.1 shows, there are lower-luminosity radio-loud AGN in this sample which have correspondingly higher EWs. Conversely, PB 05062 and PG 1634+706 – radio-quiet AGN – at luminosities of $\sim 10^{46}$ erg s⁻¹ have low upper limits of $EW < 63$ eV for their lines. Hence, the anti-correlation observed is not simply due to beaming. To show the overall effect more clearly, Figure 6.3 plots the mean EW for a number of luminosity bins considering all the objects (top plot) and just the radio-quiet ones (bottom). In both plots, the decrease in EW is obvious. To produce Figure 6.3, upper limits were taken to be half of the value, together with an equally sized error bar; a similar decrease in EW is also observed if the upper limits are dropped, although the luminosity range covered is lower.

Figure 6.4 plots the EW against the power-law slope measured over the 2–10 keV rest-frame energy band. Since flatter slopes are often taken to be indicative of reflection, it might be expected that they would correspond to stronger emission lines (since the fluorescence line may come about through reflection processes). However, this is clearly not the case; if anything, there is a slight trend in the opposite direction, with some of the steeper slopes showing the highest EWs. This appears to be consistent with the work by Zdziarski, Lubiński & Smith (1999), who find that the reflection components are stronger in those objects which have steep spectra.

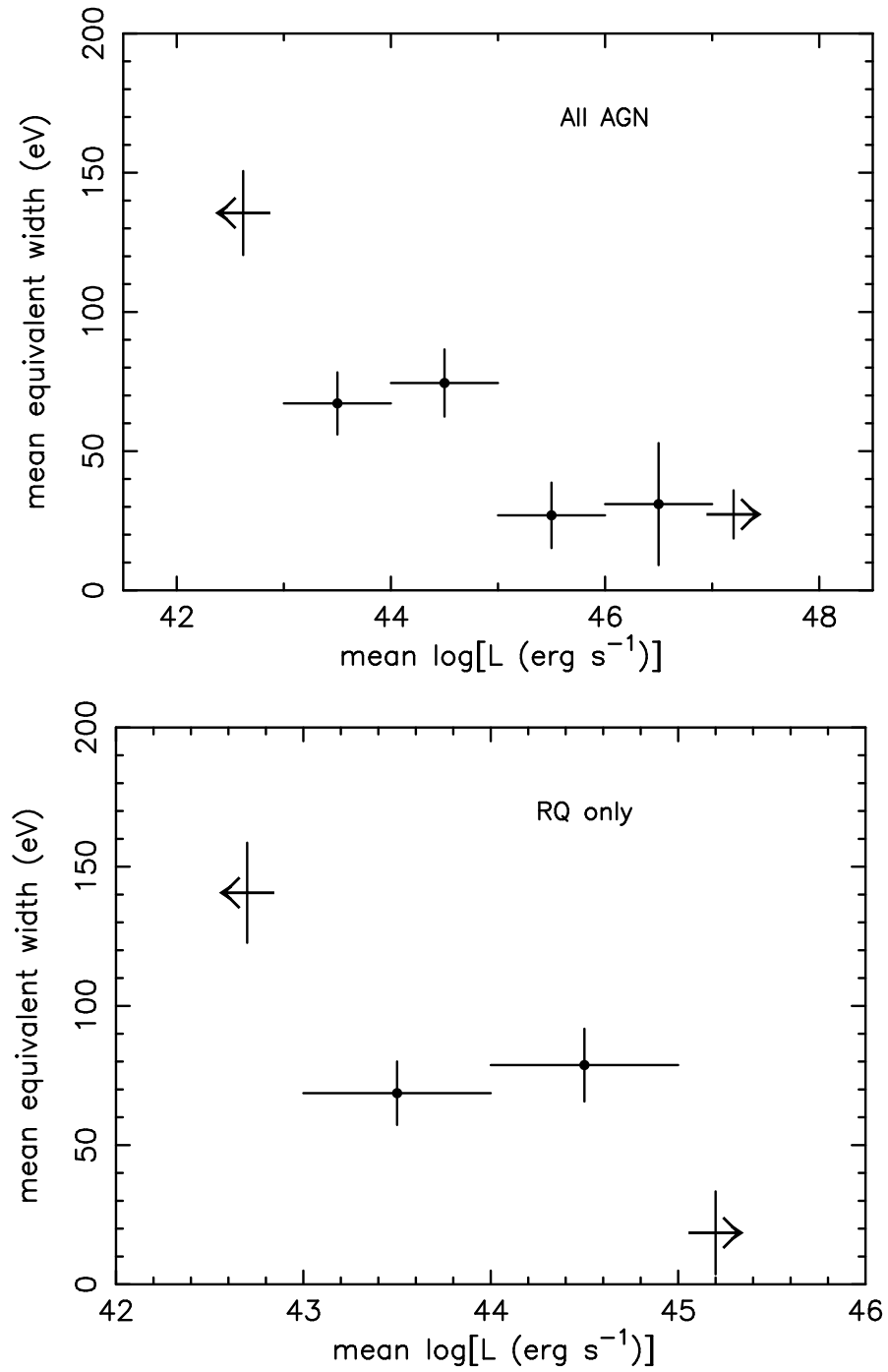


FIGURE 6.3. Averaging the iron line equivalent widths within luminosity bins clearly shows the X-ray Baldwin effect, even when excluding the radio-loud objects (bottom plot).

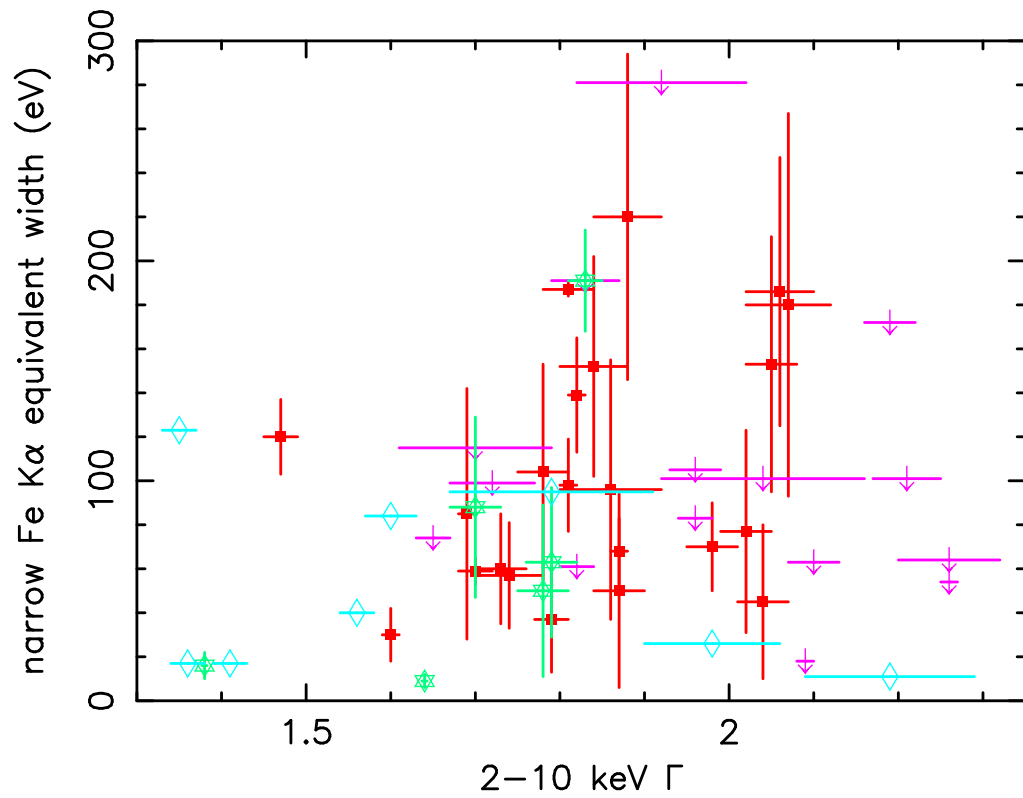


FIGURE 6.4. The equivalent width of the Fe K α line against the rest frame 2–10 keV photon index. Symbols as in Figure 6.1.

6.2 Discussion

Suggestions for the origin of the neutral Fe K α line include the putative molecular torus, or the BLR; these theories will be investigated in the following sections, considering both the feasibility of the line production and possible explanations for the X-ray Baldwin effect.

6.2.1 The broad-line region

Yaqoob et al. (2001) give the following equation for the EW of the narrow line in AGN for low optical depths, based on a model for the BLR:

$$EW_{FeK\alpha} = 42 \left(\frac{f_c}{0.35} \right) \left(\frac{\omega_K}{0.34} \right) \left(\frac{A_{Fe}}{4.68 \times 10^{-5}} \right) \left(\frac{N_H}{10^{23}} \right) \times \left(\frac{3.2}{\Gamma + 1.646} \right) \left(\frac{E_K}{7.11} \right) \left(\frac{E_{K\alpha}}{E_K} \right)^\Gamma \text{ eV} \quad (6.1)$$

where E_K is the energy of Fe K edge (7.11 keV for neutral iron) and $E_{K\alpha}$ the central energy of the line, both in units of keV. f_c is the fraction of the sky covered by BLR clouds; A_{Fe} , the abundance of iron relative to hydrogen, where 4.68×10^{-5} is the Solar value; N_H , the column density of the clouds (cm^{-2}) and ω_K , the fluorescence yield (= 0.34 for neutral Fe).

Based on this particular BLR model, Yaqoob et al. find that the strength of the Fe $K\alpha$ line in NGC 5548 is likely to be too large to come simply from the BLR; the predicted EW is 36 eV, whereas the measured value is almost four times larger, at 133 eV. They suggest that these differences could be explained by a decline in the continuum level shortly before the observation; in this event, the line would not have had time to respond to the smaller continuum level and, so, would appear unusually strong. It should be noted that Pounds et al. (2003b) obtain a lower equivalent width of ~ 60 eV during an *XMM* observation performed approximately a year and a half after Yaqoob's *Chandra* pointing, when the continuum flux was a factor of two lower. This suggests that the narrow line may have remained largely constant during this time.

Whatever the explanation for NGC 5548, if the BLR origin is correct, the reason why most of the objects in Table 6.1 have relatively high EW values compared to those predicted by the above equation must be explained. It must also be determined whether a variation in the parameters could explain the observed EW-luminosity correlation. The iron K line is produced by a different physical process (fluorescence) from the optical/UV emission lines (recombination). Nevertheless, changes in covering factor or abundance, for example, might be reflected in the BLR optical/UV lines, so the existence of such correlations is briefly examined.

One possibility is that the covering fraction of the BLR clouds is systematically underestimated in the above formula and decreases with increasing luminosity. There is no independent evidence for very high BLR covering factors, however, and the observed EW of optical/UV lines can be reproduced using modest values (few 10s of %). For the AGN sample used here, no correlation is found between the EW of the narrow iron line and those of CIV $\lambda 1549$ and Ly α (values taken from Wang, Lu & Zhou 1998 and Constantin & Shields 2003). Likewise, no correlation is found with the H β /CIV ratio which can be used as a ionisation diagnostic, or with the H β FWHM (obtained from Dewangan 2002; Kaspi et al. 2000) or EW (Marziani et al. 2003; Véron-Cetty, Véron & Gonçalves 2001); this is shown in Figure 6.5. H β line fluxes were taken from Marziani et al. (2003), Cruz-González et al. (1994) and Mulchaey et al. (1994).

Comparing the slope of the Baldwin relation is not straight-forward, as different optical/UV lines show different slopes. For example, Croom et al. (2002) find a correlation for the CIV line, produced in the BLR, of $EW \propto L^{-0.128 \pm 0.015}$. They also find $EW \propto L^{-0.07 \pm 0.008}$ for the CIII] blend (CIII], AlIII and SiIII]). Dietrich et al. (2002) give a list of Baldwin effect slopes for different emission lines, varying between ~ -0.24 and $+0.02$ and Green et al. (2001) find a similar range. The overall impression in the optical/UV is of a correlation between the slope of the Baldwin relation and the ionisation potential, suggesting a change in the average continuum shape with luminosity or redshift (depending which dominates the correlation found in a particular study). It is possible that the X-ray Baldwin effect found here is produced by a corresponding variation in the illumination pattern of the fluorescing material, although it might then be expected to see some correlations with the observed optical/UV lines.

Alternatively it could be argued that the iron abundance has been underestimated and varies with luminosity. Predicting the trend of metallicity in AGN is complicated since their evolutionary history is not sufficiently well known. BLR metallicities appear to be near-Solar, but comparison of BLR observations with detailed photoionisation models suggest that BLR metallicity *increases* with luminosity (e.g., Hamann & Ferland 1993; Shemmer & Netzer 2002). This is opposite to the trend expected if the X-ray Baldwin effect is to be explained by an abundance effect. For the present sample, there is no

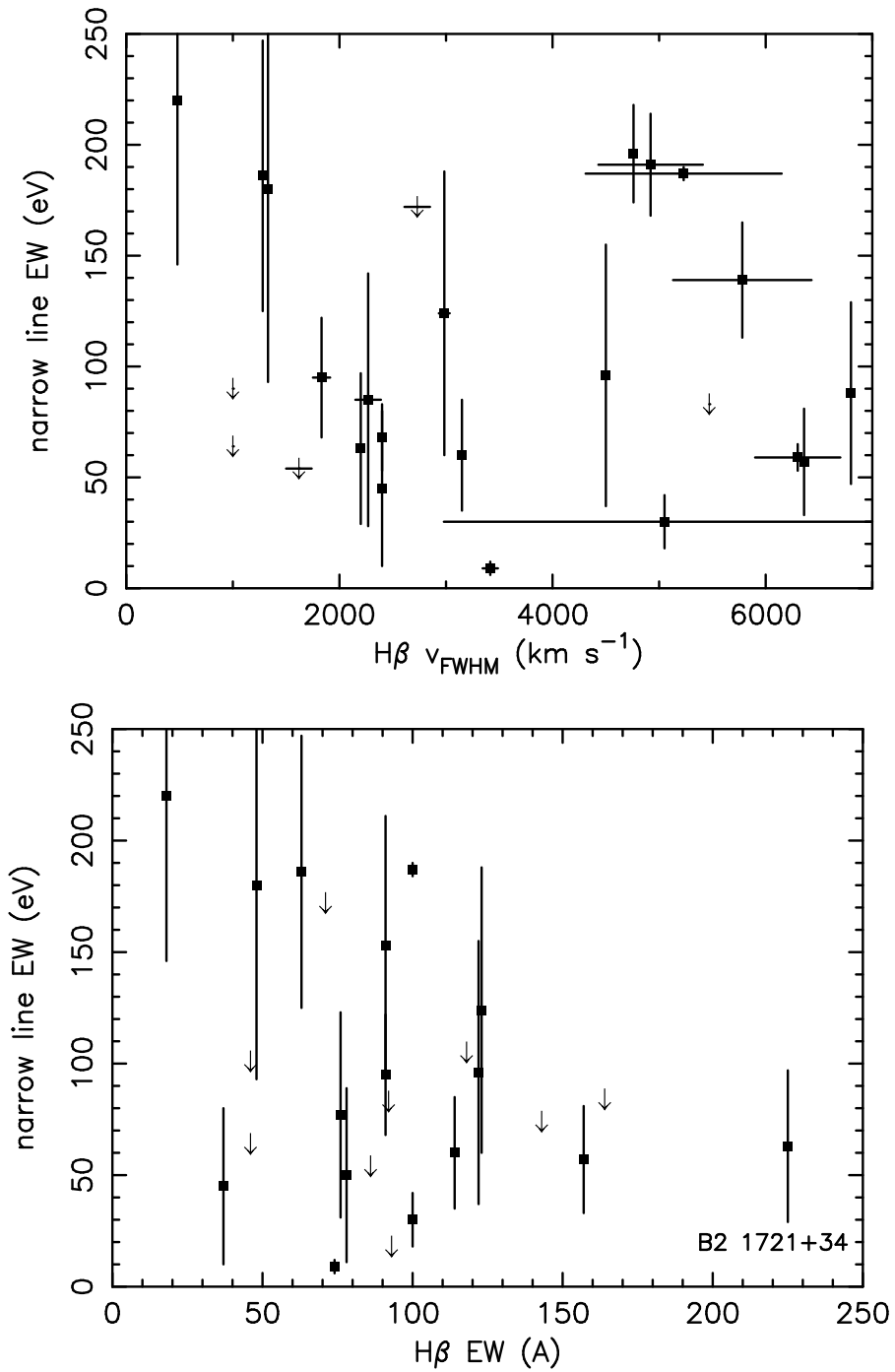


FIGURE 6.5. A comparison of the equivalent width of the narrow Fe $K\alpha$ line and the FWHM and EW of H β .

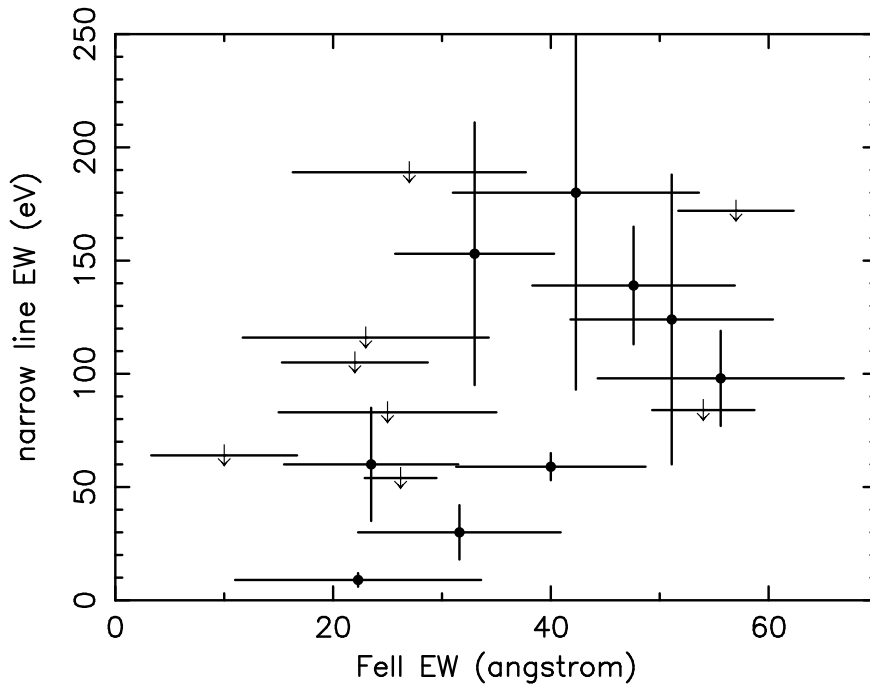


FIGURE 6.6. The equivalent widths of the optical Fe II and X-ray Fe $K\alpha$ lines.

correlation between the strength of the X-ray Fe $K\alpha$ line and the optical Fe II feature at $\lambda 4590$ (Figure 6.6; Marziani et al. 2003).

The predicted EW is linearly dependent on column density in Equation 6.1, but Yaqoob et al. (2001) note that the approximations are only valid for $N_H < 5.6 \times 10^{23} \text{ cm}^{-2}$ (i.e. assuming an Fe K absorption optical depth much less than unity). Although some BLR models suggest higher column densities (e.g., Radovich & Rafanelli 1994; Recondo-Gonzalez et al. 1997), values $\sim 10^{23} - 10^{24} \text{ cm}^{-2}$ are considered ‘normal’.

Typical BLR velocities are of the order 5000 km s^{-1} , which is resolvable by *Chandra*. To date, the velocity width of the narrow iron line has only been measured a few times, and the results are not entirely consistent. Kaspi et al. (2002) resolved the line profile of NGC 3783 with the *Chandra* High Energy Transmission Grating Spectrometer (HETGS), finding a FWHM velocity of $\sim 1700 \text{ km s}^{-1}$, which is low for a BLR but consistent with originating in the inner part of the torus. Likewise, Ogle et al. (2000) obtain a FWHM value of $1800 \pm 200 \text{ km s}^{-1}$ for the narrow Fe $K\alpha$ line detected in NGC 4151. The width of the iron lines in MCG–6–30–15 have also been measured

with the HETGS. The situation is complicated by the presence of the various different components of the line in this object, both resolved and unresolved, narrow and broad. However, Lee et al. (2002) obtain a width of $11\,000_{-4700}^{+4600}$ km s⁻¹ for the resolved narrow component when considering the full observation; this drops to 3600_{-2000}^{+3300} km s⁻¹ for the ‘high’ flux state. Within the errors, these measurements are consistent with a FWHM of ~ 6000 km s⁻¹, which would indicate that the line is not formed in the torus. Yaqoob et al. (2001) measure a FWHM of ~ 4500 km s⁻¹ for NGC 5548, which also supports an origin in the BLR.

It should be noted that, although the measurements are all broadly consistent, and indicate an origin in either the outer BLR or torus, there are relatively few grating measurements of the line, so it is unclear how narrow the line core truly is. An alternative possibility is that the ‘narrow’ lines may actually be formed in the accretion disc itself. Nayakshin (2000b,c) discusses how a Baldwin effect could be produced by the ionisation of the skin of the disc, as the luminosity increases. A recent paper by Yaqoob et al. (2003) suggests that such narrow lines may come from a disc which is viewed face-on and has a flat emissivity profile. Similar suggestions have been made for optical/UV BLR lines. However, as mentioned above, no correlation is found here between the narrow iron line EW and the H β parameters. There is a difference between the BLRs found in Narrow Line and Broad Line Seyfert galaxies – the NLS1s show much narrower emission lines, hence their name. It has been previously noted that NLS1s tend to show weaker H β emission (e.g., Gaskell 1985) and this was confirmed upon comparing the H β EW of samples of NLS1s and BLS1s (taken from Marziani et al. 2003) – Student’s T-test gave a very low probability of the two groups originating in the same population, with the NLS1s having a much lower mean EW. Considering the few objects in the present sample, this difference in line strengths is also found. When comparing the Fe K α EWs, however, there is no appreciable difference between the narrow- and broad-line samples, shown both by the T-test and ASURV (to account for the upper limits).

Possible support for the accretion disc origin lies in the variability of the narrow line in Mrk 841 (Petrucci et al. 2002). They find that the line varied between two observations separated by 15 hours, although, within the errors, the change in line flux is not large.

Such a rapid variation is hard to explain if the line is formed in distant reprocessing matter, indicating its origin might be closer to the central engine; the line width is only constrained to be < 170 eV. To date, Mrk 841 is the only object in which this variation has been observed.

Overall, the BLR remains a possible source for some of the narrow iron emission. It is not, however, presently possible to explain how the BLR alone could produce the strongest observed narrow lines, nor why the Baldwin relation should exist. In particular, it is unclear why the most luminous objects should have fairly normal BLRs compared to the lower-luminosity objects, as judged from their optical/UV BLR lines, yet have no detectable narrow 6.4 keV iron line.

6.2.2 The molecular torus

Krolik, Madau & Życki (1994) discuss the production of the iron $K\alpha$ line in the torus. They compute that for a Thomson optical depth, τ_T , of 0.5–1, the EW of the line should be of the order 100 eV, assuming a unobscured view; for $\tau_T = 2$, this value approximately halves, to 55 eV. They also find a small decrease in EW for increasing opening angle of the torus. The value of ~ 100 eV, for a low optical depth, is, as they point out, in broad agreement with the EW measured in many Seyfert 1 galaxies, suggesting that the Fe $K\alpha$ emission line could be due solely to reflection/fluorescence from the torus and not linked to the accretion disc or BLR at all. Ghisellini, Haardt & Matt (1994) also mention that the torus could produce an emission line of EW ~ 90 eV, if the column density is $\gtrsim 10^{24}$ cm $^{-2}$. It should be noted that both of these papers used a value of 3.31×10^{-5} for the Solar abundance of iron, rather than the 4.68×10^{-5} assumed by Yaqoob et al. (2001). Assuming the EW scales linearly with the abundance, the values from Krolik, Madau & Życki (1994) and Ghisellini, Haardt & Matt (1994) should be scaled to ~ 141 or ~ 127 eV, respectively, to compare to the result from Yaqoob et al. .

As mentioned earlier, the presence of a neutral reflection component would indicate the existence of cool, Compton thick material (Guilbert & Rees 1988; Lightman & White 1988; George & Fabian 1991), such as the torus. Some of the spectra here show evidence

for such reflection, although the values are generally poorly constrained. This is not entirely surprising though, since most of the objects are at fairly low redshift, meaning that the rest frame bands covered by *XMM* do not extend much above ~ 10 keV, while the Compton reflection hump is expected to peak around 30–50 keV. If, however, reflection components are not found in the spectra, this does not necessarily rule out the torus as the origin of the narrow line. Instead, the material of the torus could be Compton thin; if this were the case, no strong reflection component would be expected. Matt, Guainazzi & Maiolino (2003) show that, for a Compton thin torus with $N_H = 10^{23} \text{ cm}^{-2}$, a fluorescent iron line with $EW \sim 100 \text{ eV}$ can be formed. This is, therefore, a further possibility for production of the narrow line.

Königl & Kartje (1994) discuss a dusty disc-driven hydromagnetic wind model for the torus, finding that, if $L_{IR} \gtrsim 1.5 \times 10^{42} (M_7) \text{ erg s}^{-1}$, where L_{IR} is the 2–100 μm infrared luminosity and M_7 the black hole mass in units of $10^7 M_\odot$, then the radiation pressure force could be expected to flatten the dust distribution; this causes the opening angle of the torus to increase, leading to a reduction in the covering factor. This relates to Krolik et al. (1994), who found that the EW of the Fe $K\alpha$ line decreases slightly with increasing opening angle. Similarly, Mushotsky & Ferland (1984) proposed a luminosity-dependent ionisation parameter and, hence, covering factor to explain the original Baldwin Effect.

An alternative explanation, suggested by Ohsuga & Umemura (2001), is that relatively low-luminosity AGN are more likely to contain dusty walls of gas, supported by radiation pressure from a circumnuclear starburst; the stronger radiation pressure from the more luminous AGN may prevent these from forming.

If the X-ray Baldwin effect is, indeed, caused by a decrease in the covering factor of the torus, then this has implications for the number of Type-2 QSOs. Many Seyfert 2 galaxies are known, but very few obscured QSOs have yet been discovered (e.g., Derry et al. 2003 and references therein). A luminosity-dependent drop in the covering factor goes some way towards explaining the lack of high luminosity obscured sources, although obscuration should still arise due to mergers and the birth of the QSOs.

6.3 Summary

There is an apparent X-ray Baldwin effect for the narrow, neutral iron line observed in many AGN: as the 2–10 keV rest frame luminosity increases, the equivalent width of the line drops. The reason for this correlation is uncertain, but one possibility is a decline in the covering factor of the putative molecular torus as the luminosity increases. This decrease in covering fraction could be due to increased radiation pressure flattening the torus, leading to an increased opening angle and, hence, smaller covering factor. Although the BLR remains a possibility for the origin of the narrow line, it is difficult to explain how the strongest lines could be formed, or what it is that leads to the Baldwin effect.

The negative correlation between EW of the line and the luminosity of the object is not solely due to a dilution effect by beaming in the radio-loud sources, since the effect is also observed in the radio-quiet objects alone.

Given the resolution of EPIC and the *Chandra* HETGS, it is not currently possible to rule out the origin of the line being either the BLR clouds or reflection off a distant torus. Future observations with calorimeter-based X-ray detectors (such as the X-ray Spectrometer on-board *AstroE2*, or *XEUS*) will provide sufficient spectral resolution, of the order a few hundred km s^{-1} , to be able to resolve this issue.

Chapter 7

Summary and discussion of results

7.1 The soft excesses in low- and high-luminosity AGN

In Chapters 2 and 3, the soft excesses in low- and high-luminosity AGN (Seyfert galaxies/NLS1s and QSOs respectively) were investigated. For each object, the soft excess was first modelled with a simplistic blackbody parameterisation, where between one and three different temperature components were required to obtain a good fit, the most significant lying between ~ 100 – 200 eV. Since the temperatures obtained are too high to be reasonably due to direct emission from the accretion disc, a more physical Comptonisation model was then tried. A two-component structure allows both the power-law at high energies and the soft excess below ~ 2 keV to be understood in terms of disc photons interacting with different temperature populations of electrons. Using this model, it appears that there are two ‘stages’ to the Comptonisation of the disc photons: some photons are Comptonised twice, first by the soft excess corona, then by the power-law electrons. This is statistically preferred over disc photons either interacting with the soft excess electron population *or* the power-law one.

It was found that the correlations were generally the same for both the low- and high-luminosity samples:

- there is no link between the strength of the soft excess (ratio of BB luminosity to

power-law luminosity over the observed 0.2–10 keV band) and the X-ray luminosity of the object

- the relative strength of the soft excess is not correlated with the optical to X-ray slope, α_{ox} ; however, α_{ox} seems to anti-correlate with the slope of the soft excess
- luminous AGN have luminous soft excesses
- the temperature of the soft excess (when modelled with a Comptonised component) does not depend on the luminosity of the source.

There was found to be a difference when comparing the soft excess strength and the 2–10 keV power-law slope between samples of objects, in that there was a positive correlation for the lower luminosity objects, while the QSOs showed no such correlation, mainly because of four individual objects, as was discussed in Chapter 3. However, the Seyfert correlation is dominant when considering all the AGN (Fig. 7.1), leading to a Spearman Rank probability of 96% and a regression slope of 25 ± 2 . If the four outlying QSOs are excluded, the Spearman Rank value improves to 99%. This correlation may be linked to a cooling effect, due to increased photon number. The Comptonisation model presented in this thesis (Chapters 2, 3 and 4) implies that the photons leading to the power-law at higher energies have probably interacted with the soft excess electrons first, before being Comptonised a second time. Hence, when the soft excess is stronger, the presence of more photons provides the opportunity for more energy-exchanging interactions with the hotter electron population, thus cooling it and leading to a steeper slope. Fig. 7.1 shows that the power-law (2–10 keV) slopes are very similar for both Seyfert galaxies and QSOs, so are not dependent on luminosity or redshift. (Recall that almost all the objects in this combined sample are radio-quiet, so the harder slopes seen in radio-loud quasars will not be apparent.)

Comparing the temperatures of the soft excesses of both low- and high-luminosity objects obtained from the Comptonisation model (Fig. 7.2), it is found that there is no difference between the values measured for Seyfert galaxies and QSOs. Using weighted linear regression, there is a small indication that the more luminous objects may have

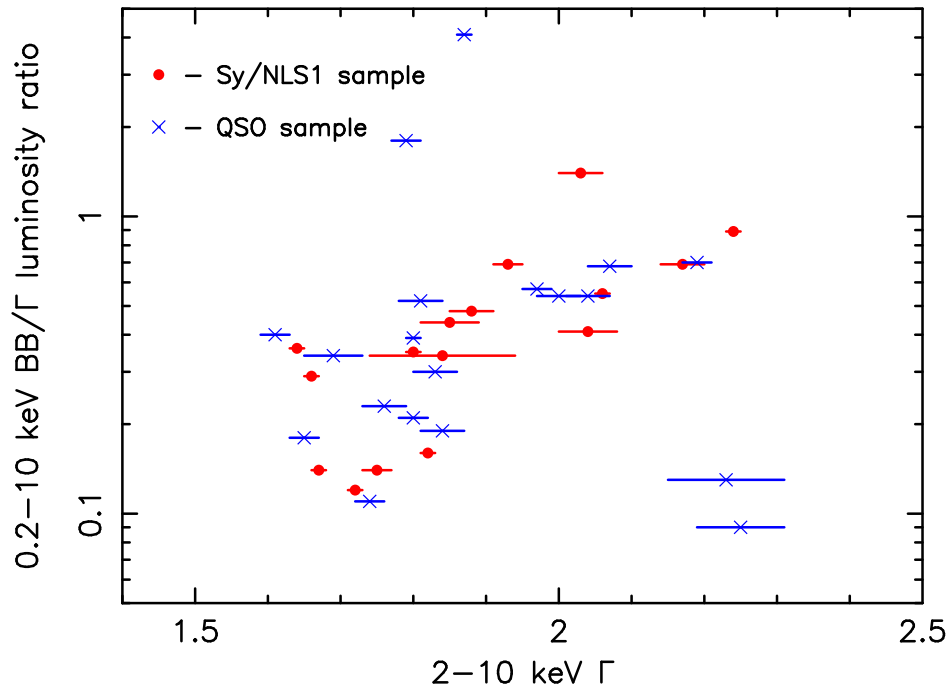


FIGURE 7.1. The stronger soft excesses correspond to those objects with the steeper 2–10 keV power-law slopes. This is likely to be a cooling effect. To simplify matters in this, and subsequent, plots, no differentiation is made between radio-quiet/radio-loud QSOs or between BL/NLS1s.

slightly hotter soft excesses [slope $\sim (6 \pm 0.4) \times 10^{-4}$], when considering both QSOs and Seyfert galaxies together. This is largely dependent on the two most luminous objects, although, even without them, the slope is still positive. Spearman Rank only gives a probability of 14%, however, which is insignificant.

Figure 7.2 also plots the results of the relative strength of the soft excess against the object luminosity for both Seyferts and QSOs. The ratio only varies by about an order of magnitude, and over the same range for both samples, implying there is no difference between the relative strengths of the soft excesses in Seyfert galaxies and QSOs. Statistical tests confirm there is no real correlation, with Spearman Rank giving a probability of only $\sim 60\%$ for a negative relationship. Ignoring the unusually strong soft excess in PDS 456, the mean ratio for the Seyfert galaxies is ~ 0.47 , very similar to the mean value of 0.44 for the QSOs. Comparing the optical depths found for the soft excesses also shows no difference between the values for QSOs and Seyferts (Fig. 7.3;

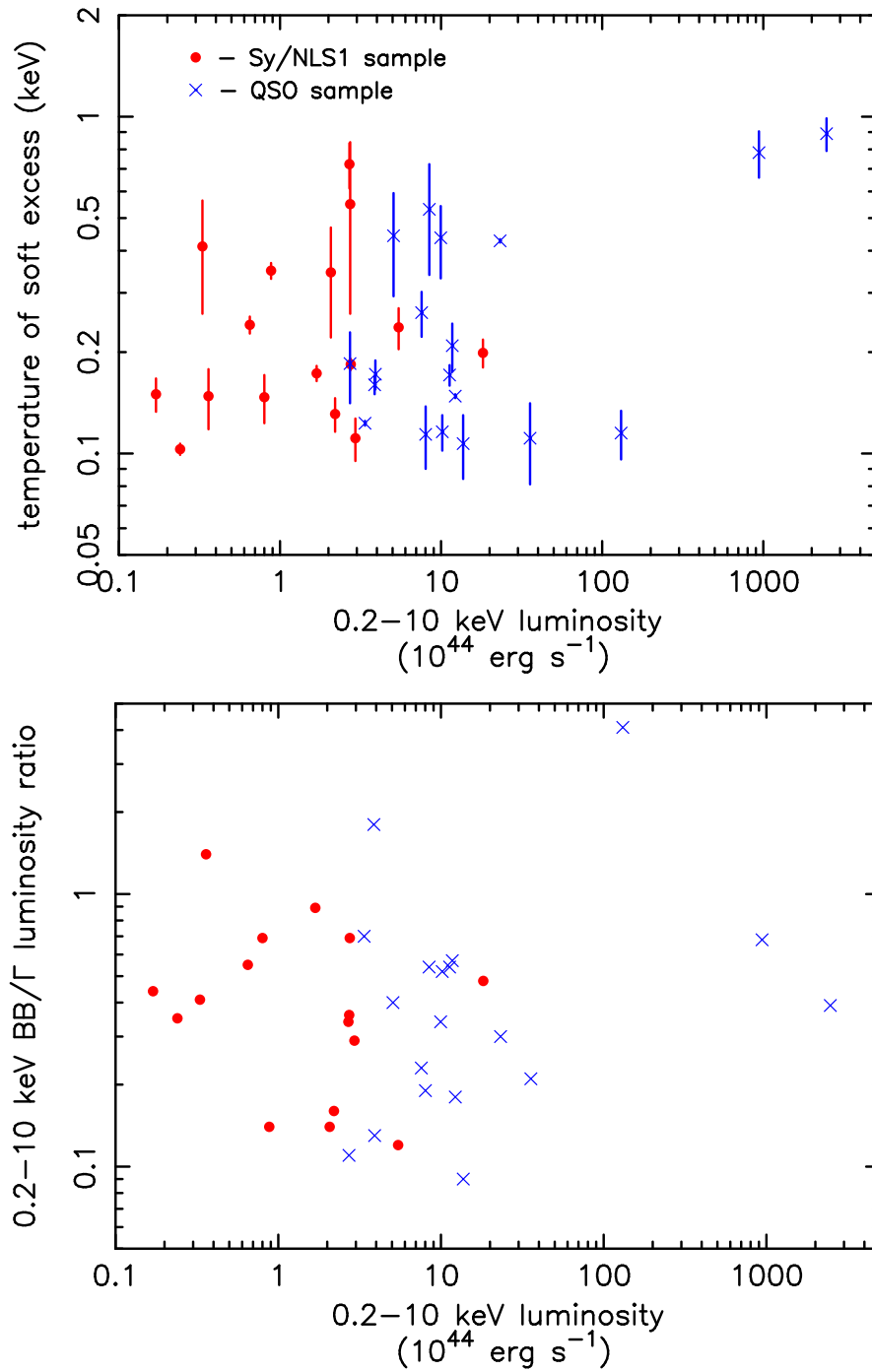


FIGURE 7.2. The soft excesses of Seyferts and QSOs have comparable temperatures and strengths.

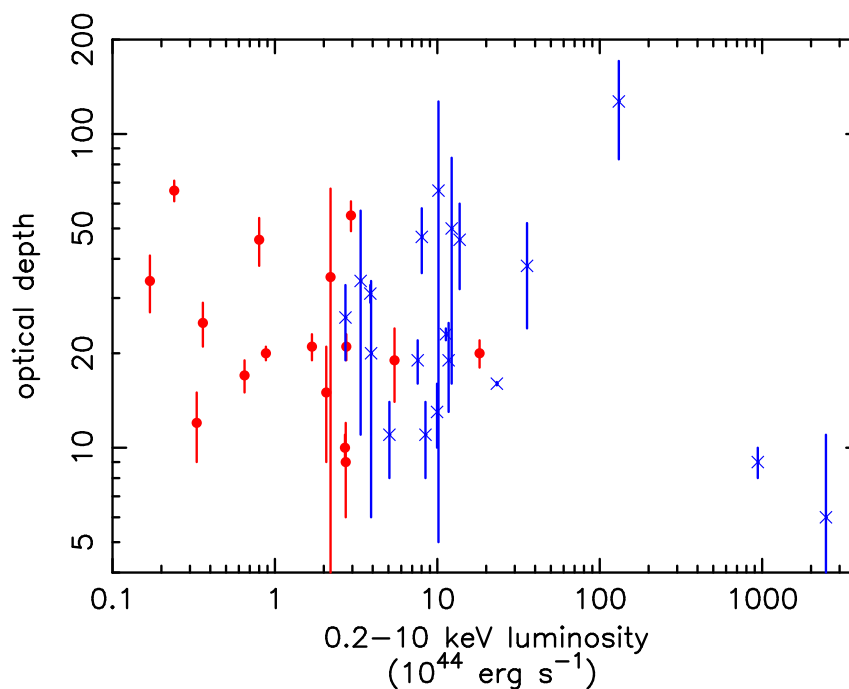


FIGURE 7.3. The soft excesses of QSOs and Seyfert galaxies show the same range of optical depths. Legend as in Fig. 7.2.

probability of 64% for a negative correlation).

Finally, the slope of the soft excess was plotted against the 0.2–10 keV luminosity and the luminosity of the Comptonised soft excess component (Fig. 7.4); no correlation is found between the values. $\Gamma \sim 1/(kT \tau^2)^{1/2}$ (from Equation 1.9), which implies that, if the temperature, kT , and the optical depth, τ , were related to the luminosity in the same way (i.e., both positive or both negative correlations), then they would reinforce each other, making the Γ -luminosity correlation stronger. However, as shown above, there is a *hint* of kT being slightly higher for the more luminous objects (when using the linear regression method), while the optical depth decreases (although neither Spearman Rank correlation is statistically significant). As is shown in the lower section of Figure 7.4, when comparing all the Seyferts and QSOs the steeper soft excesses are not necessarily brighter. Such a correlation (steeper \Rightarrow brighter) was found for the three individual objects in Chapter 4; this appears to be a characteristic ‘internal’ to the objects. That is, if the slope and luminosity of the soft excess were to be measured repeatedly for any one object, it is possible that, certainly over the extended 1 eV–10 keV band, there would be

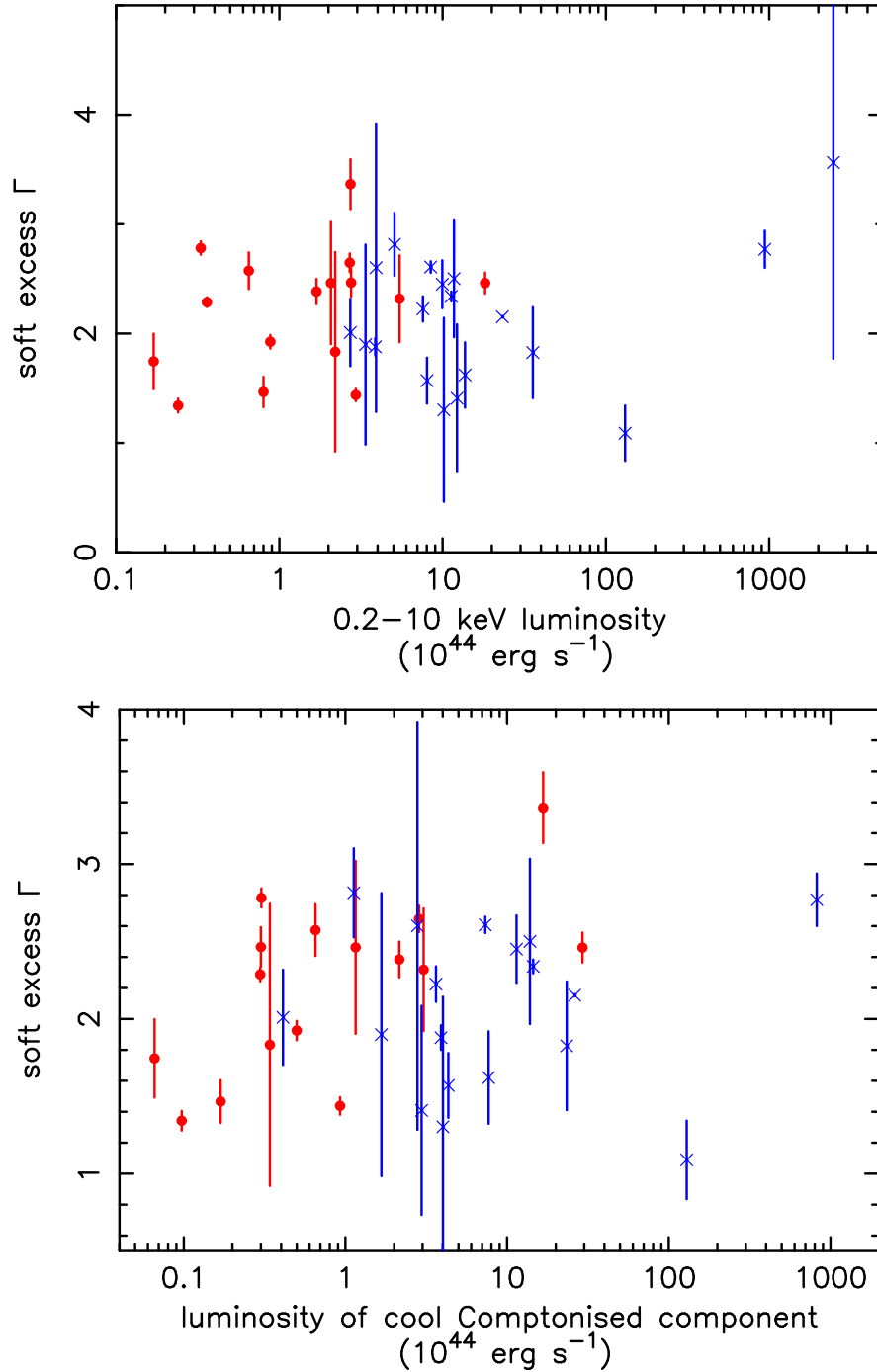


FIGURE 7.4. There is no difference in the soft excess slopes between the Seyfert and QSO samples: soft excess Γ is independent of 0.2–10 keV luminosity. Likewise, the steeper slopes do not necessarily correspond to the more luminous soft excesses. Symbols as in Fig. 7.2.

a positive correlation.

Of the different groups of AGN covered in this work, Broad Line Seyfert galaxies are thought to have relatively low mass black holes, together with a low(ish) accretion rate, while QSOs are high mass, high accretion rate objects (e.g., Wandel 2003; Boroson 2002). Narrow Line Seyfert galaxies lie in-between, with similar masses to the Broad Line Seyferts, but accretion rates comparable to those found in the more luminous QSOs (e.g., Czerny et al. 2001). The results appear to indicate that the almost ubiquitous soft X-ray excess found in AGN is not directly related to accretion rate or black hole mass: temperatures, optical depths and relative strengths cover the same ranges for both Seyferts and QSOs. Alternatively, it can be said that the soft excess does not depend on the temperature of the accretion disc, since $T_{disc} \propto (\dot{M}/M)^{1/4}$ from Equation 1.7.

So what is it that drives the differences in the soft excesses *between* objects? (The variations found within separate objects are discussed below.) Objects with differing accretion rates and black hole masses seem to have similar soft excesses. The apparent lack of dependence on accretion rate implies that the over-heated disc model, discussed in Section 1.3.5, may not be the route for the formation of the soft excess corona, since this depends on an increasing accretion rate leading to the ionisation of the disc and, hence, the formation of the corona. If this were to be the case, then it would be expected that differing accretion rates between AGN would lead to variations in the soft excess corona; this does not seem to occur. The other suggestions for the formation of the corona/soft excess (e.g., advection dominated accretion flows, an ionised skin on the disc due to irradiation by hard X-rays; see Section 1.3.5) are not so reliant on changes in accretion rate.

One idea is that there could be changes in the soft excess corona linked to magnetic fields within the accretion disc. Magnetic reconnection has been suggested as the method of heating the hotter electron population – that which is theorised to produce the apparent power-law (e.g., Merloni & Fabian 2001); it is also thought to be the method by which the Solar corona is heated to such high temperatures [a review of the Solar corona and its heating mechanisms is given by Parnell (2002)]. It could be that magnetic effects also cause the differences in the soft excess. Further work is clearly needed in this area.

7.2 Time variability of the soft excess

In Chapter 4, the soft excesses of three AGN were studied over periods of time ranging from 1.5 to 4.5 years. Over these timescales, each of the objects showed variability in their soft excess, with the changes identified in 3C 273 and 1H 0419–577 being consistent with Compton cooling of the soft excess corona. It is also possible that PKS 0558–504 shows this same cooling effect, although the decrease in both temperature and optical depth of the corona cannot be separated. The cooling results from an excess flux of photons from the accretion disc; the thermal photons are Comptonised by the electrons in the postulated corona above the disc, thus removing energy and cooling the population. In this way, the resultant power-law softens, becoming noticeably steeper.

For all three objects in Chapter 4, it is found that, when considering the total soft excess (that is, when extrapolating the Comptonisation model to energies below the *XMM* band), the soft components are brighter when their slopes are steeper. This is likely to occur when the accretion rate of the object increases.

To summarise, if the black hole mass is constant (most easily investigated for a single object) and the accretion rate increases, the Comptonising, soft excess corona is cooled by the influx of more photons; the cooling of the corona manifests itself as a steeper slope, since $\Gamma \sim 1/(kT \tau^2)^{1/2}$, which is found to be more luminous. If, however, both mass and accretion rate vary (i.e., when comparing large samples of objects such as in Chapters 2 and 3), correlations become entangled and confused, leading to the similarities between the soft excesses observed in QSOs (thought to have relatively high accretion rates and black hole masses) and Seyferts (lower rates, for the broad-line objects at least, and lower mass black holes).

7.3 High redshift QSOs

Chapter 5 investigated a sample of relatively distant radio-quiet QSOs, with a mean redshift of 1.40. No spectral evolution was found, with the 2–10 keV power-law slopes

showing a scatter which is not related to redshift. This dispersion in photon index was found to be intrinsic and not due to obscuration effects. The observed lack of correlation between slope and redshift/luminosity may suggest that the luminosity of these QSOs is simply scaling as the black hole mass – i.e. \dot{M} remains constant with respect to the Eddington value, as the overall spectral energy distribution remains unchanged. Different values of the accretion rate could then be responsible for some of the dispersion of the spectral slopes that is observed (e.g., Liu, Mineshige & Shibata 2002). This is, as discussed previously, thought to be the case for NLS1s, with the soft spectra being explained if the objects are accreting at a greater fraction of the Eddington rate, when compared to the broad line AGN (Pounds, Done & Osborne 1995). Alternatively, the spread of slopes may be due to different disc-corona geometries (Czerny & Elvis 1987; Fabian et al. 2002a).

No rest frame absorption was measured, agreeing with previous work which found that radio-loud QSOs tend to show additional N_H , while the radio-quiet objects do not. The objects covered in this high- z sample are relatively faint and only weak soft excesses were found, with $L_{SoftExcess} < 10\% L_X$; this is broadly consistent with the results from Chapters 2 and 3, though.

Finally, the indication of a flattening of the spectral slope above ~ 3 keV suggests the presence of a reflection component. This was, however, only noticeable when considering the entire sample of AGN, with the effect being too weak to measure in the individual spectra. Such a reflection component could naturally arise from X-rays scattering off optically thick material, such as the inner accretion disc, subtending $\sim 2\pi$ steradians to the X-ray source. Another possible contribution is by reflection off the distant molecular torus predicted from AGN unification schemes (Chapter 1).

7.4 The narrow Fe $K\alpha$ line

The ubiquity of the narrow Fe $K\alpha$ line was investigated in Chapter 6. Plotting the equivalent widths of the narrow lines against the intrinsic 2–10 keV luminosity of the objects, it was found that the strength of the line decreases in the higher-luminosity objects. This

is not simply a dilution effect due to beaming in the radio-loud objects and is suggested to be due to a decrease in covering factor of either the molecular torus, or the Broad Line Region; it is not currently possible to state for certain in which region the narrow line is formed.

This illustrates a difference between the production methods for the soft excess and the narrow line. As discussed above, the soft excess does not appear to be dependent on X-ray luminosity. The Fe $K\alpha$ line, however, becomes weaker at higher luminosities.

Now also seems a suitable time to remark that many X-ray properties of radio-quiet and radio-loud QSOs are the same. As discussed in Chapter 5, RLQs have flatter/harder X-ray slopes and more frequently an intrinsic absorption component than do the RQQs. However, in this work, no difference is found between their soft excess parameters, albeit with a limited sample, and, although the RLQs sometimes seem to have weaker iron lines, this is due to their higher luminosities, rather than being related to the radio emission.

The soft excess appears to be a ubiquitous property of Seyferts and QSOs, at all X-ray luminosities, accretion rates and black hole masses. The Fe $K\alpha$ line, however, is only a common feature in the X-ray spectra of low-luminosity AGN. Thus, the two components are not likely to be directly related, although neither seem to be involved with emission from the radio jets.

7.5 Past and future work

This thesis has concentrated mainly on the soft excess which is found in the vast majority of X-ray spectra of active galaxies. A lot has been learnt about AGN since their ‘discovery’ by Carl Seyfert in 1943, with the first X-ray observations being performed in the 1960s. Initially the spectra were thought to be simple power-laws. Then, in the 1980s, it was discovered that some of the objects could not be fitted by a single slope over a wide energy band and that the softer band ($\sim 0.2\text{--}4.5$ keV) showed slopes different from $\Gamma = 1.7$, which was, at the time, thought to be the mean, underlying value at

higher energies; this was the first indication of the so-called soft excess. Also around this time, *Ginga* data showed Fe $K\alpha$ emission to be quite common, and a spectral flattening above ~ 8 keV was identified and attributed to the reprocessing of X-ray photons by cold material. This led to the understanding that the ‘typical’ photon index was actually steeper than first thought, at around $\Gamma = 1.9$. See the introduction to Mushotsky et al. (1993) for more details and relevant references.

This thesis has investigated the X-ray spectra of a wide range of objects, both low- and high-luminosity and at low and high redshifts. It is found that all such AGN seem to show soft excesses, with no obvious differences when comparing the broad samples. If the variability of the soft excess within a certain object is followed, it is found that a higher accretion rate leads to a more luminous, though cooler, soft component. The strength of the neutral, narrow iron line is found to decrease for the more X-ray luminous AGN, implying that its formation is completely distinct from that of the soft excess.

In order to improve our knowledge of the soft excess, the samples presented here need to be extended. Most of the objects in this thesis lie within a luminosity band of $\sim 10^{44-45}$ erg s $^{-1}$, with relatively few at high luminosities. Increasing this number would obviously help to determine whether the weak correlations found (e.g., the Comptonised temperature being slightly hotter for the more luminous objects) are real, or simply artifacts of a limited sample size. Following the same train of thought, more NLS1s and, in particular, radio-loud quasars really need to be included, to allow a more detailed investigation across the whole spectrum of AGN. As mentioned in the summary of Chapter 4, monitoring of more AGN would improve our understanding of how soft excesses vary within objects. These should also span a wide range of luminosities, to try and discover whether all soft excesses vary in a similar fashion.

The work presented here has assumed that the current theories that QSOs have higher black hole masses and accretion rates than do BLS1s – and that NLS1s probably have high accretion rates for relatively small central masses – are correct. This is an area of Astrophysics where there is much room for improvement, since the vast majority of AGN do not have measured black hole masses, and accretion rate estimates rely on these values. There are various ways to estimate the mass, including reverberation mapping

of the BLR (see, e.g., Wandel 1999), photoionisation theory (i.e., the mass depends on the source luminosity and ionisation structure of the BLR; Wandel, Peterson & Malkan 1999) and the use of power density spectra (which are rescaled to the spectrum of Cyg X-1 in its hard state by a horizontal shift, the magnitude of which depends on the mass; Czerny et al. 2001); however, these methods do not always lead to identical estimates of the mass (see, e.g, Czerny et al. 2001). It seems sensible, therefore, to obtain as many estimates as possible for the black hole masses in different AGN using the same method.

With the launch of the γ -ray mission *INTEGRAL* (International Gamma-Ray Astrophysics Laboratory) towards the end of 2002 it will, hopefully, be possible to measure the roll-over point of the Comptonisation power-law at high energies, so determining the temperature of the hotter electron population; this is impossible with any of the X-ray missions, because their band-passes do not reach high enough energies. This will allow a deeper investigation into how the Comptonising populations vary between objects and may, also, determine whether the hotter electrons are thermal or non-thermal – or, indeed, whether the power-law is actually produced via Comptonisation. A particularly important task is to identify the locations of the distributions of electrons, to discover whether the soft excess and ‘power-law’ component are formed together or are completely distinct.

XEUS (X-ray Evolving Universe Spectrometer) is the European Space Agency’s follow-on to *XMM* and is due for launch in the mid 2010s. The instrument will be ~ 200 times more sensitive than *XMM*, together with having a broader energy range, of ~ 0.05 – 30 keV. One of its main scientific goals will be the detection of massive black holes in the earliest active galaxies and the estimation of their mass and spin. As mentioned above, the measurement of black hole masses is a very important area and may help to form more detailed and physical models for the accretion disc structure. Such results should lead to a better understanding of the relationship between Seyfert galaxies and QSOs.

Bibliography

- Abramowicz, M. A., Czerny, B., Lasota, J. P. & Szuszkiewicz, E. 1988, *ApJ*, 332, 646.
- Adam, G. 1985, *A&AS*, 61, 225.
- Antonucci, R. 1993, *ARA&A*, 31, 473.
- Antonucci, R. & Barvainis, R. 1988, *ApJ*, 332, L13.
- Antonucci, R. R. J. & Miller, J. S. 1985, *ApJ*, 297, 621.
- Arnaud, K. A., Branduardi-Raymont, G., Culhane, J. L., Fabian, A. C., Hazard, C., McGlynn, T. A., Shafer, R. A., Tennant, A. F. & Ward, M. J. 1985, *MNRAS*, 217, 105.
- Baganoff, F. K. et al. 2001b, *Nature*, 413, 45.
- Baganoff, F. K. et al. 2003, *ApJ*, 591, 891.
- Baldwin, J. A. 1977, *ApJ*, 214, 679.
- Ballantyne, D. R., Ross, R. R. & Fabian, A. C. 2001, *MNRAS*, 327, 10.
- Ballantyne, D. R., Ross, R. R. & Fabian, A. C. 2002, *MNRAS*, 332, L45.
- Barcons, X. et al. 2002, *A&A*, 382, 522.
- Barvainis, R. 1990, *ApJ*, 353, 419.
- Barvainis, R. 1993, *ApJ*, 412, 513.
- Bechtold, J., Elvis, M., Fabrizio, F., Kuhn, O., Cutri, R. M., McDowell, J. C., Rieke, M., Siemiginowska, A. & Wilkes, B. J. 1994, *AJ*, 108, 759.

- Bechtold, J., Siemiginowska, A., Shields, J., Czerny, B., Janiuk, A., Hamann, F., Aldcroft, T. L., Elvis, M. & Dobrzycki, A. 2003, *ApJ*, 588, 119.
- Beloborodov, A. M. 1998, *MNRAS*, 297, 739.
- Bertola, F. et al. 2003, *MmSAI*, 74, 324.
- Bian, W.-H. & Zhao, Y.-H. 2003, *PASJ*, 55, 143.
- Blaes, O., Hubeny, I., Agol, E. & Krolik, J. H. 2001, *ApJ*, 563, 560.
- Blandford, R. D. & Rees, M. J. 1974, *MNRAS*, 169, 395.
- Boller, T., Brandt, W. N. & Fink, H. 1996, *A&A*, 305, 53.
- Boller, T., Fabian, A. C., Sunyaev, R., Trümper, J., Vaughan, S., Ballantyne, D. R., Brandt, W. N., Keil, R. & Iwasawa, K. 2002, *MNRAS*, 329, L1.
- Boroson, T. A. 2002, *ApJ*, 565, 78.
- Boroson, T. A. & Green, R. F. 1992, *ApJSS*, 80, 109.
- Bowyer, C. S., Lampton, M., Mack, J. & de Mendonca, F. 1970, *ApJ*, 161, L1.
- Brandt, W. N. & Gallagher, S. C. 2000, *NewAR*, 44, 461.
- Brandt, W. N., Mathur, S. & Elvis, M. 1997, *MNRAS*, 285, L25.
- Brandt, W. N. et al. 2002, *ApJ*, 569, L5.
- Branduardi-Raymont, G., Sako, M., Kahn, S. M., Brinkman, A. C., Kaastra, J. S. & Page, M. J. 2001, *A&A*, 365, L140.
- Brinkmann, W., Yuan, W. & Siebert, J. 1997, *A&A*, 319, 413.
- Brissenden, R. J. V. 1989, PhD thesis, Australian National University.
- Bühler, P., Courvoisier, T. J.-L., Staubert, R., Brunner, H. & Lamer, G. 1995, *A&A*, 295, 309.
- Burbidge, G. R. 1956, *ApJ*, 124, 416.

- Burbidge, G. R. & Burbidge, E. M. 1967, *Quasi-stellar objects*, San Francisco:W.H. Freeman.
- Canizares, C. R. & White, J. L. 1989, *ApJ*, 339, 27.
- Cappi, M., Matsuoka, M., Otani, C. & Leighly, K. M. 1998, *PASJ*, 50, 213.
- Carroll, B. W. & Ostlie, D. A. 1996, *An Introduction to Modern Astrophysics*, Addison-Wesley.
- Cheng, K. S. & Zhang, J. L. 1996, *ApJ*, 463, 271.
- Cirasuolo, M., Magliocchetti, M., Celotti, A. & Danese, L. 2003, *MNRAS*, 341, 993.
- Clavel, J., Wamsteker, W. & Glass, I. S. 1989, *ApJ*, 337, 236.
- Colgate, S. A. & Cameron, A. G. W. 1963, *Nature*, 200, 870.
- Collin, S. & Huré, J.-M. 2001, *A&A*, 372, 50.
- Collmar, W., Schönfelder, V. & Zhang, S. 2002, γ -ray loud AGN, in 'Max-Planck Institut für Extraterrestrische Physik, Annual Report'.
- Comastri, A., Setti, G., Zamorani, G., Elvis, M., Wilkes, B. J., McDowell, J. C. & Giommi, P. 1992, *ApJ*, 384, 62.
- Comastri, A. et al. 2001, *A&A*, 365, 400.
- Constantin, A. & Shields, J. C. 2003, *PASP*, 115, 592.
- Coppi, P. S. 1999, in J. Poutanen & R. Svensson, eds, 'High Energy Processes in Accreting Black Holes', Vol. 161, p. 375.
- Courvoisier, T. J.-L. 1998, *A&ARv*, 9, 1.
- Courvoisier, T. J.-L., Turner, M. J. L., Robson, E. I., Gear, W. K., Staubert, R., Blecha, R., Bouchet, P., Falomo, R., Valtonen, M. & Terasranta, H. 1987, *A&A*, 176, 197.
- Croom, S. M., Rhook, K., Corbett, E. A., Boyle, B. J., Netzer, H., Loaring, N. S., Miller, L., Outram, P. J., Shanks, T. & Smith, R. J. 2002, *MNRAS*, 337, 275.

- Cruz-González, I., Carrasco, L., Serrano, A., Guichard, J., Dultzin-Hacyan, D. & Bisicchi, G. F. 1994, *ApJS*, 94, 47.
- Czerny, B. & Elvis, M. 1987, *ApJ*, 321, 305.
- Czerny, B., Nikolajuk, M., Piasecki, M. & Kuraskiewicz, J. 2001, *MNRAS*, 325, 865.
- Czerny, B. & Życki, P. T. 1994, *ApJ*, 431, L5.
- den Herder, J. W. et al. 2001, *A&A*, 365, L7.
- Derry, P. M., O'Brien, P. T., Reeves, J. N., Ward, M. J., Imanishi, M. & Ueno, S. 2003, *MNRAS*, 342, L53.
- Dewangan, G. C. 2002, *ApJ*, 581, L71.
- Dewangan, G. C., Griffiths, R. E. & Schurch, N. J. 2003, *ApJ*, 592, 52.
- di Salvo, T., Done, C., Życki, P. T., Burderi, L. & Robba, N. R. 2001, *ApJ*, 547, 1024.
- Dickey, J. M. & Lockman, F. J. 1990, *ARA&A*, 28, 215.
- Dietrich, M., Hamann, F., Shields, J. C., Constantin, A., Vestergaard, M., Chaffee, F., Foltz, C. B. & Junkkarinen, V. T. 2002, *ApJ*, 581, 912.
- Eckart, A. & Genzel, R. 1996, *Nature*, 383, 415.
- Eckart, A., Genzel, R., Ott, T. & Schödel, R. 2002, *MNRAS*, 331, 917.
- Eddington, A. D. 1925, *MNRAS*, 85, 408.
- Edelson, R. A. & Malkan, M. A. 1987, *ApJ*, 323, 516.
- Edelson, R. A., Pike, G. F. & Krolik, J. H. 1990, *ApJ*, 359, 86.
- Elvis, M., Fabrizio, F., Wilkes, B., McDowell, J. & Bechtold, J. 1994, *ApJ*, 422, 60.
- Elvis, M., Maccacaro, T., Wilson, A. S., Ward, M. J., Penston, M. V., Fosbury, R. A. E. & Perola, G. C. 1978, *MNRAS*, 183, 129.
- Eracleous, M. & Halpern, J. P. 1998, *ApJ*, 505, 577.

- Esin, A. A., Narayan, R., Cui, W., Grove, J. E. & Zhang, S.-N. 1998, *ApJ*, 505, 854.
- Fabian, A. C. 1998, in M. Abramowicz, G. Bjornsson & J. Pringle, eds, 'Theory of black hole accretion discs', CUP, p. 123.
- Fabian, A. C., Ballantyne, D. R., Merloni, A., Vaughan, S., Iwasawa, K. & Boller, T. 2002a, *MNRAS*, 331, L35.
- Fabian, A. C., Vaughan, S., Nandra, K., Iwasawa, K., Ballantyne, D. R., Lee, J. C., DeRosa, A., Turner, A. & Young, A. J. 2002b, *MNRAS*, 335, L1.
- Falomo, R., Kotilainen, J. & Treves, A. 2001, *ApJ*, 547, 124.
- Fanaroff, B. L. & Riley, J. M. 1974, *MNRAS*, 167, 31P.
- Fang, T., Sembach, K. R. & Canizares, C. R. 2003, *ApJ*, 586, L49.
- Feigelson, E. D. & Nelson, P. I. 1985, *ApJ*, 293, 192.
- Ford, H. A., Harms, R. J., Tsvetanov, Z. I., Hartig, G. F., Dressel, L. L., Kriss, G. A., Bohlin, R. C., Davidsen, A. F., Margon, B. & Kochhar, A. K. 1994, *ApJL*, 435, L27.
- Galeev, A. A., Rosner, R. & Vaiana, G. S. 1979, *ApJ*, 229, 318.
- Gaskell, C. M. 1985, *ApJ*, 291, 112.
- Genzel, R., Pichon, C., Eckart, A., Gerhard, O. E. & Ott, T. 2000, *MNRAS*, 317, 348.
- Ghez, A. M., Klein, B. L., Morris, M. & Becklin, E. E. 1998, *ApJ*, 509, 678.
- Ghisellini, G., Haardt, F. & Matt, G. 1994, *MNRAS*, 267, 743.
- Gierliński, M., Zdziarski, A. A., Poutanen, J., Coppi, P. S., Ebisawa, K. & Johnson, W. N. 1999, *MNRAS*, 309, 496.
- Gliozzi, M., Boller, T., Brinkmann, W. & Brandt, W. N. 2000, *A&A*, 356, L17.
- Gliozzi, M., Brinkmann, W., O'Brien, P. T., Reeves, J. N., Pounds, K. A., Trifoglio, M. & Gianotti, F. 2001, *A&A*, 365, L128.

- Gondoin, P., Orr, A. & Lumb, D. 2003, *A&A*, 398, 967.
- Gondoin, P., Orr, A., Lumb, D. & Siddiqui, H. 2003, *A&A*, 397, 883.
- Grandi, P., Maraschi, L., Urry, C. M. & Matt, G. 2001, *ApJ*, 556, 35.
- Grandi, P., Tagliaferri, G., Giommi, P., Barr, P. & Palumbo, G. G. C. 1992, *ApJS*, 82, 93.
- Green, P. J., Forster, K. & Kuraszkiewicz, J. 2001, *ApJ*, 556, 727.
- Grupe, D. 1996, PhD thesis, Universität Göttingen.
- Guainazzi, M. et al. 1998, *A&A*, 339, 327.
- Guilbert, P. W. & Rees, M. J. 1988, *MNRAS*, 233, 475.
- Haardt, F. & Maraschi, L. 1991, *ApJ*, 380, L51.
- Haardt, F., Maraschi, L. & Ghisellini, G. 1994, *ApJ*, 432, L95.
- Hamann, F. & Ferland, G. 1993, *ApJ*, 418, 11.
- Hasinger, G. et al. 2001, *A&A*, 365, L45.
- Hayashida, K. 2000, *NewAR*, 44, 419.
- Hazard, C., Mackey, M. B. & Shimmins, A. J. 1963, *Nature*, 197, 1037.
- Heckman, T. M. 1980, *A&A*, 87, 152.
- Heckman, T. M., González-Delgado, R., Leitherer, C., Meurer, G. R., Krolik, J., Wilson, A. S., Koratkar, A. & Kinney, A. 1997, *ApJ*, 482, 114.
- Hewett, P. C., Foltz, C. B. & Chaffee, F. H. 2001, *AJ*, 122, 518.
- Ho, L., Filippenko, A. V. & Sargent, W. L. W. 1994, in T.-L. Courvoisier & A. Blecha, eds, 'Multi-wavelength continuum emission of AGN', Kluwer Academic Publishers: Dordrecht, p. 275.
- Hoyle, F. & Fowler, W. A. 1963, *MNRAS*, 125, 169.

- Iovino, A., Clowes, R. & Shaver, P. 1996, *A&AS*, 119, 265.
- Ivezic, Z. et al. 2002, *AJ*, 124, 2364.
- Iwasawa, K., Brandt, W. N. & Fabian, A. C. 1998, *MNRAS*, 293, 251.
- Iwasawa, K. & Taniguchi, Y. 1993, *ApJ*, 413, L15.
- Janiuk, A. & Czerny, B. 1999, *NewA*, 5, 7.
- Janiuk, A., Kuraszekiewicz, J. & Czerny, B. 2001, in 'New Visions of the X-ray Universe in the *XMM* and *Chandra* era'. in press (astro-ph/0112388).
- Jansen, F. et al. 2001, *A&A*, 365, L1.
- Johnson, W. N. et al. 1993, *A&AS*, 97, 21.
- Jones, T. W., O'Dell, S. L. & Stein, W. A. 1974, *ApJ*, 188, 353.
- Kaastra, J. S., Mewe, R. & Raassen, A. J. J. 2002, in 'New Visions of the X-ray Universe in the *XMM* and *Chandra* era'. in press.
- Kahn, F. D. & Woltjer, L. 1959, *ApJ*, 130, 705.
- Kallman, T., Liedahl, D., Osterheld, A., Goldstein, W. & Kahn, S. 1996, *ApJ*, 465, 994.
- Kaspi, S., Smith, P. S., Netzer, H., Maoz, D., Jannuzi, B. T. & Giveon, U. 2000, *ApJ*, 533, 631.
- Kaspi, S. et al. 2002, *ApJ*, 574, 643.
- Kataoka, J., Tanihata, C., Kawai, N., Takahara, F., Takahashi, T., Edwards, P. G. & Makino, F. 2002, *MNRAS*, 336, 932.
- Kellogg, E., Gursky, H., Leong, C., Schreier, E., Tananbaum, H. & Giacconi, R. 1971, *ApJ*, 165, L49.
- Khachikian, E. Y. & Weedman, D. W. 1974, *ApJ*, 192, 581.
- Königl, A. & Kartje, J. F. 1994, *ApJ*, 434, 446.

Kormendy, J. 1988, *ApJ*, 325, 128.

Kriss, G. A. 1994, *AAS*, 184, 1308.

Krolik, J. H., Madau, P. & Życki, P. T. 1994, *ApJ*, 420, 57.

Kukula, M. J., Dunlop, J. S., Hughes, D. H. & Rawlings, S. 1998, *MNRAS*, 297, 366.

Lamer, G., Brunner, H. & Staubert, R. 1997, *A&A*, 327, 467.

Laor, A. 1991, *ApJ*, 376, 90.

Laor, A. 2000a, *ApJ*, 543, L111.

Laor, A. 2000b, *NewAR*, 44, 503.

Laor, A. & Netzer, H. 1989, *MNRAS*, 238, 897.

Lawson, A. J. & Turner, M. J. L. 1997, *MNRAS*, 288, 920.

Lawson, A. J., Turner, M. J. L., Williams, O. R., Stewart, G. C. & Saxton, R. D. 1992, *MNRAS*, 259, 743.

Leach, C. M., McHardy, I. M. & Papadakis, I. E. 1995, *MNRAS*, 272, 221.

Lee, J. C., Iwasawa, K., Houck, J. C., Fabian, A. C., Marshall, H. L. & Canizares, C. R. 2002, *ApJ*, 570, L47.

Lee, J. C., Ogle, P. M., Canizares, C. R., Marshall, H. L., Schulz, N. S., Morales, R., Fabian, A. C. & Iwasawa, K. 2001, *ApJ*, 554, L13.

Leighly, K. M. 1999, *ApJS*, 125, 317.

Lightman, A. P. & White, T. R. 1988, *ApJ*, 335, 57.

Liu, B. F., Mineshige, S., Meyer, F., Meyer-Hofmeister, E. & Kawaguchi, T. 2002, *ApJ*, 575, 117.

Liu, B. F., Mineshige, S. & Ohsuga, K. 2003, *ApJ*, 587, 571.

Liu, B. F., Mineshige, S. & Shibata, K. 2002, *ApJ*, 572, L173.

- Lubinski, P. & Zdziarski, A. A. 2001, *MNRAS*, 323, L37.
- Lynden-Bell, D. 1969, *Nature*, 223, 690.
- Maccacaro, T., Gioia, I. M., Wolter, A., Zamorani, G. & Stocke, J. T. 1988, *ApJ*, 326, 680.
- Magdziarz, P. & Zdziarski, A. A. 1995, *MNRAS*, 273, 837.
- Mainieri, V., Bergeron, J., Hasinger, G., Lehmann, I., Rosati, P., Schmidt, M., Szokoly, G. & della Ceca, R. 2002, *A&A*, 393, 425.
- Malkan, M. A. & Sargent, W. L. W. 1982, *ApJ*, 254, 22.
- Marshall, H. L., Fruscione, A. & Carone, T. E. 1995, *ApJ*, 439, 90.
- Marziani, P., Sulentic, J. W., Zamanov, R., Calvani, M., Dultzin-Hacyan, D., Bachev, R. & Zwitter, T. 2003, *ApJS*, 145, 199.
- Masnou, J. L., Wilkes, B. J., Elvis, M., McDowell, J. C. & Arnaud, K. A. 1992, *A&A*, 253, 35.
- Mason, K. O. et al. 2003, *ApJ*, 582, 95.
- Mason, K. et al. 2001, *A&A*, 365, L36.
- Mathur, S. 2000, *MNRAS*, 314, L17.
- Mathur, S., Wilkes, B. J. & Ghosh, H. 2002, *ApJ*, 570, L5.
- Matt, G., Guainazzi, M. & Maiolino, R. 2003, *MNRAS*, 342, 422.
- Matt, G., Guainazzi, M., Perola, G. C., Fiore, F., Nicastro, F., Cappi, M. & Piro, L. 2001, *A&A*, 377, L31.
- Mauder, W., Weigelt, G., Appenzeller, I. & Wagner, S. J. 1994, *A&A*, 285, 44.
- McLure, R. J. & Dunlop, J. S. 2001, *MNRAS*, 327, 199.
- Meier, D. L. 2002, *NewAR*, 46, 247.

- Merloni, A. & Fabian, A. C. 2001, *MNRAS*, 321, 549.
- Miller, J. S. & Goodrich, R. W. 1990, *ApJ*, 355, 456.
- Miller, L., Peacock, J. A. & Mead, A. R. G. 1990, *MNRAS*, 244, 207.
- Molendi, S. & Sembay, S. 2003, XMM-SOC-CAL-TN-0036, Technical report, *XMM-Newton*.
- Morales, R. & Fabian, A. C. 2002, *MNRAS*, 329, 209.
- Mulchaey, J. S., Koratkar, A., Ward, M. J., Wilson, A. S., Whittle, M., Antonucci, R. R. J., Kinney, A. L. & Hurt, T. 1994, *ApJ*, 436, 586.
- Mushotsky, R. F., Done, C. & Pounds, K. A. 1993, *ARA&A*, 31, 717.
- Mushotsky, R. F. & Ferland, G. J. 1984, *ApJ*, 278, 558.
- Nandra, K., Fabian, A. C., Brandt, W. N., Kunieda, H., Matsuoka, M., Mihara, T., Ogasaka, Y. & Terashima, Y. 1995, *MNRAS*, 276, 1.
- Nandra, K., George, I. M., Mushotzky, R. F., Turner, T. J. & Yaqoob, T. 1997, *ApJ*, 488, L91.
- Nandra, K. & Pounds, K. A. 1994, *MNRAS*, 268, 405.
- Nandra, K., Pounds, K. A., Stewart, G. C., George, I. M., Hayashida, K., Makino, F. & Ohasi, T. 1991, *MNRAS*, 248, 760.
- Narayan, R. & Yi, I. 1995, *ApJ*, 452, 710.
- Nayakshin, S. 2000, *ApJ*, 540, L37.
- Nayakshin, S. 2000a, PhD thesis, University of Arizona.
- Nayakshin, S., Kazanas, D. & Kallman, T. R. 2000, *ApJ*, 537, 833.
- Ne'Eman, Y. 1965, *ApJ*, 141, 1303.
- Netzer, H. 1990, in R. Blandford, H. Netzer & L. Woltjer, eds, 'Active Galactic Nuclei'.

Nicastro, F. 2000, *ApJ*, 530, L65.

Norman, C. & Scoville, N. 1988, *ApJ*, 332, 124.

Nowak, M. A. 1995, *PASP*, 107, 1207.

O'Brien, P. T., Page, K., Reeves, J. N., Pounds, K., Turner, M. J. L. & Puchnarewicz, E. M. 2001a, *MNRAS*, 327, 37.

O'Brien, P. T., Reeves, J. N., Turner, M. J. L., Pounds, K. A., Page, M., Gliozzi, M., Brinkmann, W., Stephen, J. B. & Dadina, M. 2001b, *A&A*, 365, L122.

Ogle, P. M., Marshall, H. L., Lee, J. C. & Canizares, C. R. 2000, *ApJL*, 545, L81.

Ohsuga, K. & Umemura, M. 2001, *A&A*, 371, 890.

Orr, A., Yaqoob, T., Parmar, A. N., Piro, L., White, N. E. & Grandi, P. 1998, *A&A*, 337, 685.

Osterbrock, D. E. 1981, *ApJ*, 249, 462.

Osterbrock, D. E. & Pogge, R. W. 1985, *ApJ*, 297, 166.

Page, K. L., O'Brien, P. T., Reeves, J. N. & Breeveld, A. A. 2003a, *MNRAS*, 340, 1052.

Page, K. L., Pounds, K. A., Reeves, J. N. & O'Brien, P. T. 2002, *MNRAS*, 330, L1.

Parnell, C. 2002, *A&G*, 43, 16.

Peterson, B. M. 1997, *An Introduction to Active Galactic Nuclei*, CUP, Cambridge, U.K.

Petrucchi, P. O., Haardt, F., Maraschi, L., Grandi, P., Matt, G., Nicastro, F., Piro, L., Perola, G. C. & de Rosa, A. 2000, *ApJ*, 540, 131.

Petrucchi, P. O. et al. 2002, *A&A*, 388, L5.

Piro, L., Matt, G. & Ricci, R. 1997, *A&AS*, 126, 525.

Porquet, D., Kaastra, J. S., Page, K. L., O'Brien, P. T., Ward, M. J. & Dubau, J. 2003. in press (astro-ph/0302413).

- Pounds, K. A., Done, C. & Osborne, J. 1995, *MNRAS*, 277, L5.
- Pounds, K. A., King, A. R., Page, K. L. & O'Brien, P. T. 2003d. in press (astro-ph/0305571).
- Pounds, K. A., Nandra, K., Stewart, G. C., George, I. M. & Fabian, A. C. 1990, *Nature*, 344, 132.
- Pounds, K. A., Nandra, K., Stewart, G. C. & Leighly, K. 1989, *MNRAS*, 240, 769.
- Pounds, K. A. & Reeves, J. N. 2002, in 'New Visions of the X-ray Universe in the *XMM* and *Chandra* era'. in press (astro-ph/0201436).
- Pounds, K. A., Reeves, J. N., King, A. R., Page, K. L., O'Brien, P. T. & Turner, M. J. L. 2003a. in press (astro-ph/0303603).
- Pounds, K. A., Reeves, J. N., Page, K. L., Edelson, R., Matt, G. & Perola, G. C. 2003b, *MNRAS*, 341, 953.
- Pounds, K. A., Reeves, J. N., Page, K. L., Wynn, G. A. & O'Brien, P. T. 2003c, *MNRAS*, 342, 1147.
- Pounds, K. A., Reeves, J., O'Brien, P., Page, K., Turner, M. & Nayakshin, S. 2001, *ApJ*, 559, 181.
- Pozdniakov, L. A., Sobol, I. M. & Sunyaev, R. A. 1976, *Soviet Astron. Letters*, 2, 55.
- Prieto, M. A. 1996, *MNRAS*, 282, 421.
- Puchnarewicz, E. M., Mason, K. O., Córdova, F. A., Kartje, J., Branduardi-Raymont, G., Mittaz, J. P. D., Murdin, P. G. & Allington-Smith, J. 1992, *MNRAS*, 256, 589.
- Puchnarewicz, E. M., Mason, K. O., Siemiginowska, A., Fruscione, A., Comastri, A., Fiore, F. & Cagnoni, I. 2001, *ApJ*, 550, 644.
- Punsly, B. & Coroniti, F. V. 1990, *ApJ*, 350, 518.
- Pye, J. P., McGale, P. A., Allan, D. J., Barber, C. R., Bertram, D., Denby, M., Page, C. G., Ricketts, M. J., Stewart, B. C. & West, R. G. 1995, *MNRAS*, 274, 1165.

Radovich, M. & Rafanelli, P. 1994, *AN*, 315, 265.

Rasmussen, A., Kahn, S. M. & Paerels, F. 2003, in J. Shull, ed., 'The IGM/Galaxy connection: The distribution of baryons at $z=0$.', Dordrecht: Kluwer. (astro-ph/0301183).

Recondo-Gonzalez, M. C., Wamsteker, W., Clavel, J., Rodriguez-Pascual, P. M., Vio, R., Ting-Gui, W., Santos-Lleó, M. & Makino, F. 1997, *A&AS*, 121, 461.

Reeves, J. N. 1999, PhD thesis, University of Leicester.

Reeves, J. N., O'Brien, P. T. & Ward, M. J. 2003, *ApJ*, 593, L65.

Reeves, J. N. & Turner, M. J. L. 2000, *MNRAS*, 316, 234.

Reeves, J. N., Turner, M. J. L., Ohashi, T. & Kii, T. 1997, *MNRAS*, 292, 468.

Reeves, J. N., Turner, M. J. L., Pounds, K. A., O'Brien, P. T., Boller, T., Ferrando, P., Kendziorra, E. & Vercellone, S. 2001, *A&A*, 365, L134.

Remillard, R. A., Bradt, H. V., Buckley, D. A. H., Roberts, W., Schwartz, D. A., Tuohy, I. R. & Wood, K. 1986, *ApJ*, 301, 742.

Remillard, R. A., Grossen, B., Bradt, H. V., Ohashi, T. & Hayashida, K. 1991, *Nature*, 350, 589.

Reynolds, C. S. 1996, PhD thesis, University of Cambridge.

Reynolds, C. S. 1997, *MNRAS*, 286, 513.

Ross, R. R. & Fabian, A. C. 1993, *MNRAS*, 261, 74.

Ross, R. R., Fabian, A. C. & Mineshige, S. 1992, *MNRAS*, 258, 189.

Rybicki, G. B. & Lightman, A. P. 1979, *Radiative processes in Astrophysics*, Wiley, New York.

Sako, M. et al. 2001, *A&A*, 365, L168.

- Saxton, R. D., Turner, M. J. L., Williams, O. R., Stewart, G. C., Ohashi, T. & Kii, T. 1993, *MNRAS*, 262, 63.
- Schartel, N., Walter, R., Fink, H. H. & Trümper, J. 1996, *A&A*, 307, 33.
- Schmidt, M. 1963, *Nature*, 197, 1040.
- Schödel, R. et al. 2002, *Nature*, 419, 694.
- Seyfert, C. 1943, *ApJ*, 97, 28.
- Shakura, N. I. & Sunyaev, R. A. 1973, *A&A*, 24, 337.
- Shemmer, O. & Netzer, H. 2002, *ApJ*, 567, L19.
- Shields, G. A. 1978, *Nature*, 272, 706.
- Shimura, T. & Takahara, F. 1993, *ApJ*, 419, 78.
- Shore, S. N. & White, R. L. 1982, *ApJ*, 256, 390.
- Shuder, J. M. & Osterbrock, D. E. 1981, *ApJ*, 250, 55.
- Siebert, J., Leighly, K. M., Laurent-Muehleisen, S. A., Brinkmann, W., Boller, T. & Matsuoka, M. 1999, *A&A*, 348, 678.
- Smith, M. G. 1976, *ApJ*, 206, L125.
- Spitzer, Jr., L. 1956, *ApJ*, 124, 20.
- Staubert, R. 1992, in W. Brinkmann & J. Trümper, eds, 'X-ray Emission from AGN and the Cosmic X-ray background', Vol. 235 of *MPE Report*, p. 42.
- Steenbrugge, K. C., Kaastra, J. S., de Vries, C. P. & Edelson, R. 2003, *A&A*, 402, 477.
- Strüder, L. et al. 2001, *A&A*, 365, L18.
- Sunyaev, R. A. & Titarchuk, L. G. 1980, *A&A*, 86, 121.
- Tanaka, Y. 1990, in N. White, ed., 'Proc. of 23rd ESLAB Symposium on Two Topics in X-Ray Astronomy', p. 3. ESA SP-296.

- Tananbaum, H. et al. 1979, *ApJ*, 234, L9.
- Telfer, R. C., Zheng, W., Kriss, G. A. & Davidsen, A. F. 2002, *ApJ*, 565, 773.
- Titarchuk, L. 1994, *ApJ*, 434, 570.
- Türler, M. et al. 1999, *A&AS*, 134, 89.
- Turner, A. K., Fabian, A. C., Vaughan, S. & Lee, J. C. 2003. submitted (astro-ph/0303418).
- Turner, M. J. L., Courvoisier, T., Staubert, R., Molenti, D. & Trümper, J. 1985, in A. Peacock, ed., 'Proc. of 18th ESLAB Symposium', Reidel, Dordrecht, p. 623.
- Turner, M. J. L. et al. 1990, *MNRAS*, 244, 310.
- Turner, M. J. L. et al. 2001, *A&A*, 365, L27.
- Turner, T. J. 1993, in 'The 1st annual *ROSAT* Science Symposium and Data Analysis', University of Maryland.
- Turner, T. J., George, I. M., Grupe, D., Nandra, K., Remillard, R. A., Leighly, K. M., Marshall, H. L., Kraemer, S. B. & Crenshaw, D. M. 1999, *ApJ*, 510, 178.
- Turner, T. J., George, I. M., Yaqoob, T., Kriss, G., Crenshaw, D. M., Kraemer, S., Zheng, W., Wang, J. & Nandra, K. 2001, *ApJ*, 548, L13.
- Turner, T. J., Mushotzky, R. F., Yaqoob, T., George, I. M., Snowden, S. L., Netzer, H., Kraemer, S. B., Nandra, K. & Chelouche, D. 2002, *ApJ*, 574, L123.
- Turner, T. J. & Pounds, K. A. 1989, *MNRAS*, 240, 833.
- Turner, T. J., Weaver, K. A., Mushotsky, R. F., Holt, S. S. & Madejski, G. M. 1991, *ApJ*, 381, 85.
- Tytler, D. & Fan, X.-M. 1992, *ApJS*, 79, 1.
- Ulrich, M.-H., Maraschi, L. & Urry, C. M. 1997, *ARA&A*, 35, 445.
- Urry, M. C. & Padovani, P. 1995, *PASP*, 107, 803.

- Vaughan, S., Boller, T., Fabian, A. C., Ballantyne, D. R., Brandt, W. N. & Trümper, J. 2002, *MNRAS*, 337, 247.
- Vaughan, S., Reeves, J., Warwick, R. & Edelson, R. 1999, *MNRAS*, 309, 113.
- Véron-Cetty, M.-P. & Véron, P. 1996, *ESO Sci. Rep.*, 17, 1.
- Véron-Cetty, M.-P., Véron, P. & Gonçalves, A. C. 2001, *A&A*, 372, 730.
- Véron-Cetty, M.-P. & Woltjer, L. 1990, *A&A*, 236, 69.
- Vignali, C., Brandt, W. N., Fan, X., Gunn, J. E., Kaspi, S., Schneider, D. P. & Strauss, M. A. 2001, *AJ*, 122, 2143.
- Vignali, C., Comastri, A., Cappi, A., Palumbo, G. G. C., Matsuoka, M. & Kubo, H. 1999, *ApJ*, 516, 582.
- Walter, R. & Fink, H. H. 1993, *A&A*, 274, 105.
- Wandel, A. 1997, *ApJ*, 490, L131.
- Wandel, A. 1999, *ApJ*, 519, L39.
- Wandel, A. 2003, in L. Ho, ed., ‘Carnegie Conference on Coevolution of Black Holes and Galaxies’. in press (astro-ph/0303562).
- Wandel, A., Peterson, B. M. & Malkan, M. A. 1999, *ApJ*, 526, 579.
- Wang, J.-M. & Netzer, H. 2003, *A&A*, 398, 927.
- Wang, T.-G., Lu, Y.-J. & Zhou, Y.-Y. 1998, *ApJ*, 493, 1.
- Wang, T.-G., Matsuoka, M., Kubo, H., Mihara, T. & Negoro, H. 2001, *ApJ*, 554, 233.
- Wang, Y. P., Biermann, P. L. & Wandel, A. 2000, *A&A*, 361, 550.
- Weaver, K. A., Mushotzky, R. F., Serlemitsos, P. J., Wilson, A. S., Elvis, M. & Briel, U. 1995, *ApJ*, 442, 597.
- Weedman, D. 1983, *ApJ*, 266, 479.

- White, R. L. et al. 2000, *ApJS*, 126, 133.
- Wilkes, B. J. & Elvis, M. 1987, *ApJ*, 323, 243.
- Williams, O. et al. 1992, *ApJ*, 389, 157.
- Wilms, J., Reynolds, C. S., Begelman, M. C., Reeves, J., Molendi, S., Staubert, R. & Kendziorra, E. 2001, *MNRAS*, 328, L27.
- Worrall, D. M., Tananbaum, H., Giommi, P. & Zamorani, G. 1987, *ApJ*, 313, 596.
- Xia, T.-S. & Zhang, J.-L. 2001, *A&A*, 371, 93.
- Yaqoob, T., George, I. M., Kallman, T. R., Padmanabhan, U., Weaver, K. A. & Turner, T. J. 2003, *ApJ*, 596, 85.
- Yaqoob, T., George, I. M., Nandra, K., Turner, T. J., Serlemitsos, P. J. & Mushotzky, R. F. 2001, *ApJ*, 546, 759.
- Yaqoob, T. et al. 1994, *PASJ*, 46, L49.
- Yaqoob, T. et al. 2000, ASCA-CAL-00-06-01, Technical report, ASCA Guest Observer Facility.
- Yuan, W., Brinkmann, W., Siebert, J. & Voges, W. 1998, *A&A*, 330, 108.
- Zamorani, G., Marano, B., Mignoli, M., Zitelli, V. & Boyle, B. J. 1992, *MNRAS*, 256, 238.
- Zamorani, G. et al. 1981, *ApJ*, 245, 357.
- Zdziarski, A. A., Lubiński, P. & Smith, D. A. 1999, *MNRAS*, 303, L11.
- Zhang, L. & Cheng, K. S. 1997, *ApJ*, 488, 94.
- Zhou, Y. Y. & Yu, K. N. 1992, *ApJ*, 400, 430.
- Życki, P. T., Done, C. & Smith, D. A. 1999, *MNRAS*, 305, 231.